

Northumbria Research Link

Citation: Ijaz, Muhammad (2013) Experimental Characterisation and Modelling of Atmospheric Fog and Turbulence in FSO. Doctoral thesis, Northumbria University.

This version was downloaded from Northumbria Research Link:
<http://nrl.northumbria.ac.uk/15255/>

Northumbria University has developed Northumbria Research Link (NRL) to enable users to access the University's research output. Copyright © and moral rights for items on NRL are retained by the individual author(s) and/or other copyright owners. Single copies of full items can be reproduced, displayed or performed, and given to third parties in any format or medium for personal research or study, educational, or not-for-profit purposes without prior permission or charge, provided the authors, title and full bibliographic details are given, as well as a hyperlink and/or URL to the original metadata page. The content must not be changed in any way. Full items must not be sold commercially in any format or medium without formal permission of the copyright holder. The full policy is available online: <http://nrl.northumbria.ac.uk/policies.html>

www.northumbria.ac.uk/nrl



Experimental Characterisation and Modelling of Atmospheric Fog and Turbulence in FSO

Muhammad Ijaz

A thesis submitted in partial fulfilment of the
requirements of the University of Northumbria at
Newcastle for the degree of Doctor of Philosophy

Research undertaken in the Faculty of Engineering and
Environment

May 2013

Abstract:

Free space optical (FSO) communication uses visible or infrared (IR) wavelengths to broadcast high-speed data wirelessly through the atmospheric channel. The performance of FSO communications is mainly dependent on the unpredictable atmospheric channel such as fog, smoke and temperature dependent turbulence. However, as the real outdoor atmosphere (ROA) is time varying and heterogeneous in nature as well as depending on the magnitude and intensity of different weather conditions, carrying out a proper link assessment under specific weather conditions becomes a challenging task. Investigation and modelling the ROA under diverse atmospheric conditions is still a great challenge in FSO communications. Hence a dedicated indoor atmospheric chamber is designed and built to produce controlled atmosphere as necessary to mimic the ROA as closely as possible. The experimental results indicate that the fog attenuation is wavelength dependent for all visibility V ranges, which contradicts the Kim model for $V < 0.5$ km. The obtained result validates that Kim model needs to be revised for $V < 0.5$ km in order to correctly predict the wavelength dependent fog attenuation. Also, there are no experimental data and empirical model available for FSO links in diverse smoke conditions, which are common in urban areas. Therefore, a new empirical model is proposed to evaluate the wavelength dependent fog and smoke attenuation by reconsidering the q value as a function of wavelength rather than visibility.

The BER performance of an FSO system is theoretically and experimentally evaluated for OOK- NRZ, OOK-RZ and 4-PPM formats for Ethernet line data-rates from light to dense fog conditions. A BER of 10^{-6} (Q -factor 4.7) is achieved at

dense fog (transmittance, $T = 0.33$) condition using 4-PPM than OOK-NRZ and OOK-RZ modulation schemes due to its high peak-to-average power ratio albeit at the expense of doubling the bandwidth. The effects of fog on OOK-NRZ, 4-PAM and BPSK are also experimentally investigated. In comparison to 4-PAM and OOK-NRZ signals, the BPSK modulation signalling format is more robust against the effects of fog. Moreover, the effects of using different average transmitted optical communication powers P_{opt} on the T and the received Q -factor using the OOK-NRZ modulation scheme are also investigated for light and dense fog conditions. The results show that for an FSO system operating at a Q -factor of 4.7 (for $\text{BER} = 10^{-6}$), the required Q -factor is achieved at T of 48% under the thick fog condition by increasing P_{opt} to 1.07 dBm, whereas the values of T are 55% and $\sim 70\%$ for the transmit power of 0.56 dBm and -0.7 dBm, respectively.

The experimental characterisation and investigation of the atmospheric turbulence effect on the Ethernet and Fast-Ethernet FSO link is reported using different modulation schemes. The experiment is carried out in a controlled laboratory environment where turbulence is generated in a dedicated indoor atmospheric chamber. The atmospheric chamber is calibrated to mimic an outdoor turbulence conditions and the measured data are verified against the theoretical predictions. The experiment also demonstrates methods to control the turbulence levels and determine the equivalence between the indoor and outdoor FSO links. The results show that the connectivity of Ethernet and Fast-Ethernet links are highly sensitive to atmospheric turbulence. The results also show that the BPSK and OOK-NRZ modulation signalling formats are more robust against the weak atmospheric turbulence conditions than PAM signal.

Table of Contents

Abstract.....	ii
List of Figures.....	x
List of Tables.....	xvii
Glossary of Abbreviations.....	xix
Glossary of Symbols.....	xxiii
Dedications	xxvii
Acknowledgements.....	xxviii
Declarations.....	xxx
Chapter One Introduction	
1.1. Background	1
1.2. Research Motivations	5
1.3. Research Objectives	12
1.4. Original Contributions.....	14
1.5. Thesis Organization.....	19
1.6. List of Publications and Awards	22
1.6.1. Journal publications	22
1.6.2. Conference publications.....	23
1.6.3. Research seminars and poster presentations	25
1.6.4. Awards	26

Chapter Two Fundamentals of FSO Communication

2.1.	Introduction	27
2.2.	The Electromagnetic Spectrum	28
2.3.	Features of FSO Communications	30
2.4.	Areas of Applications	34
2.5.	FSO System	37
2.5.1.	FSO transmitter	38
2.5.2.	FSO receiver.....	41
2.5.3.	Atmospheric channel.....	43
2.6.	Modulation Schemes	47
2.6.1.	OOK-NRZ.....	49
2.6.2.	PPM.....	51
2.6.3.	PAM	54
2.6.4.	BPSK.....	56
2.7.	Eye Safety and Standards	59
2.8.	Summary	62

Chapter Three Fog and Smoke Atmospheric Channel

3.1.	Introduction	63
3.2.	Fog Composition	64
3.3.	Smoke Composition	67
3.4.	Characterisation of Fog and Smoke Attenuation	69

3.4.1.	Theoretical approach	69
3.4.2.	Empirical approach	74
3.5.	Fog Models	76
3.6.	Summary	85
 Chapter Four Atmospheric Turbulence Channel		
4.1.	Introduction	86
4.2.	Atmospheric Turbulence Channel.....	88
4.3.	Log-Normal Turbulence Model	93
4.3.1.	Spatial coherence in weak turbulence	100
4.3.2.	Aperture averaging and BER evaluation:	102
4.3.3.	The Limit of log-normal turbulence model.....	104
4.4.	The Gamma-Gamma Turbulence Model	105
4.5.	Negative Exponential Turbulence Model	109
4.6.	Summary	111
 Chapter Five Design of Controlled Atmospheric Channel		
5.1.	Introduction	112
5.2.	Atmospheric Chamber	114
5.3.	Calibrations of Lab Based Fog and Smoke to Real Outdoor Fog.....	116
5.4.	Controlled Fog Atmosphere.....	118
5.4.1.	Homogeneous fog atmospheric channel	118
5.5.	Data Acquisition for Fog Attenuation Measurements	122

5.6.	Experimental Performance of Fog Models under Controlled Fog Channel .	129
5.6.1.	Dense fog conditions	130
5.6.2.	Thick fog conditions	131
5.6.3.	Moderate fog conditions	132
5.6.4.	Light fog conditions	133
5.7.	Controlled Atmospheric Turbulence Channel	135
5.8.	Summary	137
 Chapter Six Modelling of Fog and Smoke Attenuation		
6.1.	Introduction	139
6.2.	Enhancement in Atmospheric Visibility Measurements	141
6.2.1.	Using CCD method	141
6.2.2.	Using laser diode	143
6.3.	Comparison of Field and Indoor Measured Visibility	144
6.4.	Fog Attenuation Measurements	146
6.5.	Smoke Attenuation Measurements	147
6.6.	Empirical Modelling of Fog and Smoke	150
6.7.	Comparison of the Measured Visibility and Attenuation Data with the Proposed Model	153
6.8.	Comparison of Model with Attenuation Spectrum Measurements	156
6.8.1.	Fog	156
6.8.2.	Smoke	159

6.9. Summary	161
--------------------	-----

Chapter Seven BER Performance of FSO under Controlled Fog Conditions

7.1. Introduction	162
7.2. Bit Error Rate Evaluation in a Controlled Fog Channel	164
7.3. Experimental Setup for BER Measurement of FSO Communications under Lab-controlled Fog	166
7.4. FSO Link Performance for Different Modulation Schemes in Fog Channel	169
7.4.1. Using OOK-NRZ, OOK-RZ and 4-PPM	169
7.4.2. Using OOK-NRZ, 4-PAM and BPSK	173
7.5. FSO Link Performance for Different Launched Powers	175
7.5.1. Measured eye diagrams	178
7.6. FSO Link Budget in Fog Channel	179
7.7. Summary	182

Chapter Eight Performance Analysis of FSO under Controlled Weak Turbulence Condition

8.1. Introduction	183
8.2. Experiment Setup for Turbulence Channel	185
8.3. Experimental Characterisation of Turbulence	190
8.4. Measured Histograms of Received Signal	193
8.5. Performance Analysis Measurements for FSO	195
8.6. Performance of Different Modulation Techniques under Controlled FSO Turbulence Channel	201

8.7.	Calibration to the Outdoor FSO Link	204
8.8.	Summary	206
Chapter Nine Conclusions and Future Work		
9.1.	Conclusions.....	207
9.2.	Future Work	213
Appendix A:		216
References		219

List of Figures

Figure 1.1. Outline of the research road map and original contribution.	18
Figure 2.1. The overview of the EM spectrum with its nominated frequency bands.	29
Figure 2.2. Comparison of a range of optical and RF wireless technologies [113]...	31
Figure 2.3. Comparison on bandwidth cost for FSO, RF and Fibre based communication system [120].	33
Figure 2.4. A simple block diagram showing the building-to-building communication in last mile access network using FSO.	35
Figure 2.5. The block diagram of line of sight FSO communication system.	38
Figure 2.6. Transmission as a function of wavelength for urban aerosols conditions ($V = 5$ km), calculated from MODTRAN, reproduced from [120].	40
Figure 2.7. The divergence of the optical beam after 1 km distance.	44
Figure 2.8. Comparison between Rayleigh, Geometric and Mie scattering.	45
Figure 2.9. Power spectrum of the transmitted signals for OOK-NRZ and RZ [205].	50
Figure 2.10. Time domain waveforms for 4-bit OOK and 16-PPM.	52
Figure 2.11. BER performance for OOK (NRZ and RZ), and 4-PPM	53
Figure 2.12. Time domain waveforms of 4-PAM modulation schemes.	55
Figure 2.13. BER performance against the SNR for different levels of PAM.	56
Figure 2.14. Block diagram of BPSK subcarrier intensity modulated FSO link.	57
Figure 2.15. Response/absorption of the human eye at various wavelengths [153]..	60
Figure 3.1. The mechanism of convection fog formation.	65
Figure 3.2. The mechanism of advection fog formation.	66

Figure 3.3. Refractive index for glycerine based smoke against the wavelength.	68
Figure 3.4. Refractive index for water against the wavelength.....	71
Figure 3.5. Particle size distribution versus particle radius (μm): (a) advection fog, and (b) convection fog.	74
Figure 3.6. Attenuation versus visibility using Kruse model, T_{th} : (a) 2%, (b) 5%.....	77
Figure 3.7. Kim model for T_{th} of 2%.....	79
Figure 3.8. Comparison of the Kim model, Naboulsi advection and convection fog at $\lambda = 0.83 \mu\text{m}$	80
Figure 3.9. Comparison of the Kim model, Naboulsi advection and convection fog at $\lambda = 0.83 \mu\text{m}$	81
Figure 3.10. Comparison of the Kim model, Naboulsi advection and convection fog: (a) $\lambda = 1.55 \mu\text{m}$, and (b) $\lambda = 2.0 \mu\text{m}$	81
Figure 3.11. Comparison of different models for a range of wavelengths for different visibility values: (a) 0.1 km, (b) 0.25 km, (c) 0.5 km, (d) 1 km.....	84
Figure 4.1. Atmospheric channel based on velocity fluctuations with turbulent eddies.....	89
Figure 4.2. Log-normal pdf against the normalized irradiance for a range of irradiance variance values.	99
Figure 4.3. Plane wave transverse coherence length for $\lambda = 830 \text{ nm}$ and a range of C_n^2	101
Figure 4.4. Plane wave transverse coherence length for $\lambda = 1550 \text{ nm}$ and a range of C_n^2	102
Figure 4.5. Gamma-gamma probability density function for three different turbulence regimes, namely weak, moderate and strong.	107

Figure 4.6. $S.I.$ against the log intensity variance for $C_n^2 = 10^{-15} \text{ m}^{-2/3}$ and $\lambda = 830 \text{ nm}$	108
Figure 4.7. Values of σ and β against the log intensity variance for different turbulence regimes: weak, moderate to strong and saturation.	109
Figure 4.8. Negative exponential probability density function for different values of I_0	110
Figure 5.1. A snapshot of an atmospheric chamber in the lab.....	116
Figure 5.2. The mechanism of artificial formation.	116
Figure 5.3. Comparison of measured mean ROF attenuation for two field experiments [5, 6] and the mean lab based fog attenuation data at 0.83 m	117
Figure 5.4. Real outdoor fog scenario, considering FSO link length of 1 km	118
Figure 5.5. Block diagram of experiment setup to measure V along the length of FSO link.	119
Figure 5.6. Visibility (km) versus the change in attenuation (dB) due to $\pm 0.1 \text{ dB}$ fluctuations in loss.	121
Figure 5.7. Visibility (km) versus the change in visibility (km), black (solid line) is real V for link range $L = 5.5 \text{ m}$	121
Figure 5.8. (a) The experimental setup to measure the fog attenuation and visibility, and (b) the laboratory controlled atmospheric chamber and FSO link setup, and the (inset) shows the presence of fog and the scattering of light in the atmospheric chamber.....	122
Figure 5.9. The block diagram for the measurement of fog attenuation and visibility.	124
Figure 5.10. Time dependence of visibility within the FSO chamber.	125

Figure 5.11. Measured attenuation against the time for full fog event at wavelength of 1550 nm.	126
Figure 5.12. (a) Difference between moving average and data, and (b) Difference probability density function.	127
Figure 5.13. Comparison between filtered and non-filtered data at wavelength of 1550 nm under fog conditions.....	128
Figure 5.14. The measured fog attenuation for the visible – NIR spectrum against the visibility (km).....	130
Figure 5.15. Comparison of the selected empirical models with measured fog attenuation (dB/km) from the visible – NIR spectrum at $V = 0.048$ km.....	131
Figure 5.16. Comparison of the selected empirical models with measured fog attenuation (dB/km) from the visible – NIR spectrum at $V \sim 0.300$ km.....	132
Figure 5.17. Comparison of the selected empirical models with measured fog attenuation (dB/km) from the visible to NIR spectrum at $V \sim 0.46$ km.....	133
Figure 5.18. Comparison of the selected empirical models with measured fog attenuation (dB/km) from the visible – NIR spectrum $V = 0.78$ km.....	134
Figure 5.19. The heating elements to create turbulence inside the chamber (one plate). The electrical heater and fan are located below the metal plate.	135
Figure 5.20. The block diagram of heating elements in each block of chamber.	136
Figure 6.1. CCD camera fog measurements snapshots with light (left) and dense (right) fog conditions, both at the atmospheric chamber.....	142
Figure 6.2. The experimental set up to measure fog attenuation and visibility.	144
Figure 6.3. Comparison of the measured visibility for outdoor and atmospheric chamber.....	145

Figure 6.4. The characterisation of measured visibility and fog attenuation using CCD, laser diodes and Kim model.....	146
Figure 6.5. The measured attenuation (dB/ km) and visibility for fog.	147
Figure 6.6. Comparison of the measured average loss at wavelengths of 0.83 and 1.55 μm under the laboratory based controlled smoke.	148
Figure 6.7. The comparison of the measured smoke attenuation (dB/ km) for 0.830 and 1.55 μm for the FSO link length of 1 km.	149
Figure 6.8. The average attenuation difference between 0.83 and 1.55 μm as a function of measured visibility (km) for FSO link length of 1 km.	149
Figure 6.9. The predicted q value and linear curve of best-fit against wavelength for fog.	152
Figure 6.10. The predicted q value and linear curve of best-fit against wavelength for smoke.	153
Figure 6.11. Real time measured fog attenuation versus visibility ($V = 1$ km) and curves of modified fog and Kim models for different wavelengths.	155
Figure 6.12. Real time measured smoke attenuation versus visibility ($V = 1$ km) and curves of smoke model for different wavelengths.	155
Figure 6.13. The measured fog attenuation (dB/km) from the visible – NIR spectrum and the comparison with the selected empirical models (a) for $V = 0.048$ km, and (b) for $V = 0.3$ km.	158
Figure 6.14. The measured smoke attenuation (dB/km) from the visible – NIR spectrum and the comparison with the selected empirical models (a) for $V = 0.185$ km, and (b) for $V = 0.245$ km.....	160
Figure 7.1. The eye diagram and the distribution of bits ‘0’ and ‘1’ for BER evaluation in fog.....	164

Figure 7.2. Block diagram of experiment setup for Q -factor evaluation in fog.....	168
Figure 7.3. Q - factors versus T for OOK-NRZ, OOK-RZ and 4-PPM for different fog conditions (measured (dot points) , theory (dotted lines)).....	170
Figure 7.4. Measured eye-diagrams post-processed for (a-b) OOK-NRZ, (c-d) OOK-RZ and (e-f) 4-PPM received signals eye-diagrams for $T = 0.30$ and $T = 0.70$, for dense and light fog conditions, respectively.....	171
Figure 7.5. BER of OOK-NRZ, OOK-RZ and 4-PPM for different measured optical powers in fog (measured (solid points), theory (dotted lines)).	172
Figure 7.6. Measured Q -factor for OOK-NRZ, 4-PAM and BPSK for same P_{tx} and 5 Mbit/s data rate at different T of link values and fog conditions.	173
Figure 7.7. Measured eye-diagrams post-processed for (a-b) OOK-NRZ, (c-d) 4-PAM and (e-f) BPSK received signals eye-diagrams for $T = 0.37$ and $T = 0.70$, for dense and light fog conditions, respectively. Obtained after a $0.75 \cdot R $ Hz low pass filter.....	175
Figure 7.8. Q -factor against the transmittance, and (b) the BER versus the transmittance for channel with fog for a range of transmitted optical power.	177
Figure 7.9. The received signal eye diagram (real time) for different P_{opt} , time scale is 20 ns/div, voltage scale is 5mV/div: (a) for 100% transmittance, (b) for 50% transmittance, and (c) for 30% transmittance.	178
Figure 7.10. Link margin values against transmittance for the FSO communication under lab-controlled fog conditions.	181
Figure 8.1. (a) Block diagram of experiment setup, and (b) the chamber and FSO link setup in the laboratory.....	186
Figure 8.2. Sketch of diverted beams due to turbulence source positioned: (a) near the transmitter, (b) in the middle and (c) near the receiver.....	189

Figure 8.3. The average refractive index structure C_n^2 against the temperature gradient within a controlled atmospheric chamber.	191
Figure 8.4. The theoretical and measured scintillation index σ_I^2 against the temperature gradient for the controlled atmospheric chamber.	192
Figure 8.5. Received signal distribution: (a) without turbulence, (b) with turbulence $\sigma_I^2 = 0.009$, (c) $\sigma_I^2 = 0.06$, and (d) $\sigma_I^2 = 0.240$ (the curve fitting is shown by solid lines).	195
Figure 8.6. The measured eye-diagrams of received Ethernet signal (NRZ 4B5B, line rate 12.5Mbit/s), (a) no turbulence and (b) weak turbulence with $\sigma_I^2 = 0.0164$	196
Figure 8.7. The measured eye-diagram of received Fast-Ethernet signal, NRZ 4B5B, line rate 125Mbit/s in the condition of: (a) no turbulence, and (b) weak turbulence with the scintillation index $\sigma_I^2 = 0.0164$	197
Figure 8.8. The predicted and measured Q -factor against different scintillation index values for (a) Ethernet and (b) Fast-Ethernet.	199
Figure 8.9. BER performance against a range of scintillation indexes for Ethernet and Fast-Ethernet FSO links (note that BER values below 10^{-6} are truncated).	200
Figure 8.10. Measured Q values against a range of Rytov variance for OOK, 4-PAM and BPSK: (a) the absolute scale at 5 Mbit/s, and (b) normalized to the Q -factor of OOK-NRZ.	202
Figure 8.11. Histograms for the OOK: (a) without turbulence, (b) Rytov variance of 0.005, (c) 4-PAM, without turbulence, and (d) Rytov variance of 0.005 received signals at 20 Mbit/s	204

List of Tables

Table 2.1. Comparison between FSO and RF communication systems.	36
Table 2.2. Comparison of different features of Laser and LED.....	39
Table 2.3. Comparison of some main characteristics of PIN and APD photodiodes [166].	42
Table 2.4. The main characteristic of the photodetector materials.	43
Table 2.5. Comparison of OOK-NRZ, RZ and 4-PPM modulation techniques.	54
Table 2.6. The specifications of the mostly used semiconductor laser.	61
Table 3.1. International visibility codes and corresponding visibility (km) [243].	66
Table 3.2. Measured V and T values at $0.550\ \mu\text{m}$	68
Table 3.3. The values of refractive index for real and imaginary part for water.	71
Table 3.4. Particle size distribution for advection and maritime fog.	73
Table 4.1. Strength of Turbulence based on $S.I$	99
Table 4.2. The dependence of wavelength on spatial coherence length for $C_n^2 = 10^{-12}$ $\text{m}^{-2/3}$	101
Table 5.1. The chamber dimensions and the main parameter.....	115
Table 5.2. Attenuation of 550 nm laser at given values of V for $L = 5.5\ \text{m}$ and $11\ \text{m}$	126
Table 6.1. Values of q obtained for different wavelength from measured fog and smoke attenuation data.....	150
Table 6.2. The suitable possible wavelengths to operate in the foggy channel, measured at $V = 0.048\ \text{km}$	157

Table 7.1. Measured T and related visibility values at 830 nm.....	166
Table 7.2. Main parameters of the FSO used in the experiment.....	168
Table 7.3. Experimental measured values for 0.56 dBm transmitted signal.....	179
Table 8.1. Parameters of the FSO link under controlled turbulence conditions.....	187
Table 8.2. Measured temperatures over five experiments at four positions within the chamber.....	190
Table 8.3. Measured σ_I^2 along the chamber length.....	194

Glossary of Abbreviations

2G	Second generation
3G	Third generation
4G	Fourth generation
ADSL	Asymmetric digital subscriber line
AEL	Allowable exposure limit
ANSI	American national standards institute
APD	Avalanche photodiode
AWG	Arbitrary waveform generator
AWGN	Additive white gaussian noise
BER	Bit error rate
BPSK	Binary phase shift keying
CCD	Charged coupled camera
DAQ	Data acquisition
DMT	Discrete multi-tones
DPIM	Differential pulse interval modulation
DSL	Digital subscriber loop
DVB-T	Digital video broadcasting – terrestrial
EM	Electromagnetic
EMI	Electromagnetic interference
EPON	Ethernet passive optical networks
FCC	Federal communication commission

FIR	Far infrared
FoV	Field of view
FSO	Free space optics
FTTH	Fibre to the home
Gbps	Gigabit per second
Ge	Germanium
GaAs	Gallium arsenide
HAPs	High altitude platforms
HDTV	High definition television
ICT	Communication technology
IEC	International electrotechnical commission
IID	Independently and identical distributed
IM/DD	Intensity modulation/direct detection
InGaAs	Indium gallium arsenide
InGaAsP	Indium gallium arsenide phosphide
InP	Indium phosphide
IR	Infrared
ISR	Intelligence, surveillance and reconnaissance
Km	Kilometre
LAN	Local area network
LED	Light emitting diode
LMDS	Local multipoint distribution service
LOS	Line of sight
MANs	Metropolitan area networks

Mbps	Megabit per second
MIMO	Multiple input multiple output
MLCD	Mars laser communication demonstration
mm-Wave	Millimetre wave
MSC	Multiple subcarriers
MVR	Meteorological visual range
NEC	Nippon electric company
NIR	Near infrared
OAM	Orbital angular momentum
Ofcom	Office of communication
OFDM	Orthogonal frequency division multiplexing
OOK	On-off-keying
OOK-NRZ	On-off-keying-non return to zero
OOK-RZ	On-off-keying- return to zero
OWC	Optical wireless communication
OSA	Optical spectrum analyzer
PAM	Pulse amplitude modulation
pdf	Probability distribution function
PLC	Power line communication
PM	Phase modulator
PoLSK	Polarization shift keying
PPM	Pulse position modulation
PRBS	Pseudo random bit sequence
QAM	Quadrature amplitude modulation

RF	Radio frequency
RMSE	Root mean squared error
ROA	Real outdoor atmosphere
ROF	Real outdoor fog
RoFSO	Radio-on-free-space optics
S	Silicon
S.I	Scintillation index
SD	Standard deviation
SILEX	Semiconductor-laser inter-satellite link experiment
SIM	Subcarrier intensity modulation
SNR	Signal-to-noise ratio
SNR_0	Signal to noise ratio without turbulence
SNR_e	Electrical signal to noise ratio
SUT	Spectrum under test
Tbps	Terabit per second
THz	Terahertz
TIA	Trans-impedance amplifier
UAVs	Unmanned aerial vehicles
UV	Ultraviolet
WDM	wavelength division multiplexing
WLAN	Wireless local area network

Glossary of Symbols

$A_o(r)$	Amplitude function
$A(r)$	Amplitude function with turbulence
A_{rx}	Receiver aperture
\hat{A}	Normal value
B	Bandwidth
B_e	Electrical filter bandwidth
C_a	Molecular absorption
C_v^2	Velocity structure constant
C_T^2	Temperature structure constant
C_n^2	Refractive index structure parameter
$C_{n \text{ indoor}}^2$	Refractive index structure parameter for indoor
$C_{n \text{ outdoor}}^2$	Refractive index structure parameter for outdoor
$d(t)$	Pre-modulated data
\vec{E}	Electric field
f	Frequency
$g(t)$	Pulse shape function
H	Humidity
h	Height of the atmosphere
I_{peak}	Peak received irradiance
I_o	Intensity of the incident radiation
I_{Bg}	Background radiation

$Kn(.)$	Modified Bessel function
k	Boltzmann's constant
L_o	Large scale size
l_o	Small scale size
L_b	Luminance of the black target
L_w	Luminance of the white target
L	Distance
l (m)	Flow dimension
L_g	Geometric loss
ΔL_{indoor}	Propagation span for indoor
$\Delta L_{outdoor}$	Propagation span for outdoor
L_p	Pointing losses
m	Meter
$m(t)$	Modulated signal
M	Number of bits
$N(r)$	Particle size distribution function
n	Real refractive index
n'	Imaginary refractive index
P_a	Electromagnetic power absorbed
P_s	Electromagnetic power scattered
P_R	Received optical power
P_m	Subcarrier signal power
P_T	Transmission average power
q	Particle size parameter

$Q(\cdot)$	Marcum's Q -function
r_m	Mode radius
R_x	Optical receiver
R_F	Fresnel zone
R_L	Load resistance
R	Photo-detector responsivity
r	Radius of particle
T_{fog}	Transmittance with fog
T	Transmittance
T_{th}	Transmittance threshold
T_b	Bit duration
T_s	Slot time
T_{symp}	Symbol interval
T_e	Temperature
T_x	Optical transmitter
δT_β	Fraction of bit duration
ν_o	Kinematic viscosity
ν (m/s)	Characteristic velocity
V	Visibility
ν_w	Wind velocity
	Wavelength
	Effective number of large scale eddies
	Effective number of small scale eddies
(\cdot)	Gamma function

ρ_o	Transverse coherence length
χ	Gaussian distributed
δ	Gaussian distributed field phase fluctuation
$\psi_1(r)$	Gaussian function
$(r/)$	Size parameter
$\sigma_{lm\ indoor}^2$	Mean scintillation index for indoor
$\sigma_{lm\ outdoor}^2$	Mean scintillation index for outdoor
ξ	Optical modulation index
σ_i^2	Log irradiance variance
σ_a^2	AWGN variance
λ_o	Maximum spectrum wavelength
$\phi_o(r)$	Phase function without turbulence
$\bar{\nabla}$	Laplacian operator

Dedications

To the memory of my loving father Muhammad Ishaq!

Acknowledgements

The work leading to this thesis has been carried out in the Optical Communications Research Group (OCRG) at the Faculty of Engineering and Environment, Northumbria University, Newcastle upon Tyne, UK.

My thanks are wholly devoted to ALMIGHTY ALLAH for blessing me with health and intellectual power and helped me all the way to conclude this work.

First and foremost, I sincerely acknowledge the support received from my principal supervisor, Professor Zabih Ghassemlooy, for his inspiring guidance, valuable suggestions, keen interest, constant help, and encouragement. This work and publications could not been achieved without his discussions and research feedback. I would also like to thank him for proof reading this thesis. I also wish to express my appreciation to him for giving me the valuable opportunity to undertake my research within the OCRG. I am also very grateful to Dr Hoa Le-minh, my second supervisor for his scientific advice and knowledge and many insightful discussions and suggestions. I wish to express my gratitude to Northumbria University, Faculty of Engineering and Environment for awarding me studentship to complete my PhD.

I would like to thank Dr. Sujan Rajbhandhri, currently at Department of Engineering Sciences, Oxford University and Dr Joaquin Perez Soler, for providing me invaluable help and discussion which bring us with the joint publications. I also thank to my colleagues from E411 and E409 of Ellison building that had contributed

both directly and indirectly to my research and helped me in tough time incurred in my stay at Newcastle.

And last, but not least, I am grateful to my family for their patience, especially my mother Maqsooda Akhtar and my respected brothers Muhammad Ashfaq, Muhammad Altaf and Muhammad Shahzad for their prayers, support and encouragement during my research work. I extend my deepest thanks to my wife-Hina Ijaz and my little angel Maryam Ijaz for their constant support, patience, understanding and encouragement throughout the duration of this work.

Declaration

I declare that the work contained in this thesis has not been submitted for any other award and that it is all my own work. I also confirm that this work fully acknowledges opinions, ideas and contributions from the work of others.

Name: Muhammad Ijaz

Signature:

Date:

Chapter 1

Introduction:

1.1. Background

Free Space optics (FSO) communication is a line of sight communication where a modulated optical laser beam (visible or infrared) is used to transfer high data rates wirelessly through the atmospheric channel [1]. The idea of sending and receiving light signals for communication is prehistoric for centuries throughout the known human history. The Old Romans and incident Greeks (around 800 BC) used polished metal plates as mirrors to reflect light from one point to another for long range communications [2]. However, sending information through this transmission method was very limited due to the exchange of predetermined messages only, resulting in low information capacity [3]. In 1792, an optical telegraph based on a chain of semaphores was developed by a French naval navigator called Claude Chappe for communication [4]. The US military also used sun-light based power devices to send signals from one mountain top to another mountain top in the early 1800. The blinking of light signals has also been adopted for many years for ship to

ship communication [5]. During this development period, Alexander Graham Bell constructed a device called 'photo-phone' in 1880, which is considered as the re-birth of optical wireless communication [6]. He used the sun light modulated by the voice signals using the vibrating mirrors and detected using selenium based photo cell. In his experiment, he was able to transmit telephone based signals through the atmosphere medium over a range of 200 meters. The restrictions on this work were the crudity of the devices and the intermittent nature of the sun's radiation [6].

Experimental exploitation of optical devices for high speed communication for long distance requires a monochromatic and narrow strong optical beam at desired wavelength; such a carrier would have not been possible without the invention of Ruby laser in 1960 by Theodore Maiman, which was considered to be the first successful optical laser. However, after the invention of the semiconductor optical lasers by Robert Hall in 1962, the FSO system reliability of operation has increased sufficiently [7]. Today, the semiconductor-injection laser diodes are mostly used for long range optical wireless communication systems [8]. A remarkable television signal broadcasted over a 30 mile (48 km) distance using a GaAs based light emitting diode (LED) by researchers working in the MIT Lincoln Laboratory in 1962 [7]; a record 118 miles (190 km) transmission of voice modulated He-Ne laser between Panamint Ridge and San Gabriel Mountain, USA in May 1963 [9]. The first laser link to handle commercial traffic was built in Japan by the Nippon Electric Company (NEC) around 1970. The link was a full duplex 0.6328 μ m He-Ne laser FSO between Yokohama and Tamagawa, a distance of 14 km [7]. After this experiment, the research in FSO was continued to enhance the system capacity as well as link range and mainly used in military for secure communications in

network-centric operational concepts that promote the use of information as fundamental for gaining superiority on the battlefield [10]. FSO has also been heavily researched for deep space applications by NASA and ESA with programmes such as the Mars Laser Communication Demonstration (MLCD) and the Semiconductor-laser InteFr-satellite Link Experiment (SILEX) respectively [11, 12]. In the past decade, near Earth FSO was successfully demonstrated in space between satellites at data rates of up to 10 Gbps [13, 14].

With rapid development and maturity in the optoelectronic devices, FSO has now witnessed a restore in many applications. Recently, radio-on-free-space optics (RoFSO) technology is regarded as a new universal platform for enabling seamless convergence of fiber and FSO communication networks, thus extending broadband connectivity to underserved areas [15]. In [16] an alternative internet access method is proposed using WLAN and FSO systems as a data uplink and digital video broadcasting – terrestrial (DVB-T) as a downlink channel for broadband data access network [16]. Several successful field trials have been recorded in the last few years including the 147 km FSO transmission which have further encouraged investments in the field [17, 18]. This has now culminated into the increased commercialisation and the deployment of FSO in today's communication infrastructures.

FSO has now emerged as a commercially viable complementary technology to the radio frequency (RF) and millimetre wave wireless systems for reliable and rapid deployment of data, voice and video within the access networks [19, 20]. RF and millimetre wave based wireless networks can offer data rates from tens of Mbps (point-to-multipoint) up to several hundred Mbps (point-to-point) [21, 22]. However,

there is a limitation to their market penetration due to spectrum congestion, licensing issues and interference from unlicensed bands. The optical carrier frequencies in the range of 20-300 THz are licence free makes FSO links as promising technology for future bandwidth hungry communication applications [23].

The short-range FSO links with lengths of 500 meters are an alternative solution to the RF links for the last or first mile to provide broadband access network to homes and offices as well as a high bandwidth bridge between the local and wide area networks [24, 25]. Full duplex FSO systems running at 1.25 Gbps between two static nodes are now common sights in today's market just like FSO systems that operate reliably in all weather conditions over a range of up to 3.5 km. Medium range FSO links have been successfully implemented for high requirement applications at Gbps in [26]. In 2006, 80 Gbps FSO system was demonstrated using the wavelength division multiplexing (WDM) techniques [27]. The link capacity of the FSO system has now reached to 100 Gbps to beyond 1 Tbps [28, 29].

The earlier scepticism about FSO link performance, its dwindling acceptability by service providers and slow market penetration that bedevilled it in the 1980s are now rapidly fading away judging by the number of service providers, organisations, government and private establishments that now incorporate FSO into their network infrastructure [30]. Terrestrial FSO has now proven to be a viable complementary technology in addressing the contemporary communication challenges, most especially the bandwidth/high data rate requirements of end users at an affordable cost. The fact that FSO is transparent to traffic type and data protocol makes its integration into the existing access network far more rapid, reliable and profitable

way in comparison to the traditional fibre communications [31]. Despite these advantages FSO performance is degraded by the substantial optical signal losses due to the presence of aerosols by absorption and scattering of the propagating optical and infrared waves, since their wavelengths are very close to the wavelengths of these frequencies [32]. Fog compared to other atmospheric constituents is the dominant source for the optical power attenuation, thus potentially reducing the FSO link availability. However, in the clear weather condition, theoretical and experimental studies have shown that scintillation can severely degrade the reliability and connectivity of FSO links [33, 34]. Nevertheless, the atmospheric channel effects such as thick fog, smoke and turbulence poses a great challenge to achieve the link availability and reliability according to the *IEEE* and *ITU* link availability standards of 99.999% (five nines) for the last mile access communication network. Therefore, these channel effects still need to be understand and circumvented in order to increase the link range and link availability in terrestrial FSO systems [35-38].

1.2. Research Motivations

In the past decade, the world has witnessed a spectacular growth in the traffic carried by the telecommunication networks. As the number of users using applications requiring a large bandwidth is increasingly growing, the bandwidth limits of current wireless systems in radio frequency based technologies are being stretched [39]. Recently, FSO communication systems with a huge unlicensed modulation bandwidth capability have attracted a great deal of interest from a number of sources including academia, industry, telecommunication and standardization bodies. This

huge bandwidth represents high potentials in terms of capacity and flexibility, thus making FSO technology particularly attractive candidate for multi-gigabit wireless applications including audio, video streaming, multi-gigabit file transferring and internet revolution for last mile access network, the mobile telephony backhaul (3G), satellite communication offering better quality and user experience, in areas to complement radio frequency RF based services [40-42].

FSO technology presents number of advantages over its counterparts, for instance the RF spectrum. Such an advantage is the immunity of FSO to the electromagnetic interference (EMI). The very narrow optical signal provides a secure link with adequate spatial isolation from its potential interferers, thus making it the preferred option in certain applications where there is a requirement for a very low level of interference or no interference at all [31]. In addition, FSO has advantage over RF is the increased security inherent to the laser's narrow foot print, thus, makes detection, interception and jamming very difficult. Further advantages offered by FSO over RF include the possibility of rapid deployment and the flexibility of establishing temporary communication links, much higher data rates, low cost, small size, and limited power consumption. It consumes a low power, provides a better security against electromagnetic interference and do not require licensed spectrum, no need for trenches and digging of streets, low system and installation cost [43, 44]. For these reasons FSO has been considered as an alternative in metropolitan area networks (MANs) and local area networks (LANs) deployments, *e.g.*, backbone military applications or extensions of existing MANs and a viable solution to the "last mile" scenario where the compromise between the available data rate and the effective cost is desirable, *e.g.*, in short link building to building communications,

campus to campus communication, access to rural areas, and disaster recovery scenarios [25, 45].

The other proposed methods to tackle this “last mile” bottleneck consist of the based power-line communication (PLC) [46, 47], digital subscriber loop (DSL) or cable modems [48], fibre to the home (FTTH) [49], local multipoint distribution service (LMDS) [50], and ultra-wide band (UWB) technologies [51, 52]. PLC systems and DSL are copper based, which means potential disruption to the network operation because copper wires are susceptible to damage. In addition, it is more expensive, time-consuming and complicated to maintain and to reconfigure the wired networks [53]. FTTH offers a considerably higher data rate from 10 Mbps to 10 Tbps is feasible for the implementation of FTTH combined with WDM [54]. As from the point of view of deployment and penetration rates of the FTTH technology, South Korea and Japan are the pioneers at the global level [49, 55]. However, its prohibitive cost of implementation is the most prominent obstacle inhibiting a wider deployment. LMDS was conceived as a fixed wireless, point-to-multipoint technology originally designed for the digital television transmission operating at microwave frequencies bands of 27.5 – 31.3 GHz and 40.5 – 42.5 GHz in the US and Europe, respectively [56, 57]. The fact that its throughput capacity and link reliability depends on a common radio link makes the scheme more susceptible to severe signal attenuation and outage during rainfall [58, 59]. Additionally, the carrier frequencies within the licensed bands constrains its applications [60].

The UWB technology uses the unlicensed radio spectrum in the 3.1 – 10.6 GHz band for short-range communications [61]. It is also a copper wire based solution and its

potential data rate is at odds with several Gbps available in the backbone. The interference of UWB signals with other systems operating within the same frequency spectrum is another drawback [52].

FSO is a fibreless, laser driven technology offers similar capacity to that of optical fibre based communication with significant reduction in cost and time [62]. The integration of FSO into the access network can be done relatively cheaply and quickly as it is transparent to the traffic type and protocols. However, the channel in FSO is an atmosphere which poses a great challenge and the performance of FSO system is subject to abrupt changes in atmosphere. Therefore, it is desirable to experimentally characterise the different atmospheric conditions such as fog, smoke, and turbulence and also analyse the system performance under these atmospheric conditions [20, 63, 64].

The number of authors has studied the effect of atmospheric turbulence in [65-68], however, most of these studies are theoretical and very little work has been reported experimentally. This is because in practice, it is very challenging to measure the effect of the atmosphere turbulence under diverse conditions. This is mainly due to the long waiting time to observe and experience reoccurrence of different atmospheric events. Fog has the largest impact on FSO links, limiting link range to a few hundred meters under heavy fog conditions [69]. However, when the link length exceeds several hundred meters, irradiance fluctuations of the received optical signal due to the turbulence present a severe problem. The turbulence induced by the random fluctuation of temperature and pressure results in random variation of the atmospheric refractive index. The variations in the refractive index along the optical

path cause random fluctuations to the received optical irradiance, which can lead to severe system performance degradation [70]. A number of methods can be used to combat the effect of turbulence such as the multiple input multiple output (MIMO) system [71, 72], and the temporal and spatial diversity [68] and aperture averaging [73]. However, selecting a modulation format that is most immune to scintillation effect is also important [74-76]. Furthermore, a number of research works investigating the effect of fog on FSO systems are mostly focusing on the measurement of attenuation and channel modelling [69, 77, 78]. However, very little work on the BER performance of an FSO link in fog is reported. Therefore, this research work has been reported to test and mitigate the effect of fog by employing power efficient modulation schemes and different P_{opt} .

The dependence of the FSO transmission wavelength in the fog and smoke atmospheric channel is considered to be an important parameter in order to achieve the maximum transmission span. However, there is not any common agreement between the best wavelength to choose in FSO, particularly for the dense fog (visibility $V < 0.5$ km) [79-81]. In [79, 81, 82] different models have been studied to predict the fog attenuation depending on the measured V (km) and operating wavelengths. Kim et al (2001). showed that the fog attenuation is independent of the wavelength for the dense fog condition for $V < 500$ m [79]. However, the experimental data reported for real atmospheric fog setup shows a significant difference between the fog attenuation using 830 and 1550 nm wavelengths [83, 84]. In [85], a laboratory based setup is used similar to our previous work [86] and showed that the terahertz (THz) signal has significantly lower fog attenuation than a 1.55 μm link. In [87], a real time measurement of the fog attenuation was reported,

that shows far infrared (FIR) at 10 μm offers higher transmittance in fog. Despite the advantages of FSO links, to operate them at THz and FIR wavelength bands will require high cost components that are not readily available at the moment. Therefore, almost all commercially available FSO systems operate in the wavelength range of 0.60 μm – 1.55 μm . Consequently, the wavelength in the visible – near infrared (NIR) bands are needed to be selected in order to verify the dependency of the wavelength on the fog and smoke attenuation for $V < 0.5$ km.

Moreover, most of reported experimental data lacks the prediction of fog attenuation at the lower visibility ($V < 100$ m) range is not well defined and easily achievable. Further, in an empirical approach to model the real fog attenuation is based on the measured V and the fog attenuation at the same time. However, as the FSO link length can be greater than 1 km. In this case, due to the spatial heterogeneity, fog densities can vary from one position to few 100 metres apart. Thus, the measured fog attenuation along the FSO link and the corresponding visibility data using a visibility device at a fixed position can significantly fluctuate from the actual value. This effect can be observed in the measured data at 830 nm for two fog events as in [88]. Thus, there is still need to measure and characterise the fog attenuation at corresponding V along the length of link rather than at fix position. Therefore, in order to control and characterise the atmospheric effects such as fog, smoke and turbulence and to address the challenges caused by the atmosphere channel. A dedicated laboratory based atmospheric chamber of length 5.5 m is designed. Atmospheric chamber is a powerful tool to simulate the real outdoor FSO effects and its characterisation and measurements under a controlled environment without the

need for longer waiting times as would be in the case of outdoor FSO links, as reported in previous works [89, 90].

In this research work, the experimental results of fog attenuation in FSO for visible – NIR wavelengths ($0.6 \text{ } \mu\text{m} < \lambda < 1.6 \text{ } \mu\text{m}$) from dense to light fog conditions are reported. The experimental results are compared with the selected empirical fog models in order to validate their performance practically in Chapter 5. The experimental results show that the fog attenuation is wavelength dependent for all V ranges except when $V < 0.015 \text{ km}$ contradicting the Kim model. The visibility is measured using the wavelength of $0.55 \text{ } \mu\text{m}$ and CCD camera along the length of an FSO channel rather than at one position as in the case of traditional outdoor FSO links. This approach enables to provide the right value of fog attenuation corresponding to the measured V (km). Here, a new empirical model is proposed to evaluate the wavelength dependent fog and smoke attenuation by reconsidering the q value as a function of wavelength rather than visibility in Chapter 6. Using the measured attenuation spectrum data, recommendations are provided for the best wavelengths that could be adopted for links under fog conditions. Furthermore, an alternative approach is used to evaluate the BER performance of the FSO link under fog environment using the received signal eye diagrams. The transmittance T as well as the signal-to-noise ratio (SNR) (*i.e.*, the Q -factor) is measured for different modulation format and also by increasing P_{opt} for light-to-dense fog densities in Chapter 7.

In this thesis, experimental characterisation and investigation of the atmospheric turbulence effect on Ethernet and Fast-Ethernet FSO links are also reported in

Chapter 8. Different methods are introduced and demonstrated in order to control the different turbulence levels and to determine the equivalence between the indoor and outdoor FSO links. The results show that the connectivity of Ethernet and Fast-Ethernet links are highly sensitive to atmospheric conditions. The effect of turbulence on FSO communication systems for On-off-keying (OOK), pulse amplitude modulation (PAM) and subcarrier intensity modulation (SIM) based on binary phase shift keying (BPSK) is experimentally investigated and evaluated. The following research objectives have been devised in order to achieve these goals.

1.3. Research Objectives

The prime aim of this research work is to experimentally characterise and investigate the atmospheric channel effects, particularly fog and turbulence on the performance of FSO link. It is very difficult to practically measure and verify the atmospheric fog and scintillation effects under diverse conditions *e.g.*, (light to dense fog, different combinations of wind velocity and temperature) as reoccurrence of the same atmospheric events is unpredictable. Hence, a dedicated laboratory chamber to simulate and demonstrate the atmospheric effects on the FSO channel in a control environment is designed. The laboratory atmospheric chamber prototype enables to study the effects of atmospheric impairments, *e.g.* fog, turbulence and smoke on the optical beam propagating through the FSO channel for a range of wavelengths and modulation schemes.

A list of research objectives has been outlined in order to accomplish these aims:

- Review the state of the art literature review on terrestrial FSO communications, the challenges imposed on the system performance, the atmospheric fog channel and different mechanisms of forming the atmospheric fog and smoke.
- Study of different approaches to characterise the atmospheric fog attenuation by achieving homogeneous fog conditions as far as possible and implementation of CCD camera and laser based techniques to characterise the light to dense fog and smoke channel
- Investigation and comparison of different empirical fog models in the literature for different parameters such as visibility V (km), transmittance threshold T_{th} and wavelength .
- Measurement of fog attenuation at different wavelengths in order to verify the wavelength dependent fog attenuation for all visible – NIR range particularly at dense fog ($V < 0.5$ km) and to verify the performance of empirical fog models practically.
- Proposed a wavelength dependent model for attenuation prediction in fog and smoke channel, which is valid for the visible – NIR range for the visibility range of 1 km. The new proposed fog model is also compared to selected empirical models and the measured continuous attenuation spectrum from the visible – NIR in order to validate the laboratory-based empirical model.

- Theoretical and experimental investigation of fog effects on the transmitted optical beam over a FSO channel as well as mitigation schemes such as by increasing P_{opt} and using power efficient modulation schemes.
- Review the characteristic properties of the atmospheric channel, and understand the limits and range of validity of each model for describing the channel fading induced by turbulence.
- Experimental verification and characterisation of atmospheric turbulence and calibrate it to real outdoor FSO channel.
- Theoretical and experimental investigation of the scintillation effect and its mitigation schemes using the different modulation schemes such as OOK-NRZ, sub-carrier intensity modulation (SIM)- binary phase shift keying (BPSK) and pulse amplitude modulation (PAM).

1.4. Original Contributions

As a direct result of this research, the following original contributions have been made:

- Investigation and comparison of the empirical based fog models which estimates the outdoor fog attenuation based on the measured V from the visible – NIR range of the spectrum has been discussed in **Chapter 3**. The behaviour of the resultant fog attenuation of these models is studied and analysed for different parameters such as visibility, transmittance threshold and wavelength. The study shows that in spite of a significant number of

investigations, these models need to be explicitly verified experimentally, not for a selective or specific wavelength but for the entire spectrum from the visible – NIR range .

- The detailed description on the design of atmospheric chamber is detailed in **Chapter 5**. Moreover, methods to produce homogeneous fog and its calibration to ROF and data acquisition for fog attenuation measurement are explained. Methods to produce and control atmospheric turbulence are also described in **Chapter 5**.
- The experimental results of attenuation of free space optical (FSO) communication systems operating at visible and near NIR wavelengths ($0.6 \text{ }\mu\text{m} < \lambda < 1.6 \text{ }\mu\text{m}$) in the controlled laboratory based fog environment are presented in **Chapter 5**. The results are compared with the selected empirical fog models in order to validate their performance practically from dense to light fog conditions. The results indicate that the fog attenuation is wavelength dependent for all V ranges. Measured attenuation spectrum shows that Kim model is more realistic to use when $V > 0.5 \text{ km}$. This model does not take into account the wavelength for $V < 0.5 \text{ km}$. Therefore, Kim model need to be revised for $V < 0.5 \text{ km}$ to predict the wavelength dependent fog attenuation.
- Different methods based on CCD camera and visible laser-diode at $0.55 \text{ }\mu\text{m}$ to characterise the fog attenuation in terms of atmospheric visibility are compared described and experimentally implemented under a controlled laboratory-based fog environment in **Chapter 6**. The CCD technique show a great accuracy for a visibility range below 50 m and the laser technique for

the range beyond 100 m, therefore these techniques allow to enhance the characterisation of FSO system in thick and dense fog conditions.

- A new empirical model is proposed to evaluate the wavelength dependent fog and smoke attenuation by reconsidering the q value as a function of wavelength rather than visibility is detailed in **Chapter 6**. Moreover, using the measured attenuation spectrum data, the recommendations for the best wavelengths are provided that could be adopted for links under fog conditions. The new proposed fog model is also compared to selected empirical models and the measured continuous attenuation spectrum from the visible – NIR in order to validate the laboratory-based empirical model.
- Theoretical and experimental results has been reported in **Chapter 7** to test and mitigate the effect of fog by investigating the the FSO link BER performance in the lab controlled fog environment by implementing different modulation schemes such as OOK-NRZ, OOK-RZ, 4-PPM, BPSK and 4-PAM and by improving P_{opt} in the case of OOK-NRZ. The transmittance T as well as the signal-to-noise ratio, SNR (*i.e.*, the Q -factor) is measured for different modulation format and also by increasing P_{opt} for light-to-dense fog densities. The results demonstrate the effect of fog on the FSO link BER performance by observing transmittance values for a range of received optical power. Further to compare the results with the outdoor systems the link budget and its margin are used as the key criteria parameters.
- Methods to generate different level of turbulence and its control are presented and practically implemented in **Chapter 8**. Atmospheric turbulence is characterised and calibrated using the atmospheric chamber and verifies the statistical based log- normal model experimentally. The relation

between the indoor environment and the outdoor FSO link is also achieved in order to ensure total reciprocity of atmospheric turbulence.

- The performance of Ethernet and Fast-Ethernet FSO links under weak turbulence conditions using the controlled indoor atmospheric chamber is investigated in **Chapter 8**. The effect of turbulence on the Ethernet based FSO communication systems is also investigated experimentally using different modulation schemes such as OOK- NRZ, 4-PAM and subcarrier intensity modulation (SIM) based BPSK.

The overall contribution of this thesis is schematically illustrated using a research road map as depicted in Fig. 1.1.

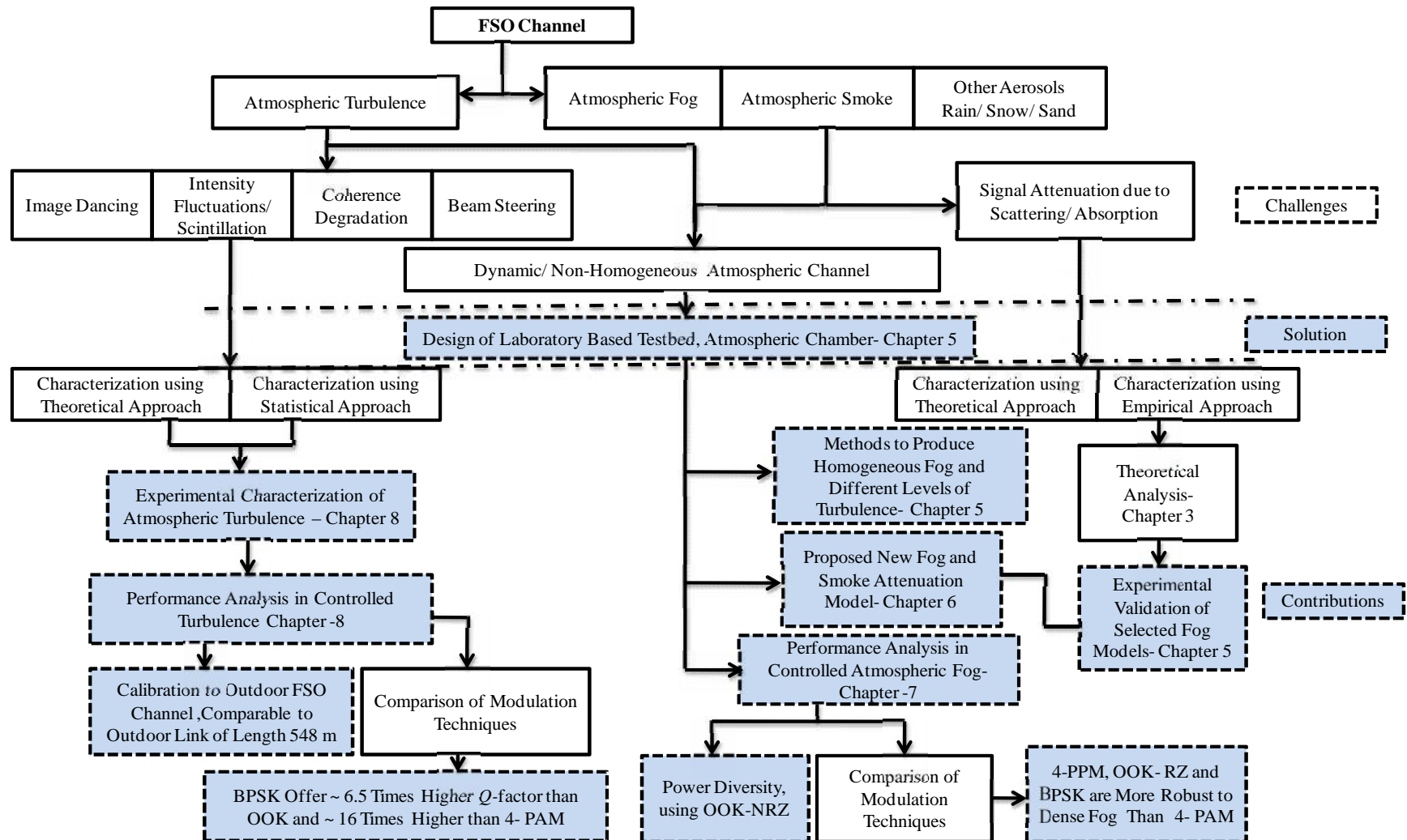


Figure 1.1. Outline of the research road map and original contribution.

1.5. Thesis Organization

This thesis has been organized in nine chapters as follows:

Chapter One Introduction: A complete introduction of the FSO technology is presented. It also consists of aims and objectives of the research as well as the original contributions.

Chapter Two Fundamentals of FSO: A complete overview of the FSO technology is presented together with its distinctive features and applications. The general block diagram for an FSO communication system is introduced, and the functions of individual parts are highlighted. The atmospheric channel effects that limit the data transmission are described. Eye safety issues are discussed in the remainder of the chapter.

Chapter Three Fog and Smoke Atmospheric Channel: This chapter outlines different types and composition of fog and smoke and also describes methods to characterise fog attenuation using the theoretical and empirical approaches. The empirical fog models which estimates the outdoor fog attenuation based on the measured V from the visible – NIR range of the spectrum are compared. The behaviour of the resultant fog attenuation of these models is studied for different parameters such as visibility, transmittance threshold and wavelength.

Chapter Four Atmospheric Turbulence Channel: In this chapter, the characterisation of the atmospheric turbulence is presented based on classical

approach and statistical models. The refraction structure parameter C_n^2 and scintillation index ($S.I$) parameters are used to characterise the turbulence.

Chapter Five Design of Atmospheric Channel: In this chapter, the detailed description on the design of atmospheric chamber is presented. Moreover, the methods to produce homogeneous fog and its calibration to ROF and data acquisition for fog attenuation measurement are explained. Methods to produce and control atmospheric turbulence are also presented. The experimental results of spectrum attenuation of free space optical (FSO) communication systems operating at visible and near infrared (NIR) wavelengths ($0.6 \text{ } \mu\text{m} < \lambda < 1.6 \text{ } \mu\text{m}$) are presented. The results are compared with the selected empirical fog models in order to validate their performance practically from dense to light fog conditions.

Chapter Six Modeling of Fog and Smoke Attenuation: The main objective of chapter is to provide a complete analysis and verification of the enhanced visibility measurements for FSO under homogeneous fog conditions. A new empirical model is proposed to evaluate the wavelength dependent fog and smoke attenuation based on measured visibility for the range of wavelengths from visible – NIR. The recommendations for the best wavelengths are provided that could be adopted for links under fog conditions. The new proposed fog model is also compared to selected empirical models and the measured continuous attenuation spectrum from the visible – NIR in order to validate the laboratory-based empirical model.

Chapter Seven BER Performance of FSO under Controlled Fog Conditions:

The system performance is theoretically and experimentally evaluated for on-off

keying non-return-to-zero (OOK-NRZ), on-off keying return-to-zero (OOK-RZ) and four pulse position modulation (4-PPM) formats for Ethernet line data-rates from light to dense fog conditions. Moreover, the effect of using different average transmitted optical communication power, P_{opt} on the transmittance and the received Q -factor for OOK-NRZ modulation scheme is also studied for light and dense fog densities.

Chapter Eight Performance Analysis of FSO under Controlled Weak

Turbulence Conditions: In this chapter, experimental characterisation and investigation of the turbulence effect on Ethernet and Fast-Ethernet FSO links are reported using different modulation schemes in a controlled laboratory environment. It also demonstrates methods to control the turbulence levels and determine the equivalence between the indoor and outdoor FSO links. The effect of turbulence on FSO communication systems for OOK, pulse amplitude modulation (PAM) and subcarrier intensity modulation (SIM) based on binary phase shift keying (BPSK) is experimentally investigated.

Chapter Nine Conclusions and Future Work: Finally, the summary of key findings is presented in this chapter. The conclusion as well as the future work is outlined.

1.6. List of Publications and Awards

1.6.1. Journal publications

1. **M.Ijaz**, Z. Ghassemlooy, J. Pesek, O. Fiser, H. le-minh, and E. Bentley "Modeling of fog and smoke attenuation in free space optical communications link under controlled laboratory conditions," *IEEE/OSA Journal of Lightwave Technology*, vol. 31, no. 11, pp. 1720-1726, 2013.
2. **M.Ijaz**, Z. Ghassemlooy, J. Perez, V. Brazda and O.Fiser "Enhancing the atmospheric visibility and fog attenuation using a controlled FSO channel," *IEEE Photonics Technology Letters*, vol. 25, no.13, pp. 1262-1265, 2013.
3. J. Perez, Z. Ghassemlooy, S. Rajbhandari, **M. Ijaz**, and H. Lee-Minh, "Ethernet FSO communications link performance study under a controlled fog environment," *IEEE Communications Letters*, vol.16, no.3, pp. 1-3, 2012.
4. Z. Ghassemlooy, H. Le Minh, S. Rajbhandari, J. Perez, and **M. Ijaz**, "Performance analysis of Ethernet/Fast-Ethernet free space optical communications in a controlled weak turbulence condition," *IEEE/OSA Journal of Lightwave Technology* , vol. 30, pp. 2188-2194, 2012.
5. V. Brazda, **M. Ijaz**, J. Parez Solar and O.Fiser, "Mereni dohlednosti digitalnim fotoaparatem," *Perner's Contacts*, vol. 7, no. 3, pp. 16-23. 2012.

1.6.2. Conference publications

6. **M. Ijaz**, O. Adebajo, S. Ansari, Z. Ghassemlooy, S. Rajbhandari, H. Le-Minh, A. Gholami, and E. Leitgeb, "Experimental investigation of the performance of OOK-NRZ and RZ modulation techniques under controlled turbulence channel in FSO systems," *11th Annual Postgraduate Symposium on the Convergence of Telecommunications, Networking and Broadcasting*, Liverpool, UK, pp. 296-300, 2010.
7. **M. Ijaz**, Z. Ghassemlooy, H. Le-Minh, and S. Rajbhandari, "All-optical fog sensor for determining the fog visibility range in optical wireless communication," *Proceeding of LCS/NEMS/Photonics*, UCL, London, 2010.
8. H. Le-Minh, Z. Ghassemlooy, **M. Ijaz**, S. Rajbhandari, O. Adebajo, S. Ansari, and E. Leitgeb, "Experimental study of bit error rate of free space optics communications in laboratory controlled turbulence," *IEEE Globecom Workshop on Optical Wireless Communications*, Miami, Florida, USA, pp. 1072-1076, 2010.
9. R. Paudel, H. Le-Minh, Z. Ghassemlooy, **M. Ijaz**, and S. Rajbhandari, "High speed train communications systems using free space optics," *IET Railway Young Professionals Best Paper Competition, The Medical Society*, London, UK, 2010.
10. **M. Ijaz**, Z. Ghassemlooy, S. Ansari, O. Adebajo, H. L. Minh, S. Rajbhandari, and A. Gholami, "Experimental investigation of the performance of different modulation techniques under controlled FSO

- turbulence channel," *5th Int. Symposium On Telecommunications (IST2010)*, IEEE, Tehran, Iran, pp. 59-64, 2010.
11. ***M. Ijaz**, Z. Ghassemlooy, H. Le-Minh, S. Rajbhandari, J. Perez, and A. Gholami, "Bit error rate measurement of free space optical communication links under laboratory controlled conditions," *16th European Conference on Networks and Optical Communications (NOC)*, Newcastle, UK, pp. 52-55, 2010. (**Selected the best conference paper amongst over 60 papers**).
 12. S. Rajbhandari, Z. Ghassemlooy, J. Perez, H. L. Minh, **M. Ijaz**, E. Leitgeb, G. Kandus, and V. Kvicera, "On the study of the FSO link performance under controlled turbulence and fog atmospheric conditions," *11th Int. Conference on Telecommunications (ConTel)* Graz, Austria, pp. 223-226, 2011.
 13. **M.Ijaz** , Z. Ghassemlooy, S. Rajbhandari, , H. L. Minh and J. Perez, " Comparison of 830 nm and 1550 nm based free space optical communications link under controlled fog conditions," *8th IEEE, IET Int. Symposium on Communication Systems,(CSNDSP)*, Poland, pp. 1-5, 2012.
 14. J. Pesek, **M.Ijaz** , Z. Ghassemlooy, O. Fiser, S. Rajbhandari, and H. L. Minh, " Measuring the fog attenuation in free space optical laboratory Chamber," *IEEE, Int. Conference on Applied Electronics,(ICAE)*, Pilsen, Czech Republic, pp. 203- 206, 2012.
 15. **M.Ijaz** , Z. Ghassemlooy, S. Rajbhandari, , H. L. Minh and J. Perez, " Analysis of fog and smoke attenuation in a free space optical communication link under controlled laboratory conditions," *Int.*

Workshop on Optical Wireless Communications (IWOW), Pisa, Italy, pp. 1-3, 2012.

16. **M. Ijaz**, Z. Ghassemlooy, H. Le Minh¹, S. Zvanovec, J. Perez, J. Pesek and O. Fiser " Experimental validation of fog models for FSO under laboratory controlled conditions " *IEEE International Symposium on Personal, Indoor and Mobile Radio Communications (PIMRC)*, pp. 19-23, May 2013.

1.6.3. Research seminars and poster presentations

1. M. Ijaz, "Experimental investigation of the performance of OOK-NRZ and RZ modulation techniques under control turbulence channel in FSO," poster, School of CEIS, Research Teaching Forum, 2010.
2. M. Ijaz, "Experimental investigation of bit error rate performance of free space optical communication due to Low visibility and turbulence in lab controlled environment," Weekly Research Seminar, Northumbria University, Dec, 2010.
3. M. Ijaz, "Bit error rate measurement of free space optical communication links under laboratory-controlled fog conditions," poster, Graduate School Show, Northumbria University, 2011.
4. M. Ijaz, " Characterisation and modelling of dense fog and smoke in FSO," Weekly Research Seminar, Northumbria University, Oct, 2012.

1.6.4. Awards

1. Partial Northumbria Studentship (2009-2012)
2. Best performing second year PhD student within the School of Computing, Engineering & Information Sciences, Northumbria University, 2011.
3. Best conference paper award in 16th European Conference on Networks and Optical Communications (NOC), Newcastle, UK, 2010.

Chapter 2

Fundamentals of FSO Communication

2.1. Introduction

FSO is a laser driven technology that entails the transmission of information laden optical radiations as the carrier signal through the atmospheric channel. FSO harnesses the richness of large capacity usage (data, voice, and video) which can effectively elucidate last mile access network problem for a foreseeable future [91, 92]. FSO systems are largely deployed as the primary, back-up and disaster recovery links offering a range of speed from 10 Mbits/s – 10 Gbit/s [93]. Most of the links are already deployed on satellites, deep-space probes, ground stations, unmanned aerial vehicles (UAVs), high altitude platforms (HAPs), and other nomadic communication partners are of practical interest [94-97]. FSO is the potential leading technology as an adjunct to conventional radio frequency (RF) wireless links offering a cost effective, unlicensed spectrum and secure communication [98].

However, this comes at the cost of a number of challenges such as substantial optical signal losses due to the atmospheric absorption and scintillations that require serious considerations [99, 100].

This chapter is organized as follows: The electromagnetic spectrum is detailed in Section 2.2. Features of FSO communications is presented in Section 2.3, whereas the areas of applications are introduced in Section 2.4. A FSO communication system is explained with an insightful literature survey is provided about the optical transmitter and receiver components in Section 2.5. The fundamental challenges and different phenomenon due to the real outdoor atmosphere (ROA) channel are also described. Section 2.6 provides the theoretical background of selected modulation schemes that can be adopted in FSO to confront the different atmospheric conditions. The discussion on the eye/skin safety issues and standards of optical sources are provided in Section 2.7. The summary of the chapter is drawn in Section 2.8.

2.2. The Electromagnetic Spectrum

The physics of electromagnetic (EM) is very well studied and Maxwell equations are mostly applied in order to understand the propagation of EM waves in different media [101]. EM waves spectrum is very wide, with wavelengths ranging from 10^{-14} up to 10^4 m. Different bands of frequency are associated with EM waves and very well defined for the communication purposes and as well as other application in health and industry [102]. These bands, while being comparable in nature, have different names for historical reasons. This is especially true in optics, which is concerned with frequencies corresponding to visible light, whereas the

electromagnetic spectrum largely extends above and beyond this band [103]. The spectrum is also divided into two regions, (i) the ionizing part of the electromagnetic spectrum that includes ultraviolet rays, gamma-rays and x-rays, whose wavelengths are very short and whose intensities are very high and thus are not feasible for wireless communications and, (ii) the non-ionizing part that includes radio waves, IR and visible light which are mostly used for wireless communications [104]. Figure 2.1 shows the electromagnetic spectrum extending with respect to the wavelength with the usual names for the various frequency bands. An enlarged view is shown for wavelengths in the band of the visible light and also encircled a band of spectrum that is mostly adopted in FSO communications [105, 106].

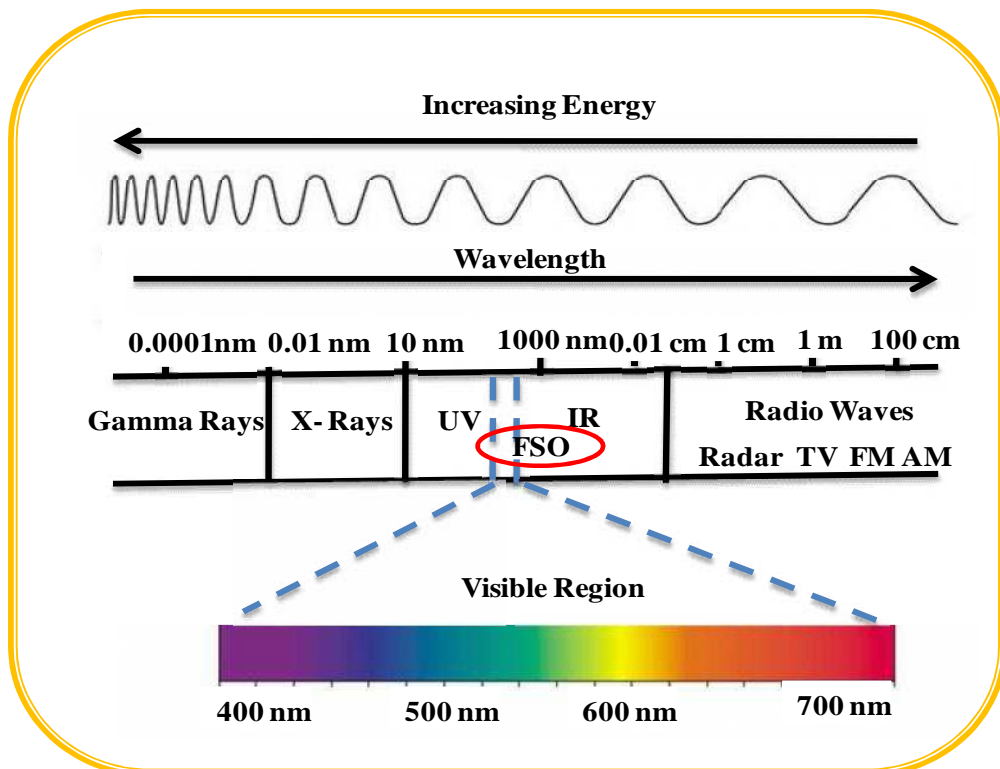


Figure 2.1. The overview of the EM spectrum with its nominated frequency bands.

2.3. Features of FSO Communications

The features of FSO technology that make it more viable compared with other existing RF, microwave and millimetre wave (mm-wave) based wireless communication technologies are outlined below:

- **Higher data rates** - A number of wireless technologies have been deployed to provide communication for short and long range in personnel and long distance links [107]. There is very little doubt that the RF and microwave technology provide enhanced mobility than the optical based technologies. However, the data rate in RF is limited to the end users [108]. The available data rates in unregulated 2.4 GHz ISM wireless LANs are 1- 2 Mbps [109], 20 Mbps at 5.7 GHz and 875 Mbps in 60 GHz [110]. As an alternative to RF technology, the FSO system offers a large data bandwidth up to 2000 THz making it a very attractive technology of meeting the future demand for broadband internet access and HDTV broadcasting services [111, 112]. Figure 2.2 shows a comparison of FSO with various wireless technologies and fibre, where the FSO communication technology offers fibre like data rates up to a link range of 5 km.

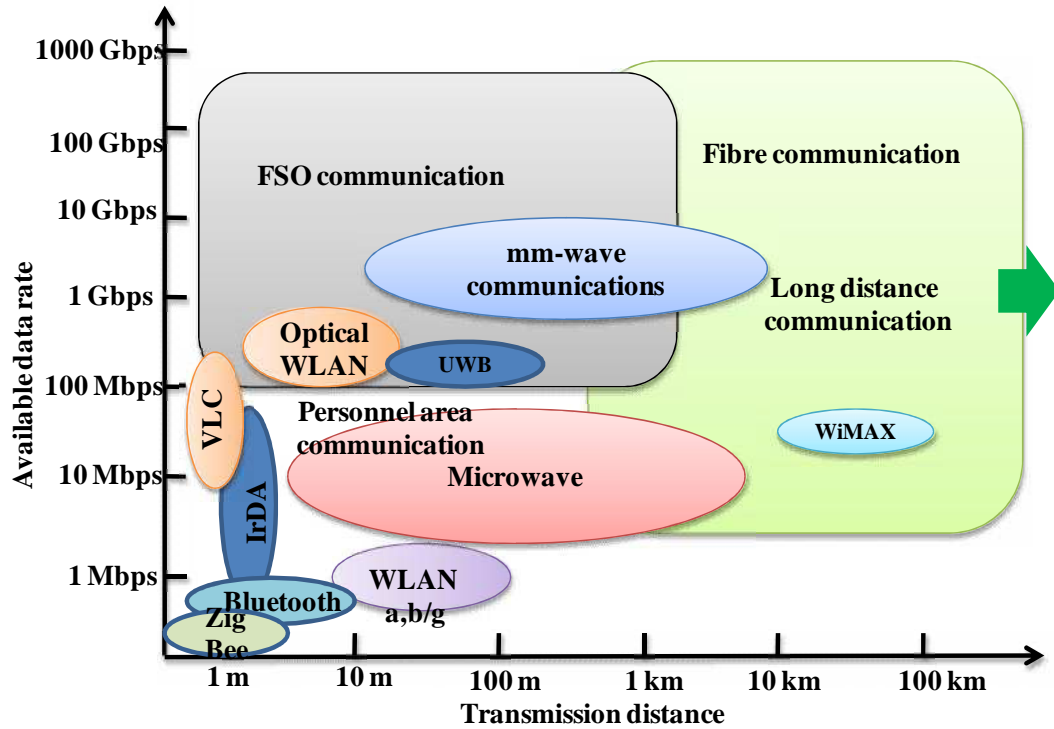


Figure 2.2. Comparison of a range of optical and RF wireless technologies [113].

- Unlicensed spectrum** - FSO uses the visible to far infrared (FIR) band of spectrum as shown in Fig. 2.1. The optical carrier frequencies have a very small footprint at this spectrum range and hence the FSO systems do not suffer from adjacent band interference effects. However, in the RF spectrum, interference occurs between adjacent allocated bands. Therefore, Federal Communication Commission (FCC) in US and Office of Communication (Ofcom) in the UK put stringent spectrum regulations [114]. However, at present, the FSO spectrum band doesn't required regulations and therefore are relatively inexpensive compared to the RF licensed spectrum. This implies that providers can incorporate FSO in their system since the initial set-up cost is lower and the deployment time is shorter [9, 114].

- **Power efficient** - Power consumption in information and communication technology (ICT) is a crucial problem because of increasing energy costs and the relevant environmental impacts [115]. According to a report Smart 2020, published in [116], ICT alone is responsible for 2% to 10% of the worldwide energy consumption and it is estimated that as the result of this the CO₂ emission will almost be doubled by 2020, reaching 1.43 Gt worldwide [117]. Moreover, the increasing growth of internet traffic is continuously inducing technological advances in transmission systems and networking equipments, causing rapidly increasing power consumptions despite the efforts to build more energy efficient devices and systems [118]. According to several studies, current trends predict that the demand of world electricity is increasing exponentially due to internet use in few years [107]. FSO uses optical lasers and LEDs to broadcast the transmission, which are more light in weight, compact and power efficient than conventional light bulbs. An LED uses twenty times lower power than conventional bulb, even 5 times less power than fluorescent based bulbs. FSO therefore is a potential green technology in order to circumvent the energy cost and also more environmentally friendly than RF based communication system [117, 118].
- **Cost effective** - The biggest advantage of FSO systems is their low cost compared to the other communication technologies. In most cases, FSO communications does not incur high cost of digging up tunnels and trenching of roads to install bulky copper cables and fibres and also the license free to pay for extra tariffs by the users [119]. Therefore, the deployment cost of an FSO link is much lower than the RF and fibre based links as shown in Fig. 2.3.

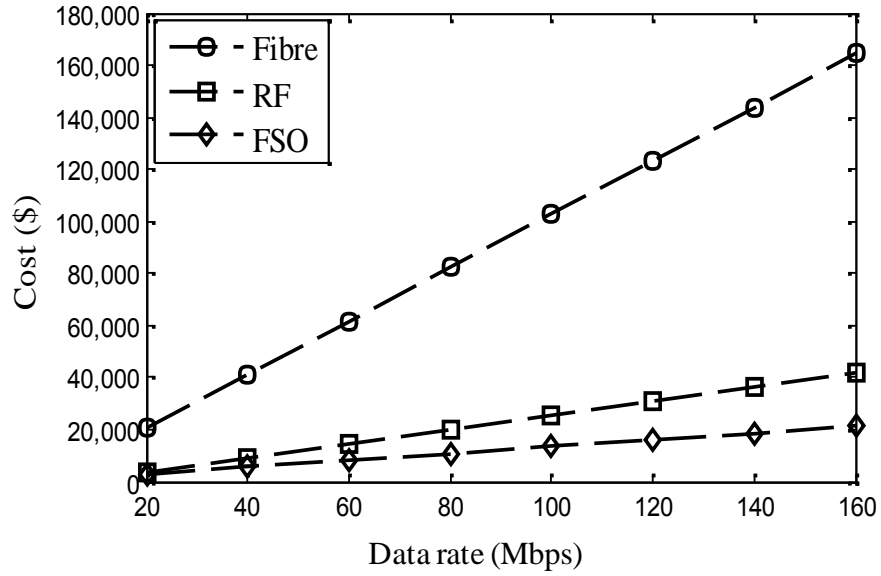


Figure 2.3. Comparison on bandwidth cost for FSO, RF and Fibre based communication system [120].

- Fast installation** - The key factor of setting up FSO system is the establishment of connectivity between the transmitter and receiver. A review survey conducted with the operators in Europe and USA companies concluded that FSO is much faster to deploy than any other fixed communication technology [121]. Moreover, the speed of installation of FSO is in hours as compared to RF wireless technology which can take up to months [120].
- Security** - The main advantage of the confined beam of FSO communications is the ability to provide a significant degree of covertness. A malicious eavesdropper would need to locate very close to the transmitted beam between the transmitter and receiver in order to intercept sufficient energy and recover information [122]. This makes the interception almost impossible as the eavesdropper's antenna is also likely to cause link outage for the intended

recipient due to beam obstruction. Jamming an FSO is also difficult because of the nature of optical beam is narrow and also invisible [123, 124].

2.4. Areas of Applications

FSO technology has a wide area of applications. The following subsections are the most important applications of FSO communications.

- **Last mile access links-** Connecting the end users to the internet (the backbone or core network). The demand for delivering high speed data transfers to end users is motivation behind developing novel network access technologies to overcome the access network bottlenecks. These bottlenecks occur in access network at two levels as (i) the last mile data transmission to the end users, and (ii) high speed data transmission within the last mile to the user [120]. There are a number of cables and wireless transmission technologies that have been deployed to bridge the last mile, however these are mostly based on the RF technology [125]. With the fibre optic technologies being increasingly deployed such as the Ethernet passive optical networks (EPONs), the bandwidth bottleneck is shifted towards the last mile access network. EPONs are designed to carry Ethernet frames at gigabit Ethernet rates but are not cost effective [126, 127]. However, wireless networks capable of offering gigabit per second data rates in the last mile access network still have bandwidth limitations, thus enabling the end users to have a full access to broadband internet. This problem is more acute in the rural areas where access to high-speed broadband using the existing technologies is rather limited [63, 128]. In such scenarios the FSO technology could offer gigabit Ethernet to the end users. Figure 2.4 shows the

building-to-building connectivity in the last mile access network using the FSO technology to overcome the bandwidth bottleneck problem [129, 130].

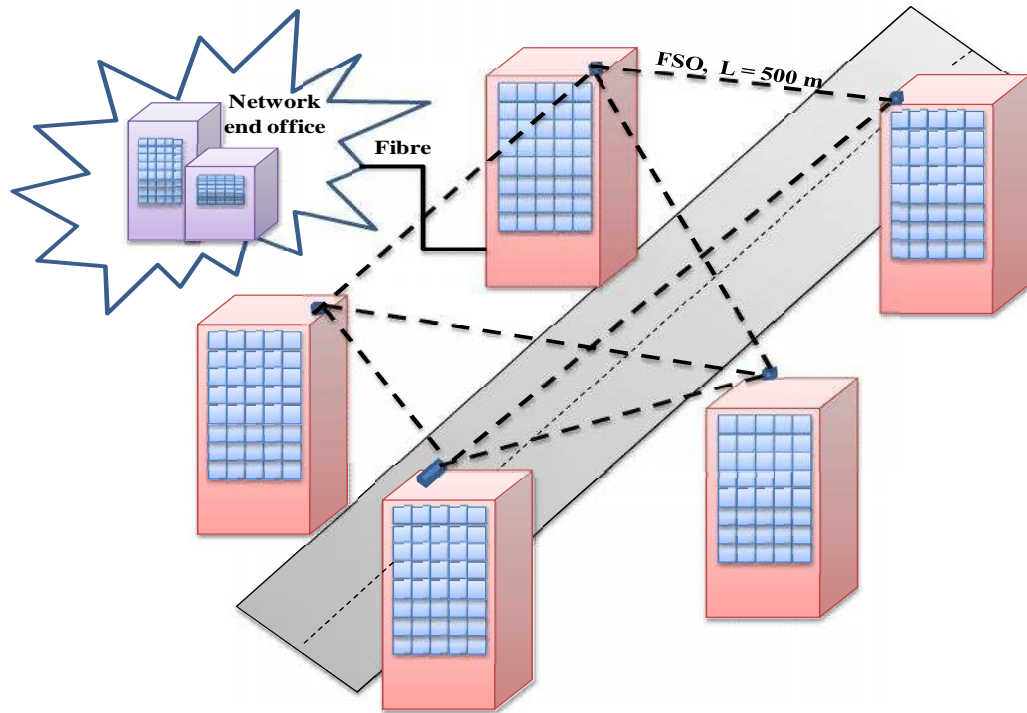


Figure 2.4. A simple block diagram showing the building-to-building communication in last mile access network using FSO.

- **Hybrid FSO/RF communications** - The practical limitations and challenges of RF based communication networks have become increasingly apparent over the past few years, thus there is the need for new hybrid communication approaches. One promising approach is the hybrid RF/FSO link [131]. FSO and RF communications can be realized as complementary schemes rather than a competitive one in order to overcome the limitations of both technologies [132]. Hybrid FSO/RF communications is proposed to be the best solution to achieve 99.999% availability in severe weather conditions such as fog and rain [133]. The scattering effects due to fog/smoke and atmospheric turbulence due to

scintillations defocuses the optical signal, thus degrades the BER performance of an FSO link. The measured fog attenuation for FSO link working at wavelength of 830 nm is 37 dB/km at $V = 200$ m, however, it is 3 dB/km, for 58 GHz RF link [134]. On the other hand RF links are more sensitive to rain scattering causing attenuation of 17 dB/km at rain rate of 40 mm/hr, however rain attenuation for FSO link working at wavelength of 830 is measured to 2 dB/km [134]. The probability of occurrence of fog and rain simultaneously is very low [135]. Hence, the RF link provides a back-up link to FSO in fog conditions [136]. Table 2.1 summarises the differences between FSO and RF communications.

Table 2.1. Comparison between FSO and RF communication systems.

Parameter	FSO Link	RF Link
Data rate	10's Mbps – 10's Gbps	< 100 Mbps
Devices size	Small	Large
Bandwidth regulated	Free license	Required
Security	High	Low
Network architecture	Scalable	Non-scalable
Link performance effects	Fog, Atmospheric turbulence misalignment or obstruction	Multipath fading, rain, interferences
Channel distance	Small	Long
Noise	Background light	Other sources
Fog Attenuation ($V = 200$ m)	37 dB/km at 830 nm	3 dB/km at 58 GHz

- **Cellular communications** - The next generation 4G networks support a multitude of protocols, interfaces and services encompassing all the previous & new technology for its realization [137]. Hence there is a need to integrate FSO

within the 4G wireless networks [138]. The available data rate supported by 2G and 3G wireless network range from E1/T1 to STM-4 level [139]. However, FSO can provide the data rate of 7.5 Gbps up to distance of 40 km [140]. Thus, FSO is a possible alternative technology to exploit within the 4G networks, which is further explored in [107, 141, 142].

- **Mobile FSO communications** - This can be used for disaster relief for both natural or man-made event that destroys the critical infrastructure and under unsafe operations due to light weight, low power and easy to install [143, 144]. Moreover, practical mobile FSO have been demonstrated which are light weight and low cost offering data rates of 10 mbps over a link span of 50 meters[145] .
- **Back up to optical fibre link** - FSO links can be used for the backup link in circumstances where the optical fibre communication link is down or unavailable due to breakage [146, 147]. FSO is also mostly deployed where fibre optics links are impractical due to physical implementations [148, 149] while maintain the high link quality.
- **Military applications** - FSO communication system is the mostly used in military, between satellites and space-to-ground or space-to-air, airborne networks and Air-to-ground links for intelligence, surveillance and reconnaissance (ISR) [10, 150].

2.5. FSO System

The basic concept of FSO communication is similar to RF communications in terms of data generation, modulation, transmission, reception, and processing of data. A generic FSO communication system consists of three main blocks; an optical transmitter, an

optical receiver separated by an atmospheric channel as described in Fig. 2.5. An FSO link require a line-of-sight communication (without any obstacles between the transmitter and receiver) and they are typically deployed in a point-to-point in a ring, star or mesh network architectures [151].

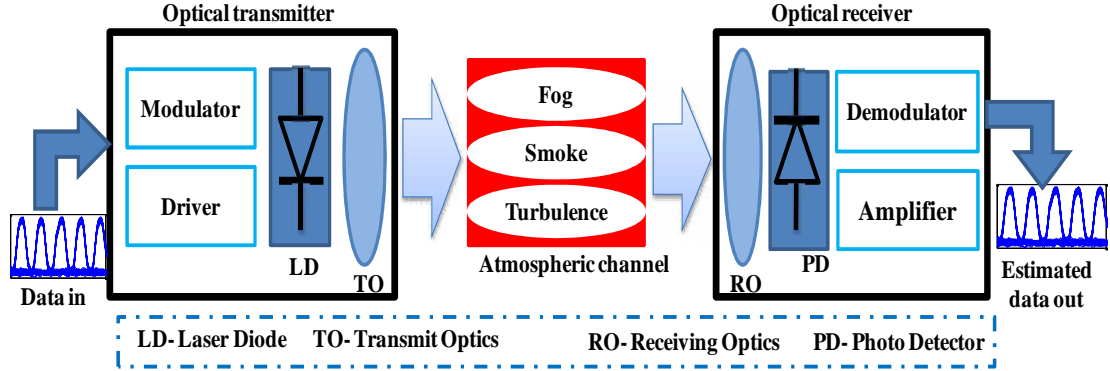


Figure 2.5. The block diagram of line of sight FSO communication system.

2.5.1. FSO transmitter

The transmitter converts the electrical signal into the optical signal using laser or LED, which is then transmitted to the receiver through the atmosphere. The transmitter side consists of a modulator, a driver, a laser diode and a transmit optics. The Modulator's purpose is to convert the information into the electrical signals with the required choice of modulation scheme. Although, there are several modulation schemes that could be used in FSO systems, the most widely adopted technique is OOK, where the input data is imprinted onto the irradiance of the optical radiation. This can be achieved by varying the driving current of the optical source directly in line with the transmitted data or using the external modulator, such as the symmetric Mach-Zehnder interferometer. The detailed description on selected modulation

schemes is provided in next section. The driver is used to regulate current flowing through the laser and stabilizes its performance; it also neutralizes temperature and aging effects on the performance of the laser [152]. The transmit optics such as telescope or lens is used to focus the optical energy towards the receiver in order to minimize the divergence [153, 154]. Both laser and LED based transmitters can be used in FSO [155]. Laser based FSO transmitters are mostly used for the long range transmission and gigabit data connection since early 2000 [156]. LED based FSO transmitters are used for short range inter-building communications [157]. However, laser diodes have shorter lifespan and also the temperature dependent output power is critical for outdoor operation [158]. LEDs also suffer from many technical -

Table 2.2. Comparison of different features of Laser and LED.

Features	Laser	LED
Output power	High	Low
Optical spectral width	0.01 – 5 nm	25 – 100 nm
Modulation bandwidth	Hundreds of GHz	Hundreds of MHz
Electrical/optical-conversion efficiency	30 – 70 %	10 – 20 %
Eye safety	Need extra precautions	Considerably eye safe
Directionality	Very focus and collimated	Broad beam
Reliability	High	Moderate
Coherence	Coherent	Non-coherent
Temperature sensitivity	Highly sensitive to temperature	Low sensitive to temperature
Drive and control circuit	Complex with threshold and temperature compensation	Simple to use and control
Cost	High	Moderate to low
Harmonic distortion	Low	High
Receiving filter	Narrow- low noise floor	Wide- high noise floor

limitations in terms of low switching rate [159]. Table 2.2 describe a succinct comparison of different features of the laser diode and LED. Figure 2.6 shows the transmission as a function of wavelength for urban aerosols conditions ($V = 5$ km), calculated from MODTRAN software in the atmosphere from visible to the near infrared (NIR) range to cope with adverse atmospheric transmission challenges. Laser sources that fall within 780 – 925 nm and 1525 – 1580 nm wavelength windows are the best to use and are well within the maximum transmission window, thus meeting the frequency requirements of most local area network (LAN) from 20 Mbit/s to 2.5 Gbit/s [63, 160-162].

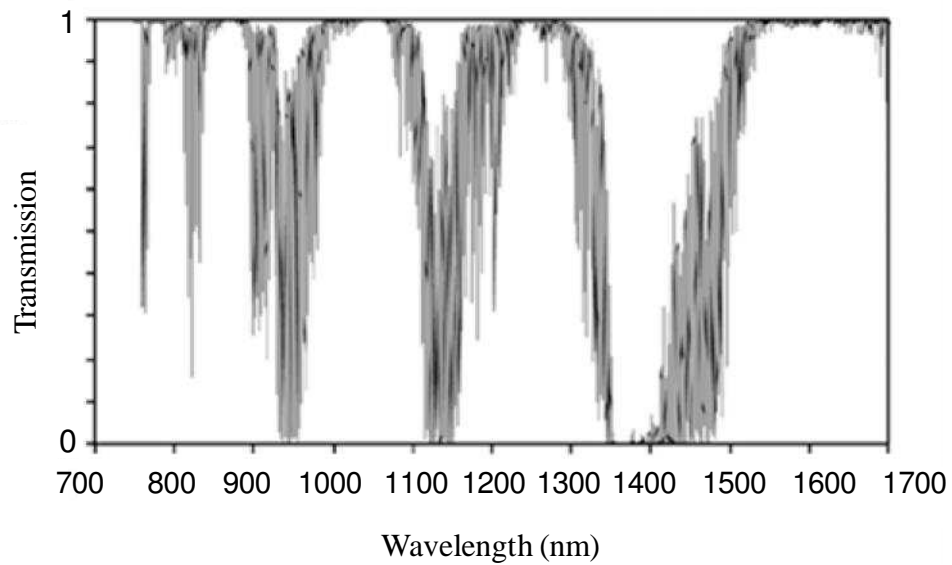


Figure 2.6. Transmission as a function of wavelength for urban aerosols conditions ($V = 5$ km), calculated from MODTRAN, reproduced from [120].

2.5.2. FSO receiver

The receiving side of the FSO link consists of a receiver optics, a photodetector, and an amplifier followed by a demodulator. The optical beam is received by the telescope and focused towards the photodetector through an optical band bandpass filter. The photo-detector converts the optical energy into the electrical energy before the signal is amplified. Following amplification the original signal is recovered using a suitable demodulation process [154]. A large receiver telescope aperture is desirable in order to collect the uncorrelated flux of optical beams and focusing their average flux onto the photodetector. This is called aperture averaging; however, this will collect more background noise intrinsic to a wide aperture area [163]. Hence, an optical bandpass filter is normally used to minimize the magnitude of the background noise. Compared to the transmitter, the receiver choice is much more limited. The two most common photodetectors used are PIN diode and avalanche photodiode (APD). APD provides sufficient internal gain thus higher sensitivity while PIN photodiode produces one electron-hole pair per photon. However, PINs are more favourable in outdoor FSO links operating in the ambient light than APD, which actually provide a decrease in SNR by amplifying the amount of noise [164]. APD also has a non-linear dependence of avalanche gain on the supply voltage and temperature, thus making it more complex and costly as it requires extra circuitry to improve this situation. Additionally, APD also needs higher bias voltages > 30 V for InGaAs to 300 V for the silicon based APDs [165]. Table 2.3 describes a summary of the characteristics of PIN and APD photodiodes.

Table 2.3. Comparison of some main characteristics of PIN and APD photodiodes
[166].

Characteristics	PIN	APD
Modulation bandwidth	Tens of MHz to tens of Ghz	Hundreds of MHz to tens of Ghz
Photocurrent gain	1	10^2 10^4
Special circuitry required	None	Temperature compensation circuitry
Linearity	High	Low- suited to digital applications
Cost	Low	Moderate to high
Bias voltage (V) for Si	45 100	220
Capacitance (pF) for Si	1.2 3	1.3 2

Most commercial visible light communications and FSO links employ silicon (Si) and GaAs based photodetectors. However, germanium (Ge) and Indium Gallium Arsenide (InGaAs) are also used to cover the operating NIR wavelength range of commercially available FSO systems such as 1550 nm. InGaAs based PIN can provide a bandwidth of greater than 40 GHz at a responsivity of 0.55 A/W [167]. Indium Phosphide (InP) / InGaAs based photodetectors provides enhanced bandwidth up to 310 GHz at a wavelength of 1550 nm [168]. However, all these materials have a rather broad spectral response, and, unlike lasers, they are not tuned toward a specific wavelength. Therefore to detect a specific wavelength, care must be taken to use a suitable photodetector [169, 170]. Some of the characteristics of the different materials used in photodetectors are illustrated in Table 2.4 [113].

Table 2.4. The main characteristic of the photodetector materials.

Material	Energy band gap (eV)	Wavelength band (nm)		Cut-off wavelength (nm)
Si	1.17	400	1060	1060
GaAs	1.424	650	870	870
Ge	0.775	600	1600	1600
InGaAs	0.73	900	1700	1700
InGaAsP	0.75 1.3	800	1650	1650

2.5.3. Atmospheric channel

The transmitted laser beam travelling through the atmosphere will experience the absorption, scattering and fluctuation depending on the atmospheric conditions like fog, rain, snow, low clouds, turbulence, smoke and dust particles [171, 172]. However, in FSO links losses induced due to the atmosphere are mainly dominated by the fog and turbulence compared to the others [173]. The laser beam normally has a very high degree of spatial coherence. However, the divergence of laser beam takes place after propagating through the atmospheric channel with a beam spot diameter of 1 m for a link length of 1 km [174]. This determines the beam intensity and the geometric loss of an FSO system as shown in Fig. 2.3. The beam divergence can be calculated using the well defined formula given as [3]:

$$\text{Spot size (m)} = \theta \text{ (mrad)} \times L \text{ (km)} . \quad (2.1)$$

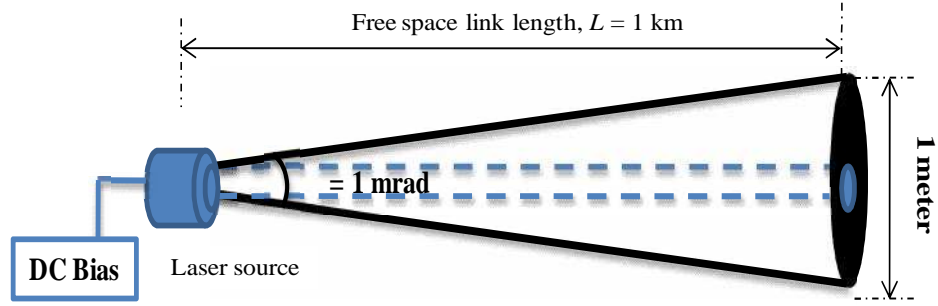


Figure 2.7. The divergence of the optical beam after 1 km distance.

The main impairment in the propagation of the laser beam in FSO is due to the atmospheric absorption and scattering resulting from the interaction with aerosol particles of different types and shapes present in the atmosphere [162]. Absorption is a quantum effect and highly dependent on the transmitted wavelength. Absorption occurs as a result of the annihilation of a transmitted light photon by the different traces of gases presents in the atmosphere [175]. The photon energy absorbed by the gas molecule increases the kinetic energy and essentially is responsible for the heating of the earth atmosphere. Absorption can be minimize by selecting suitable wavelength windows [176], where absorption effect is minimum and therefore, absorption losses can be ignored without affecting the practical results significantly. However no such band is found where the scattering loss can be minimized.

Scattering results when photons collide with molecules in the channel thus causing photon to change its direction with or without modification of its wavelength. In this process part of the optical beam energy is dispersed by particles and re-radiated into a solid angle away from the photodetector field of view (FoV). Mie scattering occurs when the sizes of particles r are equal to the incident wavelength . Fog is considered to be one of the major contributors to Mie scattering [177], as fog

particles size varies between $0.5 \mu\text{m}$ to $2 \mu\text{m}$ and harmonize to FSO wavelengths. Rayleigh scattering occurs when $r < \lambda$. However, the Geometric scattering occurs when the $r > \lambda$ [178]. A schematic diagram of comparison between three different kinds of scattering of the incident light is shown in Fig. 2.8.

In the absence of fog or other aerosols, turbulence due to temperature inhomogeneity causes corresponding changes in refractive index of the atmosphere. This creates eddies or cells of varying sizes from $\sim 0.1 \text{ cm}$ to $\sim 10 \text{ m}$ with different temperatures [179]. These mirrors like cells deviate and fluctuates the optical beam from its original path. Consequently the optical beam suffers from significant fading and phase distortion [180].

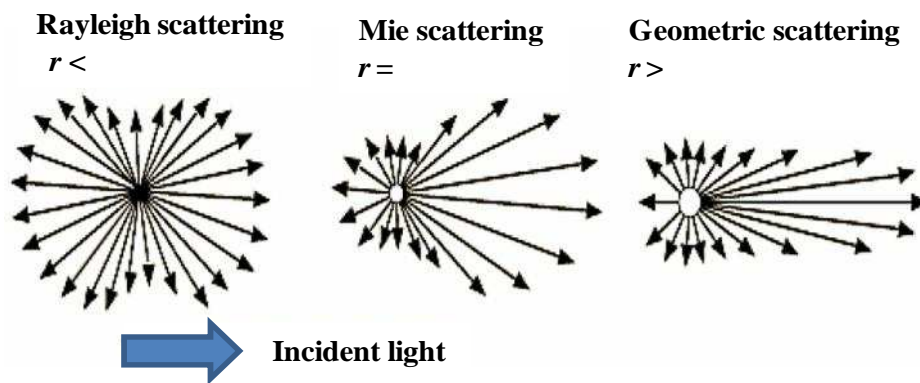


Figure 2.8. Comparison between Rayleigh, Geometric and Mie scattering.

The main effects of the turbulence are the twinkling of stars caused by random fluctuations of stars' irradiance, and the shimmer of the horizon on a hot day caused by random changes in the optical phase of the light beam, thus resulting in reduced image resolution [181]. Studies have shown that the atmospheric turbulence is also dependent on: (i) the wind velocity/ pressure, (ii) the altitude, and (iii) the air

refractive index. Some of very common effects of the atmospheric turbulence are as follows [182, 183].

- **Beam wandering** - The diameter of eddies are greater than the optical beam diameter thus causing deflection of the laser beam this leading to *beam wandering*.
- **Beam spreading** - The atmospheric turbulence causes the optical beam to spread in the propagation path by diffraction, thus leading to *beam spreading*.
- **Scintillation** - The optical beam phase front is distorted by variation in the scintillation index, thus resulting in irradiation fluctuations or *scintillations*.
- **Image dancing** - The focus of the received beam moves randomly in the image plane caused by the variations of the arrival-angle of the laser.
- **Beam steering** - Angular deviation of the beam from its initial LOS target, thus leading to the beam being out of the receiver aperture range.
- **Spatial coherence degradation** - The phase coherence across the beam phase fronts suffers losses due to the turbulence [95].
- **Polarisation fluctuation** - This is negligible for the horizontally travelling optical beam [184].

The detailed characterisation and modelling of the atmospheric fog and the turbulence channel is examined in subsequent Chapters 3 and 4, respectively.

2.6. Modulation Schemes

One of the key technical decisions in the design of any communication system is the selection of a suitable modulation scheme. Prior to the selection of the modulation scheme, it is better to define the criteria of adopting them in communication systems [185, 186]. As stated above FSO systems can carry a huge amount of data, in the visible – NIR spectrum range, but are severely affected by the turbulence and fog present in the atmosphere channel [187]. Therefore, the selection of suitable modulation scheme in terms of its type, power and bandwidth is essential in order to increase the system performance and link availability [90]. The transmission average power P_T in OWCs particularly for indoor and in some cases for terrestrial FSO is limited. These limitations are mostly linked with the eye safety, physical device limitations and the power consumption [188, 189]. However, in terrestrial FSO, these limitations put an impediment in order to alleviate the effect of fog and turbulence by increasing P_T [190]. Under these scenarios, the simplest approach is to select a suitable modulation scheme, which is more robust and competent in the atmospheric channel [191-193]. Other methods to mitigate the effects of atmospheric turbulence in FSO systems are also proposed, including: (i) the space diversity where multiple transmitters and/or multiple receivers are used [18], (ii) filters and automatic gain controller at the receiver [19], and (iii) a large aperture receiver for averaging the received optical fields over the aperture area provided its diameter is larger than the scintillation spatial coherence [20]. However, these methods are not very appealing because of the cost and their complexity to implement experimentally.

The conventional modulation schemes that could be employed in RF can not readily be used in FSO communications. This is due the constraints such as requirement of high peak-to-mean power, bandwidth efficiency, different phenomenon in the atmospheric such as scintillation and number of band-limited pulse shape, such as the *sinc* pulse [113]. Both quadrature amplitude modulation (QAM) on the discrete multi-tones (DMT) and the multilevel pulse amplitude modulation (PAM) are spectrally efficient schemes but not power efficient, which are suitable for indoor OWC [194, 195]. DMT is a baseband implementation of more generalized orthogonal frequency division multiplexing (OFDM) [196, 197]. This modulation scheme is more useful in the channel where the system non-linearity, interference and a strong low frequency noise due to the artificial light sources is dominant [196, 198].

L -PAM and L -QAM can also provide superior bandwidth efficiency at the cost of reduced power efficiency. However, L -pulse time modulations such as pulse position modulation and differential pulse interval modulation (L -PPM and L -DPIM) can provide higher power efficiencies at the expense of increased bandwidth requirement [199-201]. OOK- NRZ is the simplest and widely used modulation scheme in FSO communications due to its simplicity in the implementation. OOK-NRZ offers similar power efficiency to the 2-PPM, whereas the bandpass modulation scheme such as the binary phase shift keying (BPSK) suffers from 1.8 dB power penalty [113]. Recently, hybrid PPM-BPSK and orbital angular momentum (OAM) modulation schemes were proposed in [202, 203]. The emphasis in this thesis will be on the following digital modulations schemes: OOK- NRZ, OOK-RZ, PPM, PAM and subcarrier intensity modulation (SIM) BPSK.

2.6.1. OOK-NRZ

In NRZ-OOK, an optical pulse represents a digital symbol '1' while the transmission of no optical pulse represents a digital symbol '0'. For the simplicity of a modulator, the pulse shape is normally selected to be a rectangular [204]. If T_b is the bit duration then the bit rate is expressed as:

$$R_b = 1/T_b . \quad (2.2)$$

The normalized transmit pulse shape for OOK is given by:

$$g(t) = \begin{cases} 1 & \text{for } t \in [0, T_b) \\ 0 & \text{otherwise} \end{cases} . \quad (2.3)$$

In the demodulator, the received pulse is integrated over one bit period, then sampled and compared to a threshold to decide a '1' or '0' bit. This is called the maximum likelihood receiver, which minimizes the BER [205].

Another important parameter that needs to be considered in any modulation scheme is the bandwidth requirement. The bandwidth is estimated by the first zeros in the spectral density of the signal. The spectral density is given by the Fourier transform of the autocorrelation function. The electrical power density for NRZ-OOK assuming the independently and identical distributed (IID) input bits is given by [205, 206]:

$$S_{OOK-NRZ}(f) = (P_r R)^2 T_b \left(\frac{\sin \pi f T_b}{\pi f T_b} \right)^2 \left[1 + \frac{1}{T_b} \delta(f) \right] . \quad (2.4)$$

The OOK modulation format varies in pulse width, pulse shape is high for only a fraction of bit duration δT_b with $0 \leq \delta < 1$. Where P_r is the average electrical power and R is the response of the receiver. The advantage of this scheme is to achieve the

reduction in transmitted power. However, as δ decreases, the bandwidth requirement grows faster than the decrease in power requirement. Thus, this type of OOK is inferior to PPM, which offers less bandwidth to achieve a given reduction in power. For $\delta = 0.5$, this scheme is commonly called OOK-RZ [113, 205]. In OOK-RZ, the power requirement is reduced to half of the regular OOK-NRZ, with the expense of doubling the bandwidth. The expression for electrical power density for OOK-RZ, assuming random input bits, is given by [206]:

$$S_{OOK-RZ}(f) = (P_r R)^2 T_b \left(\frac{\sin \pi f T_b / 2}{\pi f T_b / 2} \right)^2 \left[1 + \frac{1}{T_b} \sum_{n=-\infty}^{\infty} \delta \left(f - \frac{n}{T_b} \right) \right]. \quad (2.5)$$

Figure 2.9 shows the power spectrum for the OOK-NRZ, OOK-RZ ($\delta = 0.5$). The power axis is normalized to the average electrical power P_r multiplied by T_b and the frequency axis is normalized to R_b .

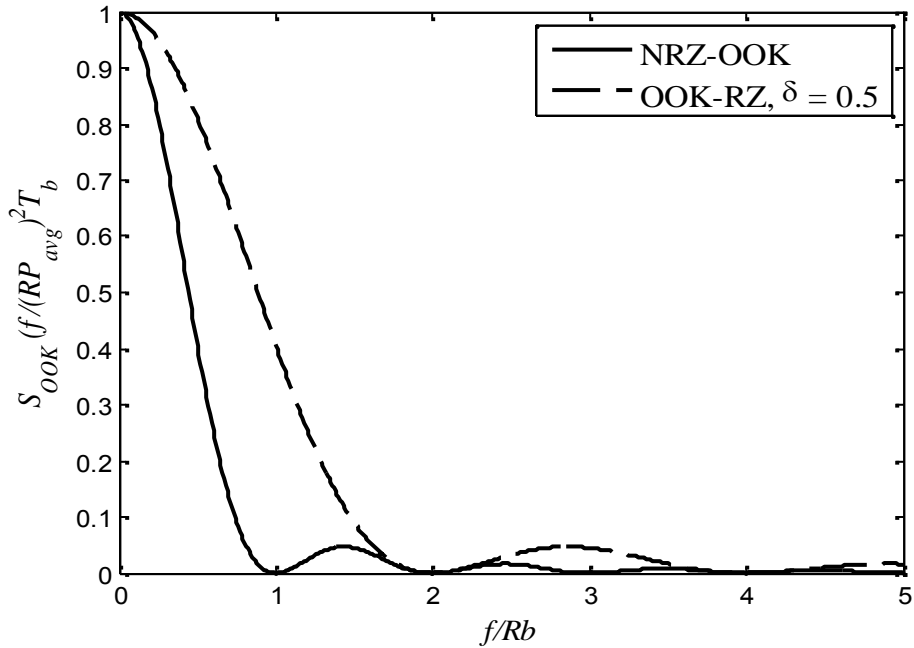


Figure 2.9. Power spectrum of the transmitted signals for OOK-NRZ and RZ [205].

2.6.2. PPM

In FSO communications, it is more desirable to adopt power efficient modulation schemes since the requirement for bandwidth is not the major concern. This is because most of the FSO links are line of sight (LOS) using a laser with abundant bandwidth. The PPM modulation scheme provides more power efficiency than OOK but at the expense of an increased bandwidth requirement and higher complexity [207]. In L -PPM, each word of M bits is mapped into one of the $L = 2^M$ symbols and transmitted through the available channel. An L -PPM symbol has the form of a pulse transmitted in one of $L = 2^M$ consecutive time slots with duration $T_s = MT_b / L$ with the remaining slots being empty (see Fig. 2.10). Information is encoded within the position of the one pulse of constant power along with $(M - 1)$ empty slots. The position of the pulse corresponds to the decimal values of the M -bit input data [208].

The transmit pulse shape for L -PPM is given by [113]:

$$x(t)_{PPM} = \begin{cases} 1 & \text{for } t \in [(m-1)T_{s_PPM}, T_{s_PPM, mT}] \\ 0 & \text{elsewhere} \end{cases}, \quad (2.6)$$

where $m \in \{1, 2, 3, \dots, L\}$.

Hence, the sequence of the PPM symbol is given as:

$$x(t)_{PPM} = LP_r \sum_{k=0}^{L-1} C_k g\left(t - \frac{KT_{symp}}{L}\right), \quad (2.7)$$

where $C_k \in \{C_o, C_1, C_2, \dots, C_{L-1}\}$ denotes the PPM symbol sequence, $g(t)$ is the pulse shape function of unity height having duration T_{symp}/L , $T_{symp}(= T_b M)$ is the symbol interval and LP_{avg} is the peak optical power of PPM symbol [113].

In L -PPM, all signals are equidistant, with:

$$d_{\min-PPM} = \min_{i \neq j} \int [x_i(t) - x_j(t)]^2 dt = 2LP^2 \log_2 \left(\frac{L}{R_b} \right), \quad (2.8)$$

Where L is the slot rate, R_b is the bit rate and P is the average power. The transmitted waveforms for 16-PPM and OOK are shown in Fig. 2.10. Detection of the L -PPM symbols requires the estimation of the slot where the pulse was most probability transmitted. Nevertheless, because of its superior power efficiency, PPM is an attractive modulation scheme for FSO communications and in deep space laser communication applications [4]. The infrared physical layer of IEEE 802.11 standard on wireless LANs recommends 16-PPM for 1Mbps and 4-PPM for 2 Mbps [113].

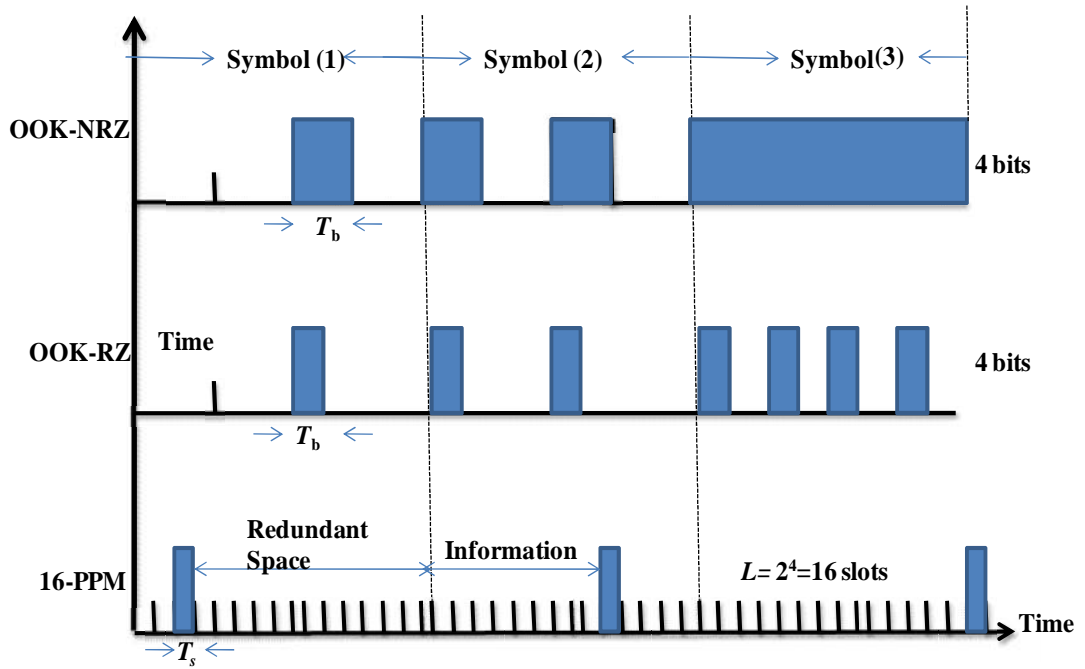


Figure 2.10. Time domain waveforms for 4-bit OOK and 16-PPM.

Since the average emitted optical power is always limited, the performance of modulation techniques is often compared in terms of the average received optical

power required to achieve a desired BER at a given data rate [209, 210]. Figure 2.11 demonstrates the required SNR to achieve particular BER for OOK-NRZ, OOK- RZ and 4-PPM. 4-PPM requires almost 6 dB less power to achieve BER of 10^{-9} compared to OOK-NRZ.

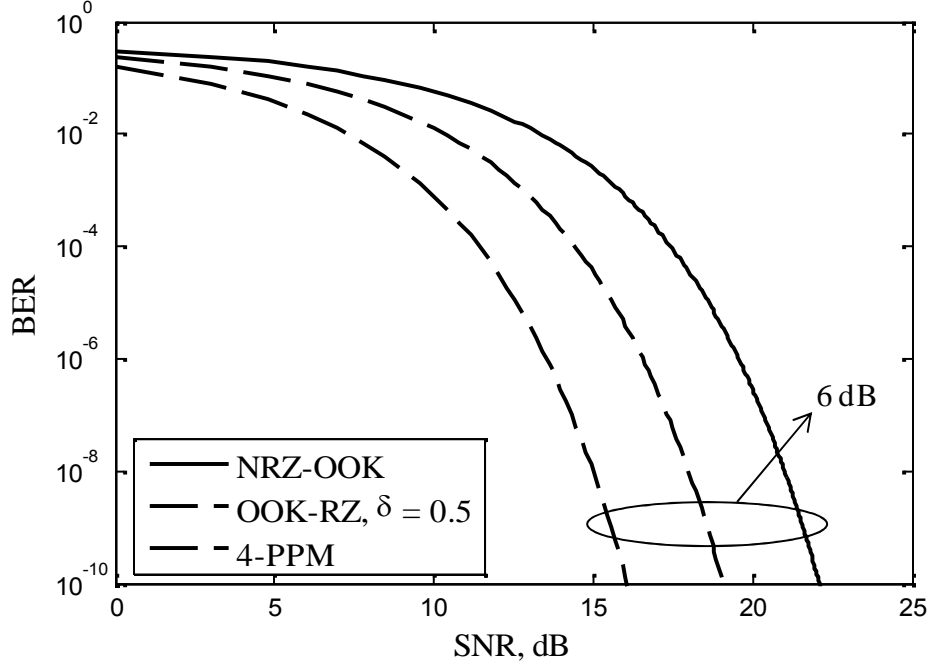


Figure 2.11. BER performance for OOK (NRZ and RZ), and 4-PPM

Table 2.5 shows the detailed comparison of the OOK-NRZ, RZ and 4-PPM. The expression for the electrical spectrum for L -PPM is given by [205, 211]:

$$S(f)_{PPM} = \frac{i_s^2}{4} \left[T_f \sin^2 \left(\frac{\pi f T_f}{L} \right) - T_f \sin^2 (\pi f T_f) + \delta(f) \right]. \quad (2.9)$$

Table 2.5. Comparison of OOK-NRZ, RZ and 4-PPM modulation techniques.

Modulation Scheme	Optical Power	Bandwidth Requirement
OOK- NRZ	P_o	R_b
OOK- RZ	$P_o - 3$	$2R_b$
L- PPM	$P_o - 5\log_{10}\left[\left(\frac{L}{2}\right)\log_2 L\right]$	$LR_b / \log_2 L$

2.6.3. PAM

PAM is a form of modulation scheme where the message information is encoded in series of varying amplitudes levels of the signal pulses [212]. In multiple-level L -PAM modulation scheme, L usually represents amplitude levels and in the case of L -PAM, each pulse conveys $\log_2(L)$ bits of information. For a given data rate, L -PAM modulation reduces the effective symbol-rate by a factor of $\log_2(L)$ compared to a conventional binary (2-PAM) system. NRZ modulation can also be considered to be 2-level PAM. The bandwidth requirement of L -PAM in comparison to OOK-NRZ is given by [213]:

$$B_{L-PAM} = \frac{R_b}{\log_2(L)} = \frac{1}{\log_2(L)} B_{OOK} . \quad (2.10)$$

Note that, using (2.10) the bandwidth B requirement in 2-PAM is equal to the OOK-NRZ, however, the bandwidth requirement is reduced to half in the case of 4-PAM when compared to OOK-NRZ. Therefore, L -PAM is more spectral efficient modulation scheme albeit the cost of lower power efficiency [214]. The waveforms of 4-PAM modulation in time domain are illustrated in Fig. 2.12.

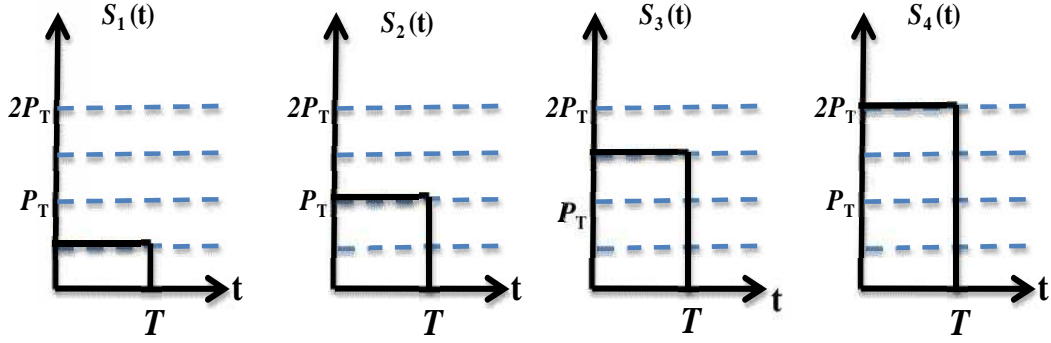


Figure 2.12. Time domain waveforms of 4-PAM modulation schemes.

The probability of a symbol error rate (*i-e*) the BER in the case of L -PAM, where L is the number of amplitude levels is given by [215].

$$BER = \frac{L-1}{L} \operatorname{erfc} \left(\frac{Q}{\sqrt{2(L-1)}} \right). \quad (2.11)$$

The BER for various values of L -PAM is shown in Fig. 2.13. As the L is increasing, the required SNR to achieve a given BER is also increased. The required SNR is 6 dB more for 8-PAM to achieve the BER of 10^{-9} than 2-PAM or OOK. However, since each L -PAM symbol can convey $\log_2(L)$ bits of information, this shows that L -PAM has an advantage over 2-PAM to achieve higher capacity albeit at the expense of power penalty. The reduction in symbol rate must yield an improvement in SNR that overcomes the increased SNR requirement for the same symbol error ratio.

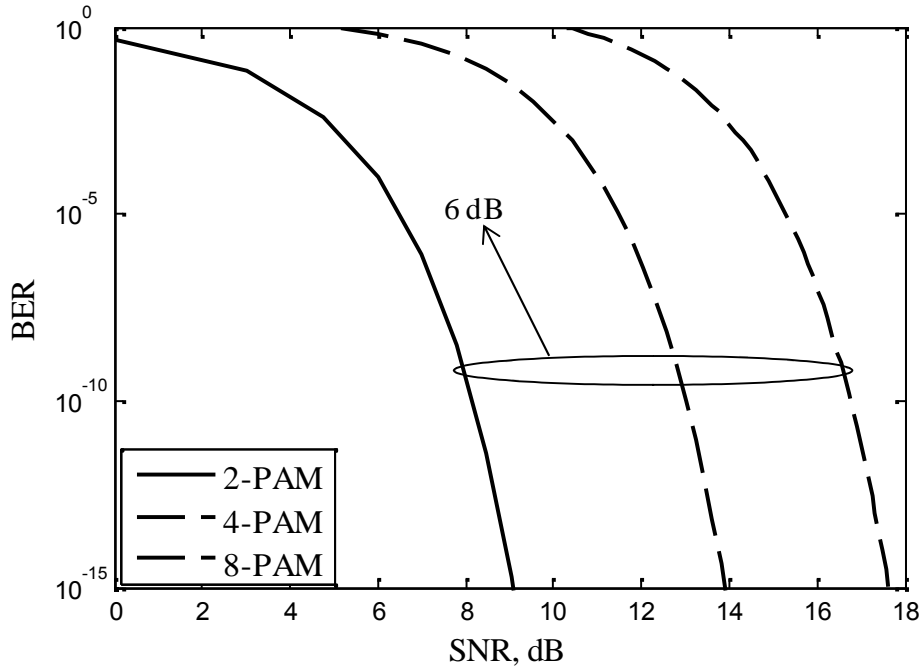


Figure 2.13. BER performance against the SNR for different levels of PAM.

2.6.4. BPSK

Subcarrier intensity modulation based BPSK is a mature and very successful scheme, which uses multiple RF carrier frequencies as in a number of applications such as digital television, asymmetric digital subscriber line (ADSL), local area networks (LANs) systems and optical fibre communications [216, 217]. In optical fibre communications, the subcarrier modulation techniques have been commercially available in transmitting cable TV signals and have also been used in conjunction with the wavelength division multiplexing [218]. Recently in [219], the effect of atmospheric turbulence using BPSK in FSO communications has been investigated showing that BPSK is a more robust modulation scheme for the turbulence channel, thus making it an attractive candidate option for FSO systems. BPSK offers a simple

and cost effective approach for exploiting the bandwidth in analogue optical communications by adding multiple subcarriers (MSC).

In BPSK-SIM, the RF subcarrier pre-modulated with data $d(t)$ is used to modulate the intensity of the optical carrier. Figure 2.14 describes the modulation and demodulation process in SIM-BPSK FSO link. Prior to modulating the optical carrier $d(t)$ is modulated onto the RF subcarrier signal using BPSK in which bits ‘1’ and ‘0’ are represented with a phase shift of 180° . Unlike baseband modulation schemes (OOK, PPM, PAM) in which information are encoded in the amplitude of carrier, the information in BPSK-SIM is encoded in the phase of the RF carrier. This offers higher immunity to the intensity fluctuation and requires no adaptive thresholding [219]. However, a DC bias must be added to the electrical signal to ensure positive amplitude prior to intensity modulation, thus making BPSK-SIM power inefficient. A standard RF coherent demodulator can be employed to recover the source data $d(t)$ as shown in Fig. 2.14.

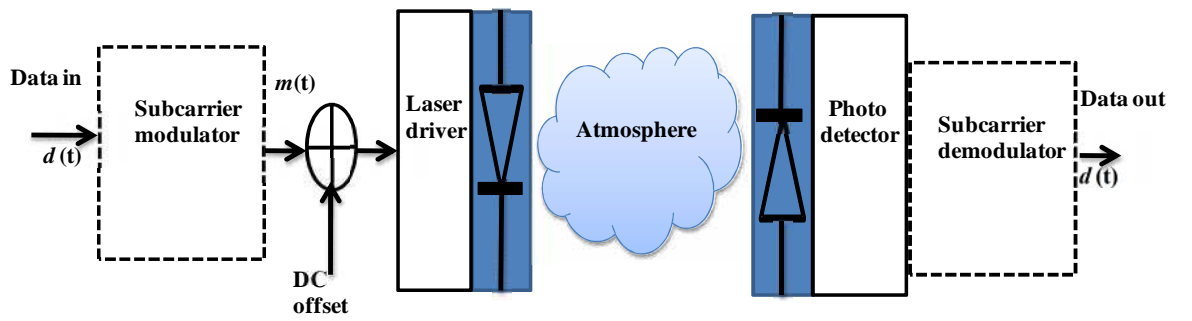


Figure 2.14. Block diagram of BPSK subcarrier intensity modulated FSO link.

The received photocurrent can be modelled as [113]:

$$i_r(t) = d_j R I \xi A g(t) \cos(w_c t) + n(t), \quad (2.12)$$

where , $d_j \in \{1, -1\}$ is the signal level for j th data symbol corresponding to the data symbol '1' and '0' , $I = 0.5 I_{peak}$, I_{peak} is the peak received irradiance, R is photodetector responsivity, $g(t)$ is the pulse shape function, $n(t) \approx N(0, \sigma^2)$ is the additive white Gaussian noise (AWGN) results from the thermal and the background noise and ξ is the optical modulation index.

BPSK reduces the need for adaptive threshold as it is keep fixed at the zero mark [113] making BPSK more simple than OOK in the atmospheric turbulence channel. Considering the AWGN channel and the post detection electrical signal-to-noise ratio (SNR_e) at the input of the BPSK demodulator is given by [9]:

$$SNR_e = \frac{(IR\xi)^2 P_m}{2B_e (qRI_{Bg} + 2kT_e / R_L)}, \quad (2.13)$$

where $P_m = (1/T) \int_T m^2(t) dt$ is the subcarrier signal power, B_e is the post detection electrical filter bandwidth required to pass information signal $m(t)$ without distortion, q and k are the electronic charge and the Boltzmann's constant, respectively. I_{Bg} represents the background radiation irradiance while T_e and R_L are the temperature and the receiver circuit load resistance, respectively. However, multiple-SIM could be implemented for higher capacity/users at the cost of poor power efficiency [220, 221]. In this thesis, The above mentioned selected modulation schemes have been experimentally implemented and compared as a means of combating the effect of atmospheric fog and scintillation in Chapters 7 and 8, respectively.

2.7. Eye Safety and Standards

The design of an FSO system is normally based on the link budget analysis for the worst atmospheric channel conditions. In this case, increasing the transmit optical power as much as possible can overcome the signal losses to achieve higher SNR. However, the transmit optical power is always limited due to the eye and skin safety reasons as well as the power efficiency [153].

Eye and skin safety are two important considerations because of the possible damage due to their exposure to the optical beam. However the skin damage is relatively insignificant if the transmit optical power is safe for the eye. The ability of the eye to concentrate the energy of near-IR radiation (*e.g.* 830 nm used in indoor laboratory FSO) on the retina, thus causing retina burns makes the eye-safety critical limiting factor on the amount of transmit optical power [153]. Retina is opaque to NIR wavelengths above 1400 nm as shown in Fig. 2.15. The wavelengths above 1400 nm tend to be absorbed by the front part of the eye (the cornea) before the energy is focused and concentrated on the retina. Thus, ultraviolet (UV) and visible radiations are more likely to focus radiation on the retina than longer wavelengths, therefore allowing 50 times higher power transmission at 1550 nm compared to 830-900 nm. This results in increased FSO link span or offering additional link margin and supporting higher data rates [222, 223].

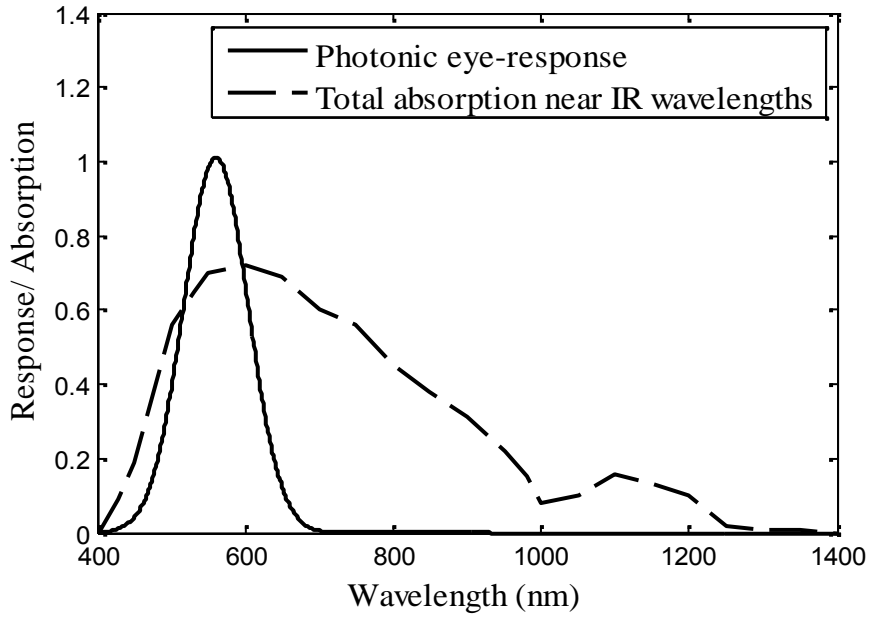


Figure 2.15. Response/absorption of the human eye at various wavelengths [153].

There are a number of international standard bodies such as the international electrotechnical commission (IEC), American national standards institute (ANSI) and European committee for electrotechnical standardization (CENELEC), which provide standards on safety on IR radiations [224]. These standards classify the main exposure limits of optical sources. The power specifications of the mostly used semiconductor laser are provided in the Table 2.6. The allowable exposure limit (AEL) depends on the wavelength and the output power of the laser beam. Class 1 and class 2 lasers are safe under reasonably foreseeable conditions of operation and usually warning labels need to be applied and the device can be used without special safety precautions. Class 3A lasers are mostly safe for viewing under unaided eye, however intra-beam view using the optics may be dangerous. Class 3 B lasers are not safe for the direct beam exposures to the eyes and direct intra-beam is hazardous. Therefore, it is always recommended to use proper goggles when using class 3B

lasers. The safety of systems operating at class 3 B is maintained by locating lasers on the rooftops or on towers to prevent any accidental exposures to eyes [225].

Table 2.6. The specifications of the mostly used semiconductor laser.

Type	650 nm	880 nm	1310 nm	1550 nm
Class 1	Up to 0.2 mW	Up to 0.5 mW	Up to 8.8 mW	Up to 10 mW
Class 2	0.2-1 mW	N/A	N/A	N/A
Class 3A	1.5 mW	0.5-2.5 mW	8.8-45 mW	10-50 mW
Class 3B	2.5- 500 mW	5-500 mW	45-500 mW	50-500 mW

2.8. Summary

This chapter outlined the literature review on the FSO communications. The fundamentals of electromagnetic spectrum and various bands of spectrum adopted in communications have been provided. The features of FSO technology that make it more viable compared with other existing RF and its potential areas of application were explained. The basic concept of FSO communication using the block diagram has been illustrated. Different blocks of optical transmitter and receiver and its functions have been detailed. A comparison of the available components for transmitter and receiver and its characteristics has been outlined in order to choose the suitable components in the design of FSO system. Also, the main challenges and its different effects such as absorption, scattering and atmospheric turbulence posed by the atmospheric channel on the transmitted optical beam have been introduced. Moreover, this chapter also discussed the theoretical background on selected modulation schemes in terms of power efficiency and bandwidth requirements with the aim to confront the different atmospheric conditions. Descriptions on the modulation schemes were given to provide a background for the subsequent Chapters 7 and 8. Eye and skin safety and classifications of lasers were discussed at the end of the chapter.

Chapter 3

Fog and Smoke Atmospheric Channel

3.1. Introduction

Since the medium of propagation of information laden optical beam in FSO is an atmosphere [134, 226], the performance of FSO systems is mostly degraded by the large optical signal attenuation. This is due to the presence of aerosols which triggers absorption and scattering of the propagating optical signals, since their dimensions are very close to the wavelengths of the optical signals [227]. The optical attenuation can be up to 130 dB/km under moderate continental fog, and up to 480 dB/km for dense maritime fog [177]. However, in a cloudy day the measured attenuation could be much higher than 50 dB/km [228]. Rain can cause attenuation up to 20-30 dB/km at a rain rate of 150 mm/h and snow can cause > 45 dB/km of loss [229-232]. However, in terms of evaluation of different weather conditions, fog and smoke are

considered to be the dominant aerosol particles that could potentially disrupt the communications by attenuating the input optical signal to the receiving side [190, 233-235]. Therefore, the chemical compositions of these types of aerosols in terms of particle size and visibility range are the important factors to understand their effects on the propagating optical beam [236-238]. This chapter outlines different types and composition of fog and smoke and also describes methods of characterisation of fog attenuation using the theoretical and empirical approaches. There are a number of empirical models which estimates the outdoor fog attenuation based on the measured V from the visible – NIR range of the spectrum. Some of the existing fog models are based on the experimental data [239-241], while others are obtained using the theoretical considerations [79, 81]. The behaviour of the resultant fog attenuation of these models is studied for different parameters such as visibility V (km), transmittance threshold T_{th} and wavelength λ . These studies have showed that in spite of a significant number of investigations, these models needs to be explicitly and experimentally verified, not for a selective or specific wavelength but for the entire spectrum from the visible to NIR regimes.

3.2. Fog Composition

Fog is the composition of very fine water particles suspended in the air forming a cloud near the ground. The formation of the water particles takes place mainly due to the evaporation of liquid water or by the sublimation of ice, where the state of ice changes into vapours. The thickness of fog is largely determined by the altitude or the distance of the inversion boundary [242]. In principle, fog particles reduce the visibility near the ground and the meteorological definition of fog is when the

visibility drops to near 1 km [88, 243]. Depending on how fog is formed there are a number of different fog types as reported in [244, 245] as discussed below.

Convection or Radiation fog is generated due to the ground cooling by radiation. This type of fog appears when the air is sufficiently cool and becomes saturated due to convection of hot radiations by cooling down the surface as illustrated in Fig. 3.1. Principally, convection appears during the night and at the end of the day with the particle diameters for this type of fog presents a weak variation around $4\ \mu\text{m}$ and the liquid water content varies between 0.01 and $0.1\ \text{g/m}^3$. A common visibility range for this type of fog is $0.5\ \text{km}$. Mostly, the radiation fog falls during early winter and is considered to be dense and localized [103].

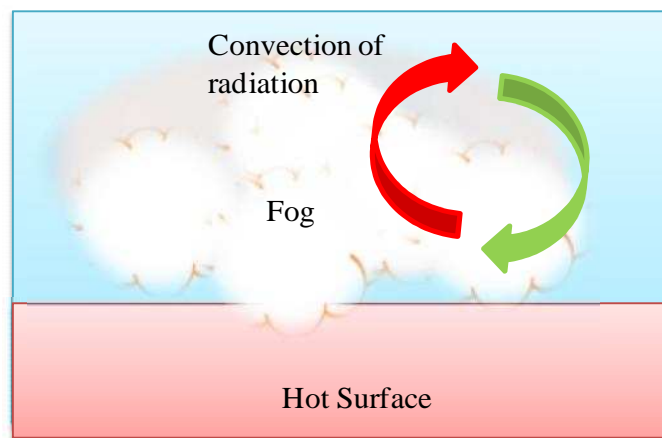


Figure 3.1. The mechanism of convection fog formation.

Advection fog occurs by the movement of wet and warm air masses above the colder maritime or terrestrial surfaces as described in Fig. 3.2. This type of fog is characterised by the liquid water content, higher than $0.20\ \text{g/m}^3$ and with a particle diameter close to $20\ \mu\text{m}$. A common visibility range is $0.2\ \text{km}$ for the advection fog

[103, 246].

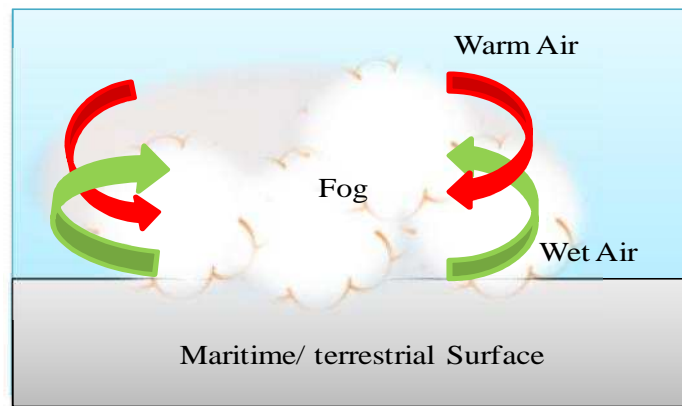


Figure 3.2. The mechanism of advection fog formation.

Table 3.1. International visibility codes and corresponding visibility (km) [243].

International visibility code					
Atmospheric conditions	Weather Constituents		mm/hr	Visibility (m)	Attenuation (dB/Km)
Dense fog				50	315
Thick fog				200	75
Moderate fog				500	28.9
Light fog	Snow	Storm	100	770	18.3
very light fog				1000	13.8
		Strong rain	25	1900	6.9
Light mist				2000	6.6
		Average rain	12.5	2800	4.6
Very light mist				4000	3.1
		Light Rain	2.5	5900	2
			10 000	1.1	
Clear air	Drizzle		0.25	18 100	0.6
				20 000	0.54
Very clear air				23 000	0.47
				50 000	0.19

The precipitation fog falls when fine rain falls into dry air below the cloud and the droplets shrink into vapours. The water vapours cool down and at the dew point, it condenses to form fog. The valley fog forms in mountain valleys as a result of temperature inversion. It can last for several days in still conditions. Valley fog is also known as Tule fog [247]. Steam fog is localized and is created by cold air passing over much warmer water or moist land [244]. Power plants that emit large quantities of steam may also be included in this category for real fog. Any visibility setting that ranges from 0 km to 1 km is reasonable for water based steam fog [244]. Further, details on the relationship between the atmospheric weather constituents and the visibility are given in Table 3.1.

3.3. Smoke Composition

Smoke is generally formed in ROA from the combustion of different substances such as carbon, glycerol and house hold emission [247]. Smoke is considered to be a visible gaseous substance in which small dry solid particles stays and disperse in the atmosphere for long time. It is commonly an unwanted by- product of fires and fireplaces, however, can also be used for pest control and communication as smoke signals [103, 248]. The most common method for smoke suspension measurements today employs a light source and a photoelectric, arranged such that the electrical output of the light source may be used as a measure of the attenuation of light by smoke. Scattering measurements are generally limited to particles whose size is of the order of the wavelength of visible light. However, since the aim is measurement of smoke as it relates to the visibility, the light attenuation method appears to be the most direct and practical approach at wavelength of 0.55 μm [249]. The density of

the smoke according to the measured visibility at corresponding transmittance (T) in lab-controlled smoke conditions is provided in Table 3.2.

Table 3.2. Measured V and T values at $0.550\ \mu\text{m}$.

Smoke	Dense	Thick	Moderate	Light
$V\text{ (m)}$	< 70	70- 250	250-500	500-1000
T	< 0.28	0.28-0. 68	0.68- 0.82	0.82-0. 90

The scattering of the optical beam depends on the refractive index of the material used for the smoke particles. In the case of glycerine based smoke the reflective index n is the wavelength dependent from visible – NIR spectrum as depicted in Fig. 3.3 [250].

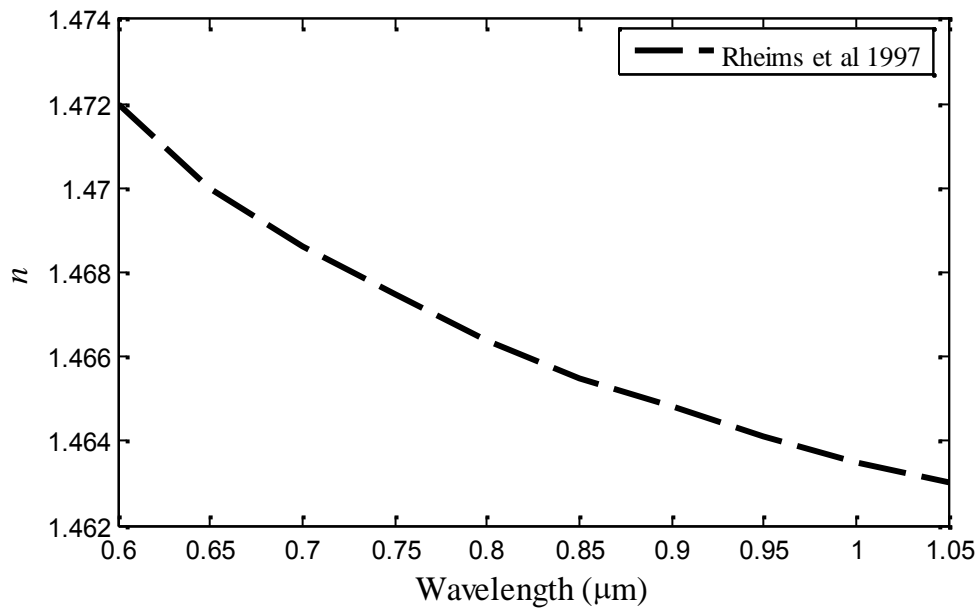


Figure 3.3. Refractive index for glycerine based smoke against the wavelength.

3.4. Characterisation of Fog and Smoke Attenuation

3.4.1. Theoretical approach

Assuming the shape of the aerosol particles is spherical presenting in the ROA, mainly those constituting the fog. The exact Mie theory can be applied to measure the scattering and absorption cross sections of the particles. Mie theory determines the scattered electromagnetic field by homogeneous spherical particles by calculating the Mie scattering and absorption cross sections of the particles define by [251]:

$$C_s = \frac{P_s}{I_o}, \quad (3.1)$$

$$C_a = \frac{P_a}{I_o}, \quad (3.2)$$

where $P_s(W)$ is the electromagnetic power scattered across the surface of an imaginary sphere cantered on the particle, $P_a(W)$ is the electromagnetic power absorbed across the surface of an imaginary sphere cantered on the particle, and $I_o(W / m^2)$ is the intensity of the incident radiation. The FSO wavelengths are mostly selected in the atmospheric transmission windows, where the molecular absorption due to gases is considered to be negligible, *i.e.* ($C_a \approx 0$) using (3.2). In principle, the selection of the wavelength in FSO communications can be selected using the wavelength windows of 0.69, 0.85 and 1.55 μm in order to minimize the absorption co-efficient. The normalized cross section or absorption efficiency Q_a can be defined as [252]:

$$Q_a = \frac{C_a}{\pi r^2}. \quad (3.3)$$

However, considering fog and smoke, the major contribution in the attenuation is

due to the scattering of the optical signal due to the Mie scattering. In order to calculate the attenuation due to Mie scattering, the value of the normalized cross section or scattering efficiency Q_s must be known. It is defined by [251, 252]:

$$Q_s = \frac{C_s}{\pi r^2}, \quad (3.4)$$

The Q_s is the function of the size parameter (r/λ) unitless quantity, the maximum value of the normalized scattering cross section reaches to 3.8 at $r/\lambda = 1$ i.e., maximum scattering of the optical signal [253]. However, the particle radius r of the fog varies in the spatial domain in the atmosphere. Due to the lack of the fixed particle size along the length of the FSO link, we may have different values of Q leading to the total attenuation due to the fog. The total attenuation β_λ of the optical signal due to the scattering and absorption coefficients γ_λ and α_λ , respectively of fog is given by [172]:

$$\beta_\lambda = \gamma_\lambda + \alpha_\lambda = \int_0^\infty \pi r^2 Q_s \left(\frac{2\pi r}{\lambda}, n \right) n(r) dr + \int_0^\infty \pi r^2 Q_a \left(\frac{2\pi r}{\lambda}, n' \right) n(r) dr, \quad (3.5)$$

Where n represents the real part of the refractive index, which depends on the material composition of the fog, in the case of water based fog n is wavelength dependent from visible – NIR spectrum as shown in Fig. 3.4 [254].

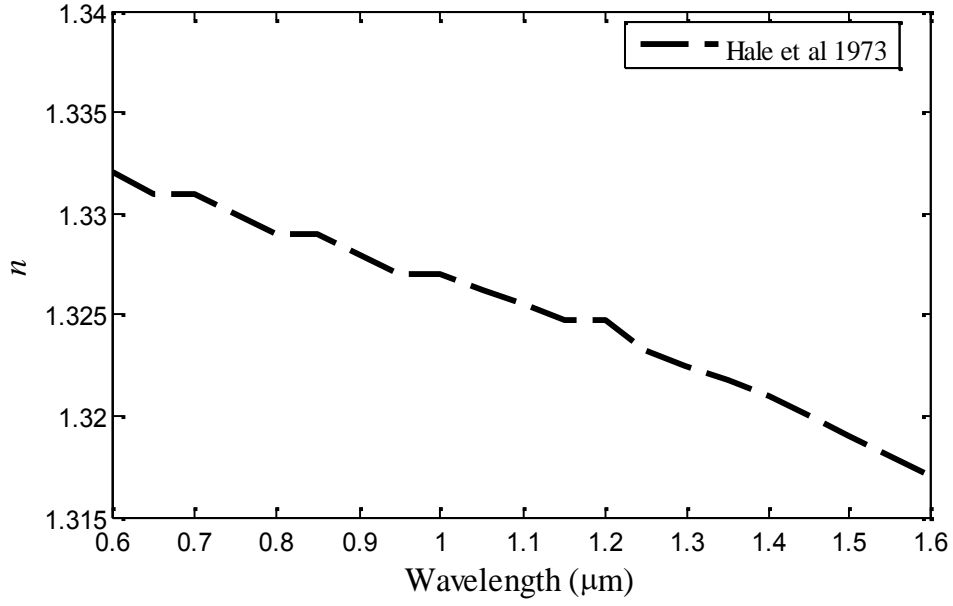


Figure 3.4. Refractive index for water against the wavelength.

However, n' represents the imaginary part of the refractive index, which contributes to α_λ due to the fog particles. In general values of n' for the water based particles are very small for the visible – NIR wavelengths compared to the FIR as shown in Table 3.3 and can be ignored. Here $\frac{2\pi r}{\lambda}$ is the size parameter that depends on the incident and r . $N(r)$ is the particle size distribution function of the aerosols and is an important parameter to determine the physical and optical properties of the fog [253, 254].

Table 3.3. The values of refractive index for real and imaginary part for water.

Wavelength (μm)	n	n'
0.5	1.34	1.0×10^{-9}
10	1.22	0.05

Fog consists of an accumulation of water particles with a variable drop size in the range of 0.01 – 25 μm in the ROA. In general, this accumulation of water particles spread is represented by $N(r)$. Considering, $N(r)$ is the number of particles per unit interval of r and $r + dr$, per unit volume, the distribution function is given by [247]:

$$n(r) = \frac{dN(r)}{dr} . \quad (3.6)$$

However, due to the concentration of the particles of radius r is of many orders of magnitudes presents in the atmosphere, this distribution is therefore often expressed as a logarithmic size distribution given as:

$$n(r) = \frac{dN(r)}{d \log(r)} . \quad (3.7)$$

In [255], for the very first time, the particle size distribution function in terms of the power law has been presented by Junge which is given as:

$$n(r) = \frac{dN(r)}{d \log(r)} = Cr^{-\alpha} , \quad (3.8)$$

where, C is the normalizing constant parameter to adjust the particle total concentration and α is the shaping parameter. Mostly, the values of the measured particle distribution does fit closely for the Junge's distribution when $3 < \alpha < 5$ for haze and aerosols with the particle size between 0.01 – 10 μm . The number of particles decreases monotonically by increasing the particles radius based on the power law. However, in real measurement, there can be collection of small range of particles. Thus, the actual particle distribution can differ from the Junge's distribution. In [256], a modified power law distribution has been proposed and given as:

$$q(\lambda) = \begin{cases} C & \text{for } 0.02 \mu m < r < 0.1 \mu m \\ Cr^{-\alpha} & \text{for } 0.1 \mu m < r < 10 \mu m \\ 0 & \text{for } r < 0.02 \mu m \end{cases} \quad (3.9)$$

However, the modified power law distribution does not demonstrate various changes in the shape parameter of the distribution. This does not take into account the drop off in the density at lower values of the particle radius, thus a modified Gamma distribution has been introduced, which is given as [237, 257]:

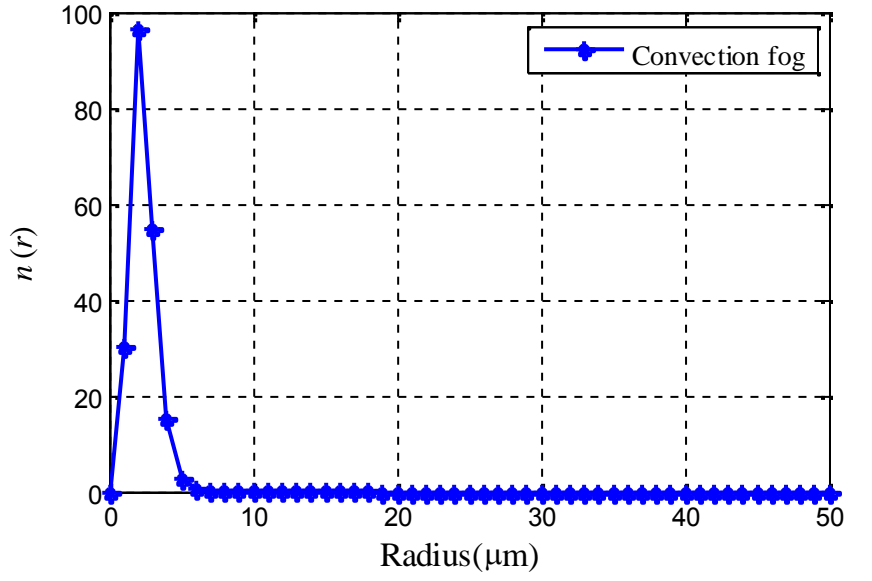
$$n(r) = ar^{\alpha} \exp(-br_m), \quad (3.10)$$

where a is the total number density, and α, a, b are the parameters that characterise the shape of the distribution with mode radius r_m . Table 3.4 shows the measured values of the shape parameters for advection and convection type of fog.

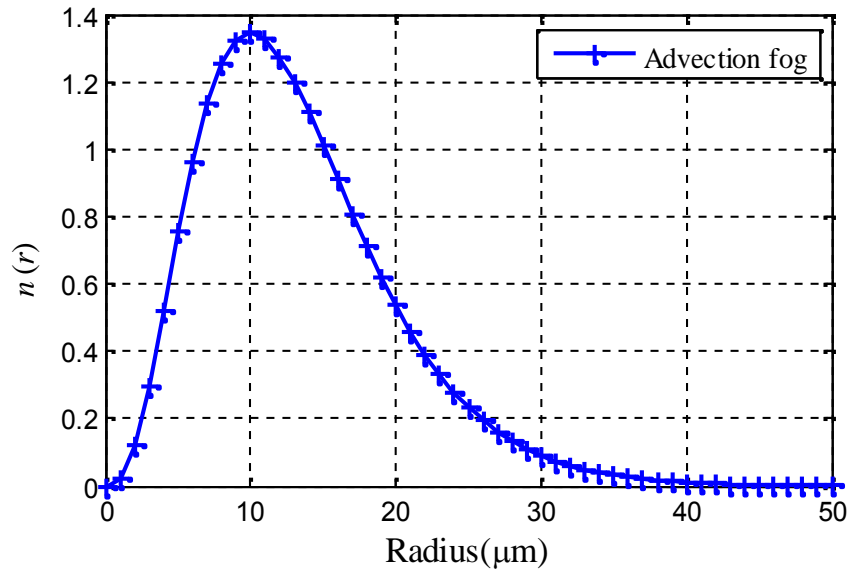
Table 3.4. Particle size distribution for advection and maritime fog.

Fog type	α	a	b	N (num/ cm ³)	W (g/ m ³)	r_m (μm)	V (m)
Advection fog	3	0.027	0.3	20	0.37	10	130
Convection fog	6	607.5	3	200	0.02	2	450

Figure 3.5 shows the particle size distribution of the advection and the convection fog using the modified Gamma distribution given in (3.10). The measured fog droplet size distribution falls within the variation of the mentioned models.



(a)



(b)

Figure 3.5. Particle size distribution versus particle radius (μm): (a) advection fog, and (b) convection fog.

3.4.2. Empirical approach

From the previous section, it shows that the attenuation due to the fog depends on the physical factors of atmosphere including the location, refractive index, relative

humidity particle size distribution and on liquid water content. Since the particle concentration and size distribution vary in spatial domain from one position to another so it is challenging to predict the fog-induced attenuation by using theoretical approach in the FSO channel. Generally, due to the complexity involved in the physical properties of the fog, like the particle size, the distribution is not readily available and reported in standard meteorological data. Therefore, the fog-induced attenuation of the optical signal can be predicted using simple empirical fog models. The empirical fog models use the measured visibility V data in order to characterise the fog. Note by definition fog is present in ROA when $V \leq 1$ km. Therefore, the link visibility *i.e.* the meteorological visual range, MVR) is used to measure the attenuation due to the fog [40, 63, 258, 259].

The fundamental law to measure attenuation of optical signal on the basis of the atmospheric V (in km) is Koschmieder law, which defines the visibility as the distance to an object at which the visual contrast/ transmittance of an object drops to certain value of the visual/ transmittance threshold T_{th} of the original visual contrast (100%) along the propagation path. The meteorological visibility V (km) can be therefore expressed in terms of the atmospheric attenuation coefficient and T_{th} as [259]:

$$V = \frac{10 \log_{10}(T_{th})}{\beta_{\lambda}}, \quad (3.11)$$

where β_{λ} , is the scattering co-efficient of the fog and normally expressed in (dB/km).

Mathematically defined by Beer- Lambert law [260] :

$$\beta_{\lambda} = -\frac{Loss}{4.343 L}. \quad (3.12)$$

The value of T_{th} of the atmospheric propagation path varies from 0.0077 to 0.06. The smaller value of T_{th} defines a larger the MVR for a certain atmosphere environment. In 1924 Koschmieder defined a value of $T_{th} = 2\%$ following by Helmholtz theory. However, the value of T_{th} is considered to 5% for aeronautical requirements as the contrast of an object (runway markings) with respect to the surrounding area is much lower than that of an object against the horizon. The most adopted values of T_{th} are 2% and 5% [243]. The selection of both changes the definition of the visibility and the corresponding attenuation of the optical signal for a given MVR. In order to define the universal definition of attenuation due to fog in the atmosphere using empirical approach, one needs to carefully select one value of T_{th} . The further study explains the behaviour of the different well known empirical models for fog attenuation and characterisation for two different types of T_{th} which are 2% and 5%. This study is done by considering the presence of the fog in the atmosphere, taking the MVR equals to 1 km, see Table 3.1.

3.5. Fog Models

The scattering co-efficient due to the fog is the parameter that is dependent on the wavelength of the propagating optical beam and the visibility. Kruse model was developed to take into account the effect of wavelength on the fog induced attenuation. Therefore (3.11) can be written as [82]:

$$V(km) = \frac{10 \log_{10} T_{th}}{\beta_{\lambda}} \left(\frac{\lambda}{\lambda_o} \right)^{-q}, \quad (3.13)$$

Here, λ_o is the maximum spectrum of the solar band, q is the coefficient related to the particle size distribution in the fog atmosphere defined by Kruse [82] and is given as:

$$q = \begin{cases} 1.6 & \text{for } V > 50 \text{ km} \\ 1.3 & \text{for } 6 < V < 50 \text{ km} \\ 0.585V^{1/3} & \text{for } 0 < V < 6 \text{ km} \end{cases} \quad (3.14)$$

Figure 3.6 (a-b), show the resultant atmospheric fog attenuation (in dB/km) using three different wavelengths of interest in FSO communications for V up to 1 km using Kruse model for T_{th} of 2% and 5%, respectively. According to this mode, the predicted attenuation is lower at the NIR wavelength than at the visible wavelengths, *i-e.* 1.55 μm has a lower attenuation than 0.67 μm for all V ranges. The attenuation difference between wavelengths of 0.67 and 1.55 μm is 10 dB at V of 0.5 km using $T_{th} = 2\%$. This difference gradually increases to 37 dB towards the dense fog at V of 0.1 km as shown in Fig. 3.6 (a). However, using $T_{th} = 5\%$, the attenuation difference is 8 dB at V of 0.5 km and it gradually increase to 22 dB at V of 0.1 km. This difference in fog attenuation using two different values of T_{th} of 2% and 5% in the prediction of the fog attenuation using the empirical model needs to be considered carefully. However, the estimation of the fog attenuation using Kruse model is considered to be not so accurate for fog [79]. This is because the value of q using (3.14) was defined for haze particles present in the atmosphere rather than fog [82].

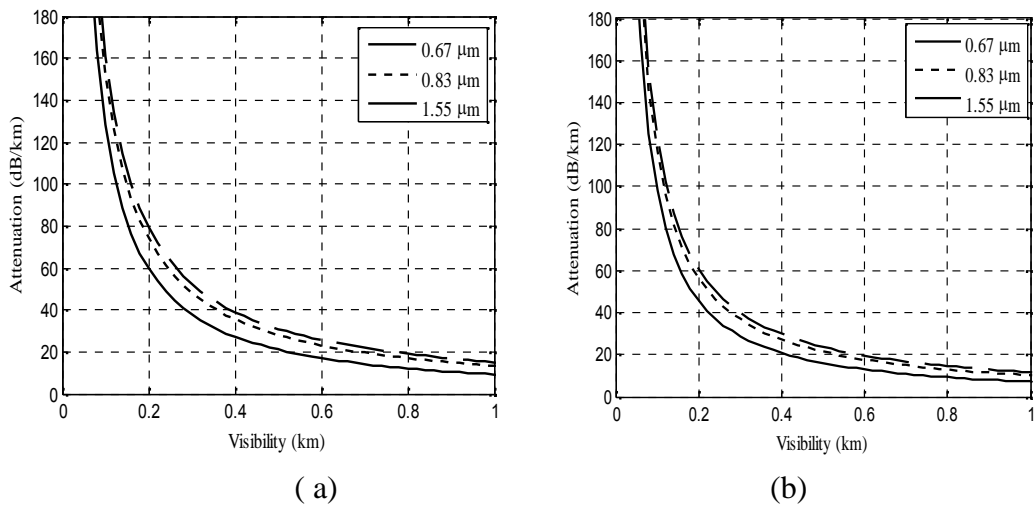


Figure 3.6. Attenuation versus visibility using Kruse model, T_{th} : (a) 2%, (b) 5%.

In [8], Kim model was developed to estimate the fog attenuation, which indicates that the atmospheric fog attenuation is wavelength independent for $V < 0.5$ km. Kim modified the Kruse model using theoretical assumptions for the fog by defining q as follows [79]:

$$q = \begin{cases} 1.6 & \text{for } V > 50 \text{ km} \\ 1.3 & \text{for } 6 < V < 50 \text{ km} \\ 0.16V + 0.34 & \text{for } 1 < V < 6 \text{ km} \\ V - 0.5 & \text{for } 0.5 < V < 1 \text{ km} \\ 0 & \text{for } V < 0.5 \text{ km} \end{cases} . \quad (3.15)$$

Figure 3.7 shows that the fog attenuation is independent of the wavelength for $V < 0.5$ km using (3.13) and (3.15), respectively. According to this model, for moderate to the dense fog conditions (*i-e*) $V < 0.5$ km, the selection of higher wavelength range is not a suitable solution in order to mitigate the fog attenuation for FSO communications. However, further theoretical and practical investigation of this model are needed at low visibility in order to explicitly confirm the attenuation is actually independent of the wavelength for moderate to dense fog ($V < 0.5$ km) conditions as mentioned in [261].

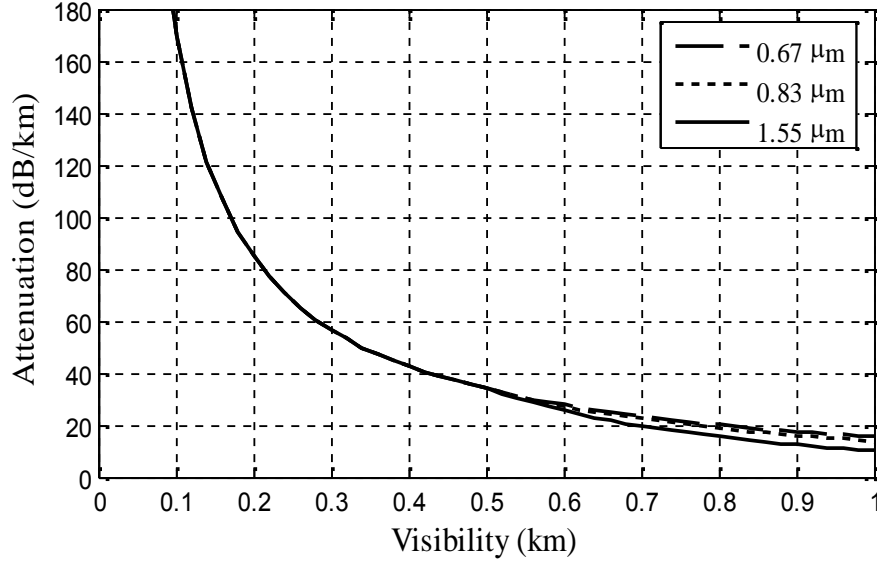


Figure 3.7. Kim model for T_{th} of 2%.

Further studies of the attenuation due to fog were conducted by a number of other researchers. Naboulsi proposed an empirical relation to estimate the attenuation caused by radiation and advection fog for wavelengths from 0.69 to 1.55 μm for V from 0.050 to 1 km [81]. The attenuation coefficient for radiation fog is given by:

$$\beta_{Con}(\lambda) = 4.343 \left(\frac{0.11478\lambda + 3.8367}{V} \right). \quad (3.16)$$

The attenuation coefficient for advection fog is given by:

$$\beta_{Adv}(\lambda) = 4.343 \left(\frac{0.18126\lambda^2 + 0.13709\lambda + 3.7205}{V} \right). \quad (3.17)$$

Figure 3.8 shows the comparison of the attenuation due to fog using Kim model using (3.13) and (3.15) by considering $T_{th} = 5\%$ and the Naboulsi advection and convection fog at $\lambda = 0.83 \mu\text{m}$ using (3.16) and (3.17), respectively. The attenuation difference between the advection and the convection fog is very small. However, Naboulsi advection and convection fog models estimate higher attenuation due to the

fog compared to Kim model. The graphical presentation of the Kim, Naboulsi advection and convection fog for $T_{th} = 2\%$ is shown in Fig. 3.9. The behaviour of the Kim model shows a good agreement to Naboulsi advection and convection models at of $0.83 \mu\text{m}$.

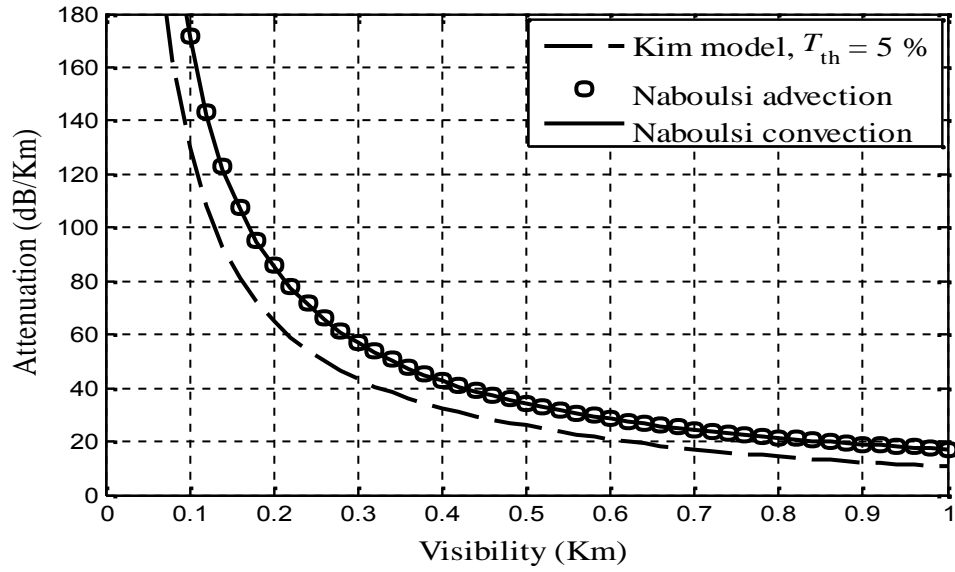


Figure 3.8. Comparison of the Kim model, Naboulsi advection and convection fog at $\lambda = 0.83 \mu\text{m}$.

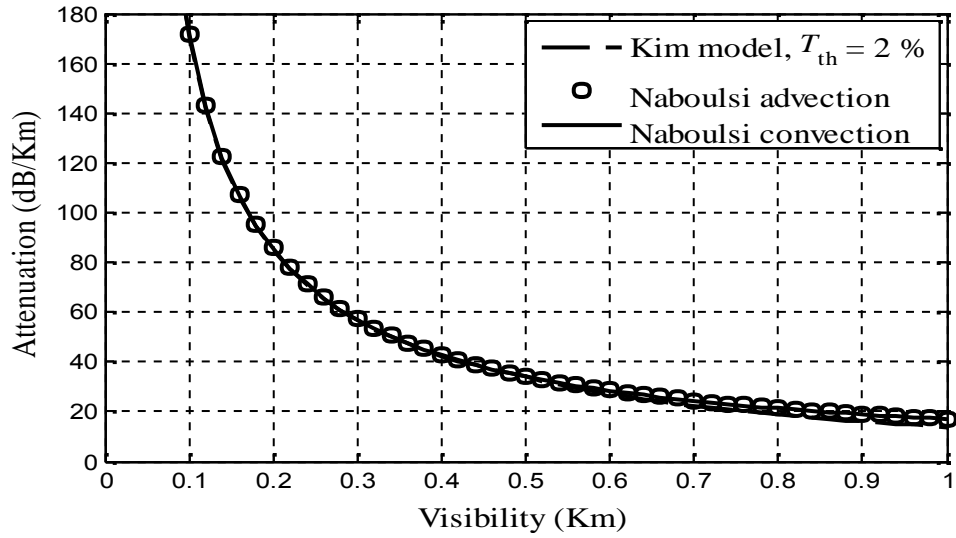


Figure 3.9. Comparison of the Kim model, Naboulsi advection and convection fog at $\lambda = 0.83 \text{ m}$.

However, Naboulsi advection and convection models again starts to deviate from Kim model for the wavelengths $> 0.90 \text{ }\mu\text{m}$. This deviation can be clearly seen from Figs. 3.10 (a) and (b) for $\lambda = 1.55 \text{ m}$ and 2.0 m .

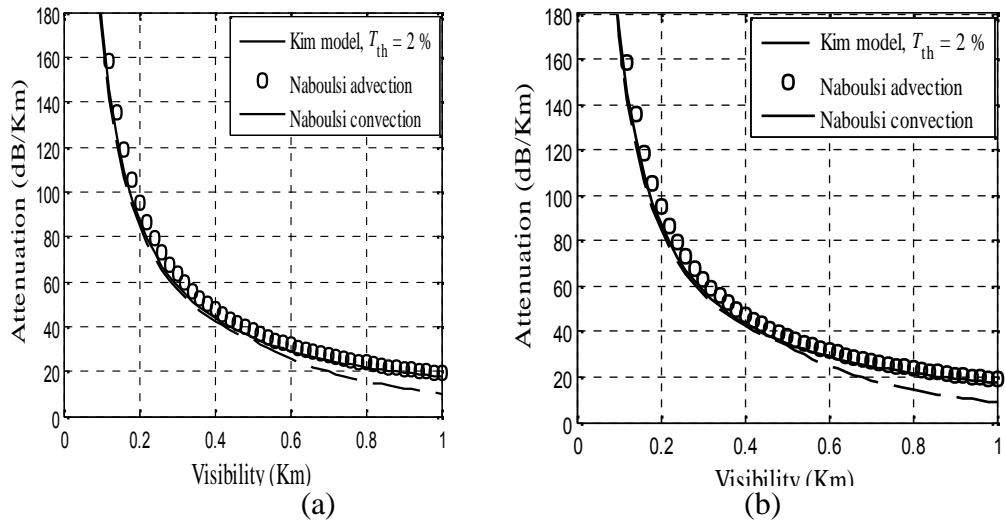


Figure 3.10. Comparison of the Kim model, Naboulsi advection and convection fog: (a) $\lambda = 1.55 \text{ m}$, and (b) $\lambda = 2.0 \text{ m}$.

Recently, the research work in [262] has proposed a wavelength dependent model for fog and haze based on the single scattering Mie theory. The model is applicable for the wavelength range of $0.2 \text{ } \mu\text{m} < \lambda < 2 \text{ } \mu\text{m}$ and for visibility range of 10 km. The model is defined as:

$$\beta_{\lambda} = \frac{10 \log_{10} T_{th}}{V (km)} \left(\frac{\lambda}{\lambda_o} \right)^{s(r_e)}, \quad (3.18)$$

where, $s = 2(\tanh(p_1(w + p_4)) - 1) + \exp(p_3(w + p_5))$ is a function of effective radius (r_e) of the fog particle distribution, $w = \log(r_e)$ and $r_e = r_{e0}(0.05/V)^{1/2}$. p_i is the parameter dependent on the selected wavelength interval and is given in [262]. However, this model is more complex to use due to the lack of particle size distribution and effective radius data at given visibility and wavelength.

Figure 3.11 (a-d) shows the fog attenuation (dB/ km) plotted for most important fog models in the range of $0.5 \text{ } \mu\text{m} < \lambda < 1.55 \text{ } \mu\text{m}$ for $V = 0.1, 0.25, 0.5$ and 1 km . However, some empirical models are not considered in this comparison based on the validity of the models (see Appendix A). Comparison of empirical models shows that Ferdinandov is not a suitable model as it did not verified by experimental work and there is an adequate difference between the Kim, Naboulsi and Ferdinandov model for range of wavelength from $0.4 - 1.1 \text{ } \mu\text{m}$ [263]. Fischer also developed a model from empirical data available for fog at $\lambda = 1.55 \text{ } \mu\text{m}$, but it does not seem to be a valid model, this is an experimental study to verify the validity of Kruse model, which is not recommended model to consider for fog [264]. Grabner presented the inverse and the power law derived from the empirical data. This model seems to be valid locally. However, the root mean squared error (RMSE) values of this model are

close to Naboulsi convection model and are clearly large to say it is an independent model [236]. Pierce model looks like same as Fischer model [265]. Pesek from Czech-Republic data developed an empirical model, but is not suitable model as developed for the single wavelength [241] and short range of 60 m. In [266], a new model has been proposed using the measured attenuation and visibility data using two wavelength of 830 nm and 1550 nm for the continental fog. However, this model has a sufficient RMSE compared to Kim and Naboulsi models. Figure 3.11 illustrates the selected models, which show a correlation for a range of $0.5 \text{ m} < \lambda < 0.9 \text{ m}$ for $V < 0.5 \text{ km}$. In [88, 134, 267], an attempt has been made in order to verify these selected models experimentally using selective wavelengths. Theoretical simulations show that Kim model underestimates the optical attenuation than Naboulsi advection and convection fog models as shown in Fig. 3.11(a-d). Kim and Naboulsi convection are best models to use in estimating the attenuation of the optical signal in fog for the wavelength range of 0.5 m to 0.9 m for $V = 1 \text{ km}$. However, both of these models contradicts each other in order to estimate the fog attenuation for $V = 1 \text{ km}$. This clearly demonstrates that in spite of a significant number of investigations, these models needs to be explicitly verified experimentally, not for a selective or specific wavelength but for the entire spectrum (visible – NIR range). The experimental verification of selected empirical models is discussed in Chapter 5.

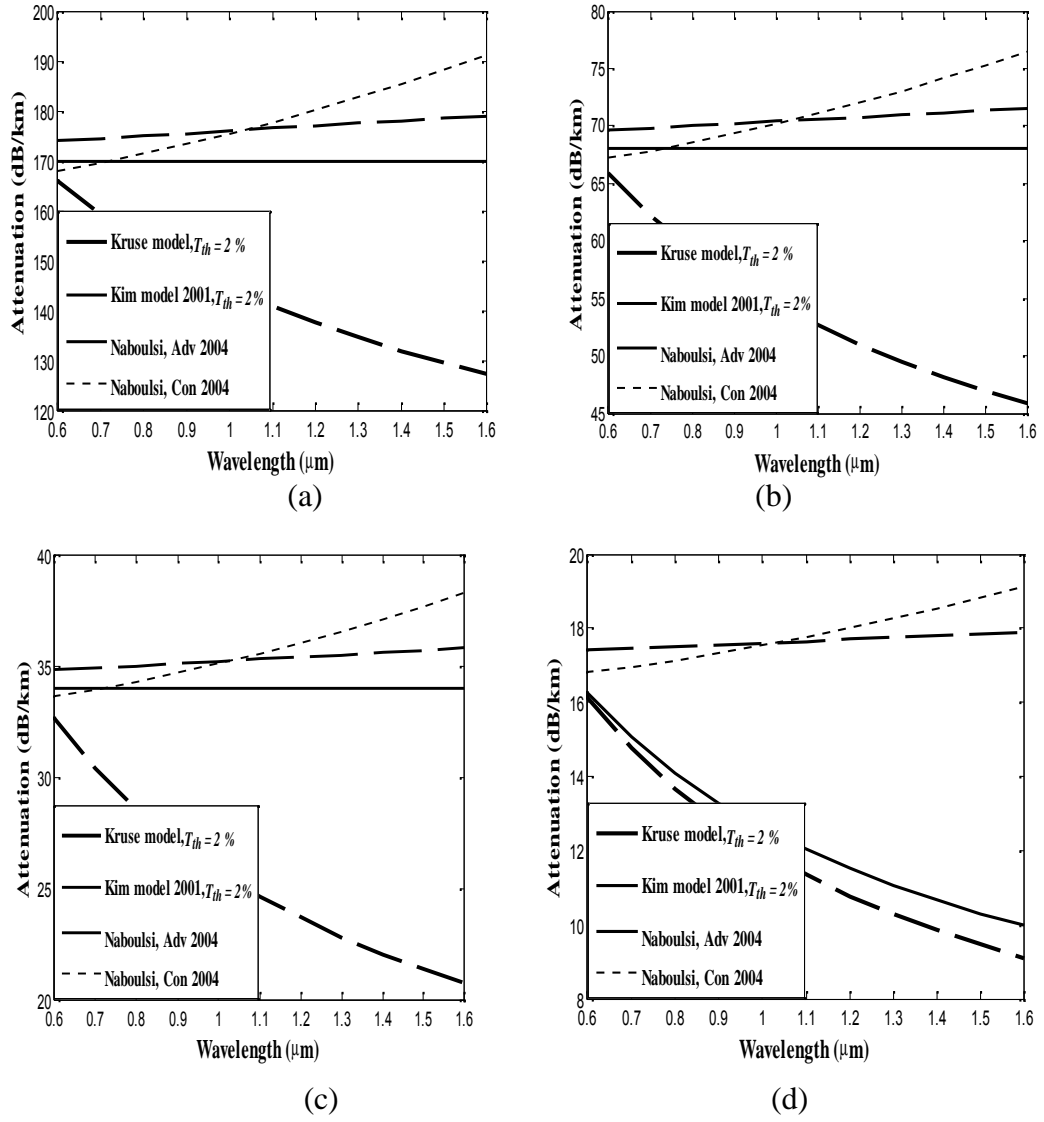


Figure 3.11. Comparison of different models for a range of wavelengths for different visibility values: (a) 0.1 km, (b) 0.25 km, (c) 0.5 km, (d) 1 km.

3.6. Summary

This chapter has outlined the theoretical and empirical approaches to model and characterise the attenuation of optical signal for visible and near infrared wavelengths ($0.6 \text{ } \mu\text{m} < \lambda < 1.6 \text{ } \mu\text{m}$) from dense to light fog conditions. A number of empirical fog models were considered and evaluated. In comparison of the models, Kim and Naboulsi convection are found to be the best models to use in estimating the attenuation of the optical signal in fog for the wavelength range of $0.5 \text{ } \mu\text{m}$ to $0.9 \text{ } \mu\text{m}$ for $V = 1 \text{ km}$. However, both of these models contradicts each other in order to estimate fog attenuation for $V = 1 \text{ km}$. This clearly demonstrates that in spite of a significant number of investigations, these models needs to be explicitly verified experimentally, not for a selective or specific wavelength but for the entire spectrum from the visible – NIR range from dense to light fog conditions. The experimental results for fog attenuation from the visible – NIR range for dense to light fog conditions are presented in chapter 5 and the selected empirical models are compared with the measured fog attenuation data to validate their performance experimentally.

Chapter 4

Atmospheric Turbulence Channel

4.1. Introduction

In clear weather conditions, apart from attenuation, atmospheric turbulence also impairs the FSO link performance [268-270]. The earth absorbs solar radiation and radiates the heat through the air around the earth surface. This makes the earth surface become warmer than that at higher altitudes. Hence, warmer air being lighter rises to mix turbulently with the surrounding cooler air causing the air temperature to fluctuate randomly [113, 271]. Turbulence is caused by the temperature inhomogeneities presents in the atmosphere [101, 272]. This can be understand as indices of different sizes with changing temperatures floating in the air. The direction of an optical beam could be altered due to interaction with discrete cells of variable temperatures, or eddies, acting like prisms with different refractive indices, thus resulting in fluctuation of the received optical signal amplitude variations (*i.e.*, scintillation) and random phase changes [273]. This leads to reduction in signal

intensity of an information-bearing optical beam, which ultimately results in performance degradation of FSO links [274, 275].

Kolomogorov theory of turbulence based on classical studies of velocity, temperature and refractive index fluctuations and statistical based modelling of the atmospheric turbulence induced fluctuations of the received optical power (or irradiance) is discussed in detail in this chapter. The statistical approach has been studied and well established in describing the atmospheric turbulence and its various effects on the optical beam propagation. Based on the statistical modelling, the strength of atmospheric turbulence is usually categorised from weak to strong regimes, see Section 4.3 [269, 276]. The strength of turbulence is dependent on the magnitude of the variation in refractive index and inhomogeneities in temperature as a function of the distance travelled by the optical radiation through the atmosphere. Theoretical models for statistical distribution for the random fading irradiance signals have already been developed, comprising the lognormal, the Gamma-Gamma, and the negative exponential models corresponding to weak, weak-to-strong and saturation regimes, respectively [277-279]. This chapter addresses the characterisation of atmospheric turbulence from weak to strong regimes based on the statistical distribution of the received signal irradiance. The lognormal model is used and verified experimentally in subsequent Chapter 8 for the characterisation of atmospheric turbulence.

4.2. Atmospheric Turbulence Channel

The atmosphere can be usefully modelled and studied based on the laminar and turbulent movement of viscous fluid. The turbulent flow of a viscous liquid is defined by Reynolds using a non-dimensional quantity $R_e = \nu l / \nu_o$, where ν (m/s) is the characteristic velocity of flow, l (m), is the dimension of the flow and ν_o is the kinematic viscosity (m^2/s). When the flow of the viscous fluid increases from the critical Reynolds number, the nature of the flow transforms from laminar to a more disordered form called the turbulence. Similarly, atmospheric turbulence results from velocity fluctuations, and thermal and refractive index gradients established along the length of the FSO link caused by the variation in the air temperature and pressure [280, 281].

Turbulence in nature is a nonlinear process and can be modelled by the Navier-Stokes equations [282]. However, in order to avoid the complexities involve in solving these equations, a statistical theory of turbulence in a simple form based on the dimensional analysis and approximations is given by the Kolmogorov theory. According to this, a classical form of turbulence theory is based on random fluctuations in the velocity field of a fluid. However, based on the velocity fluctuations, to understand the atmosphere turbulence, we adopt here energy cascade theory of turbulence [283]. According to cascade theory the wind velocity increases to the point at which the critical Reynolds number exceeded the normal air flow. Random distributed cells of variable sizes of different temperature are formed known as eddies. Furthermore, the influence of inertial forces breaks up the larger eddies into smaller eddies forming an inertial range between the outer scale also called the

large scale size L_o to the inner scale called the small scale size l_o . The energy of eddies at large scale can be due to form of wind shear or convection. However, the dissipation energy range of these eddies belong to the scale size smaller than the inner scale [280, 283]. These small sized prism like eddies trigger a randomised interference effect between different points of the propagating beam causing the wavefront to be distorted in the process as shown in Fig. 4.1.

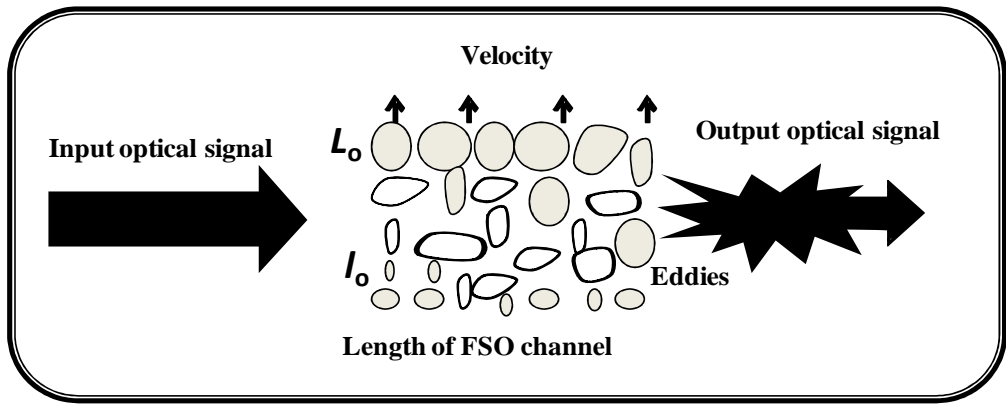


Figure 4.1. Atmospheric channel based on velocity fluctuations with turbulent eddies.

Normally, the outer scale L_o grows linearly as the function of the height above the ground from the observer to approximately 100 meters. Eddies smaller than L_o are considered to be statistically uniform and isotropic. This implies that the mean value of the field is constant and that correlations between random fluctuations in the velocity field from point to point are independent of the chosen observation points, thus depending on their vector separation. According to Kolmogorov, the longitudinal structure function, $D_v(L)$ of the wind velocity between the two points, a and b along the length L of the FSO link for inner and outer scale range follows a power law equation given as [284, 285]:

$$D_v(L) = \langle (v_a - v_b)^2 \rangle = \begin{cases} C_v^2 l_o^{-4/3} L^2, & 0 \leq L \ll l_o, \\ C_v^2 L^{2/3}, & l_o \ll L \ll L_o, \end{cases} \quad (4.1)$$

where v_a and v_b are the velocity components at point a and b and C_v^2 represents the velocity structure constant, which is a measure of the total amount of energy in the turbulence. The basic idea and characterisation of atmospheric turbulence is mostly based on velocity fluctuations. Alternatively, temperature fluctuations can also be used to characterise and explain atmospheric turbulence. The structure functions based on the temperature fluctuations resemble the power law relations as found with longitudinal velocity fluctuations, given by [283, 284]:

$$D_{T_e}(L) = \langle (T_a - T_b)^2 \rangle = \begin{cases} C_T^2 l_o^{-4/3} L^2, & 0 \leq L \ll l_o, \\ C_T^2 L^{2/3}, & l_o \ll L \ll L_o, \end{cases} \quad (4.2)$$

where T_a and T_b are the temperature of two points separated by distance L and C_T^2 is the temperature structure constant. This is a useful and easy approach to characterise atmospheric turbulence based on the measured temperature T_e difference between two points. Therefore, this approach is implemented to characterise the atmospheric turbulence in Chapter 8.

On the other hand, refractive index fluctuations of the atmosphere are an important parameter in optical wave propagation. These fluctuations are triggered by the change in the wind velocity v_w and temperature T_e of the atmosphere. A combination of small changes in v_w and T_e induces a random behaviour in the atmospheric refractive index at point R and time t , which is mathematically given as [9, 284]:

$$n(R, t) = n_o + n_1(R, t), \quad (4.3)$$

Where $n_o = \langle n(R, t) \rangle \sim 1$ is the mean index of refraction without turbulence and $n_1(R, T)$ is turbulence induced component due to spatial variation of pressure and temperature of the air.

The value of the $n_1(R, T)$ is given by [101, 283]:

$$n_1(R, t) = 1 + 77.6 \times 10^{-6} (1 + 7.52 \times 10^{-3} \lambda^{-2}) \frac{P}{T_e}, \quad (4.4)$$

where P is the pressure in millibars and T_e is the temperature in degree Kelvin. λ is the optical wavelength in μm . However, the dependency of the wavelength on the refractive index fluctuations is significantly small and can therefore be ignored for optical frequencies [284]. The contribution of humidity in refractive index fluctuation is insignificant in the FIR region and pressure fluctuations are also usually negligible [3]. Therefore, the refractive index fluctuations in the range of visible and NIR regions are mostly dependent on the random temperature fluctuations [268, 286]. For most engineering applications, refractive index fluctuations can be defined as:

$$\frac{dn_1}{dT} = -\frac{77.6P}{T_e^2} \times 10^{-6}. \quad (4.5)$$

In addition, a well-recognized Taylor's 'Frozen-flow' hypothesis is adopted, which describes that the turbulent eddies are still or frozen and can move with the transverse component of wind in the atmosphere. Thus, the temporal variations in the beam pattern (*i-e*) statistical distribution result from the perpendicular flow of wind to the direction the light. However, the temporal coherence time τ_0 is very large compared to the duration of a typical data symbol [287]. Therefore, an atmospheric turbulence channel can be attributed as a 'slow fading channel', as it is almost static during the symbol period. The turbulence induced fluctuation part in (4.3) due to the wind velocity v_w can then be written as[113]:

$$n_1(R, t) = n_1(r - v_w t). \quad (4.6)$$

In order to characterise the atmospheric turbulence based on the altitude h in meters of the atmosphere, the widely used index of refraction structure parameter C_n^2 is given as [288, 289]:

$$C_n^2(h) = 0.005(v_w/27)^2(10^{-5}h)^{10} \exp(-h/1000) + 2.7 \times 10^{-6} \exp(-h/1500) + \hat{A} \exp(-h/100), \quad (4.7)$$

where \hat{A} is a normal value of $C_n^2(0)$ at the ground level in $m^{-2/3}$, and $v_w \sim 21$ m/s. The value of C_n^2 varies with h of the atmosphere, however, it is almost considered to be constant for a horizontally propagating field. The typical average values of C_n^2 is $10^{-12} m^{-2/3}$ and $10^{-17} m^{-2/3}$ for the strong and weak turbulence regimes, respectively [290]. Practically, C_n^2 is a measure of the strength of the fluctuations in the refractive index. The value of C_n^2 along the propagation path can be calculated by incorporating the temperature structure function $D_{T_e}(L)$ and is given as [280, 291]:

$$C_n^2 = \left(\frac{dn_1}{dT} \right) C_T^2. \quad (4.8)$$

The temperature difference is obtained from point measurements of the mean-square temperature difference between two thermometers. This allows us to determine C_T^2 for any given length L using (4.2). The values of the refractive index fluctuation can be obtained using (4.5). Thus, the values of the C_n^2 can be inferred directly by using (4.8): In terms of power spectrum of refractive-index fluctuations, the power spectral density for refractive index fluctuations over turbulence channel is given by [284, 292]:

$$\phi_n(k) = 0.033C_n^2 k^{-11/3}, \quad 2\pi/L_o \ll k \ll 2\pi/l_o, \quad (4.9)$$

where k is the spatial wave number and valid only for inertial sub-range defined in (4.9). In general, the spatial power spectrum of refractive index fluctuations is considered to be the same for temperature and velocity fluctuations. For a wide range of k , equation (4.9) is modified by Tatarskii and von Karman as given in [292].

To evaluate and characterise the turbulence based on theory is very challenging and complex. This is because the observable atmospheric channel quantities such as temperature, pressure, aerosols and wind velocity. are mixed and behave in a non-linear fashion. Therefore, the atmospheric turbulence can be simply expressed and characterised based on the statistical distributions *e.g.*, probability distribution function (pdf) of received irradiance and its related properties. The following assumptions have been made to simplify the mathematics [293, 294]:

- The atmospheric FSO channel is non-dispersive for wave propagation. In the process of scattering and absorption of the optical beam, the radiated heat is insignificant in comparison with diurnal contributions.
- The energy loss is insignificant due to the atmospheric scattering arising from turbulence eddies. Therefore, the mean energy in the absence or presence of turbulence is the same. This assumption is true for spherical and plane waves. Note that, in general, a laser beam propagating over a long link span is mostly considered to be a plane wave [287].

4.3. Log-Normal Turbulence Model

In order to explain the propagation of a monochromatic electromagnetic wave represented by its constituent electric field \vec{E} in an atmospheric turbulence channel

one can employ Maxwell's equations following the vector wave expression as [269, 295]:

$$\vec{\nabla}^2 \vec{E} + k^2 n^2 \vec{E}^2 + 2\vec{\nabla}[\vec{E} \cdot \vec{\nabla} \log(n)] = 0, \quad (4.10)$$

Where n is the refractive index, $k = \frac{2\pi}{\lambda}$ is the wave number and $\vec{\nabla}$ is the Laplacian

operator defined by $\vec{\nabla} = \frac{\partial}{\partial x} \vec{i} + \frac{\partial}{\partial y} \vec{j} + \frac{\partial}{\partial z} \vec{z}$.

The weak turbulence regime is normally characterised by a single scattering event [296]. Thus, the turbulence induced depolarization part of the propagating wave may be ignored under the condition that the wavelength is much smaller than the scale of turbulence [277]. Therefore, vector wave equation (4.10) reduces to:

$$\vec{\nabla}^2 \vec{E} + k^2 n^2 \vec{E}^2 = 0. \quad (4.11)$$

For simplicity, \vec{E} hereafter is denoted in scalar form as $E(r)$. Based on the random nature of n , the best solution to the (4.11) is based on the Rytov method. This method holds interesting and practical consequences for the characterisation of the wave propagation in a random turbulence media. Additionally, this method is also true for weak turbulence based on a single scattering event. Thus, according to Rytov method the scalar field can be denoted in the complex exponential form as [292]:

$$E(r) = \exp(\psi). \quad (4.12)$$

Hence,

$$\psi = \log[E(r)]. \quad (4.13)$$

Therefore, the scalar Maxwell equation in terms of the exponential becomes the Riccati equation whose solution already exists:

$$\nabla^2 \psi + (\nabla \psi)^2 + k^2 n = 0. \quad (4.14)$$

The exact solution of (4.14) is not possible. However, using the perturbation expansion of $E(r)$, we can write [284]:

$$E(r) = \exp(\psi_o + \psi_1), \quad (4.15)$$

Where $E_o = \exp(\psi_o)$ is the incident field and ψ_1 represents the perturbed field related with the presence of turbulence and given as:

$$\psi_1(r) = \psi(r) - \psi_o(r). \quad (4.16)$$

And consequently using (4.13),

$$\psi_1(r) = \ln[E(r)] - \ln[E_o(r)] = \ln\left[\frac{E(r)}{E_o(r)}\right], \quad (4.17)$$

Where the electric field in terms of amplitude, $A(r)$ and phase, $\phi(r)$ in the case of turbulence is defined as:

$$E(r) = A(r) \exp(i\phi(r)). \quad (4.18)$$

The electric field in terms of amplitude, $A_o(r)$ and phase, $\phi_o(r)$ with no turbulence is defined as:

$$E_o(r) = A_o(r) \exp(i\phi_o(r)). \quad (4.19)$$

As a consequence, these transformations can then be used to drive for the solution of (4.14), which describes the behaviour of a field in the weak atmospheric turbulence. In finding the irradiance fluctuation statistical distribution due to turbulence, equations (4.17) and (4.18) are combined to derive the turbulence induced field amplitude fluctuation given as:

$$\psi_1(r) = \ln\left[\frac{E(r)}{E_o(r)}\right] + i[\phi(r) - \phi_o(r)] = \chi + i\delta, \quad (4.20)$$

Here, $\psi_1(r)$ is Gaussian function, therefore, χ is the Gaussian distributed field log-amplitude fluctuation and δ is the Gaussian distributed field phase fluctuation. As the phase fluctuations is ignorable compared to the turbulence induced amplitude field fluctuations [219, 221, 297]. This is because, the important scale sizes in amplitude field fluctuations are small scales on the order of the Fresnel zone $R_F = (L/k)^{1/2}$ or inner scale l_0 , and whereas it is the larger scale sizes (including the outer scale) that affect phase fluctuations. As a result, a geometrical optics approximation is often used in studying the latter rather than full diffraction theory [283].

Therefore, considering only on the field amplitude fluctuations, the pdf of χ is given as:

$$p(\chi) = \frac{1}{\sqrt{2\pi\sigma_x^2}} \exp\left\{-\frac{(\chi - E[\chi])^2}{2\sigma_x^2}\right\}, \quad (4.21)$$

where $E[\chi]$ denotes the probability of χ and σ_x^2 is the log-amplitude variance, commonly referred to as the Rytov parameter. According to [171], σ_x^2 , which characterises the strength of field amplitude fluctuation due to atmospheric turbulence, is related to C_n^2 and the horizontal distance L travelled by the optical field as [283, 284]:

$$\sigma_x^2 = 0.56k^{7/6} \int_0^L C_n^2(x)(L-x)^{5/6} dx. \quad \text{for a plane wave} \quad (4.22)$$

And

$$\sigma_x^2 = 0.563k^{7/6} \int_0^L C_n^2(x)(x/L)^{5/6}(L-x)^{5/6} dx. \quad \text{for a spherical wave (4.23)}$$

Note that, for a field propagating horizontally through the atmospheric turbulence, as in the case of terrestrial FSO applications, C_n^2 is considered to be constant. Therefore, the log irradiance variance for a plane wave becomes:

$$\sigma_l^2 = 1.23C_n^2k^{7/6}L^{11/6}. \quad (4.24)$$

The field irradiance in terms of intensity fluctuations in the atmospheric turbulent medium is $I = |A(r)|^2$. However, the intensity with no turbulence fluctuations is given by $I_o = |A_o(r)|^2$, the log-intensity is then defined by:

$$l = \log_e \left| \frac{A(r)}{A_o(r)} \right|^2 = 2\chi. \quad (4.25)$$

Hence

$$I = I_o \exp(l). \quad (4.26)$$

The intensity pdf can be obtained by invoking the transformation of variable, $p(I) = p(\chi) \left| \frac{dx}{dI} \right|$, to arrive at the log-normal distribution function given by (4.27)

[298]:

$$p(I) = \frac{1}{\sqrt{2\pi\sigma_l^2}} \frac{1}{I} \exp \left\{ -\frac{\left(\ln \left(\frac{I}{I_o} \right) - E[l] \right)^2}{2\sigma_l^2} \right\}. \quad I > 0 \quad (4.27)$$

Following equation (4.25) the log-intensity variance $\sigma_l^2 = 4\sigma_x^2$ and the mean log intensity, $E[l] = 2E[x]$. According to the second assumption in Section 4.2, it

follows that $E[\exp(l)] = E[I/I_o] = 1$. Since there is no energy loss during the turbulence induced scattering process, $E[I] = I_o$. The probability, $E[I]$ is obtained by invoking the standard relation (4.28), which is valid for any real valued Gaussian random variable [293]. Thus $E[l]$ is obtained as outlined below:

$$E[\exp(az)] = \exp\left(aE[z] + 0.5a^2\sigma_z^2\right) \quad (4.28)$$

$$1 = \exp([E(l)] + 0.5\sigma_l^2). \quad (4.29)$$

Hence

$$E(l) = -\frac{\sigma_l^2}{2}. \quad (4.30)$$

Figure 4.2 illustrates the log-normal pdf for different values of log irradiance variance σ_l^2 using (4.27). Note that, as the value of σ_l^2 increases, the distribution becomes more skewed with longer tails towards the infinity. This explains the extent of intensity fluctuations as the channel heterogeneity increases due to atmospheric turbulence. However, the pdf of the irradiance fluctuation using (4.27) is valid for a weak turbulence medium. For weak atmospheric turbulence conditions, the statistics of the intensity fluctuations have been experimentally found to obey the log-normal distribution [299].

The expression for the normalized variance σ_l^2 of the propagating optical beam intensity I (also called the scintillation index or log irradiance variance) detected at the receiver, which characterises the strength of the turbulence is given as [113, 286, 300].

$$\sigma_I^2 = \frac{\sigma_I^2}{I_o^2} = \exp(\sigma_I^2) - 1, \quad (4.31)$$

where I_o is average intensity of the received irradiance. This approach has also been used to characterise the strength of turbulence generated within the atmospheric chamber in chapter 8. Table 4.1 relates the turbulence strength with the different values of scintillation index ($S.I$).

Table 4.1. Strength of Turbulence based on $S.I$.

Turbulence	SI
Weak	$\sigma_I^2 < 0.3$
Medium	$\sigma_I^2 \approx 1$
Strong	$\sigma_I^2 \gg 1$

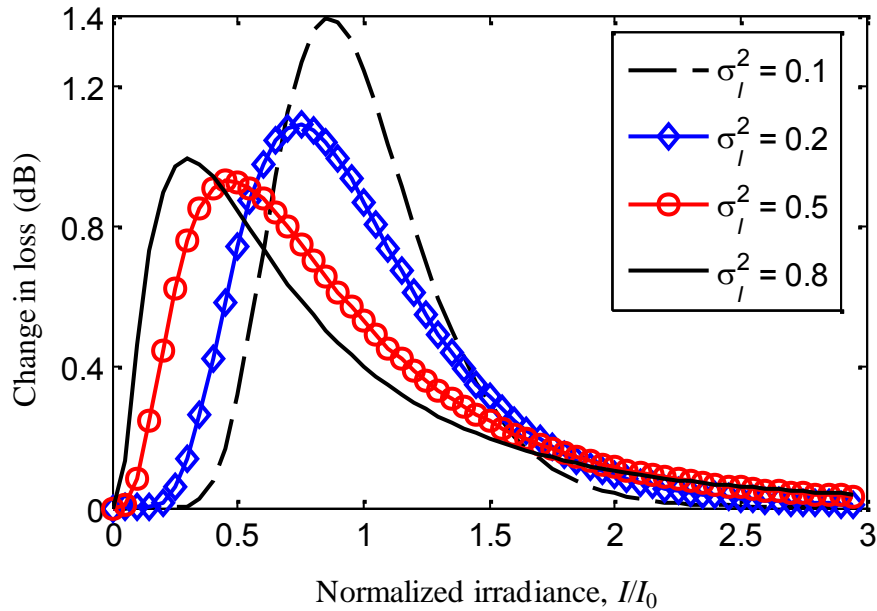


Figure 4.2. Log-normal pdf against the normalized irradiance for a range of irradiance variance values.

4.3.1. Spatial coherence in weak turbulence

When a coherent optical beam propagates through the atmosphere, the spatial coherence of the beam degrades due to temperature, velocity and refractive index fluctuations. The extent of this coherence degradation is a function of the atmospheric turbulence strength and the propagation distance. The atmospheric turbulence channel divides the coherent beam into various fragments whose diameters represent the reduced spatial coherence distance. Following from the Rytov approach used in the modelling of the weak atmospheric turbulence, the spatial coherence of a field travelling through the atmosphere can be derived as [171, 284, 296]:

$$\Gamma_x(\rho) = A^2 \exp\left[-(\rho / \rho_o)^{5/3}\right], \quad (4.32)$$

where ρ_o is the transverse coherence length of the field, at which the coherence of the field is reduced to $1/e$. The ρ_o for the plane and spherical beams are given respectively in (4.33) and (4.34) as [171].

$$\rho_o = \left[1.45 k^2 \int_0^L C_n^2(x) dx \right]^{-3/5}, \quad (4.33)$$

$$\rho_o = \left[1.45 k^2 \int_0^L C_n^2(x) (x/L)^{5/3} dx \right]^{-3/5}. \quad (4.34)$$

Figures 4.3 and 4.4 illustrate the coherence length for a horizontal link at two commonly used FSO wavelengths of 850 nm and 1550 nm for typical values of C_n^2 . The spatial coherence length is generally longer at higher wavelengths and decreases with the increase of both the strength of turbulence and the propagation distance. The comparison of spatial coherence length (in meters) for the plane wave for strong

turbulence, $C_n^2 = 10^{-12} \text{ m}^{-2/3}$ at wavelength of 830 nm and 1550 nm is given in Table 4.2.

Table 4.2. The dependence of wavelength on spatial coherence length for $C_n^2 = 10^{-12} \text{ m}^{-2/3}$.

Link Distance (km)	0.1	1	10	100
Spatial coherence length (m) at 830 nm	2.9	0.7	0.17	0.04
Spatial coherence length (m) at 1550 nm	6.5	1.5	0.3	0.09

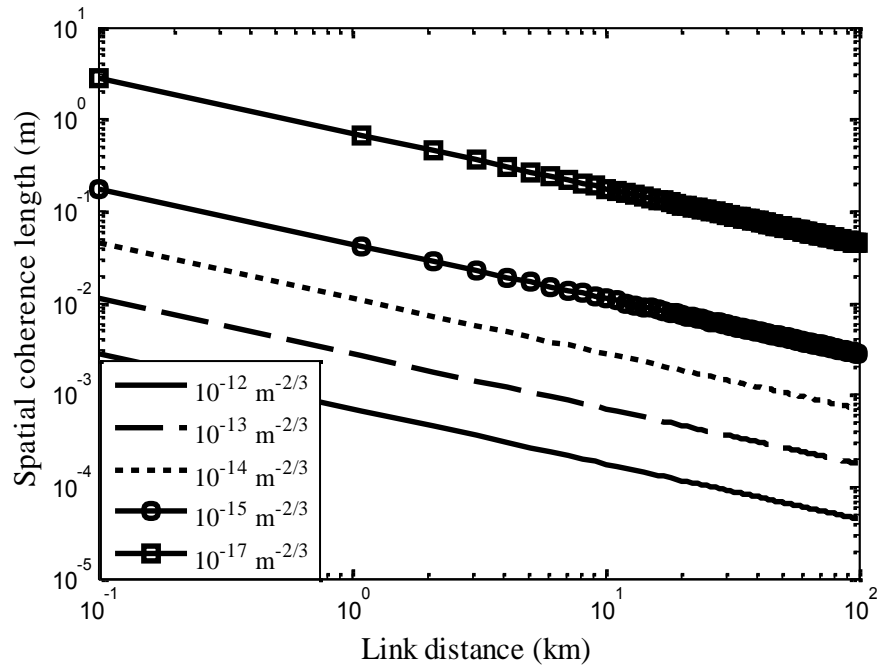


Figure 4.3. Plane wave transverse coherence length for $\lambda = 830 \text{ nm}$ and a range of C_n^2 .

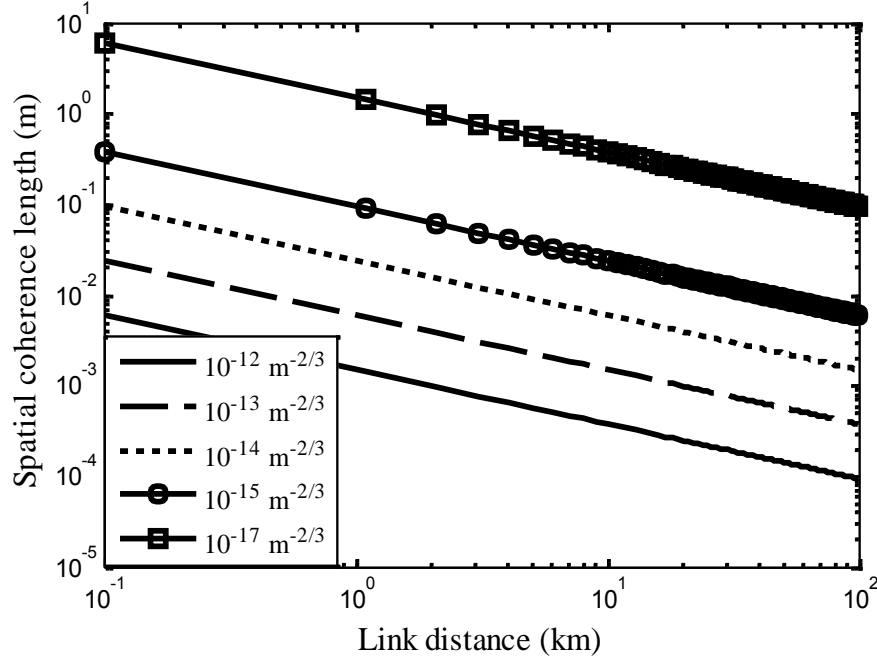


Figure 4.4. Plane wave transverse coherence length for $\lambda = 1550$ nm and a range of C_n^2 .

4.3.2. Aperture averaging and BER evaluation

The coherence length ρ_o is particularly useful in determining the size of the receiver aperture needed to collect the bulk of the propagating field through the process known as the aperture averaging, and also to determine the separation distance of detectors in a multiple receiver system [73]. In order for detectors in the array to receive uncorrelated signals they must be spaced at a minimum distance ρ_o apart. The fading effect can be reduced significantly if the receiver aperture $A_{rx} > \rho_o$ (*i.e.*, by the process known as the aperture averaging). The aperture averaging factor, which is widely used to quantify the fading reduction, is given by [301]:

$$A = \frac{\sigma_I^2(D)}{\sigma_I^2(0)}, \quad (4.35)$$

where $\sigma_I^2(D)$ and $\sigma_I^2(0)$ denotes the scintillation index for a receiver lens of diameter D and a “point receiver” ($D = 0$), respectively.

For the plane wave propagation with a smaller inner scale $l_o \ll (L/k)^{0.5}$, the scintillation index is given by [283]:

$$\sigma_I^2(D) = \exp \left[\frac{0.49\sigma_I^2}{\left(1 + 0.65d^2 + 1.1\sigma_I^{\frac{12}{5}}\right)^{\frac{7}{6}} + \left(-0.5\sigma_I^2(1 + 0.69\sigma_I^{\frac{12}{5}})\right)} \right] - 1, \quad (4.36)$$

where $d = \sqrt{kD^2/4L_p}$, $k=2\pi/\lambda$, D is receiver aperture diameter and L_p is the propagation distance.

In the presence of turbulence, the instantaneous irradiance is fluctuated, thus leading to the variation in the instantaneous SNR. Hence, the average value of SNR is used to evaluate the FSO link performance. The ensemble mean of SNR can be expressed as [302]:

$$\langle SNR \rangle = \frac{SNR_0}{\sqrt{\sigma_I^2(D)(SNR_0)^2 + \frac{I_0}{\langle I \rangle}}}, \quad (4.37)$$

where SNR_0 is for the turbulence free condition. Therefore, with no turbulence $\langle SNR \rangle = SNR_0$, where $\langle . \rangle$ denotes the ensemble average.

The bit error rate (BER) for the FSO link with intensity modulation/direct detection (IM/DD) using OOK, under the turbulence condition is calculated as:

$$BER = Q(\sqrt{SNR}), \quad (4.38)$$

where $Q(\cdot)$ is Marcum's Q -function, which is the area under the Gaussian tail, given by:

$$Q(x) = \frac{1}{\sqrt{2\pi}} \int_x^{\infty} e^{-\frac{\alpha^2}{2}} d\alpha . \quad (4.39)$$

4.3.3. The limit of log-normal turbulence model

In previous sections, Rytov approximation has been used to describe the atmospheric turbulence using the log-normal turbulence model. Rytov approximation predicts that Rytov parameter increases with the index of refraction structure parameter C_n^2 and/or the propagation path length. However, based on experimental data as reported in [287], this prediction holds only for the weak turbulence regime when $\sigma_x^2 \geq 0.3$. As the turbulence strength increases beyond the weak regime, due to a combination of increased path length and/or increased C_n^2 , turbulent eddies result in multiple scatterings that are not accounted for by Rytov in his approximation [171, 283]. Based on experimental data reported in [171, 283], $S.I$ increases linearly with Rytov parameter within the weak regime and continues to increase to a maximum value greater than unity. At this point, when $S.I.$ is maximum which characterises the highest strength of inhomogeneity. The $S.I.$ then starts to decrease due to self interference as a result of multiple scattering and approaches the unity as C_n^2 increases [287]. This observation is in contrast to the prediction of Rytov approximation beyond the weak atmospheric regime. In the next two sections, the other irradiance fluctuation models that account for the multiple scatterings will be reviewed and their pdfs will be presented.

4.4. The Gamma-Gamma Turbulence Model

The model proposed in [280] is based on the modulation process where the fluctuation of light radiation traversing a turbulent atmosphere is assumed to consist of small scale (scattering) and large scale (refraction) effects. The former includes contributions due to eddies/cells smaller than the Fresnel zone $R_F = (L/k)^{1/2}$ or the coherence radius ρ_o , whichever is smaller, where L is the distance and k is wave number. Large scale fluctuations on the other hand are generated by turbulent eddies larger than that of the first Fresnel zone or the scattering disk $L/k\rho_o$, whichever is larger. The small scale eddies are assumed to be modulated by the large scale eddies. Consequently, the normalised received irradiance I is defined as the product of two statistically independent random processes I_x and I_y :

$$I = I_x I_y, \quad (4.40)$$

I_x and I_y arise from the large scale and small scale turbulent eddies, respectively and it is suggested that both obey the gamma distribution [276, 279, 280]. Their pdfs are given by:

$$p(I_x) = \frac{\alpha(\alpha I_x)^{\alpha-1}}{\Gamma(\alpha)} \exp(-\alpha I_x), \quad I_x > 0; \alpha > 0 \quad (4.41a)$$

$$p(I_y) = \frac{\beta(\beta I_y)^{\beta-1}}{\Gamma(\beta)} \exp(-\beta I_y), \quad I_y > 0; \beta > 0 \quad (4.41b)$$

By fixing I_x and using the change of variable $I_y = I / I_x$ the conditional pdf given by

(4.42) is obtained in which I_x is the (conditional) mean value of I :

$$p(I/I_x) = \frac{\beta(\beta I/I_x)^{\beta-1}}{I_x \Gamma(\beta)} \exp(-\beta I/I_x). \quad I > 0 \quad (4.42)$$

To obtain the unconditional irradiance distribution, the conditional probability $p(I/I_x)$ is averaged over the statistical distribution of I_x given by 4.41(a) to obtain the following gamma-gamma irradiance distribution function:

$$p(I) = \int_0^{\infty} p(I/I_x) p(I_x) dI_x, \quad (4.43)$$

$$p(I) = \frac{2(\alpha\beta)^{(\alpha+\beta)/2}}{\Gamma(\alpha)\Gamma(\beta)} I^{\left(\frac{\alpha+\beta}{2}\right)-1} K_{\alpha-\beta}(2\sqrt{\alpha\beta}I), \quad I > 0 \quad (4.44)$$

where α and β , respectively represent the effective number of large and small scale eddies of the scattering process. $Kn(.)$ is the modified Bessel function of the 2nd kind of order n , and $\Gamma(.)$ represents the Gamma function. If the optical radiation at the receiver is assumed to be a plane wave, then the two parameters α and β that characterise the irradiance fluctuation pdf are related to the atmospheric conditions by [1, 303, 304]:

$$\alpha = \left[\exp\left(\frac{0.49\sigma_I^2}{(1+1.11\sigma_I^{12/5})^{7/6}} \right) - 1 \right]^{-1}. \quad (4.45a)$$

$$\beta = \left[\exp\left(\frac{0.51\sigma_I^2}{(1+0.69\sigma_I^{12/5})^{5/6}} \right) - 1 \right]^{-1}. \quad (4.45b)$$

While the scintillation index is given by:

$$\sigma_N^2 = \exp\left[\frac{0.49\sigma_I^2}{(1+1.11\sigma_I^{12/5})^{7/6}} + \frac{0.51\sigma_I^2}{(1+0.69\sigma_I^{12/5})^{5/6}} \right] - 1. \quad (4.46)$$

A plot of the distribution, using (4.44) is given in Fig. 4.5 for three different turbulence regimes, namely weak, moderate and strong. The plot shows that as the turbulence increases from a weak to a strong regime, the distribution spreads out more, with an increase in the range of possible values of the irradiance.

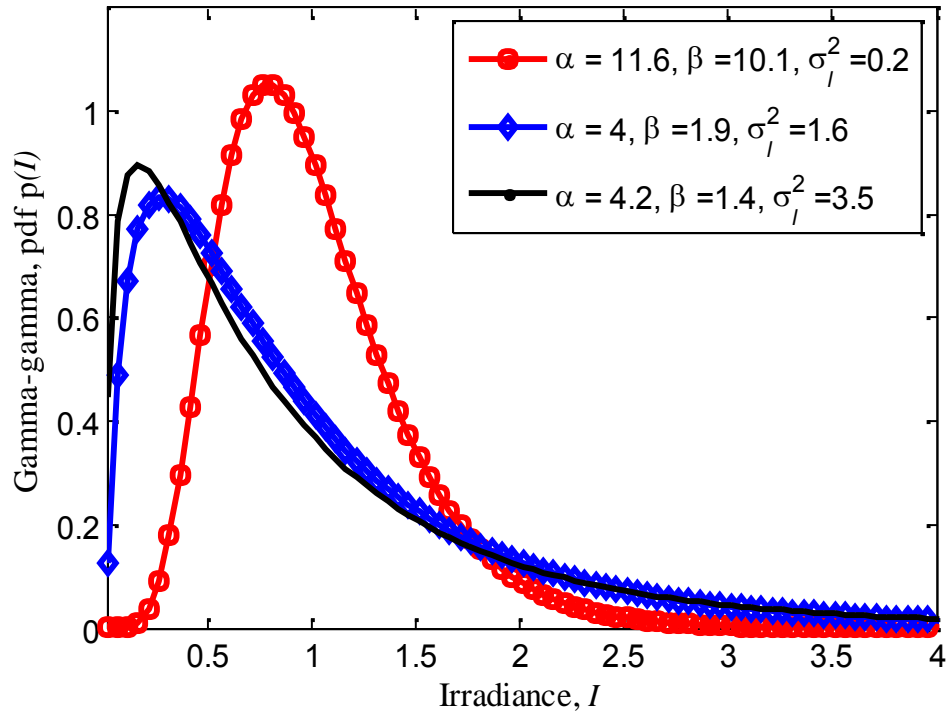


Figure 4.5. Gamma-gamma probability density function for three different turbulence regimes, namely weak, moderate and strong.

The Gamma-Gamma turbulence model given by (4.44) is valid for all turbulence scenarios from weak to strong and the values of α and β at any given regime can be obtained using 4.45 (a) and (b), respectively. Figure 4.6 depicts the variation of $S.I.$ as a function of the Rytov parameter based on (4.46), this graph shows that as Rytov parameter increases, the $S.I.$ approaches a maximum value greater than one, and then approaches the unity as the turbulence induced fading reaches the saturation regime. The values of α and β under different turbulence regimes are depicted in Fig. 4.7.

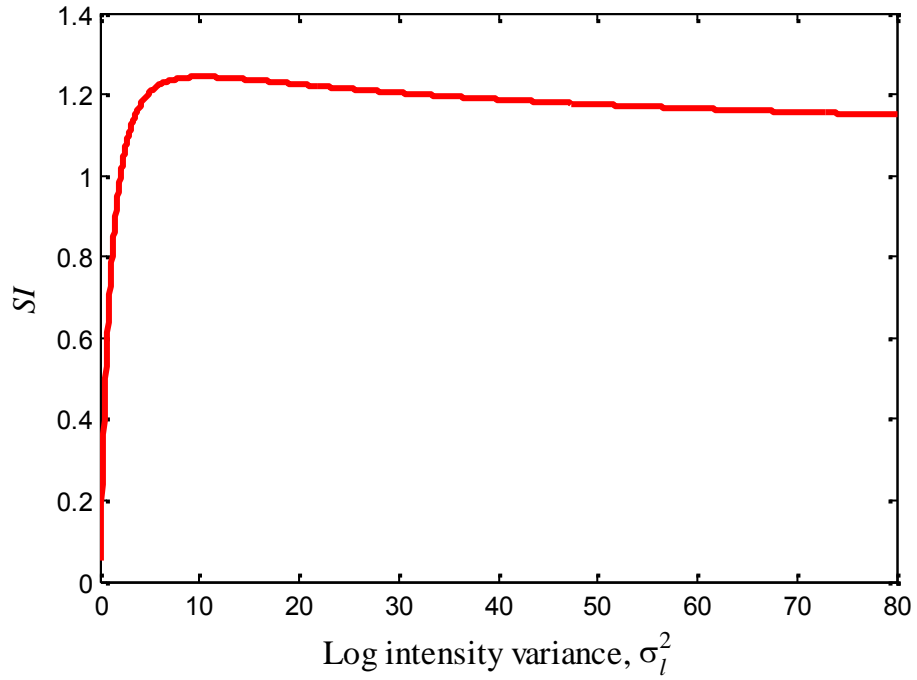


Figure 4.6. *S.I.* against the log intensity variance for $C_n^2 = 10\text{-}15 \text{ m}^{-2/3}$ and $\lambda = 830\text{nm}$.

The values of σ_l^2 and σ_r^2 are described from the weak to strong turbulence regimes in Fig. 4.7. For the very weak turbulence regime, the values of the σ_l^2 and σ_r^2 are greater than unity. In this region the effective numbers of small and large scale eddies are very large. However, beyond the $\sigma_l^2 = 0.2$, the focusing regime is approached, where σ_l^2 and σ_r^2 decrease substantially as shown in Fig. 4.7. After the focussing (moderate to strong) regime, for $\sigma_l^2 > 25$, where $\sigma_l^2 = 1$ is called the saturation regime. The implication of this according to [34, 305], is that the effective number of small scale cells/eddies ultimately reduces to a value determined by the transverse spatial coherence radius of the optical wave. On the other hand, the effective number of discrete refractive scatterers increases again with increasing turbulence and finally becomes unbounded in the saturation regime as shown in Fig. 4.7. Under these conditions, the gamma-gamma

distribution approaches the negative exponential distribution, which is illustrated in section (4.5).

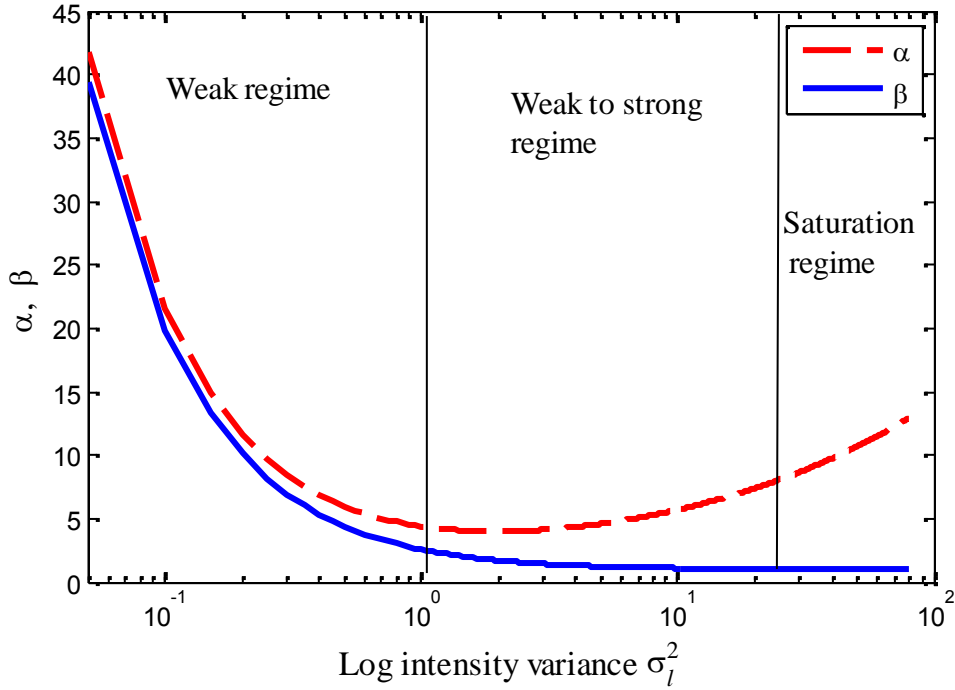


Figure 4.7. Values of α and β against the log intensity variance for different turbulence regimes: weak, moderate to strong and saturation.

4.5. Negative Exponential Turbulence Model

The multiple scattering effects must be taken into account as the strength of turbulence increases [306]. Beyond the saturation regime, the turbulence approaches its limit, also known as the fully developed speckle regime where the link range extends several kilometres and the number of independent scatterings becomes large [281, 283]. The irradiance fluctuation of the optical field propagating over a turbulence channel in the saturation regime is governed by the Rayleigh distribution implying negative exponential statistics, which is expressed as [307]:

$$p(I) = \frac{1}{I_o} \exp\left(-\frac{I}{I_o}\right), \quad I_o > 0 \quad (4.47)$$

where $E[I] = I_o$ is the mean received irradiance. During the saturation regime, the value of the $S.I.$ 1. It is noteworthy that other turbulence models such as the log-normal-Rician [308, 309] and the I-K distributions [310], which are both valid from weak to strong turbulence regime; the K-model [311, 312], which is only valid for the strong regime, and the gamma-gamma turbulence model all reduces to the negative exponential in the limit of the strong turbulence. The negative exponential pdf is shown in Fig. 4.8. The plot shows that as I_o increases, the mean values of the distribution reduces significantly with the irradiance.

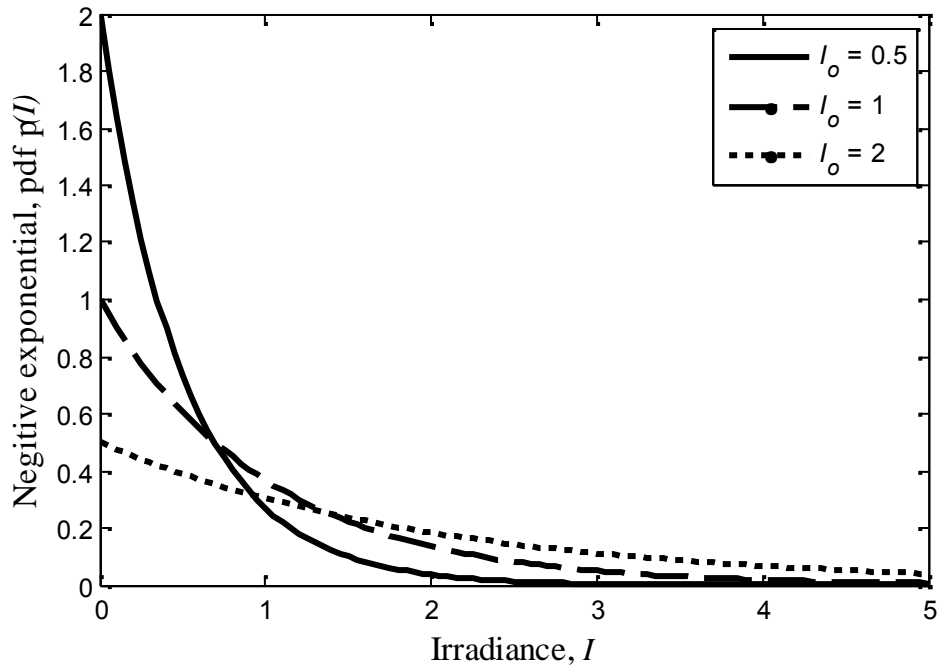


Figure 4.8. Negative exponential probability density function for different values of I_o .

4.6. Summary

In this chapter, the characterisation of the atmospheric turbulence has been presented based on the classical approach and statistical models. Kolomogorov theory of turbulence based on classical studies of velocity, temperature and refractive index fluctuations has been discussed in order to understand the atmospheric turbulence. The refraction structure parameter C_n^2 and the scintillation index parameter were explained in order to measure the strength of turbulence. The dependence of the temperature, pressure and wavelength on the refractive index fluctuations has been described. The log normal model was detailed with its limitations. This model is mathematical well tractable and experimentally validated for the weak regime. Aperture averaging and BER evaluation in the presence of atmospheric turbulence were described. For the strong turbulence, where multiple scattering was needed to be accounted, the gamma-gamma model was more suitable but lacks the mathematical convenience of the log-normal distribution. This model could be used to characterise both the weak and strong turbulence regimes. In the saturation regime, which is also called the fully developed speckle regime, the appropriate model was the negative exponential model. Note that, Log normal model is used in the subsequent Chapter 8 to characterise the turbulence in the atmospheric chamber and consequently the BER performance of the FSO link.

Chapter 5

Design of Controlled Atmospheric Channel

5.1. Introduction

Real outdoor atmosphere (ROA) channel imposes a number of interesting challenges to FSO links [313-315]. ROA is time varying and depends on the magnitude and intensity of weather conditions [316-318]. These conditions will have different impacts on the FSO link performance, with dense fog and intense scintillation causing the most severe impairment to the FSO link [319-321]. ROA could be a mixture of a number of atmospheric conditions such as fog, smoke, aerosols, rain, snow, dust and turbulence. Therefore, carrying out a proper link assessment under specific weather conditions becomes a challenging task. For example real outdoor fog (ROF) atmosphere is heterogeneous and very unpredictable in nature. In order to investigate and model the ROF under diverse atmospheric conditions is still a great challenge in

FSO communications link [322, 323]. This is due to various reasons mainly: (i) the unavailability of the experimental setup for outdoor links due to the long observation time and reoccurrence of fog, *e.g.*, dense fog events for visibility $V < 0.5$ km, (ii) the difficulty in controlling and characterising the atmosphere due to the inhomogeneous presence of aerosols such as fog and smoke along the FSO link path and (iii) the outdoor measurement instruments are expensive and are not readily available, and (iv) it is not feasible to repeat the same measurement condition again when necessary.

On the other hand atmospheric turbulence (scintillation) has been investigated extensively and a number of theoretical models have been proposed to describe scintillation induced fading [324-327]. However, in practice it is very challenging to measure the effect of the atmospheric turbulence under diverse weather conditions. This is mainly due to the (i) long waiting time to observe and experience reoccurrence of atmospheric turbulence events, which sometimes can take weeks or months, (ii) the difficulty in controlling and characterising the atmosphere turbulence. Hence an indoor atmospheric laboratory chamber is designed so that the ROF, smoke and atmospheric turbulence channel can be simulated under controlled conditions. Therefore, specific measurements to investigate the effects of ROF, smoke and turbulence on the propagating optical beam can be carried out. The chamber offers the advantage of full system characterisation and assessment in much less time compared with the outdoor FSO link, where it could take a long time for the weather conditions to change.

In this chapter, the detailed description on the design of the laboratory atmospheric

chamber is presented. Moreover, the methods to produce homogeneous fog and its calibration to ROF and data acquisition for fog attenuation measurement are explained. Methods to produce and control atmospheric turbulence are also presented. The experimental results of attenuation of FSO communication systems operating at visible and near infrared (NIR) wavelengths ($0.6 \text{ } \mu\text{m} < \lambda < 1.6 \text{ } \mu\text{m}$) in the controlled laboratory based fog environment are presented. The results are compared with the selected empirical fog models in order to validate their performance practically from dense to light fog conditions. The results indicate that the fog attenuation is wavelength dependent for all V ranges.

5.2. Atmospheric Chamber

A snapshot of laboratory based testbed *i.e.*, an atmospheric chamber to control and mimic the ROA conditions is shown in Fig. 5.1. The block diagram of the chamber is detailed in [162]. The atmospheric chamber is composed of seven compartments, each having air outlets for air circulation with built-in fans and thermometers. Each compartment has also a powerful internal heating source which is a combination of the powerful resistors and aluminium based plates fitted with fans to its vent to generate different intensity of hot air circulation inside chamber. By using a number of heaters and fans, it is possible to generate and control temperature induced turbulence within the chamber. The controlled temperature and the wind velocity within the chamber can be readily controlled to mimic the outdoor atmospheric conditions as closely as possible. The designed chamber allow to carry out the outdoor FSO system characterisation and performance measurement under a various levels of turbulences without the need for longer waiting times as would be the case

in out-door FSO links. The complete parameters for the designed chamber are given in Table 5.1.

Table 5.1. The chamber dimensions and the main parameter.

Parameters	Value
Dimension	550×30×30 cm ³
Temperature range	20 - 80 °C
Wind speed	4 - 5 m/s
Fog machine	HC 155 H, steamer
Smoke machine	GT 400
Resistors	50 watt (rated), 1.2 k

The atmospheric chamber is used to control and simulate individual effects of fog, smoke and turbulence as necessary to mimic the ROA as far as possible. The fog is produced using a commercial water vaporising machine (water steam), with 100% humidity to mimic ROF [328]. Similarly, smoke is introduced to the atmospheric chamber using a smoke generator at a rate of 0.94 m³/sec. More details on the fog and smoke machine are provided in Table 5.1. The amount of fog injected into the chamber is controlled by a number of fans and ventilation inlet/outlets to achieve different densities. Thus, allowing to manage the fog flux inside the chamber homogeneously and control the visual contrast (transmittance) of the FSO link.

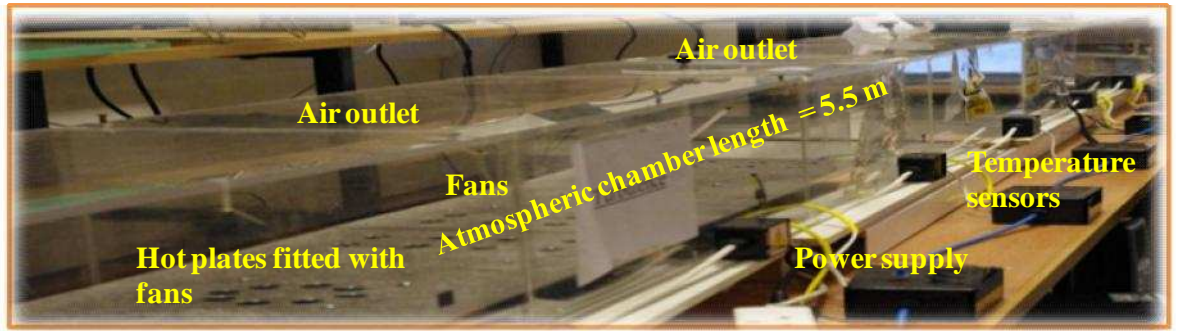


Figure 5.1. A snapshot of an atmospheric chamber in the lab.

5.3. Calibrations of Lab Based Fog and Smoke to Real Outdoor Fog

In [328], measurements show that the occurrence of fog starts when the relative humidity (H) of the real outdoor atmosphere (ROA) approaches 80 %. The density of the resulting fog reaches 0.5 mg/cm^3 for $H > 95\%$. Thus, under conditions of high water vapour concentration, the water condenses into tiny water droplets of radius $1 - 20 \text{ }\mu\text{m}$ in the atmosphere. It is possible to simulate fog in the lab by achieving H close to 95%. Hence, artificial generated steam fog is produced to mimic the ROF as shown in Fig. 5.2.

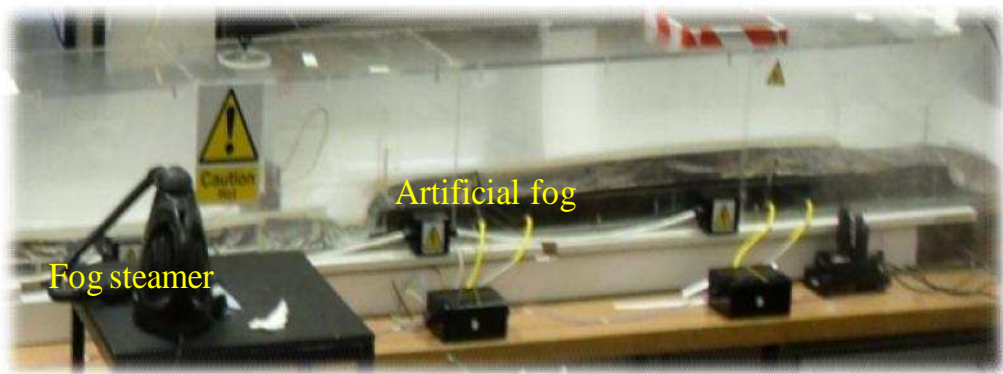


Figure 5.2. The mechanism of artificial formation.

In addition , to demonstrate the physical similarity of the lab based fog to ROF, the ROF attenuation data from field experiments at Prague published in [236] and metrological institute, Czech Republic [266] are compared with the obtained laboratory based fog attenuation data. The mean attenuation data from Prague for $0 < V < 1$ km and Nadeem et al, for $V < 0.6$ Km shows a very good agreement with the measured lab data at $0.83 \mu\text{m}$ as illustrated in Fig. 5.3. This confirms the physical characteristics of lab based fog that resembles the ROF.

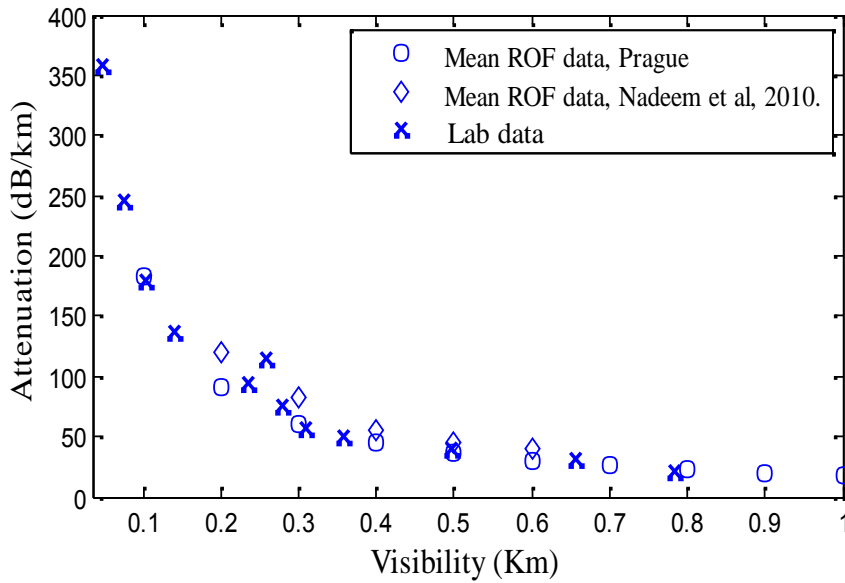


Figure 5.3. Comparison of measured mean ROF attenuation for two field experiments [5, 6] and the mean lab based fog attenuation data at $0.83 \mu\text{m}$.

However, to relate the steam fog to the other type of fog mentioned in Chapter 3, the humidity should be approximately 100%. Steam fog is used in our lab based indoor atmosphere chamber to evaluate the FSO in controlled fog chamber in chapter 6 and 7. Smoke is simulated in the lab based atmospheric chamber by mimicking the natural process using a smoke machine, in which a glycerine based liquid is used to create dry smoke particles.

5.4. Controlled Fog Atmosphere

5.4.1. Homogeneous fog atmospheric channel

The time series analysis of ROF shows that due to the rigid and very robust changes in outdoor FSO atmospheric conditions, the fog rather is very dynamic in size and heterogeneous along the length of FSO link [329]. Generally, due to this fact the characterisation of the fog is based on the measured visibility V (km).

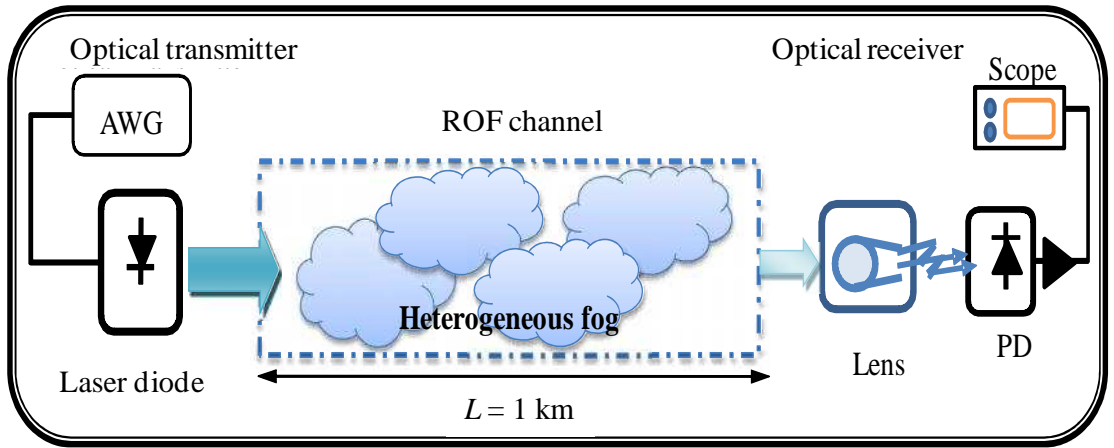


Figure 5.4. Real outdoor fog scenario, considering FSO link length of 1km.

However, as the real FSO link length can be greater than 1 km. In this case, due to the spatial heterogeneity of fog densities can vary from one position to few 100 metres apart as shown in Fig. 5.4. In result to this, the measured fog attenuation β_λ along the FSO link and the corresponding V data using a visibility device (transmissometer) at a fixed position can significantly fluctuate from the actual value. This effect can be observed in the measured data at 830 nm for two fog events as in [88]. In order to minimize this error in measured V , several transmissometers

can be used consecutively after few hundred meters [239]. However, this approach is complex and is not cost effective to install for long link range FSO systems. Thus, the atmosphere chamber is a simple approach to control and produce homogenous fog conditions to measure V using wavelength of 550 nm along the length of chamber as shown in Fig. 5.5. Therefore, it permits to measure the right values of fog attenuation corresponding to the actual V along the length of the FSO link.

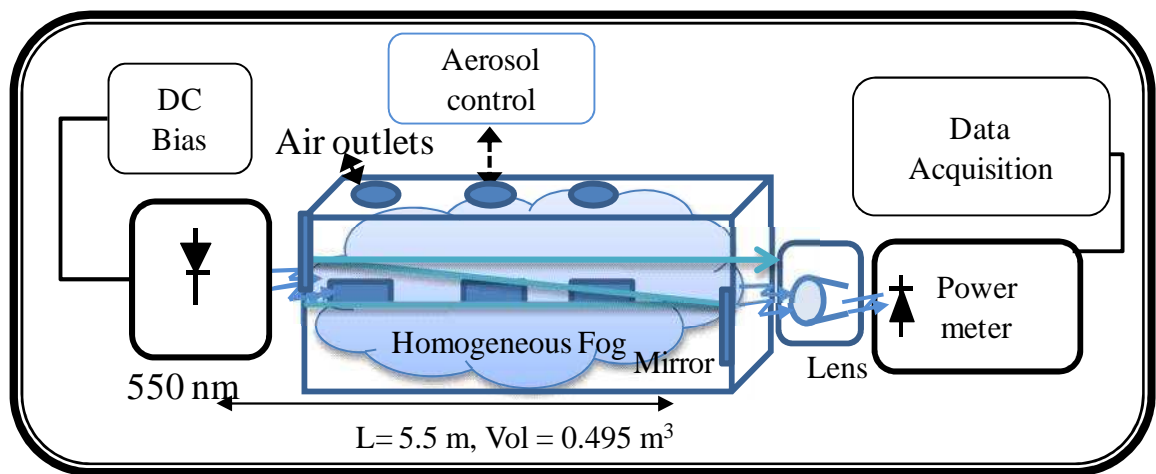


Figure 5.5. Block diagram of experiment setup to measure V along the length of FSO link.

The condition for achieving the homogeneity depends on a number of factors. Firstly the important condition for spreading is proper enclosure of the chamber. Secondly, to create different fog density vents are used along the chamber. Proper spreading of fog is very important to measure the exact V and to make a good correlation of corresponding measured fog attenuation for the transmitted wavelengths of an FSO system. The fog is distributed homogenously using a combination of fans within the chamber.

However, using the atmosphere chamber under homogenous fog conditions, for very small change in the movement of fog inside the chamber results a significant change in β_λ at wavelength of 550 nm using (3.11). Hence, this can fluctuate the corresponding measured V values to more than 50 m from the actual values. This has been compensated by increasing the path length L of laser beam by creating multiple reflections inside the chamber using mirrors as shown in Fig. 5.5. Figures 5.6 and 5.7 illustrate the theoretical verification using (3.11) that small signal fluctuation in loss (± 0.1 dB) of laser beam with no reflection ($L = 5.5$ m) can cause significant change in β_λ at a given value of V *e.g.*, at 0.6 km (see Fig. 5.6). The corresponding change in V can be 80 m in magnitude at 0.6 km as depicted in Fig. 5.7. However, by doubling the link distance using multiple reflections ($L = 11$ m) inside the chamber, the effect of small scale fluctuations is compensated as the range of loss is increases to 2.5 dB as shown in Fig. 5.6. This minimizes the change in V to 25 m in magnitude at 0.6 km as shown in Fig. 5.7. Hence, increasing the number of reflections can reduce the small changes in the V and consequently increases the homogeneity in the fog channels to characterise fog attenuation with enhanced accuracy. The atmosphere chamber facilitates predicting the fog attenuation at the lower visibility ($V < 100$ m) range due to the dense fog, which is not well defined and easily achievable. Moreover, in the best of our knowledge, there are no experimental data available for FSO links in diverse smoke conditions, which are common in urban areas. Thus, the atmospheric chamber is used to carry out the outdoor FSO system characterisation and perform the measurement under a homogeneous light to dense fog and smoke conditions.

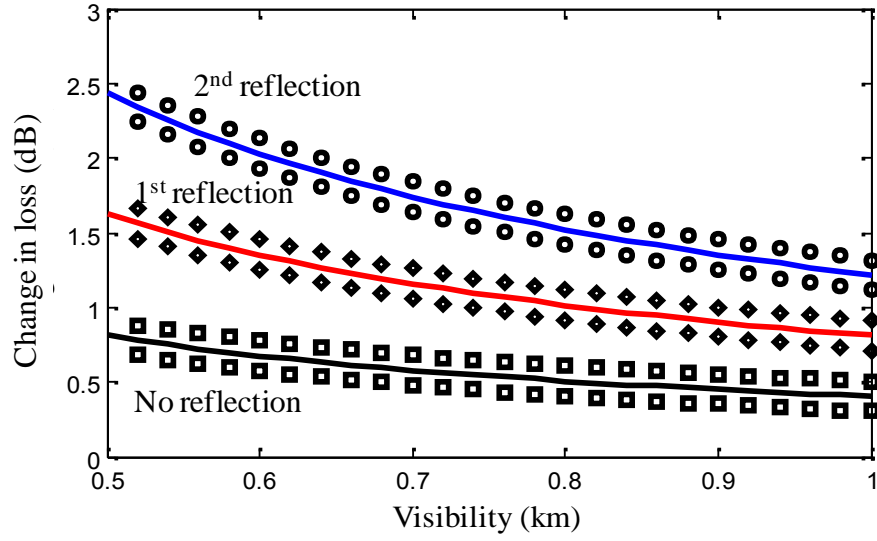


Figure 5.6. Visibility (km) versus the change in attenuation (dB) due to ± 0.1 dB fluctuations in loss.

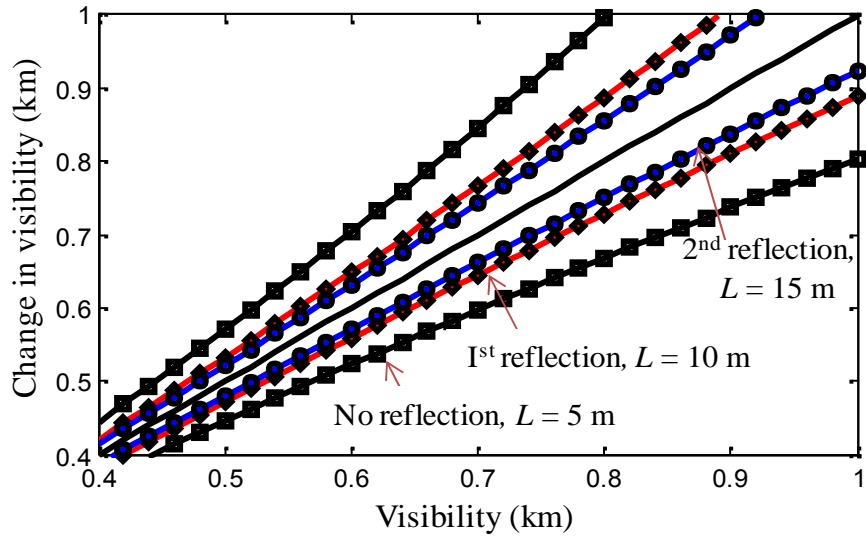


Figure 5.7. Visibility (km) versus the change in visibility (km), black (solid line) is real V for link range $L = 5.5$ m.

5.5. Data Acquisition for Fog Attenuation

Measurements

A block diagram for the automated measurement and characterisation of the fog attenuation in the atmospheric chamber is illustrated in Fig. 5.8 (a). The laboratory test bed for the FSO link composed of an optical transmitter end T_x , an optical receiver R_x , an atmospheric chamber an optical and electrical modules is shown in Fig. 5.8 (b).

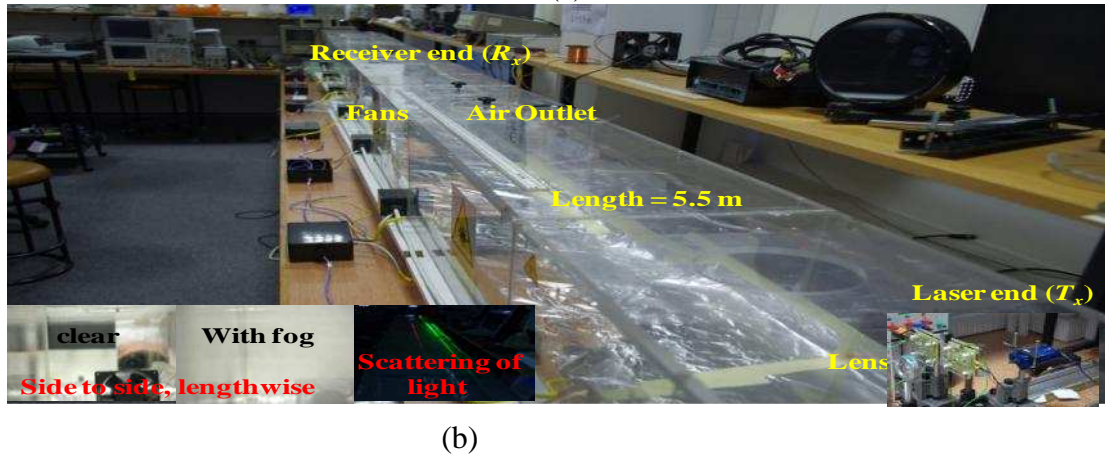
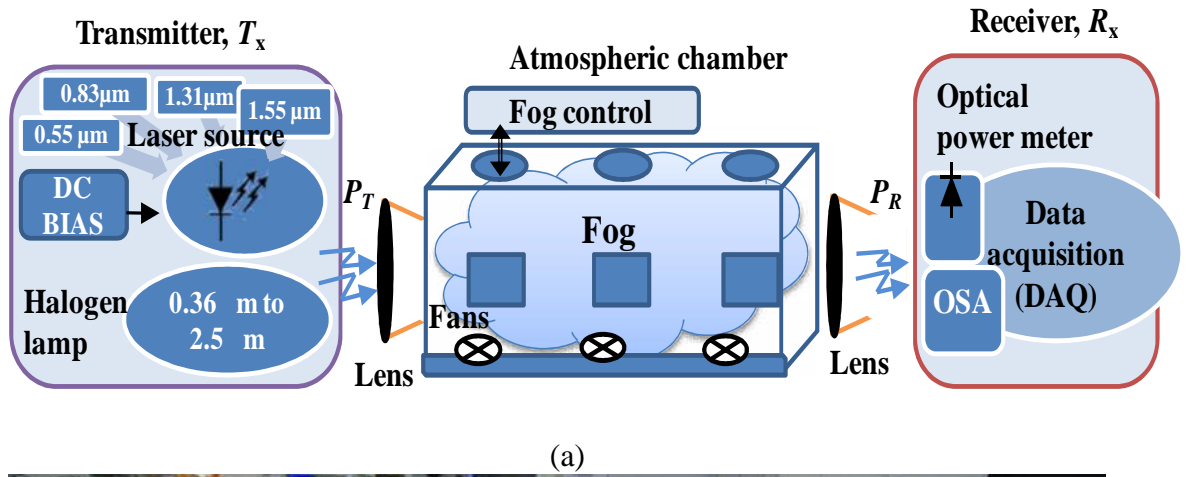


Figure 5.8. (a) The experimental setup to measure the fog attenuation and visibility, and (b) the laboratory controlled atmospheric chamber and FSO link setup, and the (inset) shows the presence of fog and the scattering of light in the atmospheric chamber.

Two different approaches have been adopted in the experimental work to characterise fog and smoke attenuation, (i) a number of individual laser sources at wavelengths of 0.55, 0.67, 0.83, 1.31 and 1.55 μm with the average transmitted optical powers P_T of -3.0 dBm, 0 dBm, 10 dBm, 6.0 dBm and 6.5 dBm and an optical power meter, respectively, and (ii) a continuous LS-1 tungsten halogen source with a broad spectrum (0.36 to 2.5 μm) and an Anritsu MS9001B1 optical spectrum analyzer (OSA) with a spectral response of 0.6 to 1.75 μm to capture the attenuation profile.

Following (i), the received optical power P_R without fog is measured for the reference as well as for normalization at the optical receiver R_x by using appropriate power meter at each transmission wavelengths of 0.55, 0.67, 0.83, 1.31 and 1.55 μm . Then a controlled amount of fog is injected into the chamber allowing it to uniformly spread along the chamber. Time duration of 30 seconds was allowed for fog/smoke particles to settle down homogeneously within the chamber before the data acquisition (DAQ). The next step is to measure the received optical power P_R with fog, at a time step of 1 second for each wavelength. The normalized transmittance or loss was calculated from the average received power with fog to the average received power with no fog. The fog attenuation β_λ (in dB/km) was measured using (3.12) corresponding to the measured loss at each transmission wavelengths of 0.55, 0.67, 0.83, 1.31 and 1.55 μm from light to dense fog conditions. The link V was measured along the length of the chamber using (3.11) at 0.55 μm and compare with the visibility threshold. The acquisition of the data is completed when the visibility is equal to the threshold value (see Fig. 5.9).

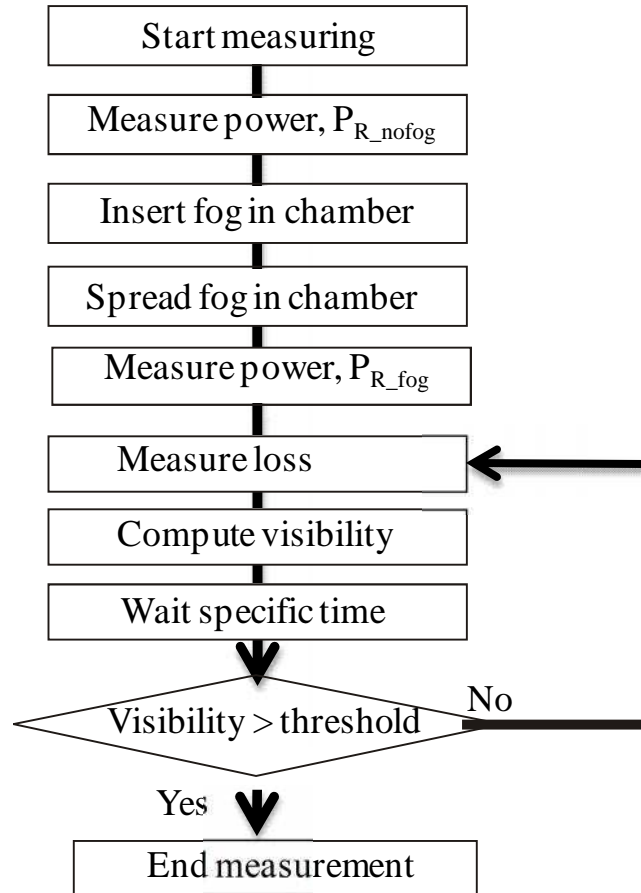


Figure 5.9. The block diagram for the measurement of fog attenuation and visibility.

The received optical power is acquired at the sampling rate of 1 sec. This allows to observe at very small scale changes in the V and the corresponding measured β_λ . The measured V for the total time of the fog events are shown in Fig. 5.10.

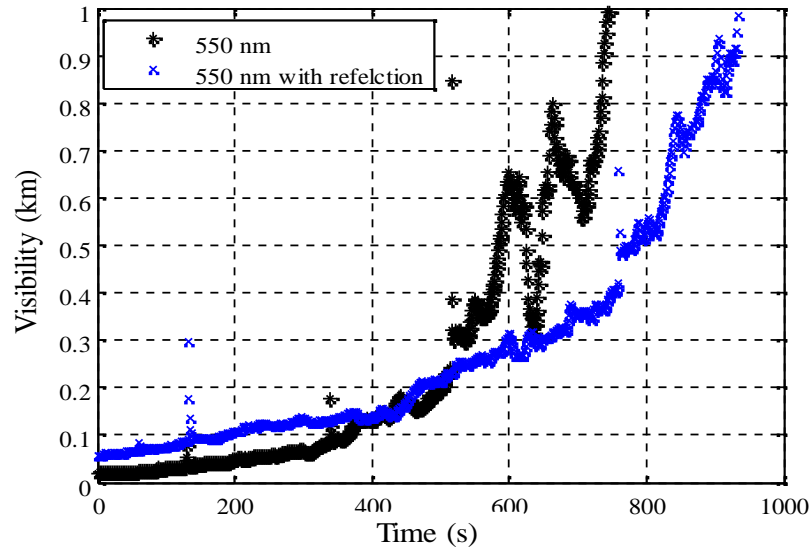


Figure 5.10. Time dependence of visibility within the FSO chamber.

The fog density in the chamber decreases with the passage of time and hence the V increases. Figure 5.10 shows the maximum V to a range of 1 km using the wavelength of 550 nm. However, the measured data has some large variation starting at 450 m. This is due to the small fluctuations of (± 0.1 dB) in the loss due to the movement of fog while acquiring the data at 550 nm. The measured losses (dB) are given against the calculated data as shown in Table 5.2. This shows that a small variation in the measured loss will result in significant fluctuation of V . The solution to this problem is adopted by doubling the link distance for 550 nm by means of reflection of the optical signal inside the chamber. This can lead to increase in the optical attenuation and therefore minimizing the changes in the V data (see Table 5.2). The measured V versus the total time of full event of fog after the reflection is compared and shown in Fig. 5.10, which illustrates no big fluctuation for $V \geq 45$

Table 5.2. Attenuation of 550 nm laser at given values of V for $L = 5.5$ m and 11 m.

Visibility (m)	Loss (dB)	Reflection Loss (dB)
600	0.6768	1.3536
400	1.0152	2.0304
200	2.0304	4.0607
50	8.1214	16.2428

The analysis of data for the fog attenuation against the full time event of fog at 1550 nm is shown in Fig. 5.11. The results show large peaks caused by small fluctuation in the measured loss. These peaks are removed by filtering the far points data due to fluctuations from the real data. The average data is used and the difference is computed from the mean value. However, as the data is continually changing, a moving average is used in order to filter the peaks from the real data. The best performance moving average was discovered for 50 samples. Figure 5.11 shows the comparison of the real data with the moving average. Hence, the variation in the fog attenuation is further minimized by using the moving averaging filter.

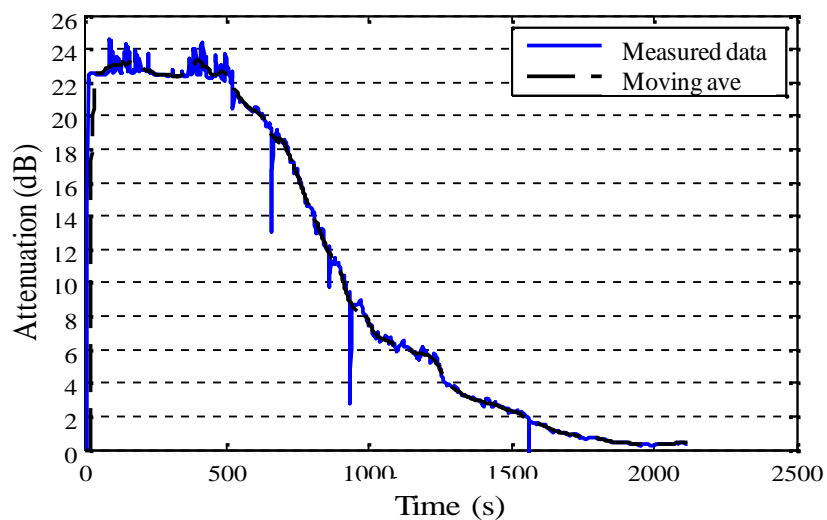


Figure 5.11. Measured attenuation against the time for full fog event at wavelength of 1550 nm.

Figure 5.12 (a) illustrates the difference between data with high fluctuations and the mean moving average data values after the moving average. The difference shows peaks of 6 dB and need to be filtered from the measured attenuation data. Using the far point criteria from the probability density function (pdf), the difference is found to be 0.7 dB *i.e.*, the threshold value (see Fig. 5.12 (b)). As a result, the threshold value is filtered for any peak value higher than 0.7 dB from the measured attenuation data to make it much smoother.

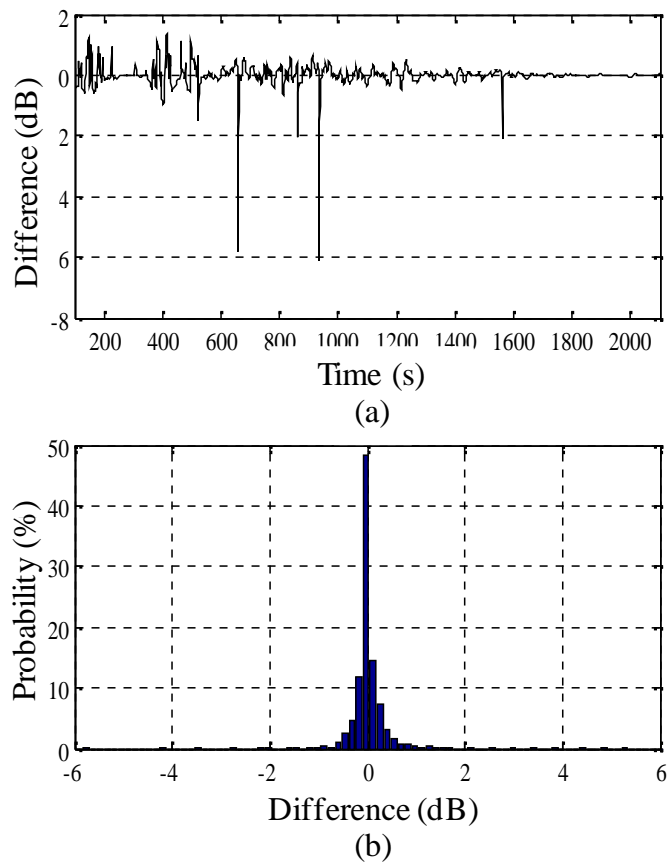


Figure 5.12. (a) Difference between moving average and data, and (b) Difference probability density function.

The measured fog attenuation after filtering against the measured visibility for a 1 km range is depicted in Fig. 5.13. The measured non-filter attenuation data has significant

fluctuations of the order of 20 dB. However, after filtering the data, the fluctuations in the obtained attenuation data against the measured V are lowered (see Fig. 5.13).

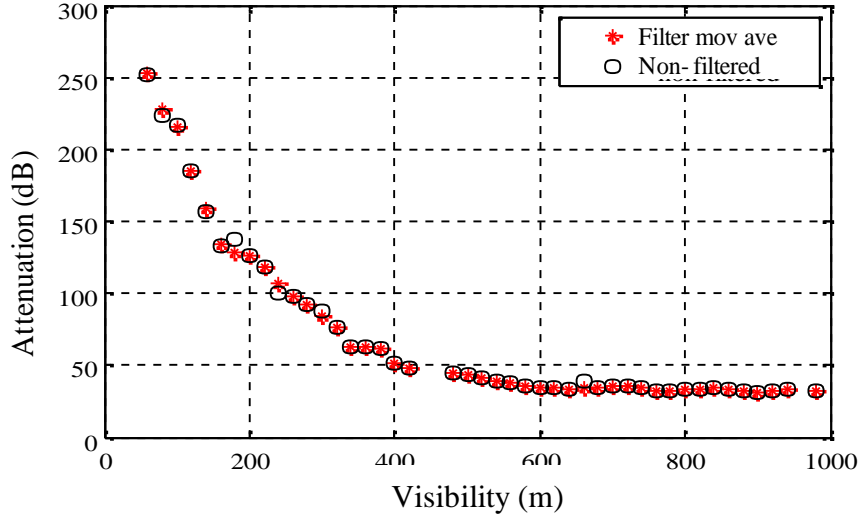


Figure 5.13. Comparison between filtered and non-filtered data at wavelength of 1550 nm under fog conditions.

Following (ii) as described before in Section 5.5, the experiment was also carried out to measure the spectrum attenuation using a continuous LS-1 tungsten halogen light source with a broad spectrum from 0.36 to 2.5 μm and an optical receiver R_x using an Anritsu MS9001B1 optical spectrum analyzer (OSA) with a spectral response of 0.6 to 1.75 μm as shown in Fig. 5.8 (a). An automatic data acquisition (DAQ) system is developed by connecting the OSA to a computer using GPIB bus and LABVIEW control environment. In order to measure the fog effect for spectrum attenuation, the average received optical power P_R is measured at R_x before and after the injection of the fog into the atmospheric chamber. The normalized transmittance T was calculated from P_R with and without fog. The attenuation spectrum is measured corresponding to the measured T from light to dense fog condition for all wavelengths. The link V was measured simultaneously with β_λ along the length of

the chamber using $0.55\ \mu\text{m}$ to ensure the maximum transmission to the human eye. Note that, the goal of the experiment is to characterise the attenuation, therefore, having identical powers at different wavelengths are not essential. The geometric and other losses were also not taken into account for T_x , as P_R was measured both before and after fog and smoke at R_x to attain the wavelength dependent losses.

5.6. Experimental Performance of Fog Models under Controlled Fog Channel

The measured fog attenuation (in dB/km) for the wavelength spectrum of $0.6 - 1.6\ \mu\text{m}$ for the dense to the light fog conditions ($0.015\ \text{km} < V < 1\ \text{km}$) is shown in Fig. 5.14. The experimental data shows that the received optical signal was significantly lower than the OSA minimum sensitivity for $V < 0.015\ \text{km}$, hence no conclusive measurement could be taken to explore the wavelength dependence for $V < 0.015\ \text{km}$. However, the measure optical power clearly demonstrates the fog attenuation dependency on operating wavelength for $V > 0.015\ \text{km}$. The fog attenuation decreases from 232 dB/km to 216 dB/km from visible – NIR spectrum at $V = 0.100\ \text{km}$ and from 83 dB/km to 75 dB/km at $V = 0.27\ \text{km}$.

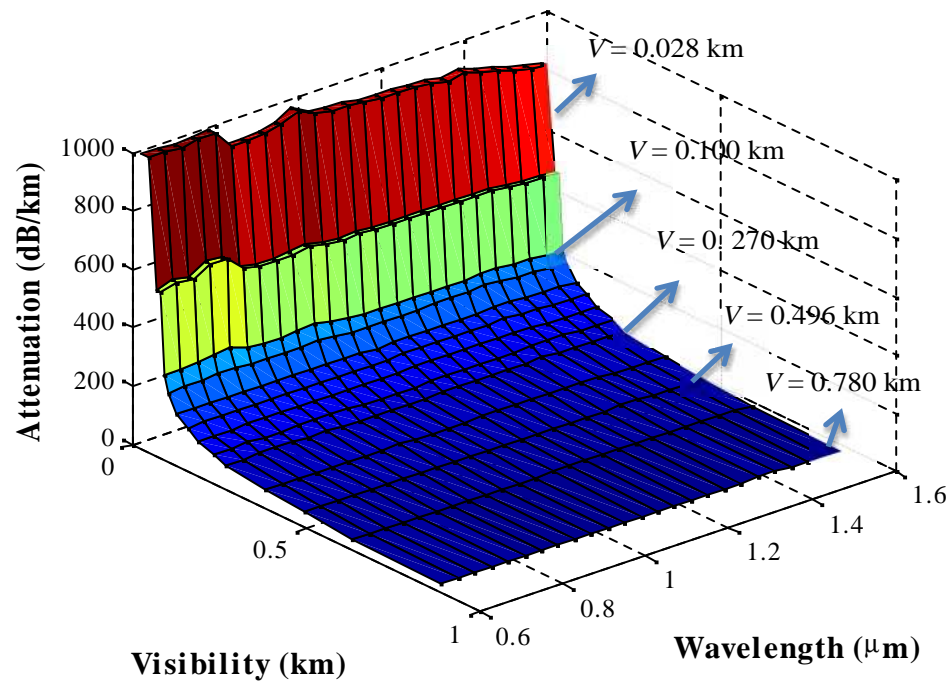


Figure 5.14. The measured fog attenuation for the visible – NIR spectrum against the visibility (km).

5.6.1. Dense fog conditions

Figure 5.15 illustrates the measured fog attenuation for the visible – NIR spectrum at dense fog conditions ($V = 0.048$ km), see Table 3.1. The measured fog attenuation is notably higher at the visible range than at the NIR range for the dense fog. The comparison of the selected empirical fog models with the measured spectrum attenuation shows that Kruse model underestimates the fog attenuation. Kim model contradicts the measured data and showing wavelength independent fog attenuation. However, Naboulsi advection and convection models overestimate the measured fog attenuation for NIR range.

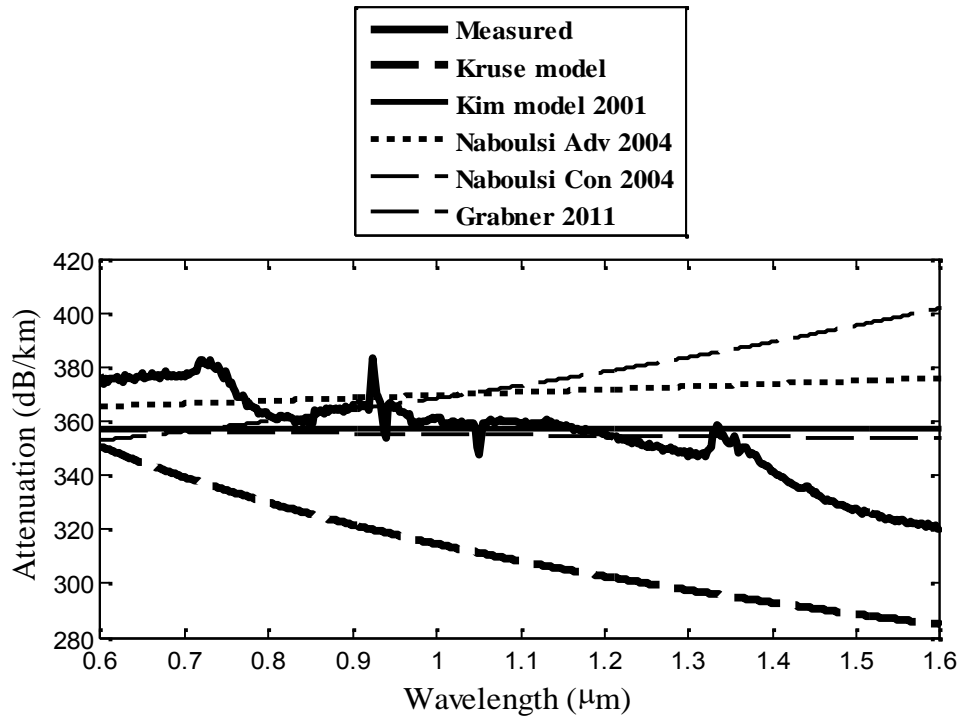


Figure 5.15. Comparison of the selected empirical models with measured fog attenuation (dB/km) from the visible – NIR spectrum at $V = 0.048$ km.

The Grabner model shows that the attenuation decreases linearly from the visible to NIR range of the spectrum at a much slower slope since it underestimates in the visible range. This model expresses the best fit over almost whole investigated band, however overestimates the fog attenuation at the NIR spectrum as depicted in Figs. 5.15 and 5.16. Note that, a small discrepancy between indoor measured data from visible to NIR range and outdoor fog model is expected.

5.6.2. Thick fog conditions

The measured fog attenuation for the thick fog ($V = 0.3$ km) for the visible – NIR is shown in Fig. 5.16. The measured fog attenuation for the visible range is 58 dB/km, decreasing to 53 dB/km for the NIR range of the spectrum for the thick fog. However,

the peak attenuation at wavelength range of 1.35-1.45 μm is due to strong water absorption which is consistent with the published results in [330], and has to be underestimated to fair comparison with previous mentioned models. The comparison of the selected empirical fog models with the measured spectrum attenuation shows that Kruse model underestimates the fog attenuation. Kim model shows wavelength independent fog attenuation for thick fog. Naboulsi advection and convection models overestimate the measured fog attenuation for NIR range. Grabner model shows that the attenuation decreases linearly from the visible – NIR range of the spectrum and best fits the measured fog attenuation form visible to NIR wavelength range.

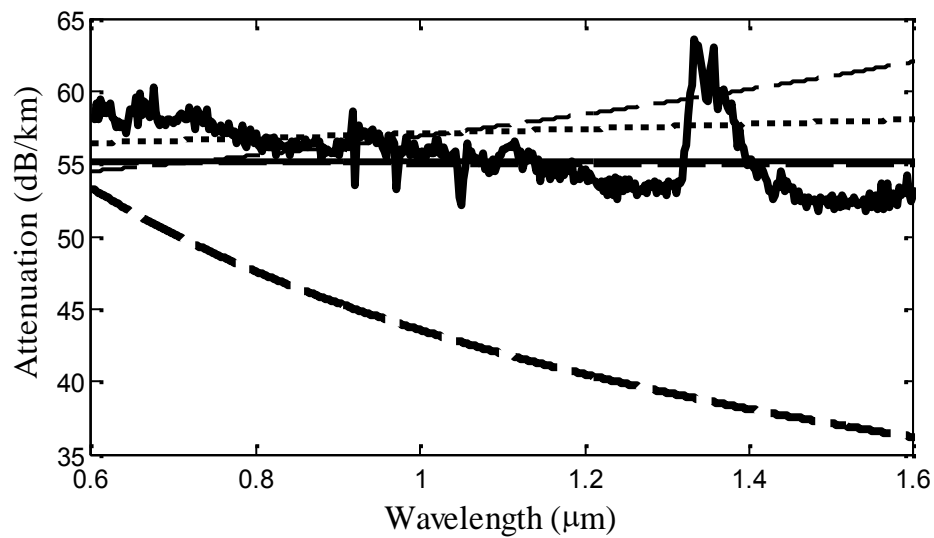


Figure 5.16. Comparison of the selected empirical models with measured fog attenuation (dB/km) from the visible – NIR spectrum at $V \sim 0.300$ km.

5.6.3. Moderate fog conditions

Figure 5.17 illustrates the fog attenuation for the visible – NIR spectrum at moderate fog conditions ($V = 0.46$ km). The measured fog attenuation for the visible range is

42 dB/km, decreasing to 35 dB/km for the NIR range of the spectrum at moderate fog condition. The comparison of the selected empirical fog models with the measured spectrum attenuation shows that Kruse model underestimates the fog attenuation. The measured fog attenuation for the visible – NIR spectrum is also compared to the wavelength independent Kim model for $V < 0.5$ km. The experimental results contradict the Kim model towards the visible range for the attenuation spectrum. Naboulsi advection and convection models underestimate the measured fog attenuation toward the visible range. Grabner model shows a similar behaviour as Kim model at moderate fog conditions as the difference between Kim and Grabner model is almost negligible.

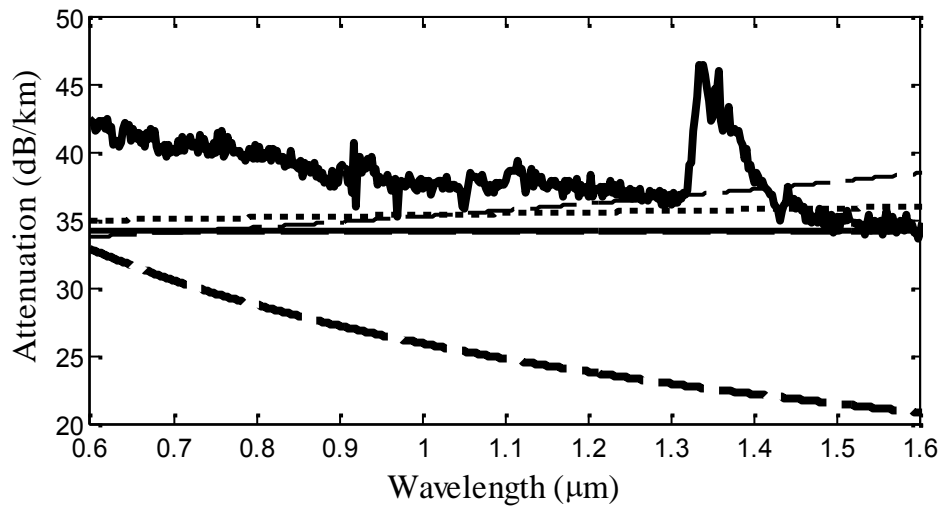


Figure 5.17. Comparison of the selected empirical models with measured fog attenuation (dB/km) from the visible to NIR spectrum at $V \sim 0.46$ km.

5.6.4. Light fog conditions

The measured fog attenuation for light fog ($V = 0.783$ km) for the visible – NIR is shown in Fig. 5.18. The comparison of the selected empirical fog models with the

measured spectrum attenuation shows that the Kruse model underestimates the fog attenuation at $V \sim 0.783$ km. Naboulsi advection, convection and Grabner models overestimate the measured fog attenuation for the NIR range of the spectrum. However, the measured attenuation spectrum is very close to Kim model at $V = 0.783$ km. This validates that Kim model is more realistic to use when $V > 0.5$ km. This model does not take into account wavelengths for $V < 0.5$ km. However, the experimental data and selected empirical models show that the spectral attenuation is wavelength dependent for $V < 0.5$ km. This validates that Kim model needs to be revised for $V < 0.5$ km to predict the wavelength dependent fog attenuation. The wavelength dependent fog model based on the visibility data from light to dense fog atmosphere is presented in the following Chapter 6.

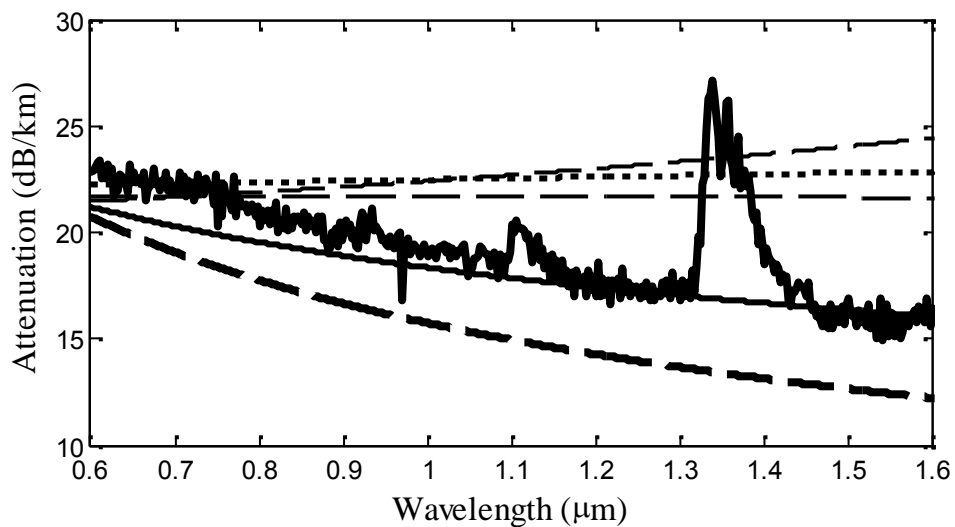


Figure 5.18. Comparison of the selected empirical models with measured fog attenuation (dB/km) from the visible – NIR spectrum $V = 0.78$ km.

5.7. Controlled Atmospheric Turbulence Channel

There are two approaches that could be adapted to generate controlled turbulence inside the atmospheric chamber.

- a). External heater and fans are used to blow hot and cold air in the direction perpendicular to signal propagation to generate the variation in temperature and wind speed ensuring a constant temperature gradient between the source and the detector.
- b). Each compartment has a powerful internal heating source inside the chamber and a fan attached to its vent so that a very strong turbulence effect can be generated as shown in Fig. 5.19.

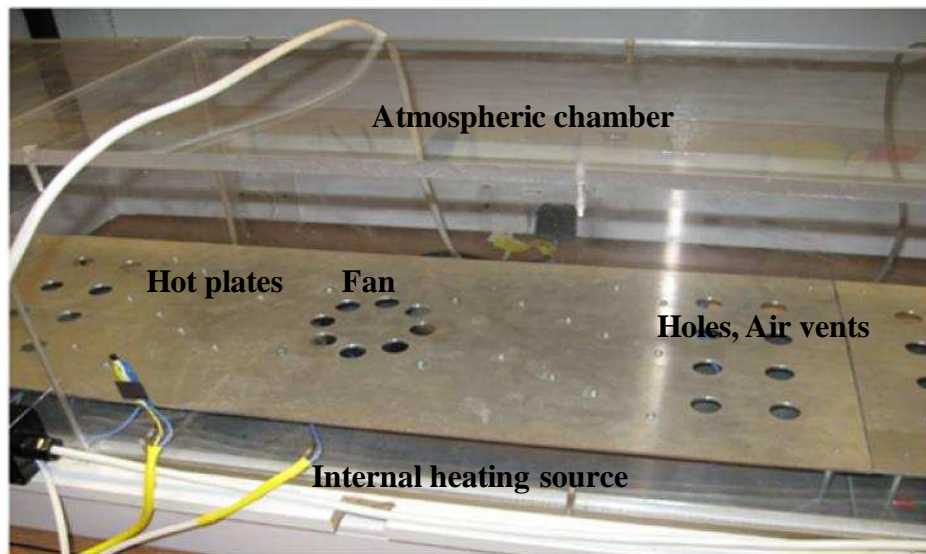


Figure 5.19. The heating elements to create turbulence inside the chamber (one plate). The electrical heater and fan are located below the metal plate.

The internal heating system consists of seven hotplates (700 x 270 x 5 mm; aluminium), each with ten 50 watt (rated) 1.2 k Ω resistors acting as the heating elements as shown in Fig. 5.20. At the supply voltage (230 V A.C.), each resistor

produces 44 W of heat, giving 440 W per hotplate, and 3080 W for the whole system. Each hotplate is electronically switched by a triac (4 A rated), which is controlled by a 5 volt signal via an opto-isolator. A temperature sensor placed 50 mm above the hotplate monitors the air temperature. The signal from this is applied to a thermostatic controller, where it is compared to a reference voltage which sets the control temperature. The thermostatic controller includes a Schmitt comparator, which provides hysteresis in the temperature control. The circuit is adjusted to give a hysteresis of $\pm 1^\circ\text{C}$ about the set point. The output of this controller is applied to the opto-isolator, to control switching of the triac and the heating resistors. A fan is provided to blow air through holes in the centre of the hotplate, to produce convective circulation, thus enhancing the turbulence levels. Holes at each end of the hotplate return this circulating air to flow under the plate and past the resistors, being reheated in the process.

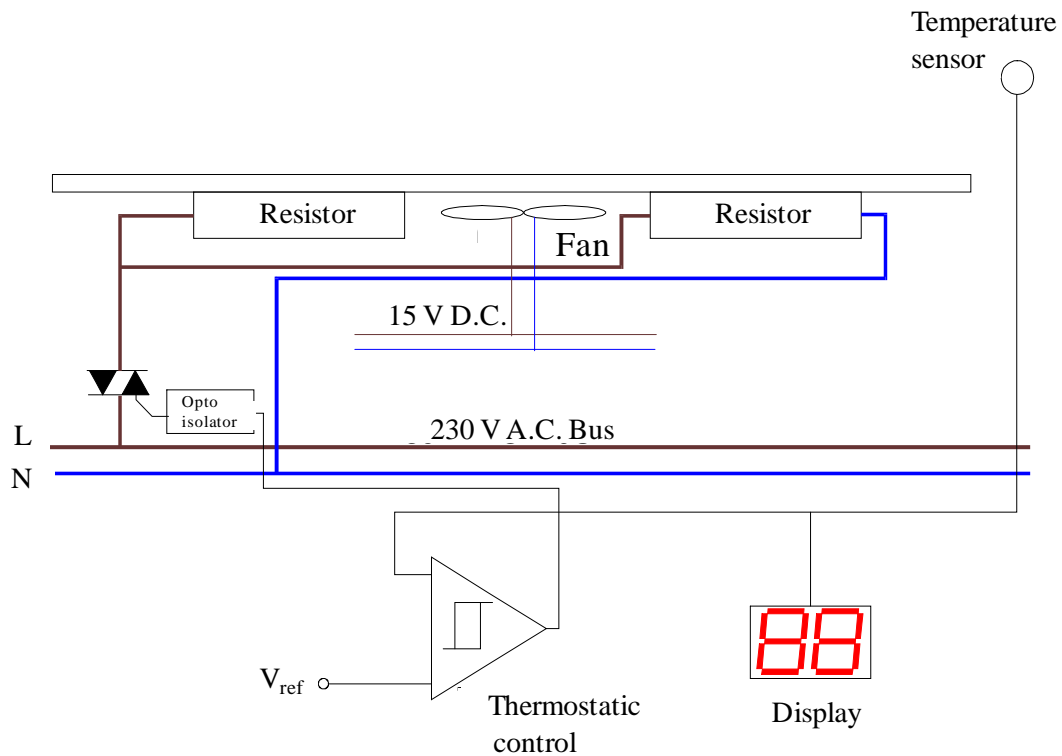


Figure 5.20. The block diagram of heating elements in each block of chamber.

5.8. Summary

This Chapter has described and detailed the design of indoor atmospheric chamber and methods to control and simulate individually such as fog, smoke and turbulence as necessary to mimic the ROA as close as possible. Using the atmosphere chamber, V is measured using wavelength of 550 nm along the length of chamber to characterise the exact value of fog attenuation corresponding to measured visibility (km). The obtained simulation results also show that by increasing the number of reflection can experimentally reduce the small changes in the visibility and consequently increases the homogeneity in the fog channels to characterise fog attenuation with enhanced accuracy. Using the atmosphere chamber the fog attenuation at the lower visibility ($V < 100$ m) was possible to predict due to dense fog. The atmospheric chamber could be used to carry out the outdoor FSO system characterisation and perform the measurement under a homogeneous fog and smoke conditions. Different approaches to generate and control turbulence inside the atmospheric chamber were also presented.

This Chapter has also outlined the experimental data of fog attenuation in FSO for visible to near infrared (NIR) wavelengths ($0.6 \text{ } \mu\text{m} < \lambda < 1.6 \text{ } \mu\text{m}$) from dense to light fog conditions. The obtained experimental results were compared with the selected empirical fog models in order to validate their performance practically. The experimental results showed that the fog attenuation is wavelength dependent for all the visibility V ranges except when $V < 0.015$ km contradicting the Kim model. The resultant fog attenuation decreases linearly from the visible – NIR as predicted by Kim model for $V > 0.5$ km, however, contradict the Naboulsi model except for

selected wavelengths. The Grabner model did not fit the experimental data as the visibility increasing to > 0.5 km. The experimental data has validated that Kim model is more realistic to use when $V > 0.5$ km. This model did not take into account the wavelength for $V < 0.5$ km. However, the experimental data and selected empirical models have showed that the spectral attenuation is wavelength dependent for $V < 0.5$ km. This has validated that the Kim model need to be revised for $V < 0.5$ km in order to predict the wavelength dependent fog attenuation.

Chapter 6

Modelling of Fog and Smoke Attenuation

6.1. Introduction

In thick fog condition ($V < 0.5$ km) the FSO link failure is high due to the scattering and absorption of propagating optical beam, which is not desirable by the end users [331-333]. As a result the study of the relationship between the atmospheric aerosols and FSO wavelengths for thick and dense fog conditions are important in order to enhance the FSO link design and therefore improve the link availability [121, 152, 334]. However, due to the difficulty of measuring the particle density and shape of the aerosols in the atmosphere, measurement of V is the most common technique to characterise the fog attenuation in FSO links. [335-337]. Currently, the most accepted methods to measure V is based on the proportional amount of scattered light captured by the optical receiver at certain angle. However, another approach to

measure the V is to estimate the total loss at peak wavelength of $0.55\text{ }\mu\text{m}$ in visible spectrum [338, 339]. Determining V from CCD images based on the edge detection of various distant objects in the image is an alternative technique that has been employed to complement the visibility measurement at airports [340]. In this chapter both techniques are compared and experimentally evaluated in a dedicated indoor atmospheric chamber that enables us to characterise the atmospheric fog and smoke in the FSO link.

The main objective of this chapter is to provide a complete analysis and the verification of the enhanced visibility measurements for FSO under homogeneous fog conditions. A new empirical model is proposed to evaluate the wavelength dependent fog and smoke attenuation by reconsidering the q value as a function of wavelength rather than visibility. Using the measured attenuation spectrum data, the recommendations for the best wavelengths are provided that could be adopted for links under fog conditions. The new proposed fog model is also compared to selected empirical models and the measured continuous attenuation spectrum from the visible – NIR in order to validate the laboratory-based empirical model.

This chapter is organized as follows: Enhancement in atmospheric visibility measurement is outlined in Section 6.2, whereas the comparison of field and indoor measured visibility is explained in Section 6.3, fog attenuation measurements are presented in Section 6.4, smoke attenuation measurements are analyzed in Section 6.5, empirical modeling of fog and smoke is introduced in Section 6.6, comparison of the measured visibility and attenuation data with the proposed model is investigated in Section 6.7, where as the, comparison of the model with the

attenuation spectrum measurements are presented in Section 6.8. The Summary of the chapter is presented in Section 6.9.

6.2. Enhancement in Atmospheric Visibility

Measurements

Two cost-effective methods are used to develop a system of visibility measurement in an indoor environment, which are based on using a camera and a laser diode are outlined below.

6.2.1. Using CCD method

Theoretical approach is inspired from [87, 341], in which visibility V is defined as a range where a contrast ratio C_T between ideal black and white targets is reduced to value of 2%. Therefore, a similar approach has been used in the lab based experiment using a CCD camera (model GE X5, 14 megapixels) in the presence of two optical links at $0.83\ \mu\text{m}$ and $1.55\ \mu\text{m}$. Figure 6.1 shows an experimental setup to measure visibility using the CCD camera.

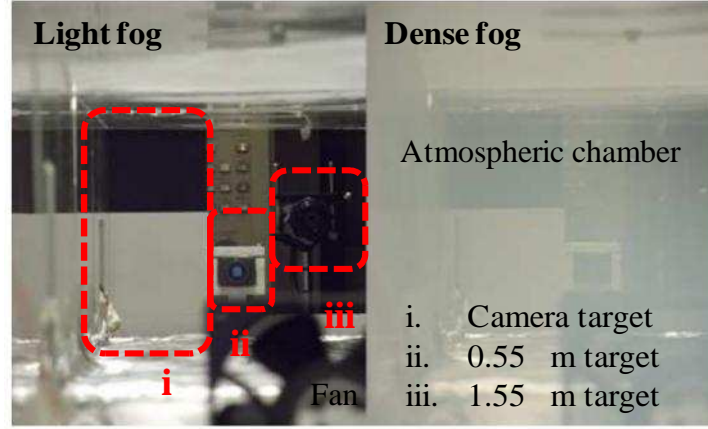


Figure 6.1. CCD camera fog measurements snapshots with light (left) and dense (right) fog conditions, both at the atmospheric chamber.

A black and white target is placed at the receiver, the picture without fog is on the left ($C_o = 0.9447$) while with fog with a reduced visibility is on the right ($C = 0.1703$). Here, C is the ratio of contrast measured with fog to intrinsic contrast C_o without fog.

The normalized C/C_o between the black and white areas was computed by measuring the luminance of the white L_w and black L_b parts of the target before and after the fog event as in [87]. The contrast is defined by the following relation:

$$C = \frac{L_w - L_b}{L_w + L_b}. \quad (6.1)$$

For the fog based channel, C_T is defined as the ratio of contrast C measured with fog to intrinsic contrast C_o without fog along the length of the channel given by:

$$C_T = \frac{C}{C_o}. \quad (6.2)$$

Therefore, V is the visual range where C_T drops to the visual threshold T_{th} of 2% along the propagation path L (km). Using Koschmieder relation [342] and Beer-Lambert-Boguer's law, V is given by [343]:

$$V = \frac{\ln(0.02)}{\ln(C_T)} \cdot L. \quad (6.3)$$

Note that, the contrast ratio of black and white background is measured from the pictures before and after the fog and postprocessed using Matlab. The function *imread()* is used to decompose every pixel of a picture to a RGB component in an interval of 0 to 255. The standard conversion from RGB to XYZ component is completed using the following equation:

$$C = 0.212R + 0.7152G + 0.0722B. \quad (6.4)$$

6.2.2. Using laser diode

Link visibility *i.e.*, the meteorological visual range) is also measured by using an optical source at 0.55 μm to characterise the fog as illustrated in Fig. 6.2. V (km) is the distance to an object at which the visual contrast of an object drops to 2% of the original visual contrast (100 %) along the propagation path [344]. Hence V (km) can be calculated in terms of the measured fog attenuation coefficient β_λ and T_{th} at 550 nm wavelength using (3.11).

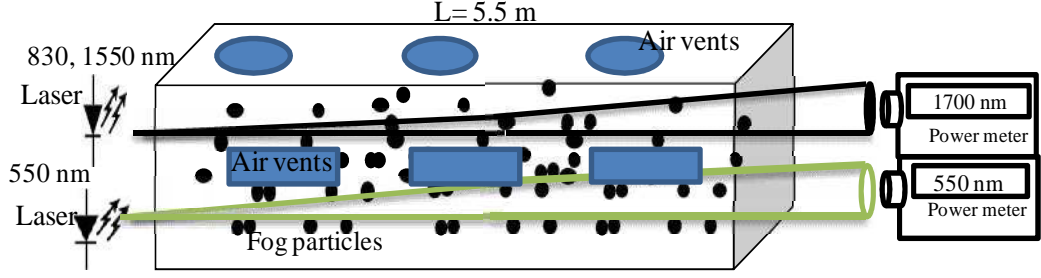


Figure 6.2. The experimental set up to measure fog attenuation and visibility.

The 2% visual threshold value is adopted here in order to follow the Koschmieder law as opposed to the airport consideration of $T_{th} = 5\%$. The attenuation due to fog and normally expressed in terms of transmittance using Beer- Lambert law as [258]:

$$\beta_{\lambda} = -\frac{10\log_{10}(T)}{4.343L}. \quad (6.5)$$

We measured β_{λ} using (6.5) corresponding to the measured transmittance T at 550 nm using an appropriate power meter under the lab based controlled fog atmosphere as shown in Fig 6.2. The visibility V is evaluated using (3.11). However, the attenuation (dB/km) of the FSO link at wavelengths of 830 nm and 1550 nm is also carefully measured simultaneously with the V measurement using the setup shown in Fig 6.2.

6.3. Comparison of Field and Indoor Measured Visibility

Fog is a random dynamic atmospheric phenomenon and the probability of occurrence of the dense in the real outdoor atmosphere is very low. Fig. 6.3 illustrate the typical measured distribution of V from two field experiments at the Newcastle

airport, UK and Milesovka Hill, Czech Republic over a year and is compared to the average data generated from two experiments over one hour time period using an atmospheric chamber. The minimum V achieved from the data at Milesovka and the Newcastle airport are 33 m and 50 m for probabilities of 0.1% and 0.01%, respectively. However, using the indoor –

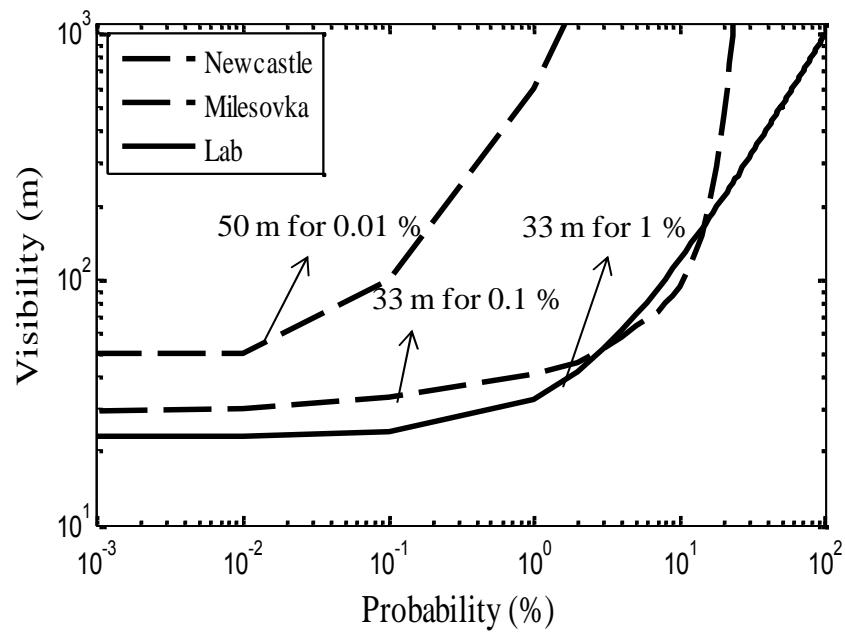


Figure 6.3. Comparison of the measured visibility for outdoor and atmospheric chamber.

atmospheric chamber in the lab controlled environment, a very dense fog condition with $V = 33$ m for 1% of the time are achieved, which demonstrates the proposed indoor chamber capabilities to replicate outdoor dense fog field trial conditions without waiting for a year.

6.4. Fog Attenuation Measurements

Figure 6.4 shows plots for the concurrent measured V and the fog attenuation (in dB/km) at $0.83\ \mu\text{m}$ and $1.55\ \mu\text{m}$ using CCD and a laser diode at $0.55\ \mu\text{m}$. Kim model is compared with the experimental data in order to validate the accuracy of the experiment in the atmospheric chamber. CCD technique shows higher accuracy for $V < 0.05\ \text{km}$ and the laser technique for the range $> 0.1\ \text{km}$. Therefore, these techniques allow enhancement of the characterisation of an FSO link in thick and dense fog conditions. The measured V , using both methods, is in good agreement with Kim model. This validates the accuracy of V measurement and the corresponding fog attenuation when using an indoor atmospheric chamber.

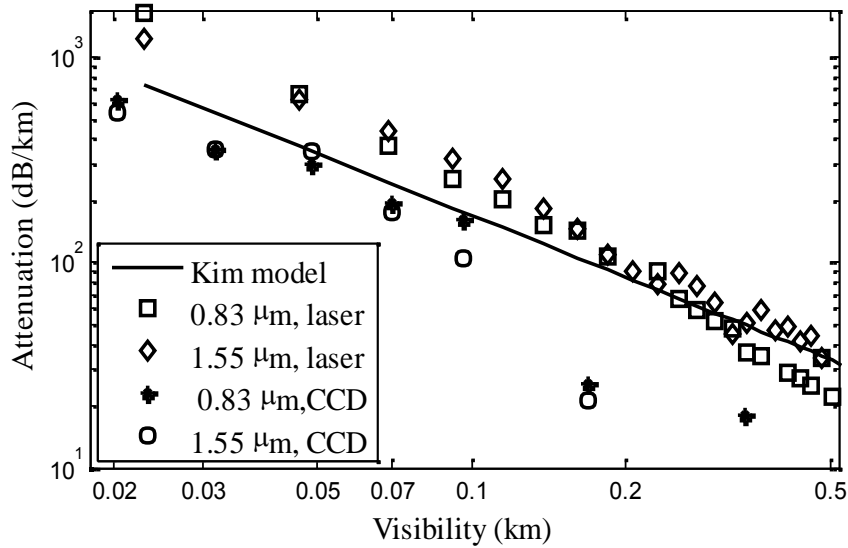


Figure 6.4. The characterisation of measured visibility and fog attenuation using CCD, laser diodes and Kim model.

The logarithmic plot of the measured average fog attenuation (in dB/ km) against the measured V for $0.67\ \mu\text{m}$ and $1.55\ \mu\text{m}$ wavelengths are shown in Fig. 6.5. The measured attenuation is notably higher for $0.67\ \mu\text{m}$ than at $1.55\ \mu\text{m}$ for the given

visibility range ($0.032 \text{ km} < V < 1 \text{ km}$). There is an attenuation difference of 50 dB/km, 10dB/ km and 7 dB/ km at V of 0.048 km, 0.103 km and 0.5 km, respectively. The measured attenuation is wavelength dependent at $0.67\mu\text{m}$, and $1.55 \mu\text{m}$ for the dense fog condition, *i.e.*, $V < 0.5 \text{ km}$. The measured attenuation at $0.67 \mu\text{m}$ is higher than at $1.55 \mu\text{m}$ for $V < 0.5 \text{ km}$, contradicting the wavelength independency of Kim model. The experimental results show the wavelength dependency of fog attenuation on the selected wavelengths for $V < 0.5 \text{ km}$.

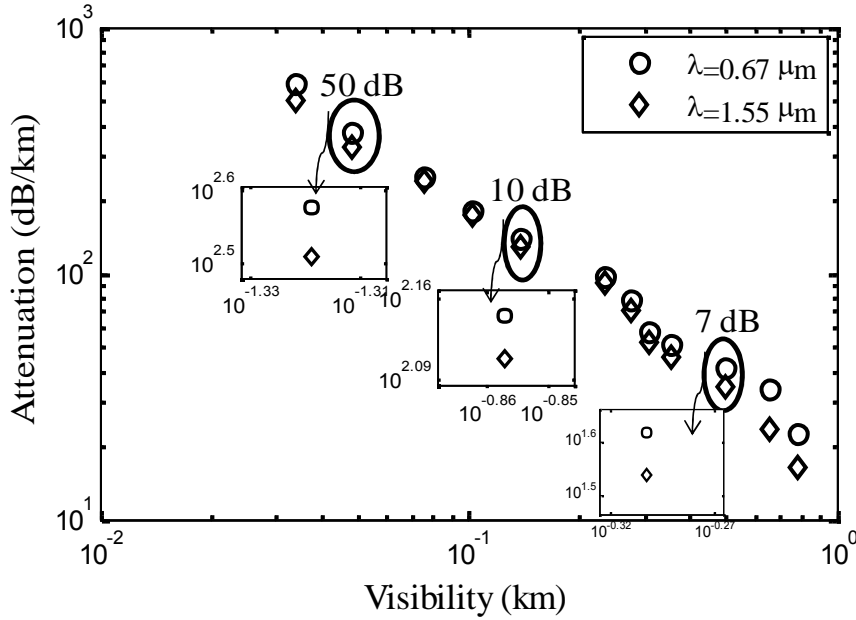


Figure 6.5. The measured attenuation (dB/ km) and visibility for fog.

6.5. Smoke Attenuation Measurements

Figure 6.6 depicts the average smoke loss for dense to light smoke densities for the entire smoke event for a link length of 6 m. The measured smoke loss at time interval of 11 minute is 0 dB prior to the injection of smoke. Thus, at $T = 1$, the loss is zero. However, after the injection of smoke into the chamber and allowing the

smoke to settled homogeneously (for about one minute), the measured losses were 27 dB and 7 dB at dense smoke for 830 nm and 1550 nm, respectively for the link length of 6 m. The optical loss continues to decrease with time as the smoke is dispersed and in the chamber is finally free from smoke (*i.e.*, $T = 1$ for both the lasers).

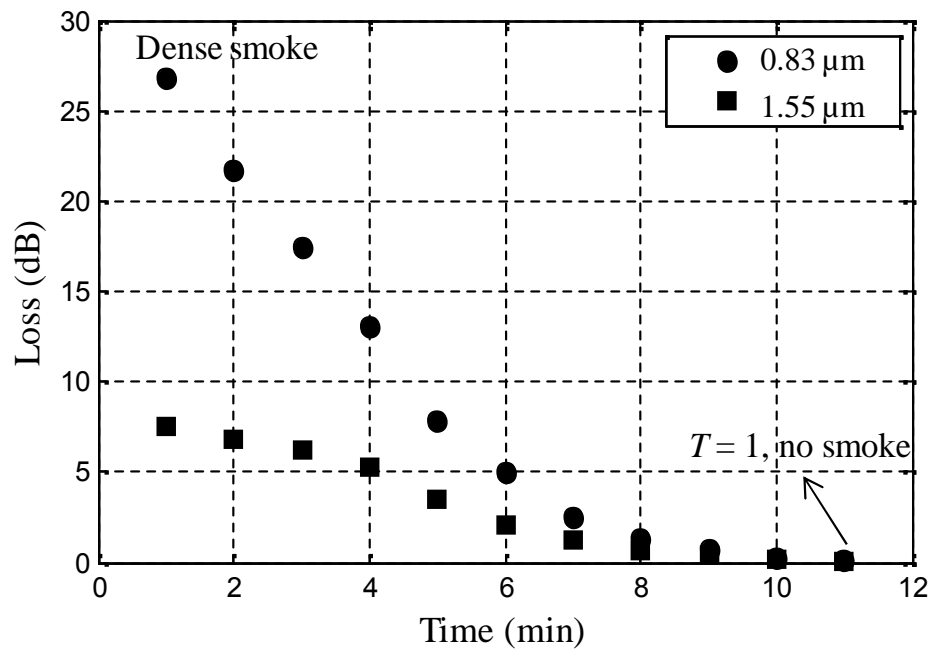


Figure 6.6. Comparison of the measured average loss at wavelengths of 0.83 and 1.55 μm under the laboratory based controlled smoke.

Furthermore, logarithmic plots of the measured attenuation of smoke (in dB/ km) against the V for 0.83 μm and 1.55 μm wavelengths are depicted in Fig.6.7. The experimental result clearly demonstrates the dependency of the wavelength on the resultant smoke attenuation even if V is below 0.5 km. In general, the smoke attenuation difference is more than the fog attenuation. For smoke the average attenuation difference between 0.83 μm and 1.55 μm are 108 dB/ km, 23 dB/km and 8 dB/ km at V of 0.07 km, 0.25 km and 0.5 km, respectively as illustrated in Fig.

6.8. This depicts that selection of $1.55\ \mu\text{m}$ is more favourable in the fog and smoke channels for the dense ($V < 0.07\ \text{km}$), thick ($V = 0.25\ \text{m}$) and the moderate fog and smoke ($V = 0.5\ \text{km}$) conditions, respectively.

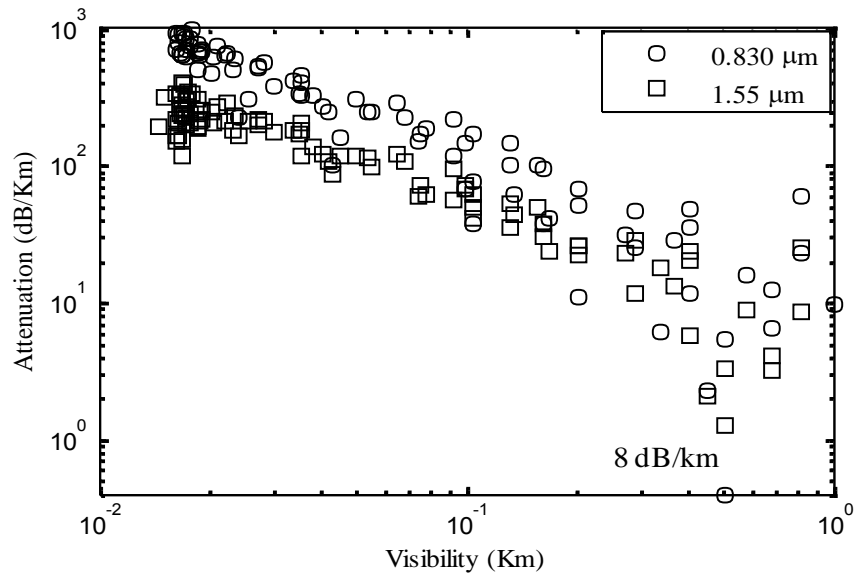


Figure 6.7. The comparison of the measured smoke attenuation (dB/ km) for 0.830 and $1.55\ \mu\text{m}$ for the FSO link length of $1\ \text{km}$.

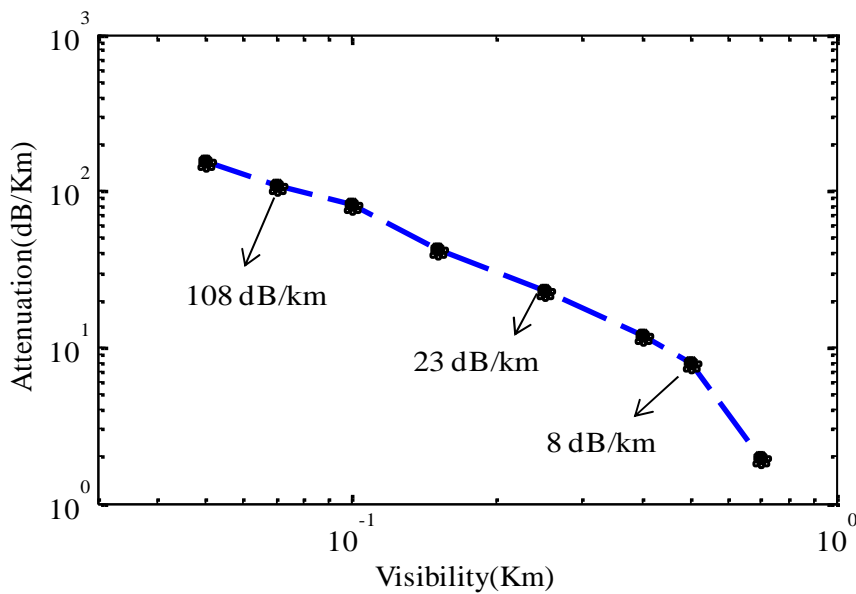


Figure 6.8. The average attenuation difference between 0.83 and $1.55\ \mu\text{m}$ as a function of measured visibility (km) for FSO link length of $1\ \text{km}$.

6.6. Empirical Modelling of Fog and Smoke

The attenuation due to the scattering and absorption is highly dependent on the size parameter q , recalling (3.4). However, Kim had also defined the value of q for fog in [261], which describes the wavelength dependency of the fog attenuation and the type of scattering. Values of q are -4, -1.6 and 0 for Rayleigh scattering ($r \ll \lambda$), Mie scattering ($r \sim \lambda$), and geometric scattering ($r \gg \lambda$), respectively [253]. In order to predict a suitable model for the attenuation of fog and smoke based on measured data, the following is carried out.

Table 6.1. Values of q obtained for different wavelength from measured fog and smoke attenuation data.

For Fog			
Wavelength-μm	q	R^2-value	RMSE
0.6	0.002	0.9670	0.1950
0.8	0.020	0.9850	0.1400
0.9	0.030	0.9846	0.1470
1	0.045	0.9827	0.1560
1.1	0.050	0.9813	0.1620
1.2	0.070	0.9803	0.1590
1.3	0.093	0.9802	0.1690
1.4	0.105	0.9800	0.1750
1.5	0.130	0.9760	0.1760
1.6	0.135	0.9751	0.1890
For Smoke			
0.55	0	0.9985	0.0467
0.67	0.100	0.9680	0.2000
0.83	0.180	0.9220	0.3100
1.31	0.580	0.9121	0.2100

Values of q are obtained for individual wavelengths from 0.60 – 1.6 μm , respectively by using the empirical curve fitting method with a reference wavelength of 0.55 μm , see Table 6.1. The values of the root mean square error (RMSE) and R^2 confirm that the curve fitting is in a good correlation with the measured data for both fog and smoke. The value of q is found to be within 0 to 0.6 for fog and smoke indicating the predominance of the Mie scattering ($r \sim \lambda$). This verifies that in the ($r \sim \lambda$) region for the dense fog condition, the q value is the function of wavelength not the visibility. The plot of predicted q values against the wavelength and the curve of best-fit against a wavelength range of 0.6 – 1.6 μm for fog and smoke conditions are shown in Figs. 6.9 and 6.10, respectively. The best curve fit satisfied the (6.7) with R^2 and RMSE values of 0.9732 and 0.0076 for the fog and similarly for the smoke with R^2 and RMSE values of 0.9797 and 0.0497, respectively:

$$q(\lambda) = \begin{cases} 0.1428\lambda - 0.0947 & \text{Fog} \\ 0.8467\lambda - 0.5212 & \text{Smoke} \end{cases} \quad (6.6)$$

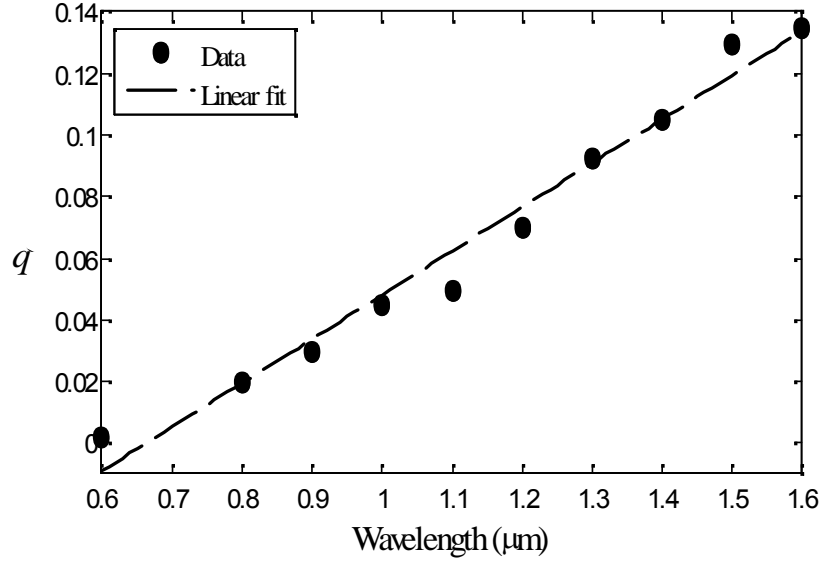


Figure 6.9. The predicted q value and linear curve of best-fit against wavelength for fog.

The new proposed model for the prediction of the attenuation due to fog and smoke can be presented as:

$$\beta_{\lambda} (dB / km) = \frac{17}{V(km)} \left(\frac{\lambda}{\lambda_o} \right)^{-q(\lambda)}, \quad (6.7)$$

where, the wavelength with a range from $0.55 \mu m < \lambda < 1.6 \mu m$ is valid for the V range of $0.015 km < V < 1 km$. The function for $q(\lambda)$ for the fog and smoke is expressed in (6.7). The experimental data shows that as $V \rightarrow 0$ for the very dense fog conditions, the received optical signal is significantly lower than the OSA minimum sensitivity at $V = 0.0135 km$. This fact validates that the measurements below $0.015 km$ are not very practical to show the wavelength dependent fog attenuation. Thus, validating the model for the V range of $0.015 km < V < 1 km$.

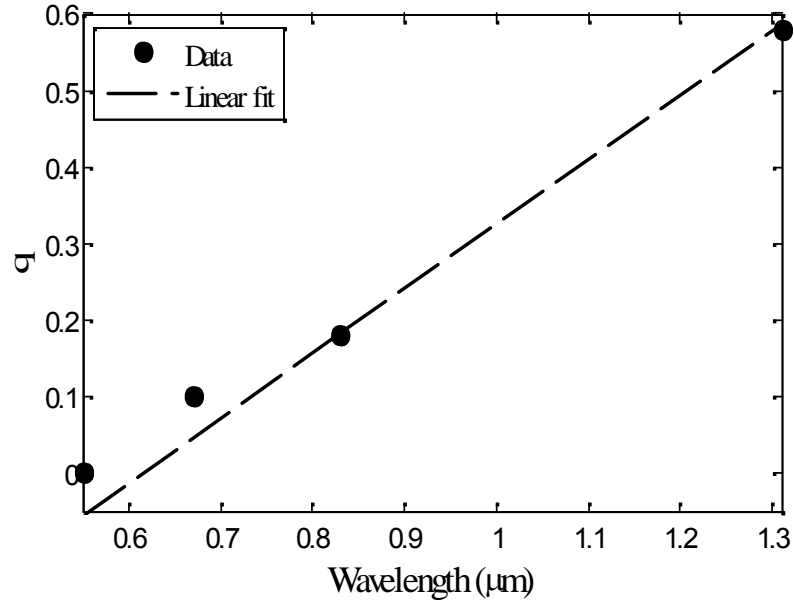


Figure 6.10. The predicted q value and linear curve of best-fit against wavelength for smoke.

6.7. Comparison of the Measured Visibility and Attenuation Data with the Proposed Model

Figure 6.11 shows the logarithmic plot for the measured fog attenuation against the concurrent V data for the selected wavelengths of 0.67, 0.83, 1.1, 1.31 and 1.55 μm for modified and Kim fog models. The logarithmic plot of the attenuation curve obtained from the proposed model defined by (6.7) and the comparison with the measured data shows a good agreement. However, comparison of the Kim model at $\lambda = 1.55 \mu\text{m}$ with the measured data for $V < 0.5 \text{ km}$ show that the model over estimates the fog attenuation. This is because Kim model does not take into account the wavelength to estimate the fog attenuation. However, Kim model fits well with the experiment data for $V > 0.5 \text{ km}$ (see inset Fig. 6.11). This indicates the

dependency of the fog attenuation on the wavelength.

Figure 6.12 displays the logarithmic plot for the measured smoke attenuation against the concurrent V data for the selected wavelengths of 0.55, 0.67, 0.83, and 1.31 μm . Comparison of the proposed smoke model shows a good agreement between the measured data for the selective individual wavelengths. This clearly indicates the dependency of attenuation on the wavelength. The plot shows a difference of 50 dB/km is observed between 1.31 and 0.83 μm for the dense smoke condition ($V < 0.07$ km), with progressive reduction in the attenuation difference for thick and moderate smoke conditions. Thus, clearly indicating suitability of NIR wavelengths at the dense smoke condition. The proposed model, where the available V data needs to be considered instead of the liquid water content (LWC) and the particle radius, is a simple approach using (6.7). It is most suitable for the FSO link budget analysis in the urban area where fog and smoke are more likely to occur all year round.

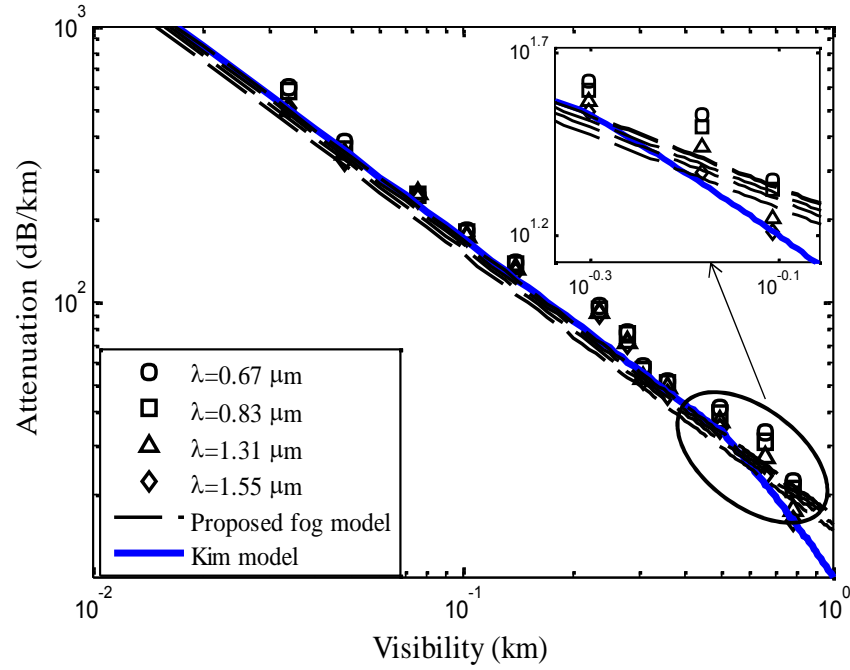


Figure 6.11. Real time measured fog attenuation versus visibility ($V = 1$ km) and curves of modified fog and Kim models for different wavelengths.

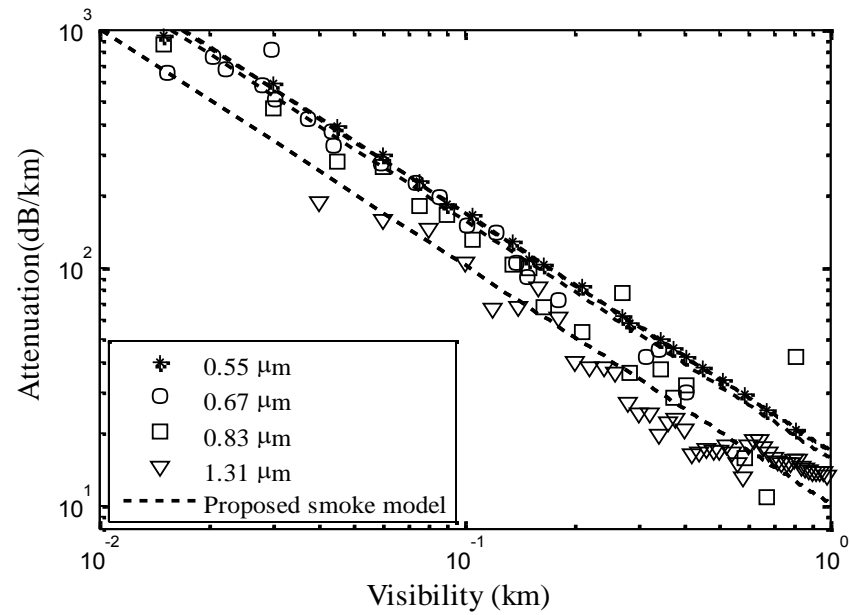


Figure 6.12. Real time measured smoke attenuation versus visibility ($V = 1$ km) and curves of smoke model for different wavelengths.

6.8. Comparison of Model with Attenuation

Spectrum Measurements

6.8.1. Fog

The measured fog attenuation (in dB/km) for the very dense fog ($V \sim 0.05$ km) for the visible – NIR spectrum under test (SUT) is shown in Fig. 6.13 (a). The measured attenuation for the SUT at the very dense fog condition ($V \sim 0.05$ km) displays three possible attenuation windows, (i) $0.60 \text{ m} - 0.85 \text{ m}$, which has an attenuation range of $375 \text{ dB/km} - 361 \text{ dB/km}$ with the peak attenuation of 382.4 dB/km at 0.72 m , (ii) $0.85 \text{ m} - 1.0 \text{ m}$, showing a lower attenuation (360 dB/km) at 0.830 m than at 0.925 m with a peak attenuation of 383.6 (dB/km) . However, at 0.940 m the attenuation has a lower peak value of 354 dB/km , and (iii) $1.0 \text{ m} - 1.55 \text{ m}$, with an attenuation range of $360 \text{ dB/km} - 323 \text{ dB/km}$. Results show that 1.33 m has a higher attenuation peak of 357 dB/km than the 1.05 m with an attenuation dip of 347.6 dB/km . However, 1.55 m has the lowest attenuation of (324 dB/km) in a very dense fog at $V = 0.05 \text{ km}$.

Table 6.2 shows the possible wavelengths with the minimum fog attenuation suitable for use in FSO links. The behavior of the attenuation spectrum is almost the same for $V = 0.3 \text{ km}$ with the maximum attenuation of $\sim 59.5 \text{ dB/km}$ to 53.5 dB/km for 0.6 m and 1.55 m , respectively (see Fig. 6.13(b)).

Table 6.2. The suitable possible wavelengths to operate in the foggy channel, measured at $V = 0.048$ km.

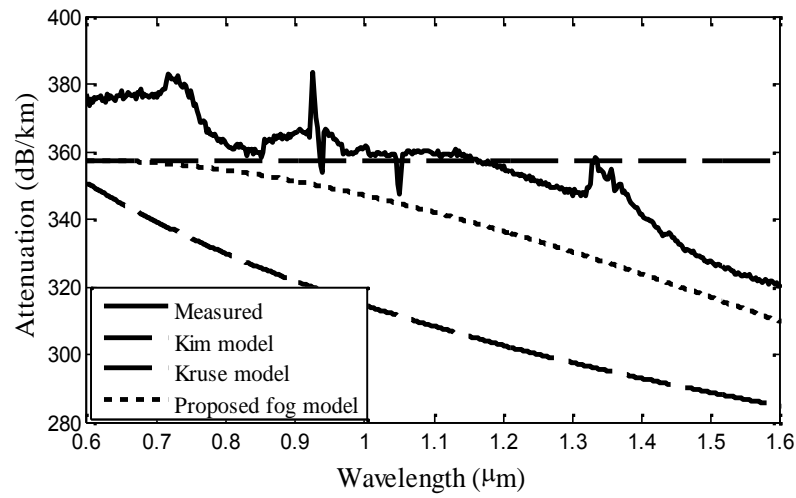
Wavelength windows (μm)	Window attenuation (dB/km)	Peak attenuation (dB/km)	Suitable wavelengths (μm)
0.6 – 0.85	375 – 361	382.4	0.830
0.85 – 1.0	361 – 360	383.3	0.940
1.0 – 1.55	360 – 323	57.0	1.55

Table 6.3. RMSE and SD values between the measured attenuation and the estimated using fog and smoke models.

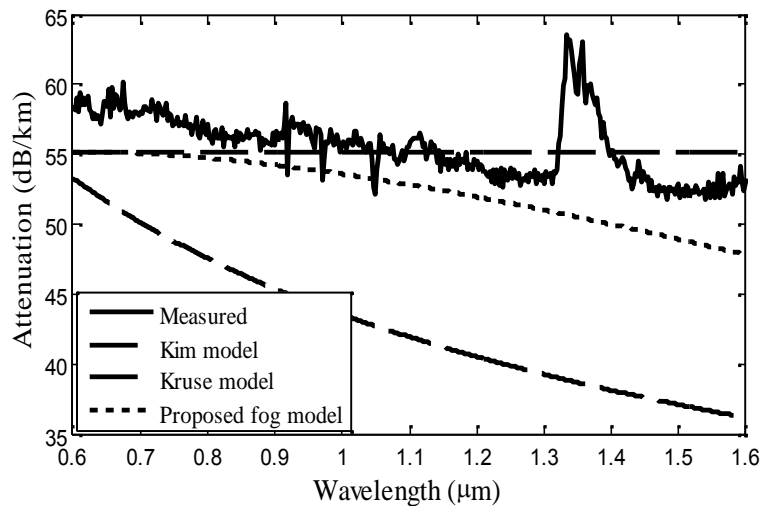
Models			
	Kim	Kruse	New proposed model
Fog, $V = 48$ m (Fig 7 a)			
RMSE	16.2465	44.4926	16.5137
SD	16.1316	8.0221	5.0157
Fog, $V = 300$ m (Fig 7 b)			
RMSE	2.3473	13.3434	3.8009
SD	2.3048	3.7834	2.0378
Smoke, $V = 185$ m (Fig 8 a)			
RMSE	26.5577	10.3355	3.4382
SD	15.8700	5.8027	2.4107
Smoke, $V = 245$ m (Fig 8 b)			
RMSE	19.3016	6.9398	3.9225
SD	11.8443	3.6034	2.4021

The proposed model is experimentally verified for SUT using the controlled indoor chamber for fog and smoke. The proposed model is also compared with selected Kim and Kruse models, which are widely used in the literature for outdoor FSO channels. Kim model at $V \sim 0.05$ km and 0.3 km shows that the fog attenuation for

SUT is wavelength independent contradicting the experimental data. Kruse model underestimates the fog attenuation at $V \sim 0.05$ km and 0.3 km for SUT (see Figs. 6.13 (a) and (b)). However, the new proposed fog model shows a close correlation for SUT. This verifies that the proposed model follows the profile of measured fog attenuation more precise than both Kim and Kruse models for $V < 0.5$ km.



(a)



(b)

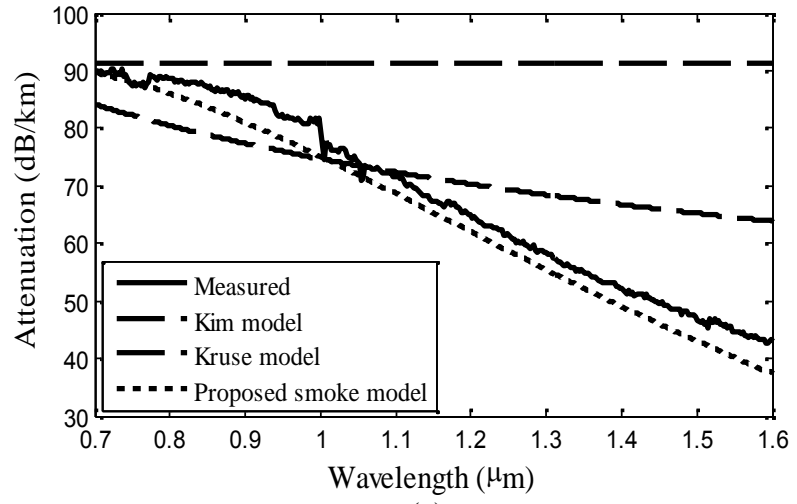
Figure 6.13. The measured fog attenuation (dB/km) from the visible – NIR spectrum and the comparison with the selected empirical models (a) for $V = 0.048$ km, and (b) for $V = 0.3$ km.

The RMSE values for Kim, Kruse and the new proposed fog models from the measured attenuation are shown in Table 6.3. The RMSE values are 2.3473, 13.3434 and 3.8009 from the measured attenuation; and the standard deviation (SD) values are 2.3048, 3.7834 and 2.0378, respectively at $V = 300$ m. The RMSE and SD values of the attenuation spectrum from visible – NIR range shows a better agreement compared to RMSE and SD of published data for ROF at individual wavelengths [338, 345].

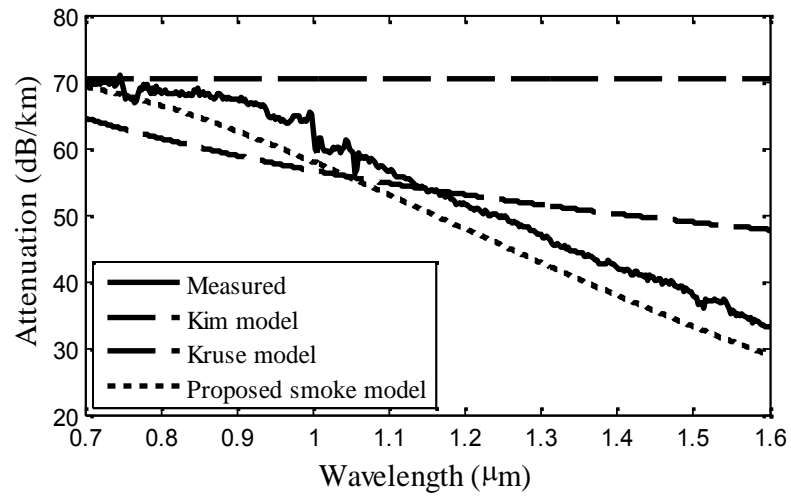
6.8.2. Smoke

In the case of smoke, the measured smoke attenuation (in dB/km) at $V \sim 0.185$ km and 0.245 km for SUT is depicted in Fig. (6.14). The resultant smoke attenuation at $V = 0.185$ km is almost 90 dB/km for the visible range and drops to 43 dB/km at the NIR range of SUT, see Fig. 6.14 (a). A similar behavior of the smoke attenuation is observed at $V = 0.245$ km with the attenuation of 70 dB/km at the visible range decreasing to 33 dB/km at the NIR range of SUT, see Fig. 6.14 (b). The new proposed smoke model is also compared to Kim and Kruse models for the smoke attenuation. Kim model overestimates the measured smoke attenuation and shows wavelength independent attenuation for $V < 0.5$ km. However, Kruse model underestimates the smoke attenuation for $0.7 \text{ } \mu\text{m} < \lambda < 1 \text{ } \mu\text{m}$ and overestimates the smoke attenuation for $1.1 \text{ } \mu\text{m} < \lambda < 1.6 \text{ } \mu\text{m}$ (see Figs. 6.14 (a) and (b)). The new proposed model fits the experimental data showing a close correlation with the measured smoke attenuation spectrum, thus verifying the validity of the proposed model for smoke conditions in the visible – NIR SUT range. The model is definitely better than the other models in predicting the smoke attenuation but not in predicting

the fog attenuation.



(a)



(b)

Figure 6.14. The measured smoke attenuation (dB/km) from the visible – NIR spectrum and the comparison with the selected empirical models (a) for $V = 0.185$ km, and (b) for $V = 0.245$ km

6.9. Summary

In this chapter, two methods to characterise the fog attenuation in terms of the atmospheric V in FSO communications have been analysed and compared. Both methods were based on the real time measurement of fog based on V using a charge coupled device (CCD) camera and a visible laser-diode at 0.55 μm . Methods have been evaluated in a laboratory controlled FSO atmospheric chamber operating at wavelengths of 0.83, 1.31 and 1.55 μm and over a continuous spectrum range of 0.6 to 1.6 μm . CCD technique has showed a great accuracy for $V < 50 \text{ m}$ and the laser technique for the range beyond 100 m , thus allowing enhancement of the characterisation of FSO links in thick and dense fog conditions. This accuracy is essential when implementing and installing real-time low cost V system where accuracy and early response are crucial, *e.g.*, road surveillance, airport security, local weather applications.

Moreover, a wavelength dependent model for fog and smoke channels has been proposed, which is valid for the visible – NIR range for the V range of 1 km . The experimental results have also showed the most robust wavelengths windows (0.83, 0.94 and 1.55 μm) that could be adopted for fog conditions in order to minimize the FSO link failure. Furthermore, to validate the behavior of the proposed empirical model for selected wavelengths, the proposed model has been compared with the continuous attenuation spectrum for the same fog and smoke conditions and it was found that the attenuation is almost linearly decreasing for both cases. This has verified that the proposed model follows the profile of measured fog attenuation more precise than both Kim and Kruse models for $V < 0.5 \text{ km}$.

Chapter 7

BER Performance of FSO under Controlled Fog Conditions

7.1. Introduction

The constituents of atmosphere particularly fog severely hinder the FSO performance by the scattering and absorption of photon energy [162, 346, 347]. This consequently leads to the reduced received optical power hence increasing the bit error rate (BER) performance [348-350]. Dense fog can potentially increase the BER, therefore interrupt the high data rate FSO link to achieve the availability of five nines, 99.999% [351-353]. A number of research works investigating the effect of fog on FSO systems have been reported. These are mostly focusing on the measurement of attenuation and channel modelling [354-358]. However, some research work on the BER performance of an FSO link in fog is reported in [359] which correlates the atmospheric transmission with the BER. However, this work does not study in details the atmospheric transmission characteristics of the fog channel by using

different modulation schemes and increasing P_{opt} to improve the BER performance of an FSO link.

In this chapter, the experimental work has been reported to test and mitigate the effect of fog by employing power efficient modulation schemes and different P_{opt} . Here, an alternative approach is used to evaluate the BER performance of the FSO link under different fog environment using the real time domain and post processing of the received signal eye diagrams. The transmittance T as well as the SNR, (*i.e.*, the Q -factor) is measured for different modulation format and also by increasing P_{opt} for light-to-dense fog densities.

The system performance is theoretically and experimentally evaluated for OOK-NRZ, OOK-RZ and 4-PPM formats for Ethernet line data rates from light to dense fog conditions. The theoretical and experimental results indicate that 4-PPM signalling format is the most robust to the fog attenuation effects than OOK due to its high peak-to-average power ratio at the expense of doubling the bandwidth and increasing the system complexity. The link availability at dense fog ($T = 0.33$) condition by maintaining a BER of 10^{-6} (Q -factor ≈ 4.7) is achievable using 4-PPM than OOK-NRZ and OOK-RZ modulation schemes. The effect of fog on OOK-NRZ, 4-PAM and SIM- BPSK is also experimentally investigated. In comparison to 4-PAM signal, the BPSK and OOK-NRZ modulation signalling format are more robust against the fog effects. The comparison shows that in dense fog conditions, 4-PAM scheme does not achieve BER values lower than 10^{-6} , on the other hand OOK-NRZ and BPSK schemes overcome that values for $T > 0.33$.

Moreover, the effect of using different average transmitted optical communication power P_{opt} on the transmittance and the received Q -factor for OOK-NRZ modulation scheme is also studied for light and dense fog densities. The results show that FSO system operating at Q -factor of 4.7 ($\text{BER} = 10^{-6}$), the required Q -factor is achieved at T of 48% under the thick fog condition by increasing P_{opt} to 1.07 dBm, whereas the values of T are 55% and $\sim 70\%$ for the transmit power of 0.56 dBm and -0.7 dBm, respectively.

7.2. Bit Error Rate Evaluation in a Controlled Fog

Channel

The performance of an FSO system is determined by the received SNR with respect to the total noise at the fixed or optimum threshold level. Considering Fig. 7.1, which represents the received eye diagram of the digital signal and its corresponding Gaussian distribution of the received signal current for bit '0' and '1' [360].

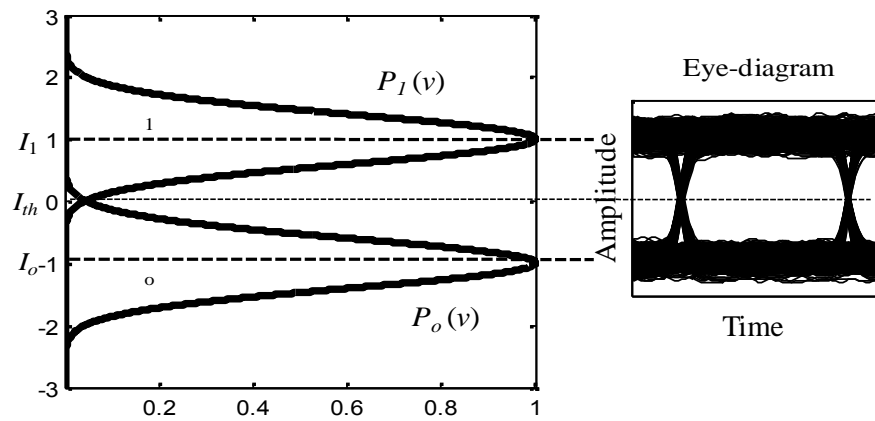


Figure 7.1. The eye diagram and the distribution of bits '0' and '1' for BER evaluation in fog.

The bit error rate (BER) is then given by:

$$BER = P(0)P(1/0) + P(1)P(1/0), \quad (7.1)$$

where, $P(0)$ and $P(1)$ are the probabilities of receiving bits '0' and '1', respectively. Since the probability of occurrence of receiving bits '0' and '1' is equally probable, thus $P(0) = P(1) = 1/2$. Here, $P(0/1)$ is the probability of deciding '0' when '1' is received and $P(1/0)$ is the probability of deciding '1' when '0' is received and are given by (7.2) and (7.3), respectively [361]:

$$P(0/1) = \int_{-\infty}^{I_{th}} \frac{1}{\sqrt{2\pi\sigma_1^2}} \exp\left(-\frac{(I-I_1)^2}{2\sigma_1^2}\right) dI = \frac{1}{2} \operatorname{erfc}\left(\frac{I_1 - I_{th}}{\sigma_1\sqrt{2}}\right) \quad (7.2)$$

$$P(1/0) = \int_{I_{th}}^{\infty} \frac{1}{\sqrt{2\pi\sigma_o^2}} \exp\left(-\frac{(I-I_o)^2}{2\sigma_o^2}\right) dI = \frac{1}{2} \operatorname{erfc}\left(\frac{I_{th} - I_o}{\sigma_o\sqrt{2}}\right), \quad (7.3)$$

Assuming $P(f)$ and $P(o)$ are the powers of the received optical signals in the cases of with and without fog, respectively, the transmittance (T) is then given by the Beer Lambert law [172] as:

$$T = \frac{P(f)}{P(o)} = \exp(-\beta_\lambda L), \quad (7.4)$$

where L is the propagation length. However, in order to correlate the Q -factor and resulting BER of the received signal for a range of measured T values for different fog conditions inside the atmospheric chamber, the Q -factor at the receiver without fog can be estimated as:

$$Q = T_o \left(\frac{I_1 - I_o}{\sigma_o + \sigma_1} \right), \quad (7.5)$$

where T_o is the maximum transmittance and is equal to the unity. I_1 and I_o are the average detected signal current for bit '1' and '0' where as σ_o and σ_1 are the standard deviation of the noise values for bit '1' and '0'. However, in the scenario with fog

and assuming that the ambient noise level does not change with fog density, the Q -factor can be approximated as:

$$Q_{fog} = T_{fog} Q. \quad (7.6)$$

For the non-return to zero on-off-keying (OOK-NRZ) data format with the intensity modulation and direct detection scheme, the BER expression for OOK-NRZ is given by:

$$BER = \frac{1}{2} \operatorname{erfc} \left(\frac{Q_{fog}}{\sqrt{2}} \right). \quad (7.7)$$

To measure the *BER* performance in different levels of fog, *i.e.*, from light to dense fog conditions. The characterisation of the fog has been carried out by relating the measured T_{fog} with the V (km). The transmittance, T of the input optical signal at the optical receiver (R_x) is related to attenuation due to fog using (6.5). Hence, the visibility V is evaluated for a range of T_{fog} values, see Table 7.1.

Table 7.1. Measured T and related visibility values at 830 nm.

Fog	Dense	Thick	Moderate	Light
V (m)	< 70	70- 250	250-500	500-1000
T_{fog}	< 0.33	0.33- 0.72	0.72- 0.85	0.85-0. 92

7.3. Experimental Setup for BER Measurement of FSO Communications under Lab-controlled Fog

The block diagram of FSO link for the BER performance analysis in the lab-

controlled fog environment is shown in Fig. 7.2. In this setup, the transmit signal could be generated by an arbitrary waveform generator (AWG) with different modulation formats and amplitude levels. The signal is used to directly modulate a laser diode which has a wavelength of 830 nm and the maximum optical peak transmitted power P_T achieved is 10 mW. The AWG is used to generate stream of $2^{13}-1$ pseudo random bit sequence in OOK-NRZ, OOK-RZ and 4-PPM formats. The baseline data-rate for OOK-NRZ, OOK-RZ and 4-PPM is 12.5 Mbit/s, which corresponds to the Ethernet 10BASE-T LAN data-link with the 4B5B coding format. Note that, the PRBS length of $2^{13}-1$ bits is based on the IEEE 802.3 Ethernet data standard for an average frame length of around 600 bytes.

In another experiment, OOK-NRZ, 4-PAM and SIM-BPSK signals are generated with a pseudorandom binary sequence (PRBS) of length $2^{13}-1$ bits. The baseline data rate of the OOK-NRZ, 4-PAM and SIM-BPSK is selected 5 Mbit/s for OOK and BPSK, and 5 Mbaud/s 4-PAM signals. The implementation of each signalling schemes has taken account the equivalence on the bit-rate, the signal power and the bandwidth to ensure that fair system performance comparison is achieved. The modulating signal amplitude has been set to 100 mV peak-to-peak (corresponding to P_{opt} of -1.32 dBm) for all the modulation schemes in order to achieve a fair comparison. The intensity modulated optical beam propagates through the atmospheric chamber and is detected at the optical receiver. The detailed description of controlling homogenous fog in the atmospheric chamber is proved in Section 5.2.

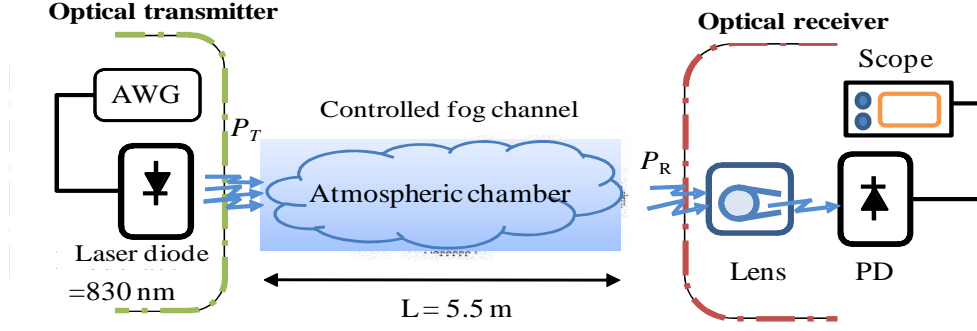


Figure 7.2. Block diagram of experiment setup for Q -factor evaluation in fog.

Table 7.2. Main parameters of the FSO used in the experiment.

Transmitter (Laser + AWG)	
Operating wavelength	830 nm
Average optical output power	10 mW
Laser modulation depth, m	20%
Laser 3-dB bandwidth	50 MHz
PRBS length	$2^{13}-1$ bits
Baseline data-rate (R)	12.5, 25 Mbit/s
Modulations formats	OOK-NRZ, OOK-RZ, 4-PPM, 4-PAM, BPSK
Maximum signal amplitude	500 mV _{p-p}
Receiver side (Photodiode + Lens)	
Lens focal length	20 cm
Lens diameter	3.4 cm
Photodetector responsivity	0.59 A/W @ 850 nm
Photodetector active area	1 mm ²
Photodetector half angle view	$\pm 75^\circ$
Electrical filter at receiver	$0.75 \cdot R $ / Hz
Transamplifier (IC)	AD8015
Receiver sensitivity	- 34 dBm
	(at 25Mbps & BER = 10^{-6})

At the receiver side, both the average received optical power (P_R) to measure the transmittance (T) and the Q -factor of the received signal are simultaneously measured for different fog conditions *i.e.*, from low to high visibilities. The optical signal is received using a photodiode followed by a wide-bandwidth transimpedance amplifier are employed to recover the electrical signal. A digital storage oscilloscope is used to capture the signal and to measure the Q -factor. A 1st order low pass filter with a cut-off frequency of $0.75 \cdot |R|$ Hz is used to reduce noise, where $R = 1/T$ and T is the minimum pulse duration. The main system parameters used in the experiment are summarized in Table 7.2.

7.4. FSO Link Performance for Different Modulation Schemes in Fog Channel

7.4.1. Using OOK-NRZ, OOK-RZ and 4-PPM

The BER performance of OOK-NRZ, OOK-RZ and 4-PPM modulation formats based FSO system is investigated by measuring the Q -factor corresponding to the T at the wavelength of 830 nm using (7.6). Figure 7.3 illustrates the experimental Q -factor and the BER performance for OOK-NRZ, OOK-RZ and 4-PPM formats for data rate of 12.5 Mbit/s at different values of T under homogeneous fog conditions. The modulation voltage of 100 mV_{p-p} for OOK-NRZ is used corresponding to P_{opt} of -1.32 dBm. However, the average optical transmitted power P_T is maintained constant for all signaling formats. This implies that the amplitude levels and the time-slot duration of OOK-RZ and 4-PPM are twice and half that of OOK-NRZ, respectively. The results show the experimental data (dots) follow closely the

theoretical prediction (for all modulation formats) using (7.6). Figure 7.3 shows that 4-PPM followed by the OOK-RZ signaling format offers the best Q -factor compared to the OOK-NRZ irrespective of the value of T , this is due to the high peak-to-average power ratio. The link availability at dense fog ($T = 0.33$) by maintaining a BER of 10^{-6} (Q -factor ≈ 4.7) is achievable using 4-PPM than OOK-NRZ and OOK-RZ modulation schemes, following (7.6).

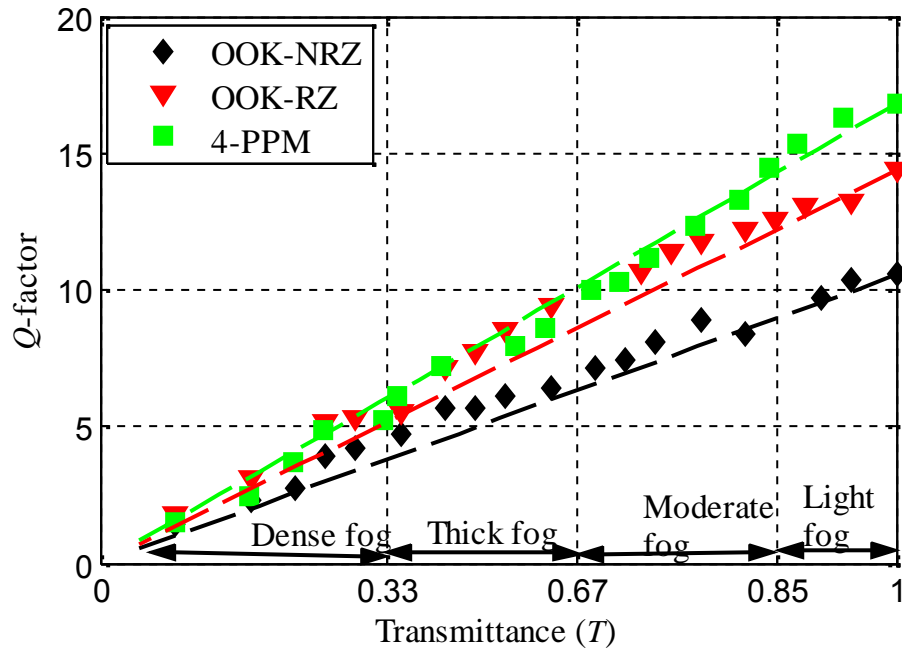


Figure 7.3. Q - factors versus T for OOK-NRZ, OOK-RZ and 4-PPM for different fog conditions (measured (dot points) , theory (dotted lines)).

The corresponding received signal eye diagrams for OOK-NRZ, OOK-RZ and 4-PPM formats are displayed in Fig. 7.4 for the dense fog ($T = 0.37$) and moderate fog ($T = 0.70$) conditions for P_{opt} of -1.32 dBm. They are obtained after $0.75 \times |R|$ Hz low pass filtering. Note that the wide eye-opening at $T = 0.70$ compared to $T = 0.37$, while both have almost identical noise variance, see Figs. 7.4 (a-b). The eye opening indicates the quality of the Ethernet FSO link for different signalling formats, *e.g.*,

the OOK-RZ and 4-PPM in Figs. 7.4 (d) and (f) at $T = 70\%$ are wider than in (c) and (e) at $T = 30\%$.

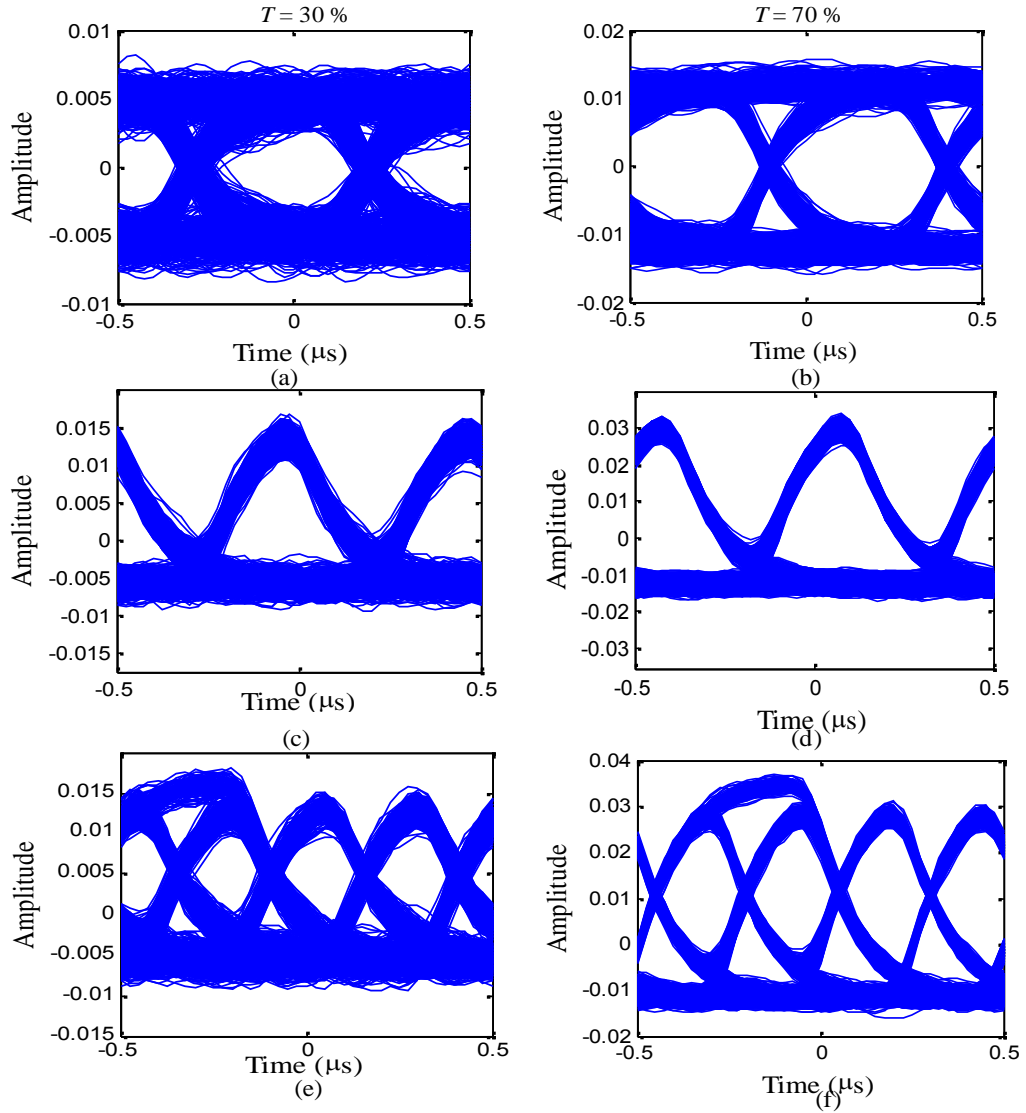


Figure 7.4. Measured eye-diagrams post-processed for (a-b) OOK-NRZ, (c-d) OOK-RZ and (e-f) 4-PPM received signals eye-diagrams for $T = 0.30$ and $T = 0.70$, for dense and light fog conditions, respectively.

Higher order of PPM would offer further improvement in performance, but at the cost of increased bandwidth and complexity. Figure 7.5 illustrates the BER performance against the received optical power for OOK-NRZ, OOK-RZ and 4-PPM schemes. It is observed that the link availability at a BER value of 10^{-6} is

related to the Q -factor of 4.7 following equation (7.7). In this setup the average power at the R_x for BER values lower than 10^{-6} is between -40 dBm to -37 dBm, which is defined by the photoreceiver sensitivity. The theoretical curves are evaluated using (7.7). The measured data shows a good agreement with the theoretical predictions. To achieve BER of 10^{-6} in fog channel, the required received optical power is 36.5 dBm for 4-PPM, - 35.0 dBm for RZ, where as it is -33.5 dBm for NRZ. The results show that 4-PPM is the best modulation scheme to mitigate the effect of fog with power margin of almost 3 dBm more than OOK-NRZ and 1.5 dBm than OOK-RZ modulation scheme.

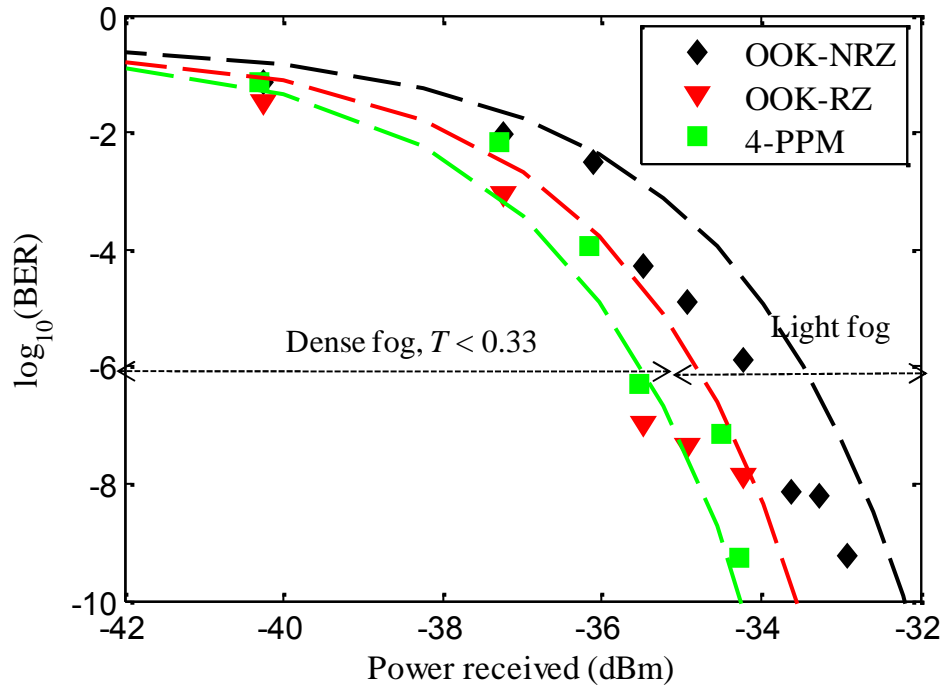


Figure 7.5. BER of OOK-NRZ, OOK-RZ and 4-PPM for different measured optical powers in fog (measured (solid points), theory (dotted lines)).

7.4.2. Using OOK-NRZ, 4-PAM and BPSK

Figure 7.6 shows the comparison of measured Q -factor for the OOK-NRZ, 4-PAM and BPSK modulation schemes against the measured T , simultaneously. The Q -factor for the 4-PAM and BPSK is normalized, so that the Q -factor at $T = 1$ are equal to OOK-NRZ. The Q -factor results depicted in Fig. 7.6 depicts that BPSK and OOK-NRZ modulation signalling format are more robust to fog impairments on the FSO link than the 4-PAM format. The behaviours of the three modulations schemes under fog conditions are similar, however at $T = 1$ the Q -factor is 30 for BPSK, 9 for OOK-NRZ and 4.5 for 4-PAM in absolute value, see inset Fig. 7.6. In dense fog conditions 4-PAM scheme does not achieve BER values lower than 10^{-6} , on the other hand OOK-NRZ and BPSK schemes overcome that values for $T > 0.3$.

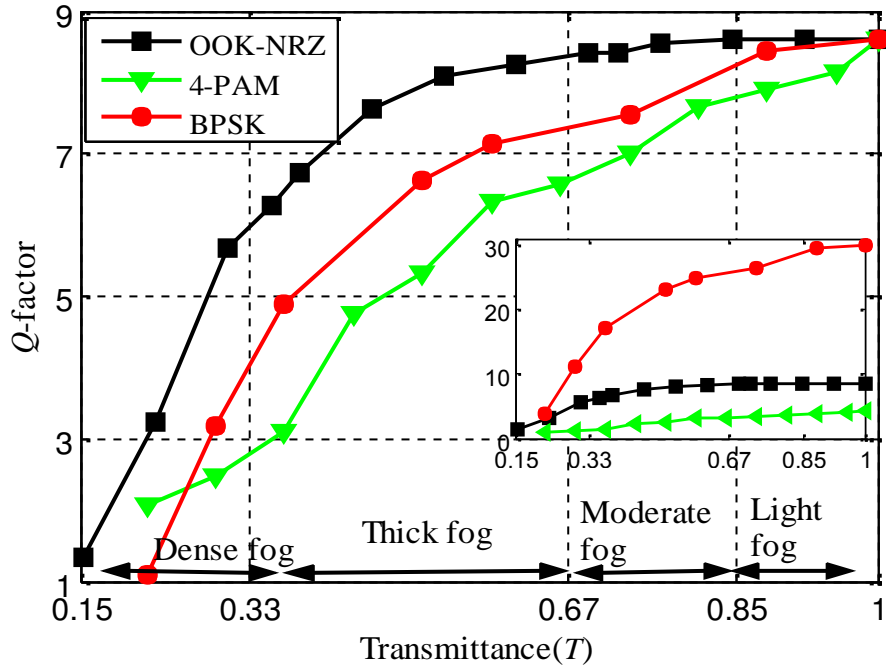


Figure 7.6. Measured Q -factor for OOK-NRZ, 4-PAM and BPSK for same P_{tx} and 5 Mbit/s data rate at different T of link values and fog conditions.

Figure 7.6 illustrates the predominant gain of OOK-NRZ format over the rest of modulations, although in term of absolute values, BPSK obtains better BER results. It is indicated that BPSK has an optimum behaviour under fog conditions, with a higher receiver complexity.

The corresponding received signal eye diagrams for OOK-NRZ, BPSK and 4-PAM formats are displayed in Fig. 7.7 for the dense fog ($T = 0.37$) and moderate fog ($T = 0.70$) conditions. Note that there is a wide eye-opening at $T = 0.70$ compared to $T = 0.37$ as shown in Fig. 7.7 (a-b). Moreover, the eye-opening in Figs. 7.7 (d) and (f) are more wide open at $T = 70\%$ than in Figs. 7.7 (c) and (e) at $T = 30\%$ for 4-PAM and BPSK, respectively.

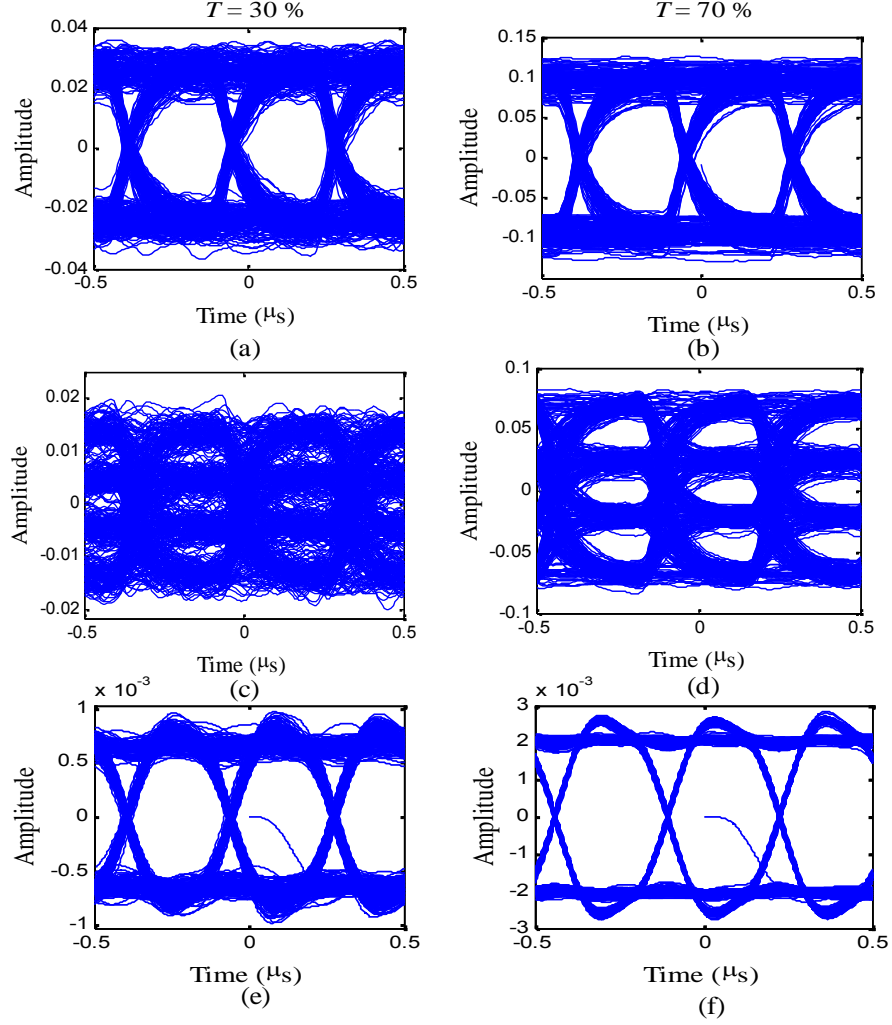


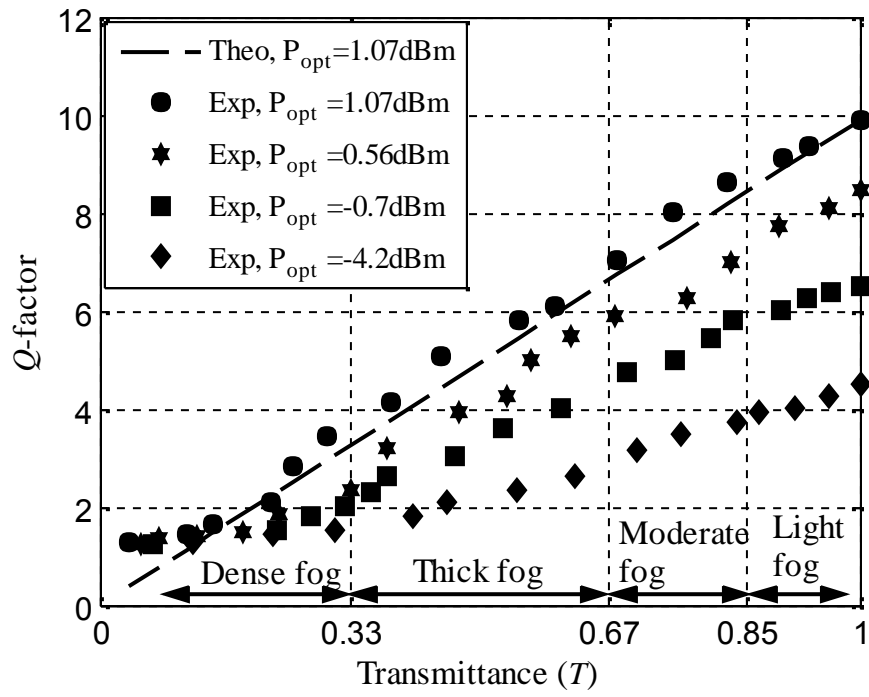
Figure 7.7. Measured eye-diagrams post-processed for (a-b) OOK-NRZ, (c-d) 4-PAM and (e-f) BPSK received signals eye-diagrams for $T = 0.37$ and $T = 0.70$, for dense and light fog conditions, respectively. Obtained after a $0.75 \cdot |R|$ Hz low pass filter.

7.5. FSO Link Performance for Different Launched Powers

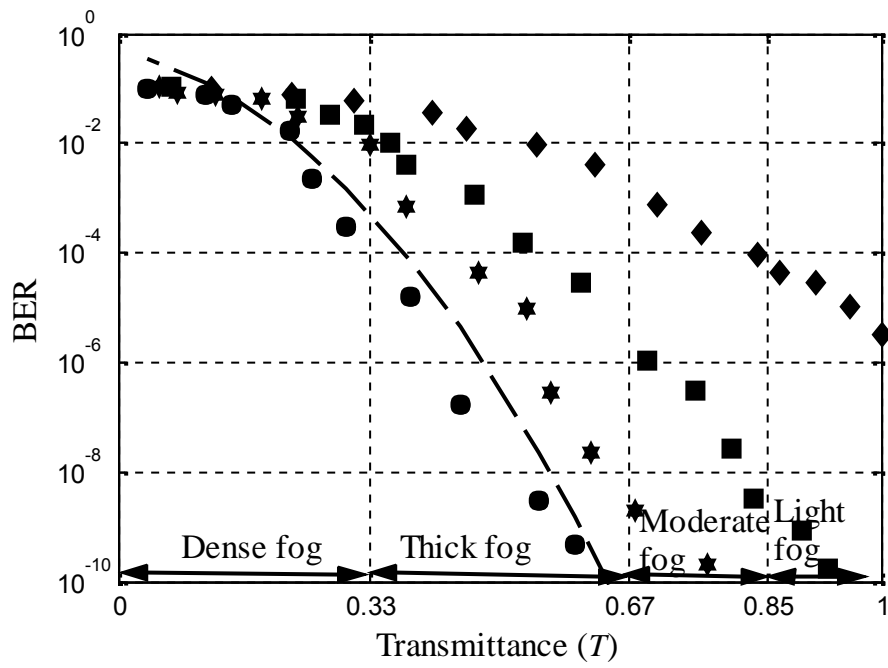
Figure 7.8 illustrates the dependence of Q -factor and the evaluated BER on the link transmittance for a range of P_{opt} using OOK-NRZ at data rate of 25 Mbps. Also

depicted are the predicted results using (7.6) for P_{opt} of 1.07 dBm showing a close agreement with the measured data. Note that in the region of $T < 20$ % (dense fog) the Q - factor values are almost the same for all values of P_{opt} . This is due to the background noise being the dominant source (see the eye diagrams in Fig. 7.9). To achieve a BER of 10^{-6} , the Q - factor value must be ~ 4.7 for the OOK-NRZ data format. However, this Q -factor value cannot be achieved under the dense fog condition (*i.e.*, $T < 33\%$) even for higher input power used $P_{\text{opt}} = 1.07$ dBm (see Figs. 7.8 (a)). With dense fog the link range drops to < 70 m with reduced link availability, thus making the FSO link less attractive. In such cases one could increase the optical power provided it is kept below the eye safety level or switch to a lower data rate RF technology to maintain maximum availability of 99.999%. For the thick fog condition ($33 < T < 72\%$) increasing P_{opt} from -0.7 dBm to 1.07 dBm will increase the Q -factor from 2 to 7, respectively, thus corresponding to the BER improvement from 10^{-3} to $>10^{-9}$.

However, for the system with a P_{opt} of - 4.2 dBm it is not possible to achieve the required BER of 10^{-6} even no fog presents, see Fig. 7.8 (b). This is because P_{opt} is very low and outside the link power margin. The results also show that for moderate and light fog conditions, increasing P_{opt} from -4.2 dBm to -0.7 dBm achieves the required $Q \sim 5$ and a BER of 10^{-6} .



(a)



(b)

Figure 7.8. Q -factor against the transmittance, and (b) the BER versus the transmittance for channel with fog for a range of transmitted optical power.

7.5.1. Measured eye diagrams

The received signal eye diagrams for T of 100%, 50% and 30% are displayed in Fig. 7.9. For $P_{opt} = 1.07$ dBm, the height of the eye decreases from the maximum value of 11.55 mV for $T = 100\%$ to 4.54 mV and 900 V for $T = 50\%$ and 30 %, respectively, thus indicating a considerable effect of fog on the received signal quality. It is also noticed that the histograms of the top and bottom of the eye diagrams, corresponding to bits ‘1’ and ‘0’, respectively, are in Gaussian shape rather the log-normal as is the case with turbulence channel reported in [362].

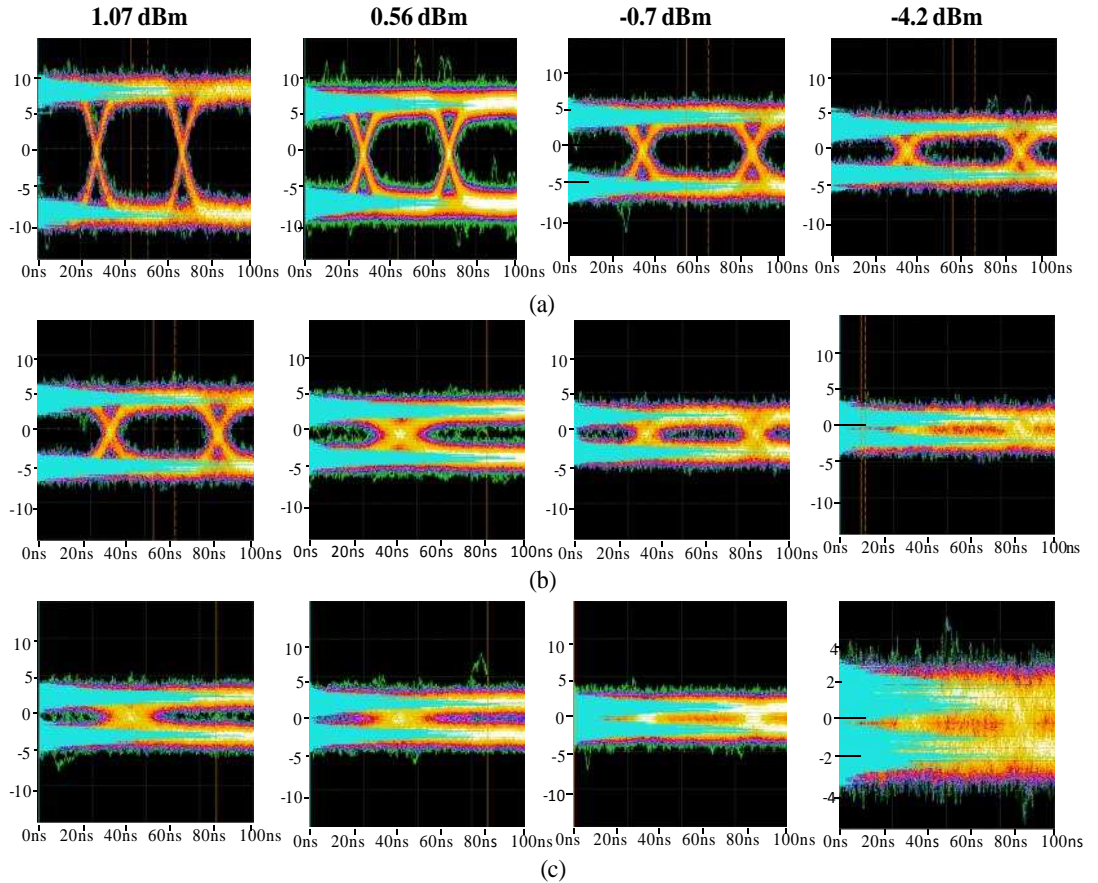


Figure 7.9. The received signal eye diagram (real time) for different P_{opt} , time scale is 20 ns/div, voltage scale is 5mV/div: (a) for 100% transmittance, (b) for 50% transmittance, and (c) for 30% transmittance.

Table 7.3 illustrates the visibility values corresponding to the measured values of T , the Q -factor corresponding to the BER and the eye height for P_{opt} of 0.56 dBm. As the amount of fog particles inside the chamber increases the corresponding visibility decreases, the optical beam is further scattered. This in turn causes the distribution of bits '1' and '0' to be more flat due to the loss in the height (opening) of the eye diagram. The magnitude of the eye height drops from 6.27 mV to 0.022 mV from moderate to thick fog conditions as the visibility also drops from 418 to 70 m.

Table 7.3. Experimental measured values for 0.56 dBm transmitted signal.

Visibility (m)	Q -Factor	Eye Height (mV)	BER
418	7.0	6.27	1.2×10^{-12}
300	6.2	5.15	2.0×10^{-10}
138	5.0	2.96	2.8×10^{-7}
103	3.9	1.51	9.3×10^{-5}
70	2.36	0.022	9.1×10^{-3}

7.6. FSO Link Budget in Fog Channel

Further to compare the results with the outdoor systems, the link budget and its margin will be used as the key criteria parameters [258, 363]. The link margin value M is calculated according to the average available transmit optical power P_{opt} (-1.32 dBm) and the measured sensitivity of the photodetector ($S_{pd} = -32\text{dBm}$ @ 12.5 Mbit/s at a BER of 10^{-6}). The fixed dominant losses related to the geometry of the beam propagation along the FSO chamber, *i-e.*, geometric loss L_g and pointing losses

L_p are measured to be -22.51 dB. L_g is measured as the relationship between transmitted power, 10 mW and the maximum received power, 56 μ W at the photo-detector active area of 1 mm² at R_x after the FSO chamber propagation. The losses due to fog are obtained by the measuring the T as $L_{fog} = 10 \cdot \log(T)$ from light to dense fog conditions. The link margin is therefore calculated as:

$$M = P_{opt} + S_{pd} - L_{fog} - L_g - L_p \quad (7.8)$$

Figure 7.10 depicts the relation between the measured T and the corresponding link margin M for the proposed FSO link for different fog conditions. The visibility zones are also outlined for a range of 1 km link span. For a clear FSO link $M = 6$ dB, which is related to the commercial non-tracking FSO systems for link range of 2 km, as reported in [8]. However, in dense fog condition, the link margin is not sufficient to maintain an error free link.

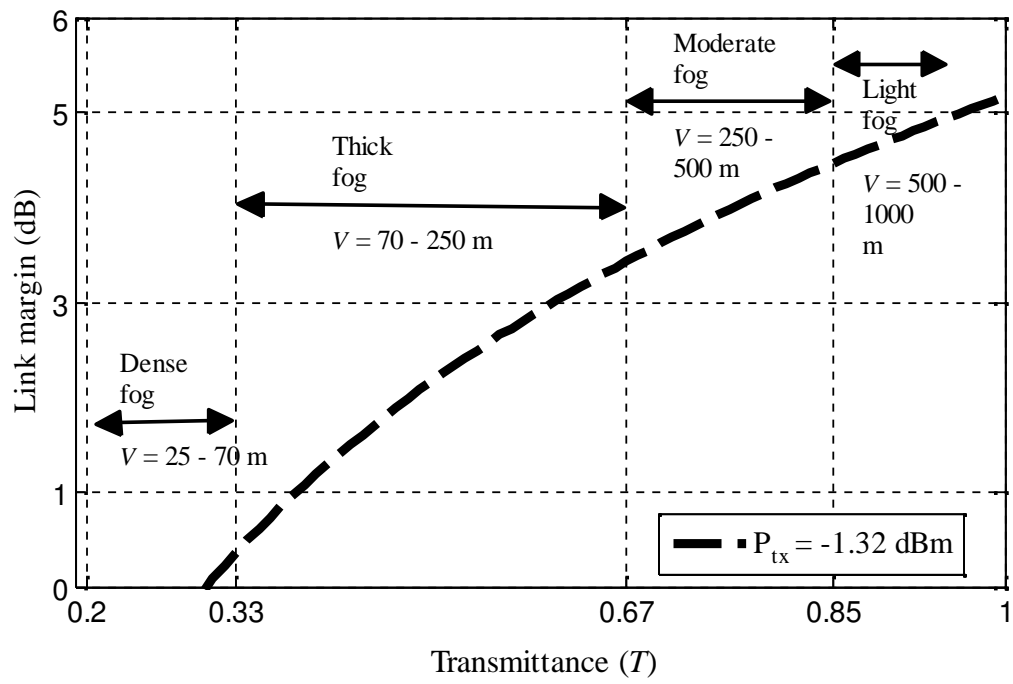


Figure 7.10. Link margin values against transmittance for the FSO communication under lab-controlled fog conditions.

7.7. Summary

This chapter has described the possible methods of mitigation the effects of fog in the lab controlled fog environment by implementing different modulation schemes such as OOK-NRZ, OOK-RZ, 4-PPM, BPSK and 4-PAM and by improving P_{opt} in the case of OOK-NRZ. The results have shown that 4-PPM and BPSK and modulation signalling formats are more robust to fog impairments on the FSO link, in comparison with OOK and 4-PAM. The use of BPSK signalling increases the performance of the FSO link under fog conditions nevertheless it requires a higher receiver complexity and lower normalized gain compared with OOK-NRZ. The results have showed that there would be a trade-off necessary to select different modulation techniques to adapt with the changes of weather effect on the FSO link (*i.e.*, fog).

The results also demonstrated the effect of fog on the FSO link BER performance by observing transmittance values for a range of received optical powers. It is found that the profile or the histogram of the bit distribution is Gaussian even in the dense fog condition. The results also showed that increasing transmit optical power (within the eye safety margin) is one approach to mitigate the effect of the thick and dense fog.

Chapter 8

Performance Analysis of FSO under Controlled Weak Turbulence Condition

8.1. Introduction

Dense fog has a detrimental impact on the FSO link performance, therefore limiting the link range to less a few hundred meters under heavy fog conditions [274]. However, in the case when link length exceeds several hundred meters, irradiance fluctuations (scintillations) of the received optical signal due to the atmospheric turbulence present a severe problem [273]. A number of methods can be used to combat the effect of turbulence such as the multiple input multiple output (MIMO) system [72], the temporal and spatial diversity [74] and aperture averaging [364,

365]. However, selecting a modulation format that is most immune to the scintillation effect is also important and simple approach [75, 366]. OOK-NRZ and OOK-RZ modulation schemes are widely used in commercial FSO communication systems because of their ease of implementation, bandwidth efficiency and cost effectiveness [367]. From the view point of the receivers' sensitivity, RZ offers improved performance over NRZ [368-370]. The RZ signalling format offers improved resistance to the turbulence than the NRZ due to its higher peak voltage albeit the need for higher bandwidth requirement and more susceptibility to the jitter noise as published in [90]. In the turbulent-induced atmosphere, data recovery using a fixed threshold level is not the optimum option when using OOK. Though the adaptive threshold detector can significantly improve the performance in turbulence [371], this is not practically feasible as it requires adaptive optical components as well as continuous monitoring of the atmospheric conditions [372]. Alternatively, modulation techniques like the subcarrier intensity modulation (SIM) and the polarization shift keying (PoLSK) which are more immune to turbulence induced amplitude fluctuation, could be employed [9, 219, 373]. The SIM-BPSK, which does not requires an adaptive threshold, also benefits from a matured RF technology and require a simple and low cost direct detection receiver design compared to the PoLSK [373]. However, SIM-BPSK requires a higher average transmitted power than OOK due to the DC bias requirement and the likelihood of signal distortion and the signal clipping [278]. PoLSK is an external modulation where the state of the polarization (SOP) of the laser beam is controlled by a polarization controller (PC) to transmit binary data. The beam is linearly polarized and has a $\pi/4$ polarization with respect to the principle axe of the external Phase Modulator (PM). PoLSK is highly

sensitive to laser phase noise and also offers 2 - 3 dB lower peak optical power compared to intensity modulation (IM)/ direct detection (DD) [288, 374].

In this chapter, experimental characterisation and investigation of the turbulence effect on the Ethernet and Fast-Ethernet FSO link is reported using different modulation schemes. The experiment is carried out in a controlled laboratory environment where turbulence is generated in a dedicated indoor atmospheric chamber. The chamber is calibrated with the ROA and the measured data are verified with the theoretical prediction. It also demonstrates methods to control the turbulence levels and determine the equivalence between the indoor and outdoor FSO links. The chapter also shows that the connectivity of Ethernet and Fast-Ethernet links are highly sensitive to atmospheric conditions. The effect of turbulence on FSO communication systems for OOK, pulse amplitude modulation (PAM) and SIM-BPSK is experimentally investigated. In comparison to PAM signal; the BPSK and OOK-NRZ modulation signalling formats are more robust against the weak atmospheric turbulence regime. In addition the BPSK system is much less susceptible to the signal amplitude fluctuation due to turbulence compared to the other two modulation formats.

8.2. Experiment Setup for Turbulence Channel

The schematic diagram of experimental line-of-sight FSO link is shown in Fig. 8.1 (a). At the transmitter a narrow divergence beam laser plus a collimated lens are used. The emitted optical beam is intensity modulated by the data source to generate stream of $2^{13}-1$ pseudo random bit sequence, which is either Ethernet (10BASE-T) or

Fast-Ethernet (100BASE-SX). The laboratory atmospheric channel is deployed on a closed glass chamber with a dimension of $550 \times 30 \times 30 \text{ cm}^3$ as described in section (5.2).

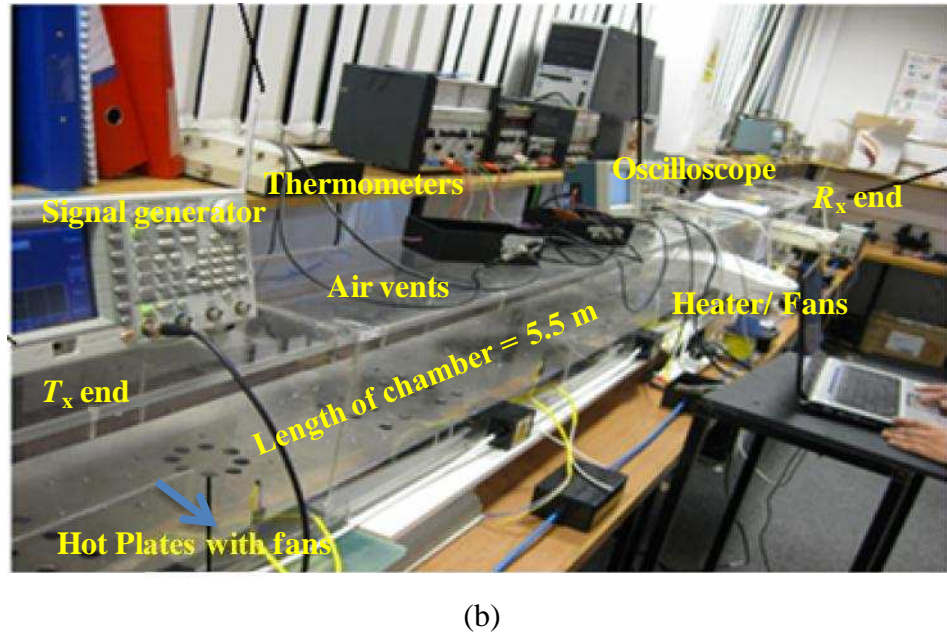
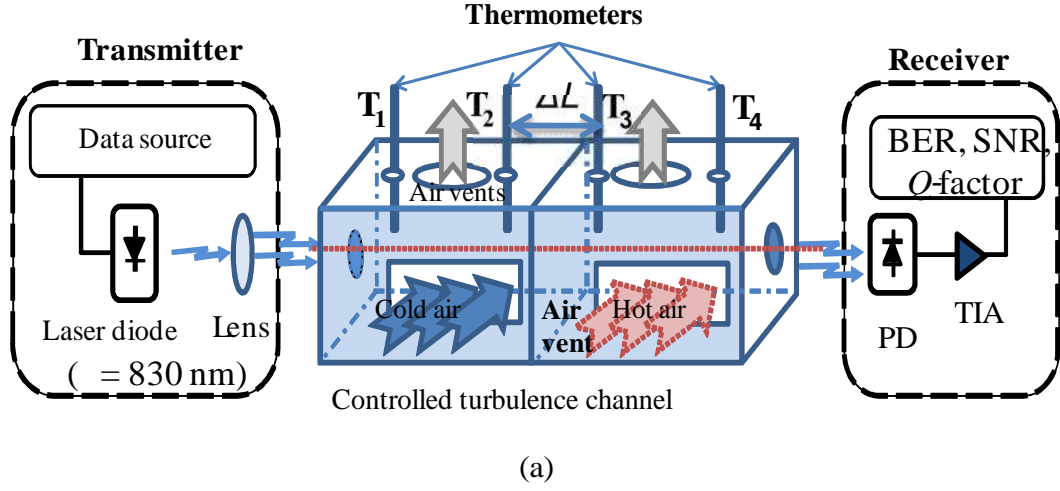


Figure 8.1. (a) Block diagram of experiment setup, and (b) the chamber and FSO link setup in the laboratory.

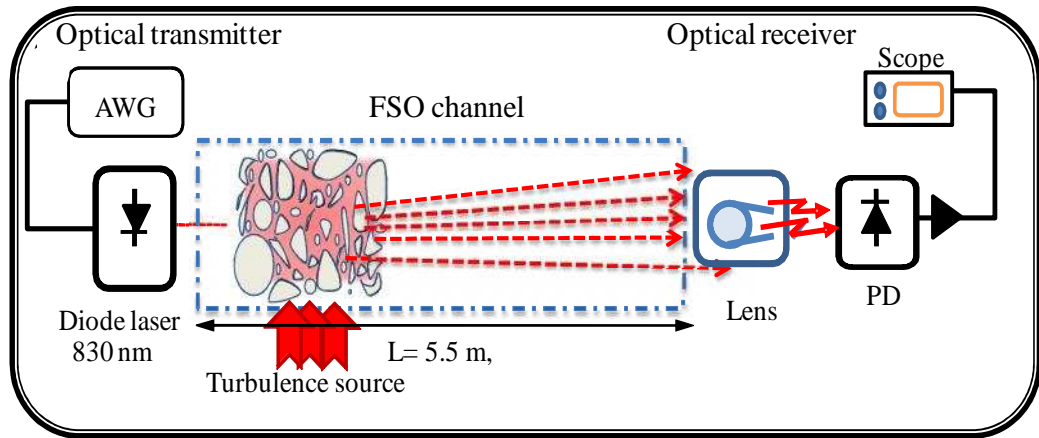
Table 8.1. Parameters of the FSO link under controlled turbulence conditions.

Parameter		Value
Transmitter		
Data source	Ethernet line rate (R_b)	12.5 Mbit/s
	Fast-Ethernet line rate	125 Mbit/s
	Line coder	4B5B
	Modulation voltage V_{p-p}	100-500 mV
Laser diode	Peak wavelength	830 nm
	Maximum optical power	10 mW
	Beam size at aperture	5 mm \times 2 mm
	Beam divergence	5 mrad
	Laser beam propagation model	Plane
	Modulation bandwidth	50 MHz
	Diameter	3.4 cm
	Focal length	20 cm
Channel		
Channel	Dimension	550 \times 30 \times 30 cm ³
	Temperature range	20 - 65 °C
	Temperature gradient $\Delta T/\Delta L$	7 K/m
	Wind speed	<10 m/s
	Link segment ΔR	1.5 m
	Rytov variance	<0.23
Receiver		
Photodetector	Spectral range of sensitivity	750 - 1100 nm
	Active area	1 mm ²
	Half angle field of view	± 75 Deg
	Spectral sensitivity	0.59 A/W at 830 nm
	Rise and fall time	5 ns
Amplifier	Transimpedance amplifier	AD8015
	Bandwidth	240 MHz
	Transimpedance amplifier gain	15 k
	Filter bandwidth	R_b

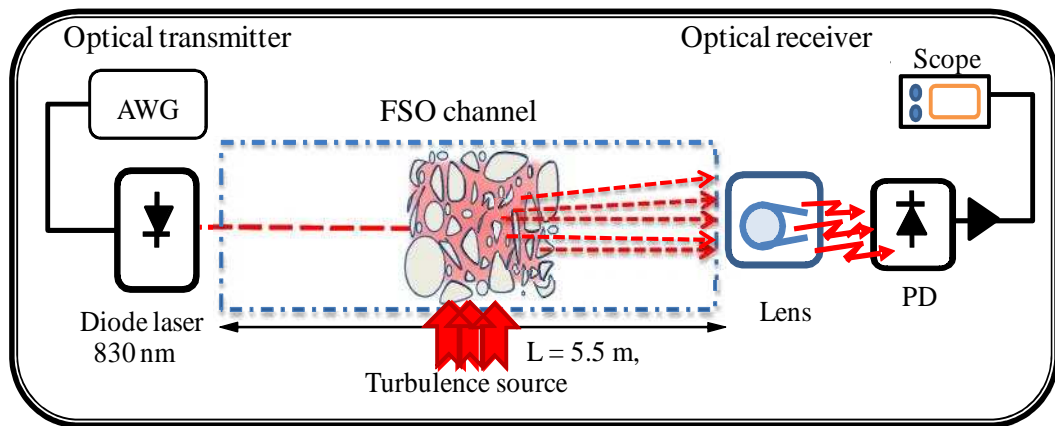
External fans with heater are used to blow hot and cold air in the direction perpendicular to optical beam propagating through the chamber to create variation in the temperature and the wind speed as shown in Fig. 8.1 (b). The cold air is kept at the room temperature (20 - 25 °C) a fan and the hot air temperature is kept in the range of 20 to 65 °C using a heaters. Using a series of air vents along the chamber, additional temperature control is achieved in order to ensure a constant temperature gradient $\Delta T / \Delta L$ between the transmitting and the receiving ends within the chamber.

The receiver front-end consists of a PIN PD followed by trans-impedance amplifier (TIA). The equivalent photocurrent at the output of PD is amplified using a TIA. The output of the TIA is captured using a high-frequency digital oscilloscope where full signal analysis (*i.e.*, the eye-diagram, received signal histograms, the Q -factor, and BER) are carried out. The main parameters for the proposed system are given in Table 8.1.

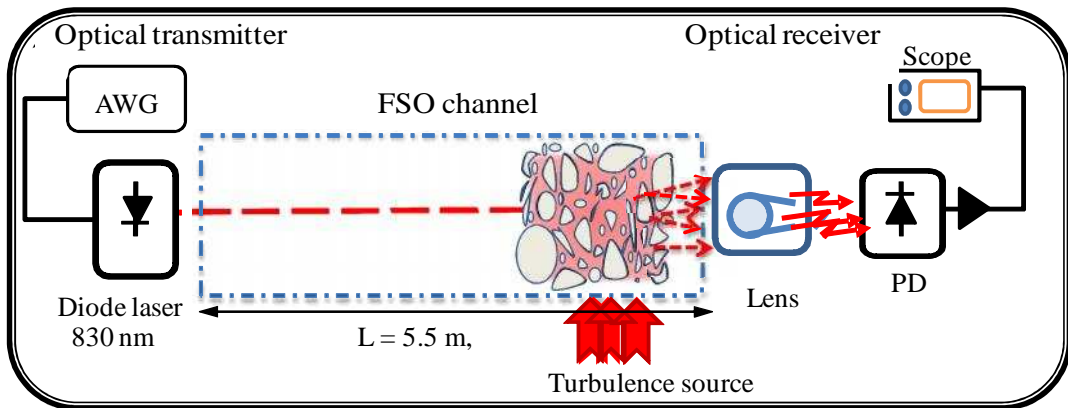
The strength of turbulence can also be controlled by placing the same heating source near and / or away from the FSO transmitter. Ray tracing diagram in Fig. 8.2 illustrates this concept. The optical beams shown in Figs. 8.2 (a), (b) and (c) could approximately experience the same degree of bending due to the same level-controlled turbulence source is used, however due to geometry configuration less power will be collected at the receiver shown in Fig. 8.2 (c) than in Figs. 8.2 (a) and (b).



(a)



(b)



(c)

Figure 8.2. Sketch of diverted beams due to turbulence source positioned: (a) near the transmitter, (b) in the middle and (c) near the receiver.

8.3. Experimental Characterisation of Turbulence

In order to compensate for the short chamber length, $\Delta T/\Delta L \approx 7$ °K/m, the temperature measured at each point along the chamber is maintained within the tolerance margin of ± 1 °K. The average temperatures recorded at four different locations along chamber are given in Table 8.2.

Table 8.2. Measured temperatures over five experiments at four positions within the chamber.

	$T_1(^{\circ}\text{C})$	$T_2(^{\circ}\text{C})$	$T_3(^{\circ}\text{C})$	$T_4(^{\circ}\text{C})$	$C_n^2 (\text{m}^{-2/3})$
Set 1	28	25	23	23	1.40×10^{-12}
Set 2	33	28	24	23	4.61×10^{-12}
Set 3	37	30	24.2	23.4	9.05×10^{-12}
Set 4	45	34	25	24	2.20×10^{-11}
Set 5	54	40	27.3	25	3.97×10^{-11}

Using (4.8) the average values of C_n^2 against a range of temperature gradients within the chamber is plotted as illustrated in Fig. 8.3 and shown in Table 8.2. The average values of C_n^2 varies from 10^{-12} to 10^{-10} which are in good agreement with the experimental data reported in [375].

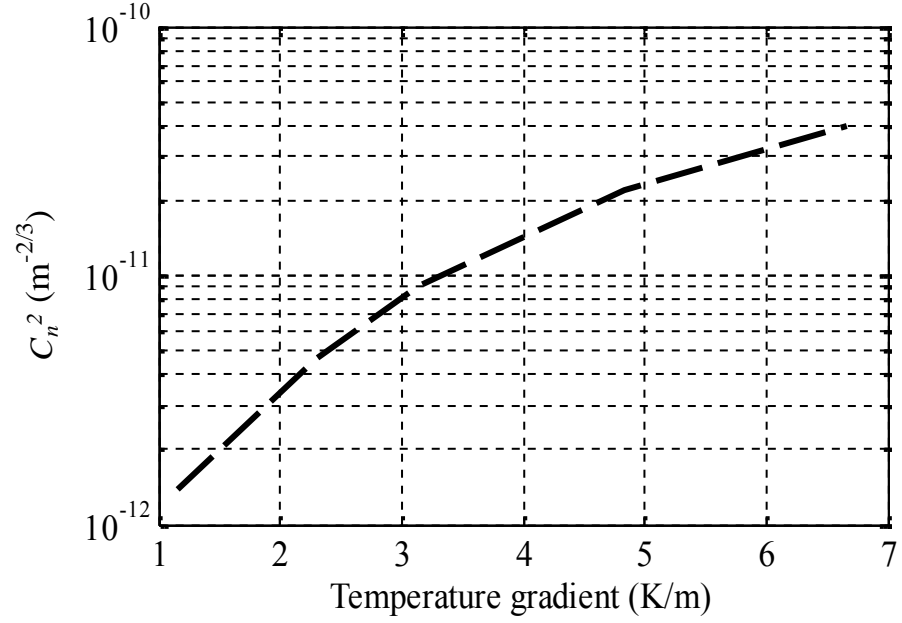


Figure 8.3. The average refractive index structure C_n^2 against the temperature gradient within a controlled atmospheric chamber.

In order to predict the scintillation index, $S.I$ or σ_I^2 in the indoor atmospheric chamber, it is assumed that C_n^2 is constant between two measured temperature points. Here, the values of the temperature are measured at four positions as shown in Fig. 8.1 (a). The scintillation index is predicted using (4.24) in which the values of C_n^2 are evaluated using (4.2) and (4.8). Figure 8.4 depicts both predicted and measured total scintillation index σ_I^2 showing a good agreement, which is used to calibrate the chamber. The measured values are obtained from the received signal using the process given in (4.31). Notice that due to high sensitivity of σ_I^2 on the temperature gradient, exact matching is difficult to obtain. For example, $\pm 1^\circ\text{C}$ change in temperate T_1 can causes ~ 2.5 time difference in predicted scintillation index values.

Since the PD used has a detection area of 1 mm^2 , which is comparable to the transverse coherence distance of $\rho_o \sim 2.8 \text{ mm}$ (calculated using (4.33)), then the aperture averaging factor A should be taken into consideration in the analysis approximated using (4.35) and (4.36) for a plane wave propagation. The factor σ_l^2 given in (4.24) is therefore multiplied by $A = 0.88$, as:

$$\sigma_l^2 = 0.88 \sigma_D^2 . \quad (8.1)$$

In order to accurately predict the log-normal variance, the AWGN variance $\sigma_a^2 = 6.58 \times 10^{-3}$ is subtracted from (8.1) and hence the measured variance is effectively the log-normal variance only.

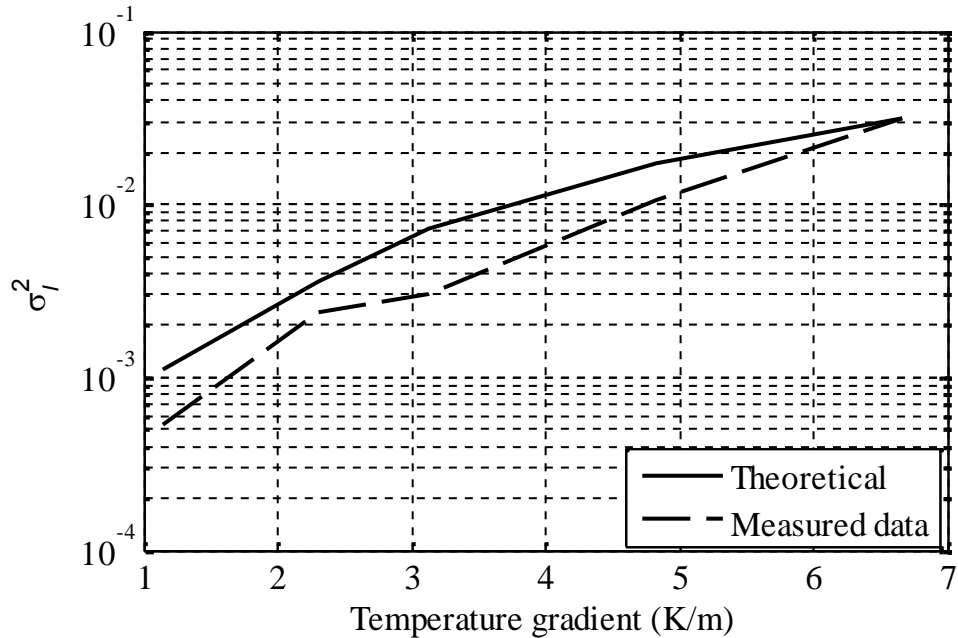


Figure 8.4. The theoretical and measured scintillation index σ_l^2 against the temperature gradient for the controlled atmospheric chamber.

Note that for outdoor terrestrial FSO systems, the refractive index structure parameter C_n^2 is assumed to be constant and (4.24) is normally applied to approximate the log irradiance variance. However, in real systems the temperature gradient $\Delta T/\Delta L$ can vary along the propagation length as the atmospheric conditions greatly changes over time and space. Therefore, the atmospheric link segmentation approach can be used as an alternative method to characterise the FSO link.

8.4. Measured Histograms of Received Signal

In order to reduce the effect of ambient light, experiments were carried out under the total darkness environment. However, it is found that the measured noise variance due the ambient light is $< 3.35 \times 10^{-5}$, which is significantly lower (by up to 7000 times) than the log-normal variance, hence the effect of ambient light can be ignored in the presence of turbulence. Figures 8.5 (a-d) show the received signal histogram for bit '1' sequence of OOK-NRZ without turbulence and with turbulence. Notice that the total number of occurrence is normalized to the unity, which represents the occurrence of pdf. Also illustrated in Fig. 8.5 are the curves fitting plots using Gaussian and lognormal models. With no turbulence the distribution is Gaussian, whereas with turbulence the pdf is best fit to the log-normal distribution as shown in Figs. 8.5 (b-d).

Table 8.3. Measured σ_I^2 along the chamber length.

Turbulence position	Near receiver	Middle of the chamber	Near transmitter
Scintillation index σ_I^2	0.009	0.067	0.240

One advantage of an indoor chamber is that the scintillation index can be readily varied by changing the position of the turbulence source, see Fig. 8.2. The measured maximum σ_I^2 values for the turbulence source located at different positions along the chamber are given in Table 8.3. As expected, σ_I^2 is the highest when the turbulence source is closer to the transmitting end as shown in Fig. 8.2 (a). The measured values of σ_I^2 given in Table 8.3, fall within the range of [0, 1], therefore the turbulence is classified as weak. This verifies that log-normal model using (4.27) is the best to model the weak turbulence as it best fits to experimental data as shown in Figs.8.5 (b-d).

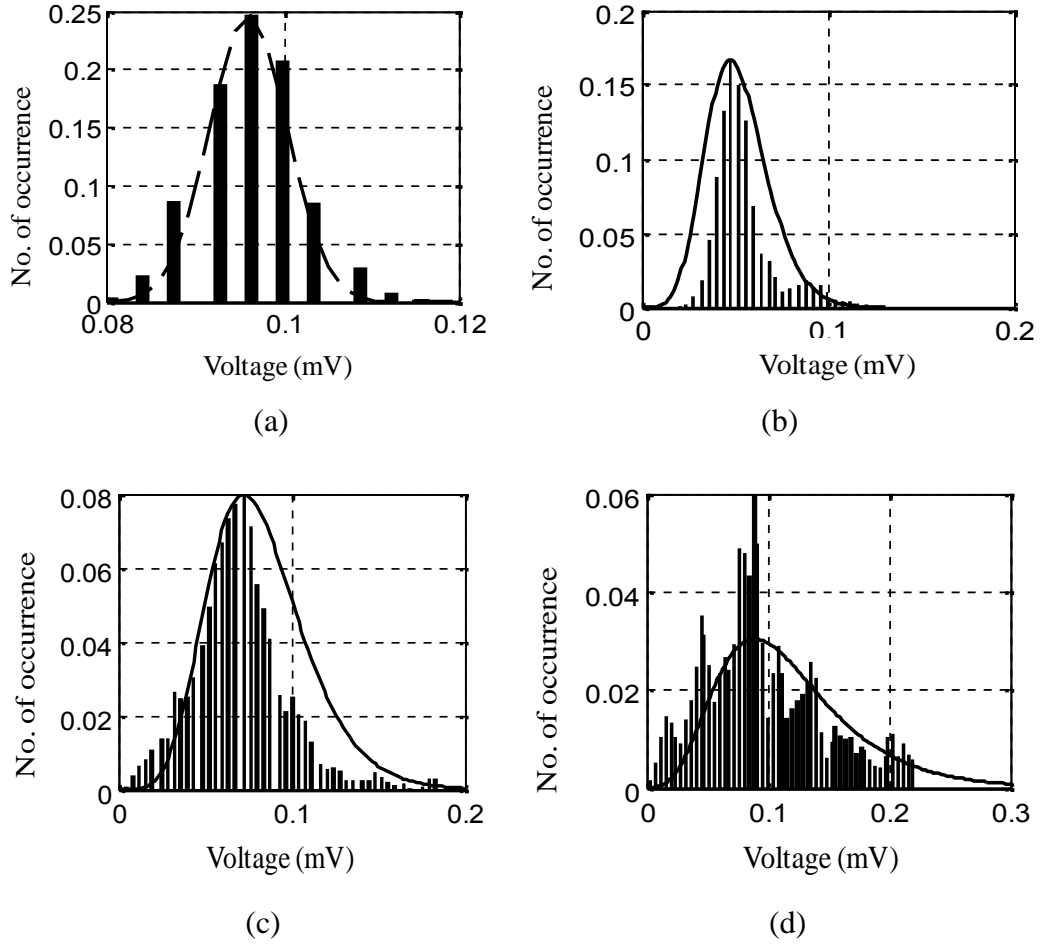


Figure 8.5. Received signal distribution: (a) without turbulence, (b) with turbulence $\sigma_l^2 = 0.009$, (c) $\sigma_l^2 = 0.06$, and (d) $\sigma_l^2 = 0.240$ (the curve fitting is shown by solid lines).

8.5. Performance Analysis Measurements for FSO

In this section, the FSO Ethernet and Fast-Ethernet links availability and the quality under different turbulence conditions are evaluated. The measured eye-diagrams for received Ethernet (10BASE-T) signal using OOK-NRZ are depicted in Fig. 8.6 (a) with no turbulence and (b) as the signal experienced the weak turbulence. Note that the eye height is 0.04 V without turbulence, while it is 0.03 V in the presence of

turbulence which results in considerable level of signal intensity fluctuation. This is due to the turbulence noise which increases the width at the top (bit 1) and the base (bit 0) of the eye-diagram, thus reducing the eye height.

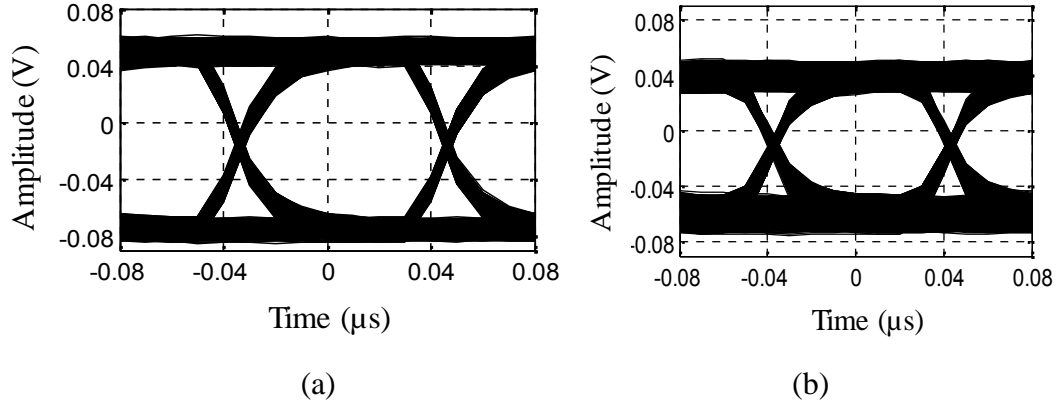


Figure 8.6. The measured eye-diagrams of received Ethernet signal (NRZ 4B5B, line rate 12.5Mbit/s), (a) no turbulence and (b) weak turbulence with $\sigma_I^2 = 0.0164$.

Under the same turbulence condition, the Fast- Ethernet (100BASE-SX) signal at 125 Mbit/s) using OOK-NRZ is transmitted through the FSO channel and obtained the eye-diagram at the receiving end, see Fig. 8.7. The eye opening in this case is very close to the one obtained for the Ethernet (10BASE-T) link as the data rate is not sensitive to the turbulence (see Fig. 8.6). However due to the laser bandwidth limitations the eye-diagrams are already distorted as shown in Fig. 8.7 (a).

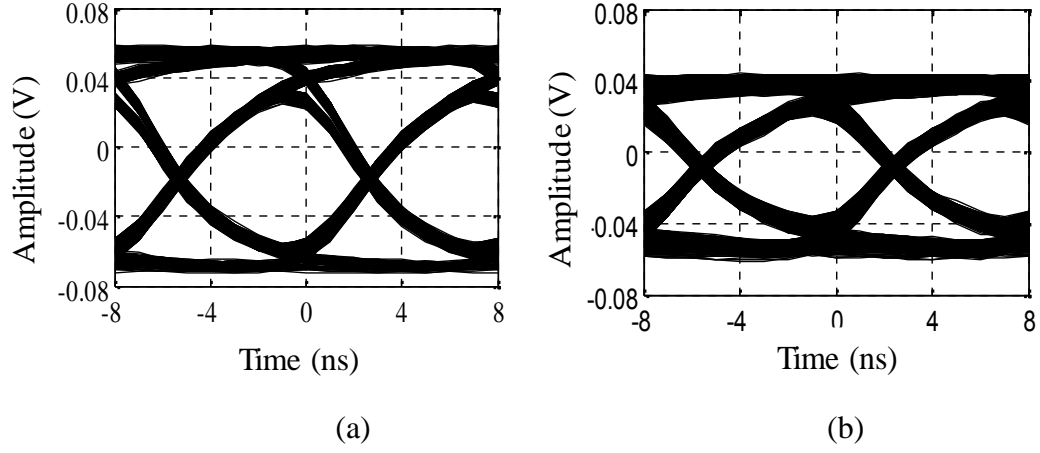


Figure 8.7. The measured eye-diagram of received Fast-Ethernet signal, NRZ 4B5B, line rate 125Mbit/s) in the condition of: (a) no turbulence, and (b) weak turbulence with the scintillation index $\sigma_I^2 = 0.0164$.

Q -factor measurement has been extensively used in order to characterise the quality of optical communication system especially in fibre optics as reported in [376-378]. Therefore, in order to quantify the FSO link performance, the Q -factor is measured from the received signal both before and after the turbulence using:

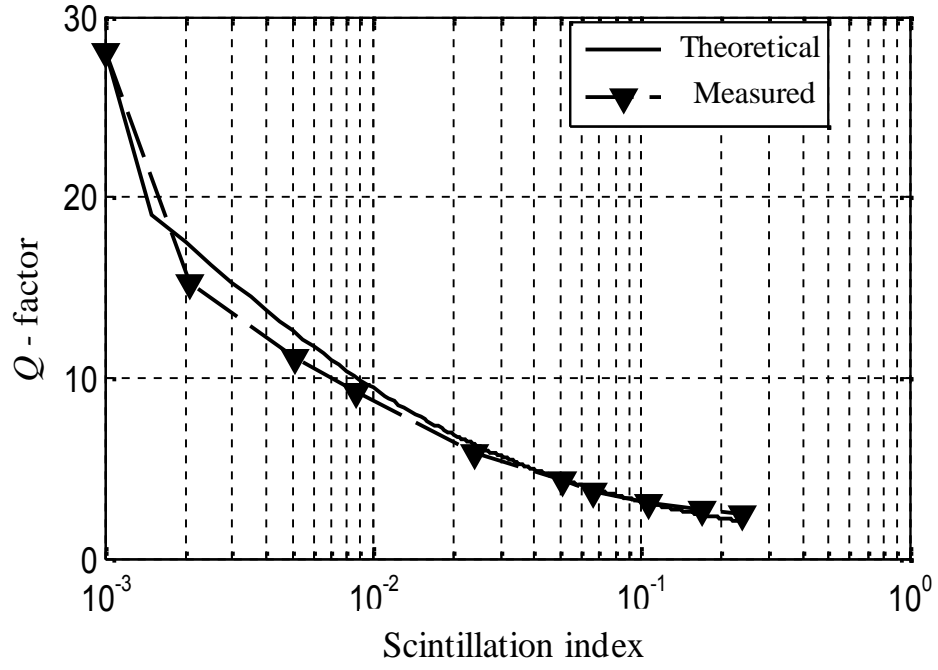
$$Q = \frac{v_H - v_L}{\sigma_H - \sigma_L}, \quad (8.2)$$

where v_H and v_L are the mean received voltages and σ_H and σ_L are the standard deviations for the 'high' and 'low' level signals, respectively. The measured Q -factor against a range of $S.I$ values is shown in Fig. 8.8 for both Ethernet transmission types using OOK-NRZ.

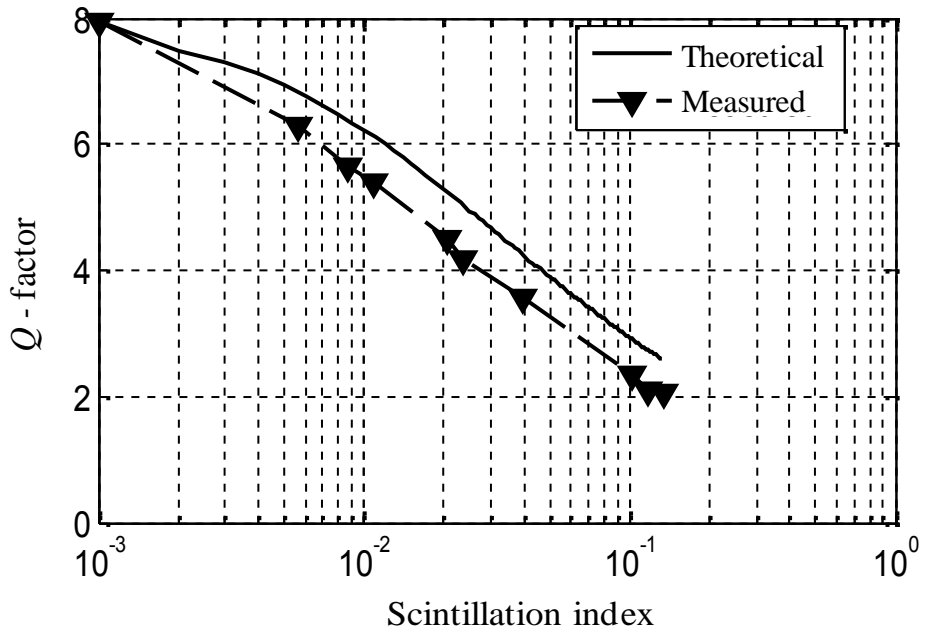
The corresponding predicted Q -factor values using (4.37) are also compared with the measured Q -factor. For the clarity of the figure, the x -axis is in the logarithmic scale.

Therefore, the initial value of scintillation index σ_I^2 is selected to be 10^{-3} rather than zero for obtaining Q -factor before the turbulence, Q_0 . Figure 8.8 presents a good

match between the predicted and experimental data for OOK-NRZ modulation formats. Since the difference between the predicted and measured Q -factor values is found to be less than 0.5. The Q -factor decreases exponentially with the increase of scintillation index values in both Ethernet and Fast-Ethernet communications links. In fact, the drop in the Q -factor does not depend on the data rates but it depends on Q_0 and values of the scintillation index. Although Q_0 values are about 28 and 8 for Ethernet and Fast-Ethernet links, respectively. This is because the data transmission for Fast-Ethernet communications at a rate of 125 Mbit/s (about the maximum rate of the FSO system) suffers less Q penalty due to the turbulence-free received signal being already distorted as a result of limited bandwidth of the laser transmitter. For the Ethernet a data rate of 12.5 Mbit/s is well within the optoelectronic bandwidth of the given FSO link (see a clear eye diagram in Fig. 8.6 (a)), therefore one can clearly observe the penalty induced by the turbulence. When no turbulence within the channel, ($\sigma_I^2 = 0.05$), Q_0 is up to 28, see Fig. 8.8 (a). However its value dropped considerably to ~ 5 when weak-medium turbulence ($\sigma_I^2 = 0.2$) is introduced. Infact, the measured Q -factors for both Ethernet and Fast-Ethernet show that they are almost identical for $\sigma_I^2 > 0.1$. This indicates that the increment in transmit optical power will have a little effect to mitigate the increased turbulence level. A number of techniques have been proposed in literature to deal with the turbulence including the aperture averaging, the spatial diversity, and the cooperative diversity [326, 327, 379].



(a)



(b)

Figure 8.8. The predicted and measured Q -factor against different scintillation index values for (a) Ethernet and (b) Fast-Ethernet.

The evaluation of BER using (4.38) for both Ethernet/Fast-Ethernet FSO links using

OOK-NRZ in different turbulence conditions is depicted in Fig. 8.9. Note that BER values below 10^{-6} are truncated. The result shows that the Ethernet and Fast-Ethernet links are highly sensitive to the turbulence strength. The availability of the FSO link to maintain a BER of 10^{-6} is possible at $\sigma_I^2 = 0.04$ for Ethernet and $\sigma_I^2 = 0.03$ for Fast-Ethernet FSO links in the weak turbulence case. However, the performance of the both links deteriorates drastically as the strength of the turbulence increases to $\sigma_I^2 = 0.05$ and the BER increases to 10^{-3} in weak turbulence of $\sigma_I^2 = 0.1$. Unlike the broadcasting schemes where the turbulence level does not have any effect on the transmitting state (on/off) of the source, it is observed that for Ethernet links the link availability becomes a problem under the weak turbulence regime, *i.e.*, connection is dropped. Therefore, different modulation schemes such as OOK-NRZ, 4-PAM and BPSK, are considered in order to evaluate their performance under turbulence channel in next section.

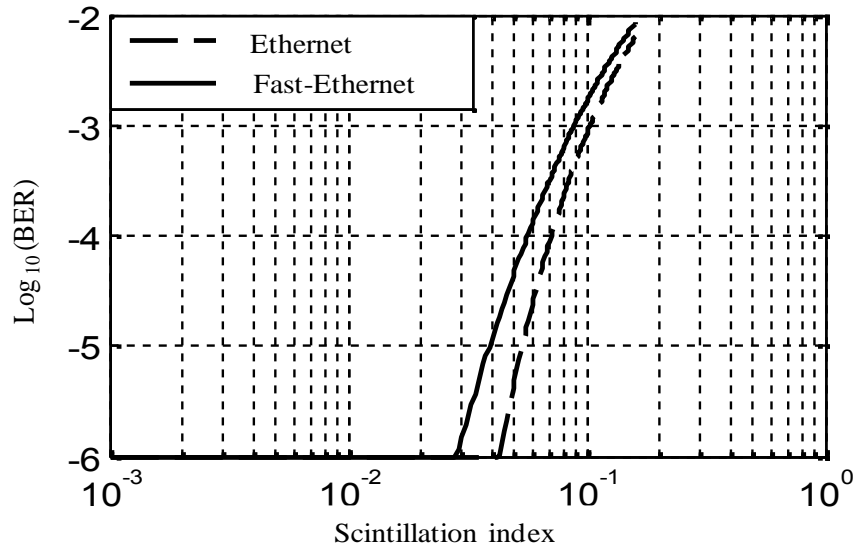


Figure 8.9. BER performance against a range of scintillation indexes for Ethernet and Fast-Ethernet FSO links (note that BER values below 10^{-6} are truncated).

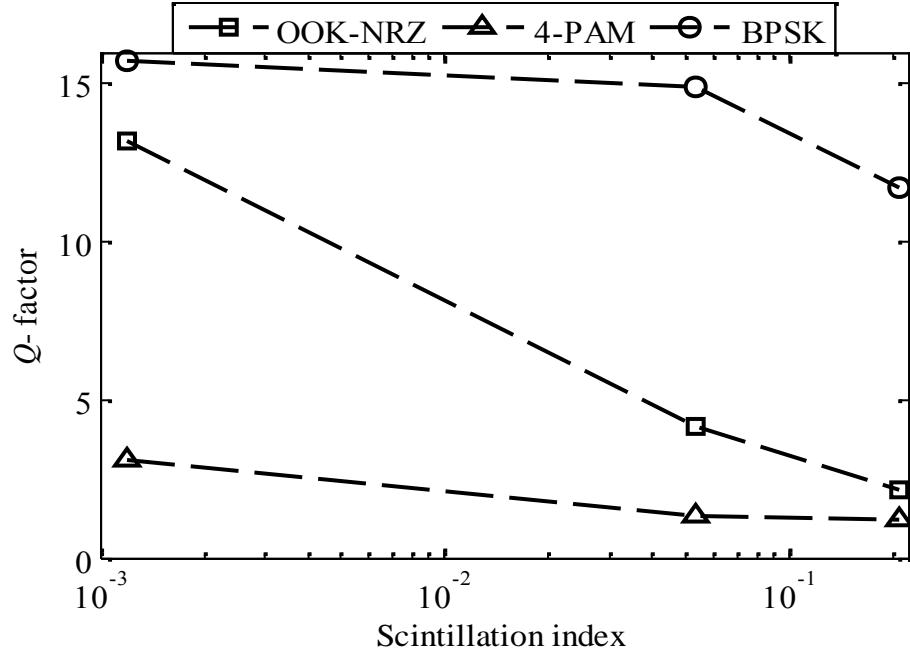
8.6. Performance of Different Modulation

Techniques under Controlled FSO Turbulence

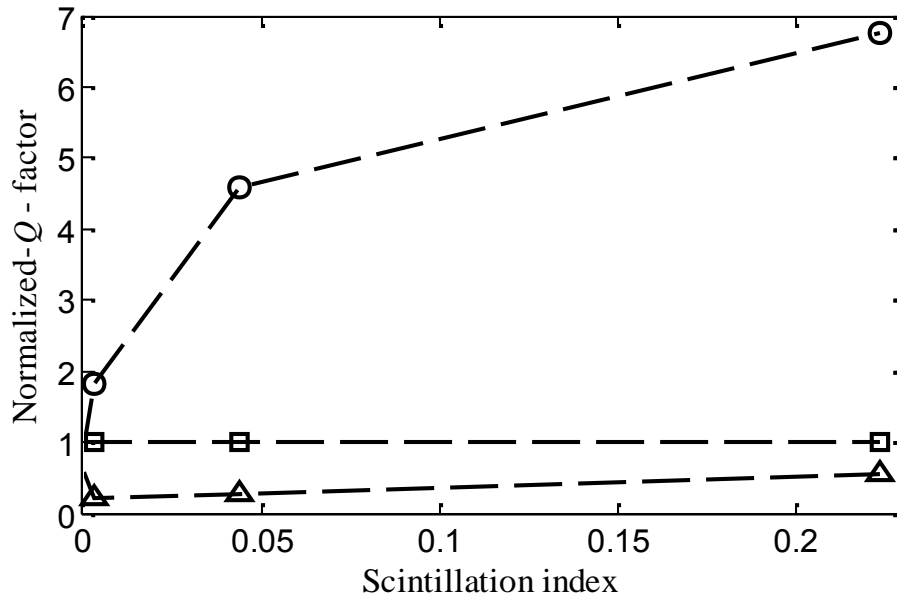
Channel

Experimental data for different modulation schemes has been recorded under a controlled weak turbulence environment and are analysed using the Q -factor and received signal distributions before and after the turbulence. The Q -factor is measured using the (8.3). The measured Q -factor against the SI for the OOK-NRZ, 4-PAM and BPSK at the same average P_{opt} level of -1.32 dBm corresponding to signal voltage, V_{p-p} of 100 mV is shown in Fig. 8.10 (a). The data rate is selected to 5 Mbps for all modulation schemes. The results showed that the Q -factor decreases linearly with the increase in the turbulence level for both OOK-NRZ and 4-PAM modulation due to random fluctuation of received signal. This can be described by observing the impact of turbulence on the fixed threshold level, which is marked as a zero level (see Figs. 8.11 (a) and (c)). The received signal distribution for bits '1' and '0' are equally spaced and comparable for both sides of the zero mark and the bits '1' and '0' are clearly distinguishable before the turbulence (see Fig. 8.11 (a)) . However, with turbulence the received signal distribution becomes heavily distorted and are no longer distinguishable (see Figs. 8.11 (b) and (d)), thus resulting in decreased Q -factor. Notice that the Q -factor linearly decreases with the logarithmic scale of the Rytov variance. However, the Q -factor for BPSK decreases less sharply and offer much improved performance compared to OOK and PAM. This is because the received signal distribution in BPSK for bits '1' and '0' remains equally spaced

with no overlap between them for the case with or without turbulence as reported in [380].



(a)



(b)

Figure 8.10. Measured Q values against a range of Rytov variance for OOK, 4-PAM and BPSK: (a) the absolute scale at 5 Mbit/s, and (b) normalized to the Q -factor of OOK-NRZ.

The average Q -factor normalized to the average Q -factor of the OOK-NRZ against the S/I for a given Rytov variance value is illustrated in Fig. 8.10 (b). The normalized Q -factor for the OOK and PAM do not vary significantly for the range of Rytov variance. This is due to the adverse effect of the turbulence on the intensity of the received signal for OOK and PAM. Note that, the information is encoded in the intensity of the optical signal in IM/DD OOK and PAM. However, the Q -factor of the BPSK diverges from the Q -factor of OOK as the level of turbulence increases and the BPSK offer ~ 6.5 times higher Q -factor than that of OOK and ~ 16 times higher than that of 4-PAM and published in [187]. Unlike OOK and PAM, the information is hidden in the phase of the carrier in BPSK and since the effect of the turbulence is trivial compared to the IM/DD than the phase of carrier. Hence, BPSK is less sensitive to the turbulence which has been experimentally investigated by studying the eye-diagrams and received signal histograms and published in [193].

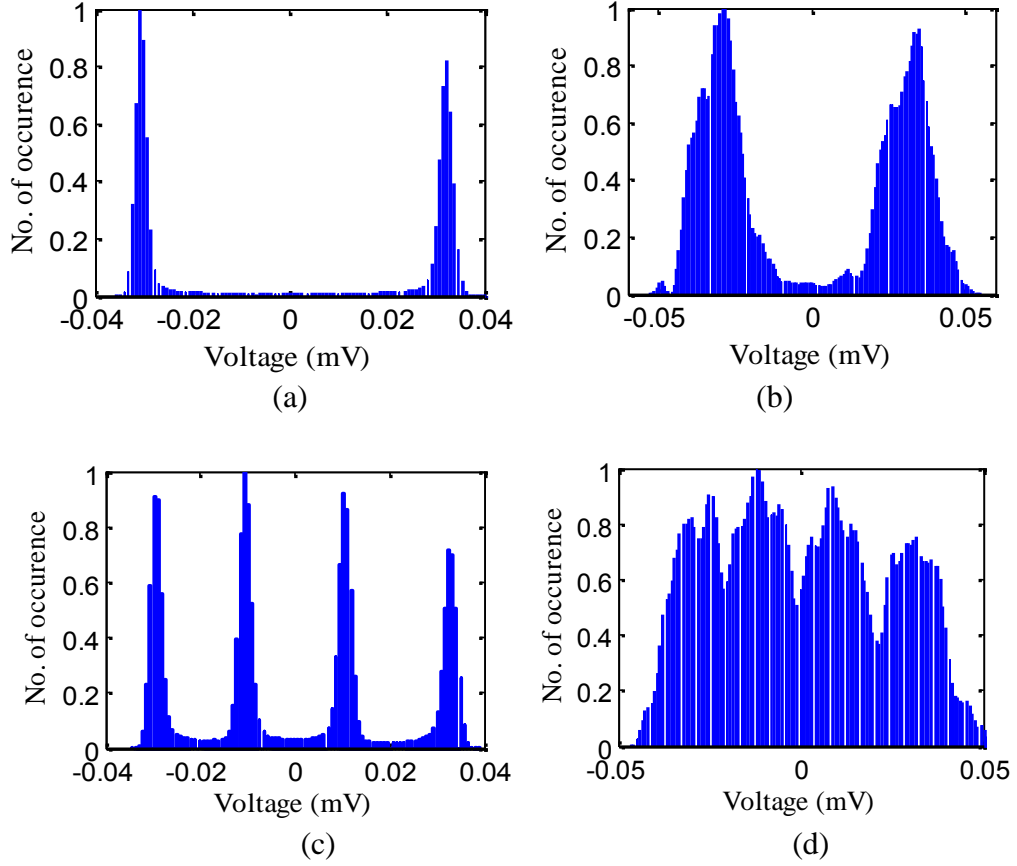


Figure 8.11. Histograms for the OOK: (a) without turbulence, (b) Rytov variance of 0.005, (c) 4-PAM, without turbulence, and (d) Rytov variance of 0.005 received signals at 20 Mbit/s

8.7. Calibration to the Outdoor FSO Link

In equation (4.24), the scintillation index σ_I^2 is dependent on the value of C_n^2 and the temperature gradient. Assuming a constant C_n^2 over a short propagation span of ΔL_{indoor} and $\Delta L_{outdoor}$ for indoor lab and outdoor FSO links, respectively the relation $R_{in/out}$ between indoor experimental and outdoor links can be derived as:

$$R_{in/out} = \frac{\sigma_{Im outdoor}^2}{\sigma_{Im indoor}^2} = \frac{C_{n outdoor}^2}{C_{n indoor}^2} \times \left(\frac{\Delta L_{outdoor}}{\Delta L_{indoor}} \right)^{11/6}, \quad (8.3)$$

where $\sigma_{lm\ outdoor}^2$ and $\sigma_{lm\ outdoor}^2$ are the mean scintillation index for indoor and outdoor turbulence mediums, respectively. Note that, the FSO link segmentation in both indoor and outdoor environments is used to keep the temperature gradient constant.

For the outdoor link, $C_{n\ outdoor}^2$ is much smaller than the indoor link. The typical range for $C_{n\ outdoor}^2$ is 10^{-16} to 10^{-14} for the weak turbulence [283]. For the outdoor FSO system operating at the sea level (minimum turbulence level) the typical $C_{n\ outdoor}^2$ is about 10^{-16} [381], whereas our measured $C_{n\ indoor}^2$ is 4×10^{-11} (see Fig. 8.3). Hence, to calibrate the FSO link performance in order to make the same as the outdoor link, $R_{in/out}$ should be unity. Following (8.2) and using $C_{n\ indoor}^2 \sim 5 \times 10^{-12}$ and $C_{n\ outdoor}^2 \sim 1 \times 10^{-16}$, it is therefore determined that the overall outdoor FSO link range is 548 m, which induces the same weak turbulence effect as our proposed system. However, by generating higher temperature gradient more than 7°K/m in the indoor experimental FSO link we can achieve the same performance as the longer outdoor FSO link.

8.8. Summary

The chapter demonstrated the Ethernet and Fast-Ethernet FSO links operation under turbulence conditions using the controlled indoor atmospheric chamber. Atmospheric turbulence is characterised and calibrated using the atmospheric chamber and verified the models theoretically and experimentally. Methods to generate turbulence and control its level were discussed and practically implemented. The obtained results showed that turbulence can severely affect the link availability of the Ethernet and Fast-Ethernet FSO systems due to the sharp response in BER performance of the link and the nature of Ethernet (TCP/IP) connectivity. The turbulence effect was also dependent on the data format being adopted to directly modulate the laser source. The BPSK signalling format has offered an improved resistance to the turbulence than the NRZ and 4-PAM. BPSK offered ~ 6.5 times higher Q -factor than that of OOK and ~ 16 times higher than that of 4-PAM. This chapter also pointed out the relation between the experimental environment and the outdoor FSO link in order to ensure total reciprocity. The analysis and demonstration presented in this chapter have shown a step forward to characterise the atmospheric channel in an indoor environment, which is by nature complex and unpredictable.

Chapter 9

Conclusions and Future Work

9.1. Conclusions

In recent years, the demand for a back-up and complementary link to the radio frequency technology particularly for the “last mile” in access network based on the FSO system has increased considerably. This is due to a number of advantageous features including a large un-regulated and license free transmission bandwidth spectrum, a large data transmission, consumes low power, security as well as immunity to the electromagnetic interference. However, the constraints imposed by the atmospheric channel such as fog, smoke and turbulence decrease the system performance and availability of the link. The characterisation and modelling of the FSO channel are important and need to be investigated to enhance the robustness of FSO link.

This thesis commenced from the brief overview on the FSO communications in Chapter 2. Applications and features of FSO technology that make it more viable

compared with the existing RF technologies and its potential areas of application were explained. The basic concept of FSO communication using block diagrams and its functions have been detailed. Also, the main challenges and different effects such as absorption, scattering and atmospheric turbulence posed by the atmospheric channel on the transmitted optical beam have been introduced. Chapter 2 also discussed the theoretical background on selected modulation schemes in terms of power efficiency and bandwidth requirements with the aim to confront the different atmospheric conditions and ending by eye and skin safety and classifications of lasers.

Different types and composition of fog and smoke were detailed in Chapter 3. Theoretical and empirical approaches to model and characterise the attenuation of optical signal for visible and NIR wavelengths ($0.6 \text{ } \mu\text{m} < \lambda < 1.6 \text{ } \mu\text{m}$) from dense to light fog conditions were illustrated. A number of selected empirical fog models were considered and compared, Kim and Naboulsi convection were found to be the best models to use in estimating the attenuation of the optical signal in fog for the wavelength range of $0.5 \text{ } \mu\text{m}$ to $0.9 \text{ } \mu\text{m}$ when $V = 1 \text{ km}$. However, both of these models contradicted each other when estimating the fog attenuation for $V = 1 \text{ km}$. Therefore, these models were required to be explicitly verified in practice for the entire spectrum in the visible – NIR range from dense to light fog conditions.

Kolomogorov theory of turbulence based on classical studies of velocity, temperature and refractive index fluctuations has been introduced in order to understand the atmospheric turbulence in Chapter 4. The refraction structure parameter C_n^2 and $S.I$ parameters were explained in order to measure the strength of turbulence. Methods to characterise the atmospheric turbulence have been presented

based on statistical models such as log normal, Gamma-Gamma and negative exponential model with its limitations. Aperture averaging and BER evaluation in the presence of atmospheric turbulence were described in order to evaluate the BER performance in turbulence channel.

Chapter 5 has outlined the design of indoor atmospheric chamber and methods to control and simulate atmospheric conditions such as fog, smoke and turbulence as necessary to mimic the ROA as close as possible. The obtained simulation results also showed that by increasing the number of reflection within the chamber reduce the small changes in the visibility. This would consequently increase the homogeneity in the fog channels to characterise fog attenuation with enhanced accuracy. The atmospheric chamber is used to carry out the outdoor FSO system characterisation and to perform the measurement under a homogeneous fog and smoke conditions. Different approaches to generate and control turbulence inside the atmospheric chamber were also presented.

The experimental results of fog attenuation in FSO for visible to NIR wavelengths ($0.6 \text{ } \mu\text{m} < \lambda < 1.6 \text{ } \mu\text{m}$) from dense to light fog conditions were also presented in Chapter 5. The obtained experimental results were compared with the selected empirical fog models in order to validate their performances practically. The experimental results showed that the fog attenuation is wavelength dependent for all the V ranges except when $V < 0.015 \text{ km}$ contradicting the Kim model. The resultant fog attenuation decreases linearly from the visible – NIR as predicted by Kim model for $V > 0.5 \text{ km}$, however, contradicted the Naboulsi model except for selected

wavelengths. The Grabner model did not fit the experimental data as the V increasing to > 0.5 km. The experimental data has also validated that Kim model is more realistic to use when $V > 0.5$ km. This model did not take into account the wavelength for $V < 0.5$ km. However, the experimental data and selected empirical models have showed that the spectral attenuation is wavelength dependent for $V < 0.5$ km, therefore validating that the Kim model is needed to be revised for $V < 0.5$ km in order to predict the wavelength dependent fog attenuation.

Two different methods to characterise the fog attenuation in terms of the atmospheric V using a CCD camera and a visible laser-diode at $0.55 \mu\text{m}$ has been analysed and compared in Chapter 6. CCD technique has showed a great accuracy for $V < 50$ m and the laser technique for the range beyond 100 m, thus allowing enhancement of the characterisation of FSO links in thick and dense fog conditions. Moreover, a wavelength dependent model for fog and smoke channels has been proposed, which was valid for the visible – NIR range for the V range of 1 km. The experimental results also showed the most robust wavelengths windows (0.83 , 0.94 and $1.55 \mu\text{m}$) that could be adopted for fog conditions in order to minimize the FSO link failure. Furthermore, to validate the behavior of the proposed empirical model for selected wavelengths, the proposed model has been compared with the continuous attenuation spectrum for the same fog and smoke conditions. It is found that the attenuation is almost linearly decreasing for both cases. This has verified that the proposed model followed the profile of measured fog attenuation more precisely than both Kim and Kruse models for $V < 0.5$ km. The experimental result has also demonstrated the dependency of the wavelength on the resultant smoke attenuation even if V is below

0.5 km. The difference for the smoke attenuation values was 108 dB/ km, 23 dB/km and 8 dB/ km for 0.83 m and 1.55 m at V of 0.07 km, 0.25 km and 0.5 km, respectively.

Chapter 7 described the possible methods of mitigating the effects of fog in the lab controlled fog environment by implementing different modulation schemes such as OOK-NRZ, OOK-RZ, 4-PPM, BPSK and 4-PAM and by improving the transmit optical communication power P_{opt} in the case of OOK-NRZ. The theoretical and experimental results have showed that 4-PPM and BPSK modulation signalling formats were more robust to fog impairments in comparison with OOK and 4-PAM in FSO link. The link availability at dense fog ($T = 0.33$) condition by maintaining a BER of 10^{-6} (Q -factor > 4.7) was achieved using 4-PPM than OOK-NRZ and OOK-RZ modulation schemes. The effect of fog on OOK-NRZ, 4-PAM and SIM- BPSK was also investigated experimentally. In comparison to 4-PAM signal, the BPSK and OOK-NRZ modulation signalling format were more robust against the fog effects. The comparison shows that in dense fog conditions, 4-PAM scheme does not achieve BER values lower than 10^{-6} , on the other hand OOK-NRZ and BPSK schemes overcome that values for $T > 0.33$ nevertheless it requires a higher receiver complexity. The results also demonstrated the effect of fog on the FSO link BER performance for OOK-NRZ by observing transmittance values for a range of P_{opt} values. The results showed that increasing transmit optical power P_{opt} (within the eye safety margin) is one approach to mitigate the effect of the thick and dense fog. It is also found that the profile or the histogram of the bit distribution is Gaussian even in the dense fog condition which is different from the turbulence effect.

Chapter 8 has demonstrated the Ethernet and Fast-Ethernet FSO links operation under turbulence conditions using the controlled indoor atmospheric chamber. Atmospheric turbulence was characterised and calibrated using the atmospheric chamber and verified the models theoretically and experimentally. Methods to generate turbulence and control its level were discussed and practically implemented. The obtained results showed that turbulence can severely affect the link availability of the Ethernet and Fast-Ethernet FSO systems due to the sharp response in BER performance of the link and the nature of Ethernet (TCP/IP) connectivity. The turbulence effect was also dependent on the data format being adopted to directly modulate the laser source. The BPSK signalling format has offered improved resistance to the turbulence than the NRZ and 4-PAM. BPSK has offered ~ 6.5 times higher Q -factor than that of OOK and ~ 16 times higher than that of 4-PAM. This chapter has also pointed out the relation between the experimental environment and the outdoor FSO link in order to ensure total reciprocity. The analysis and demonstration presented in this chapter have shown a step forward to characterise the atmospheric channel in an indoor environment, which is naturally complex and unpredictable.

9.2. Future Work

This research work has completed the objective and aims listed in Chapter One. However, the amount of time and work required to theorise and cover the comprehensive channel characterization and measurements are out of the scope of this work. The following topics are suggested to further extend the research work reported in this thesis.

Channel modelling enhancement: It is worth mentioning that Kim and Kruse models were developed for fog conditions. However, they have never been experimentally tested for all visible – NIR range of wavelengths under all fog conditions *i.e.* from very dense to the light fog. The spectrum attenuation suggests a linear relationship for fog attenuation as verified by using individual wavelengths in fog. However, there is a peak located around 1.33 μm in fog attenuation; under smoke condition for dry particles, no such peak appears. This peak is due to strong water absorption of NIR wavelength at 1.33 μm . Note that, most of the peaks has disappeared when V is increasing *e.g.*, at $V = 0.3$ km. However, at 1.33 μm , it is observed a steady small peak. In modelling of fog attenuation, linear data regression is used. However, the work described in this thesis is beyond the scope of any complex and nonlinear regression. Therefore, the purposed model is definitely better than the other models in predicting the smoke attenuation but not in predicting the fog attenuation. In future work, it is recommended to further investigate this topic, in order to provide a more comprehensive model, which accounts for the presence of these peaks in the estimation of fog attenuation.

Strong turbulence: The performance of the FSO has been theoretically and experimentally investigated for the weak turbulence condition in this thesis. As mentioned in Chapter 4, the strength of the turbulence is dependent on the length of the FSO link. Turbulence strength increases with the increase of link length. However, due to the length of the indoor atmospheric chamber is 5.5 m, the weak turbulence was created. In future work, the length of the link should be increased by using multiple reflections in order to increase the strength of the turbulence. Note that, the strength of turbulence also depends on the temperature gradients along the FSO link. This will help to verify Gamma-Gamma and negative exponential models and to investigate the BER performance of FSO under strong turbulence conditions.

Spatial Diversity: Due to the strong turbulence, the FSO signal suffers fading due to multipath propagation, which can be mitigated by spatial diversity techniques such as MIMO antennas can be equipped on the transmitter and/or receiver sides in order to mitigate the effect of turbulence [71, 382-384].

Route Diversity: FSO communications link performance is highly affected when propagating through the time-spatially variable atmospheric environment. In [364, 385], the route diversity has been adopted in order to improve signal reception under weak turbulence condition. Therefore, route diversity will be investigated for light to dense fog conditions as a mitigation technique.

Hybrid FSO/RF communication using channel coding: The reliability of FSO communication system mainly depends on the atmospheric weather conditions, especially when the link is longer than 1 km. One of the biggest challenges is the

attainment of 99.999% link availability during all weather conditions [36]. The hybrid FSO/RF link combined with the channel coding is one possible option as the RF system could be utilised as the back-up link but at a reduced data rate when the fog/turbulence is moderate to high and the channel coding can also improve the overall system reliability [386, 387].

Radio over FSO:

Transmission of modulated RF signal using FSO communications links is receiving a lot of research interest recently in [388]. Radio over free-space optics (RoFSO) communication system having potential to be a cost effective and reliable technology for bridging innovative wireless technologies networks facilities. RoFSO is a next generation access technology suitable for transmission of heterogeneous wireless service signals especially in areas which lack broadband connectivity. There is a need to conduct initial investigations focusing on studying the deployment environment characteristics, which influence the performance of RoFSO systems. Therefore, it is recommended to investigate the effects of atmosphere on RoFSO [389]

Appendix A:

Model		Model limitations	Model parameters/ Range			Conclusion
				V	T _{th}	
Kruse	$V(km) = \frac{10 \log_{10} T_{Th}}{\beta_{\lambda}} \left(\frac{\lambda}{\lambda_o} \right)^{-q}$ $q = \begin{cases} 1.6 & \text{for } V > 50 \text{ km} \\ 1.3 & \text{for } 6 \text{ km} < V < 50 \text{ km} \\ 0.58V^{1/3} & \text{for } 0 \text{ km} < V < 6 \text{ km} \end{cases}$	Developed for Haze	From optical to near IR wavelength dependent	0 – 50 km range	Mostly used 2% and 5%	Not suitable for fog study
Kim	$V(km) = \frac{10 \log_{10} T_{Th}}{\beta_{\lambda}} \left(\frac{\lambda}{\lambda_o} \right)^{-q}$ $q = \begin{cases} 1.6 & \text{for } V > 50 \text{ km} \\ 1.3 & \text{for } 6 \text{ km} < V < 50 \text{ km} \\ 0.16V + 0.34 & \text{for } 1 \text{ km} < V < 6 \text{ km} \\ V - 0.5 & \text{for } 0.5 \text{ km} < V < 1 \text{ km} \\ 0 & \text{for } V < 0.5 \text{ km} \end{cases}$	Developed for fog	Developed by considering 0.785 and 1.55 μm wavelength independent V<500 m	0 – 50km range	Mostly used 2% and 5%	Suitable, but need to test it experimentally for all wavelength ranges from visible – NIR.
Naboulsi	$\beta_{Con}(\lambda) = 4.343 \left(\frac{0.11478\lambda + 3.8367}{V} \right)$ $\beta_{Adv}(\lambda) = 4.343 \left(\frac{0.18126\lambda^2 + 0.13709\lambda + 3.7205}{V} \right)$	Developed for two types of fog using FASCOD, Experimentally tested for individual	Designed for wavelength rage from 0.69 – 1.55 m, wavelength dependent	Visibility range from 50 – 1000m	Not used / mentioned	Suitable for fog study as mentioned in performance is almost close to Kim However, the attenuation profile behaviour is opposite.

		wavelengths				
Ferdinandov	$\gamma(\lambda) = a(\lambda)V^{-Q(\lambda)}$ $Q(\lambda) = 0.199 \ln(\lambda) + 1.157$ $a(\lambda) = -2.656 \ln(\lambda) + 2.449$	Developed by generalization of Koschmeider law for fog and tested with mean values of the data from the literature.	Developed for range of 0.3 – 1.1 μm wavelength, wavelength dependent	0.1 – 50km range	Not used/ mentioned	Not verified by experimental work, adequate difference between the Kim, Naboulsi and this model for range of wavelength from 0.4 – 1.1 μm [263]
Fischer	<p>For two different fog events</p> $\gamma(1.55) = \frac{10.11}{V}$ $\gamma(1.55) = \frac{7.71}{V}$	Developed from empirical data of fog but just to compare with Kruse model.	1.55 μm	0.01 – 50km range	Used 10.11dB and 7.71 dB	This is not a valid model, this is an experimental study to verify the validity of Kruse model [264]
Grabner et al. (Inverse law and power law)	$\gamma(0.830) = \frac{20.57}{V} \text{ Inverse}$ $\gamma(0.830) = aV^b \text{ power law}$ <p>a=18.31, b=-1.035</p> $\gamma(1.55) = \frac{18.22}{V} \text{ inverse}$	Developed from empirical data of fog	Used two wavelengths 0.83 and 1.55 μm	0.05 – 1km range	Used 20.57dB and 18.22 dB	This model seems to be valid locally. However, the RMSE values of this model are close to Naboulsi convection model and are clearly large to say it an independent model [236].

	$\gamma(1.55) = aV^b$ power law a=22.44, b=-0.8616					
Pierce et al.	$\gamma = \frac{T_{th}}{V}$, where $8.7 < T_{th} < 17$	Developed from empirical data of fog	NIR	Not known	$8.7 < T_{th} < 17$	This model is same as Fischer model [265]
Pesek et al.	$\gamma = 401.4V^{-0.5738} - 1.462$ (dB/ 60m)	Developed from empirical data of fog	0.83 μ m	0.1 – 20km range	Not used/ mentioned	Not suitable model as developed for the single wavelength [241]
Nadeem et al.	$\gamma\left(\frac{dB}{km}\right) = ae^{b.V} + ce^{d.V(m)}$	Developed from empirical data of fog	Used two wavelengths 0.83 and 1.55 μ m	0.1 – 1.4km range	Not used/ mentioned	Not suitable model sufficient RMSE from standard models are found [266].

References

- [1] D. M. Forin, G. Incerti, G. T. Beleffi, A. Teixeira, L. Costa, P. D. B. André, B. Geiger, E. Leitgeb, and F. Nadeem, "Free space optical technologies," *Telecommunication book' IN-TECH*, 2010.
- [2] A. G. Bell, "On the production and reproduction of sound by light," *American Journal of Sciences*, vol. 3, pp. 305 - 324, 1880.
- [3] O. Bouchet, H. Sizun, C. Boisrobert, F. d. Fornel, and P. Favenec, "Free-space optics, propagation and communication," 1st, Ed., ed London,UK: ISTE, 2006.
- [4] R. Dettmer, "A ray of light, free space optical transmission," *IEE Review*, vol. 47, pp. 32-33, 2001.
- [5] A. T. Y. Ronny, "Link Performance Analysis of a Ship-to-Ship Laser Communication System," Monterey, California: Naval Postgraduate School, 2012.
- [6] D. Killinger, "Free space optics for laser communication through the air," *Optics and Photonics News*, vol. 13, pp. 36-42, 2002.
- [7] F. E. Goodwin, "A review of operational laser communication systems," *Proceedings of the IEEE*, vol. 58, pp. 1746-1752, 1970.
- [8] S. C. Gupta, *Optoelectronic Devices And Systems*: Prentice-Hall Of India Pvt. Limited, 2005.
- [9] W. O. Popoola, "Subcarrier intensity modulated free-space optical communication systems," *School of Computing, Engineering and Information Sciences, Doctor of Philosophy, University of Northumbria, Newcastle*, 2009.
- [10] J. C. Juarez, A. Dwivedi, A. Mammons, S. D. Jones, V. Weerackody, and R. A. Nichols, "Free-space optical communications for next-generation military networks," *Communications Magazine, IEEE*, vol. 44, pp. 46-51, 2006.
- [11] G. Fletcher, T. Hicks, and B. Laurent, "The SILEX optical interorbit link experiment," *Electronics & communication engineering journal*, vol. 3, pp. 273-279, 1991.
- [12] M. Toyoshima, Y. Takayama, T. Takahashi, K. Suzuki, S. Kimura, K. Takizawa, T. Kuri, W. Klaus, M. Toyoda, H. Kunimori, T. Jono, and K. Arai, "Ground-to-satellite laser communication experiments," *Aerospace and Electronic Systems Magazine, IEEE*, vol. 23, pp. 10-18, 2008.
- [13] H. Hemmati, "Deep space optical communications," *Deep Space Communication and navigation series, California: Wiley- Interscience*, 2006.
- [14] A. Jooshesh, T. A. Gulliver, and S. Uysal, "Space to ground optical power transmission," in *Broadband, Wireless Computing, Communication and Applications (BWCCA), Seventh International Conference on*, pp. 302-307, 2012.
- [15] C. B. Naila, K. Wakamori, M. Matsumoto, A. Bekkali, and K. Tsukamoto, "Transmission analysis of digital TV signals over a radio-on-FSO channel," *Communications Magazine, IEEE*, vol. 50, pp. 137-144, 2012.
- [16] P. Mandl, P. Schrotter, and E. Leitgeb, "Hybrid systems using DVB-T, WLAN and FSO to connect peripheral regions with broadband Internet

- services," in *Telecommunications. ConTEL. 10th International Conference on*, pp. 67-71, 2009.
- [17] A. Pavelchek, R. Trissel, J. Plante, and S. Umbrasas, "Long wave infrared (10 micron) free space optical communication system," *Proceedings of SPIE*, 2004.
 - [18] J. C. Juarez, D. W. Young, J. E. Sluz, J. L. Riggins II, and D. H. Hughes, "Free-space optical channel propagation tests over a 147-km link," *Atmospheric Propagation VIII*, pp. 80380B-80380B, 2011.
 - [19] J. D. Montgomery, "Free-space optics seen as viable alternative to cable," *Lightwave (Analyst Corner)*, pp. 43-44, 2004.
 - [20] S. K. Das and K. Basu, "Emergent technology based radio access network (RAN) design framework for next generation broadband wireless systems," 2004.
 - [21] J. G. Andrews, H. Claussen, M. Dohler, S. Rangan, and M. C. Reed, "Femtocells: Past, present, and future," *Selected Areas in Communications, IEEE Journal on*, vol. 30, pp. 497-508, 2012.
 - [22] M. Gagnaire and T. Youssef, "HOWRAN: An hybrid optical wireless radio access network for wimax antennas backhauling," *AccessNets*, pp. 1-15, 2009.
 - [23] W. Hameed, S. S. Muhammad, and N. M. Sheikh, "Integration scenarios for free space optics in next generation (4G) wireless networks," in *Communication Systems Networks and Digital Signal Processing (CSNDSP), 7th International Symposium on*, pp. 571-575, 2010.
 - [24] I. K. Son, "Design and Optimization of Free Space Optical Networks," Auburn University, 2010.
 - [25] M. O. Zaatari, "Wireless optical communications systems in enterprise networks," *The telecommunications review*, pp. 49-57, 2003.
 - [26] J. P. Carvalho, N. Marques, H. Veiga, C. Ribeiro Pacheco, and A. Reis, "A Medium Range Gbps FSO Link," *Electrical Engineering and Applied Computing*, pp. 125-133, 2011.
 - [27] R. M. Sova, J. E. Sluz, D. W. Young, J. C. Juarez, A. Dwivedi, N. M. Demidovich III, J. E. Graves, M. Northcott, J. Douglass, J. Phillips, D. Driver, A. McClarin, and D. Abelson, "80 Gb/s free-space optical communication demonstration between an aerostat and a ground terminal," *SPIE 6304*, pp. 630414-630414, 2006.
 - [28] Y. Arimoto, M. Presi, V. Guarino, A. D'Errico, G. Contestabile, M. Matsumoto, and E. Ciarabella, "320 Gbit/s (8 λ — 40 Gbit/s) double-pass terrestrial free-space optical link transparently connected to optical fibre lines," in *Optical Communication, 2008. ECOC 2008. 34th European Conference on*, pp. 1-2, 2008.
 - [29] E. Ciarabella, Y. Arimoto, G. Contestabile, M. Presi, A. D'Errico, V. Guarino, and M. Matsumoto, "1.28 Terabit/s (32x40 Gbit/s) WDM transmission over a double-pass free space optical link," in *Optical Fiber Communication Conference*, 2009.
 - [30] E. Leitgeb, M. S. Awan, P. Brandl, T. Plank, C. Capsoni, R. Nebuloni, T. Javornik, G. Kandus, S. S. Muhammad, and F. Ghassemlooy, "Current optical technologies for wireless access," in *Telecommunications, 2009. ConTEL, 10th International Conference on*, pp. 7-17, 2009.

- [31] S. Ghosh, K. Basu, and S. K. Das, "An architecture for next-generation radio access networks," *Network, IEEE*, vol. 19, pp. 35-42, 2005.
- [32] A. Soibel, M. W. Wright, W. H. Farr, S. A. Keo, C. J. Hill, R. Q. Yang, and H. C. Liu, "Midinfrared Interband Cascade Laser for Free Space Optical Communication," *IEEE Photonics Technology Letters*, vol. 22, pp. 121-123, 2009.
- [33] W. Gappmair and M. Flohberger, "Error performance of coded FSO links in turbulent atmosphere modeled by gamma-gamma distributions," *IEEE Transactions on Wireless Communications*, vol. 8, pp. 2209-2213, 2009.
- [34] H. E. Nistazakis, T. A. Tsiftsis, and G. S. Tombras, "Performance analysis of free-space optical communication systems over atmospheric turbulence channels," *Communications, IET*, vol. 3, pp. 1402-1409, 2009.
- [35] S. A. Zabidi, W. A. Khateeb, M. R. Islam, and A. W. Naji, "The effect of weather on free space optics communication (FSO) under tropical weather conditions and a proposed setup for measurement," in *Computer and Communication Engineering (ICCCE), 2010 International Conference on*, pp. 1-5, 2010.
- [36] H. Wu and M. Kavehrad, "Availability evaluation of ground-to-air hybrid FSO/RF links," *International Journal of Wireless Information Networks*, vol. 14, pp. 33-45, 2007.
- [37] K. Wakamori, K. Kazaura, and I. Oka, "Experiment on Regional Broadband Network Using Free-Space-Optical Communication Systems," *J. Lightwave Technol.*, vol. 25, pp. 3265-3273, 2007.
- [38] K. W. Fischer, M. R. Witiw, and J. A. Baars, "Atmospheric Laser Communication," *Bulletin of the American Meteorological Society*, vol. 85, pp. 725-732, 2004.
- [39] A. Mahdy and J. S. Deogun, "Wireless optical communications: a survey," in *Wireless Communications and Networking Conference, 2004. WCNC. IEEE*, pp. 2399-2404 Vol.4, 2004.
- [40] O. Bouchet, M. El Tabach, M. Wolf, D. C. O'Brien, G. E. Faulkner, J. W. Walewski, S. Randel, M. Franke, S. Nerreter, K. D. Langer, J. Grubor, and T. Kamalakis, "Hybrid wireless optics (HWO): Building the next-generation home network," presented at the 6th International Symposium on Communication Systems, Networks and Digital Signal Processing, CNSDSP, 2008.
- [41] N. Cvijetic, Q. Dayou, Y. Jianjun, H. Yue-Kai, and W. Ting, "100 Gb/s per-channel free-space optical transmission with coherent detection and MIMO processing," in *Optical Communication, ECOC. 35th European Conference on*, pp. 1-2, 2009.
- [42] M. Kaushik, A. K. Kaushik, and S. Kaushik, "An overview of Technical aspect for Mobile Network Technology," *International Journal of Advances in Engineering Science and Technology (IAEST, ISSN: 2319-1120)*, vol. 1, pp. 97-103, 2012.
- [43] J. P. Perera, "A Low-Cost, Man-Portable, Free-Space Optics Communications Device for Ethernet Applications," DTIC Document 2004.
- [44] V. Ramasarma, "Free space optics: A viable last-mile solution," *Bechtel Telecommunications Technical Journal*, vol. 1, pp. 22-30, 2002.
- [45] H. Willebrand and B. S. Ghuman, *Free space optics: enabling optical connectivity in today's networks*: Sams Publishing, 2002.

- [46] D. Della Giustina, P. Ferrari, A. Flammini, and S. Rinaldi, "Experimental characterization of service latency over Broadband Power Line in Medium Voltage grid," in *Applied Measurements for Power Systems (AMPS), 2012 IEEE International Workshop on*, pp. 1-6, 2012.
- [47] A. Cataliotti, D. Di Cara, R. Fiorelli, and G. Tine, "Power-Line Communication in Medium-Voltage System: Simulation Model and Onfield Experimental Tests," *Power Delivery, IEEE Transactions on*, vol. 27, pp. 62-69, 2012.
- [48] D. Acatauassú, F. Muller, and A. Klautau, "Capacity of MIMO DSL systems using 100 MHz measured channel data," in *Telecommunication, ICT'09. International Conference on*, pp. 266-269, 2009.
- [49] H. Shinohara, "Broadband access in Japan: Rapidly growing FTTH market," *Communications Magazine, IEEE*, vol. 43, pp. 72-78, 2005.
- [50] P. B. Papazian, G. A. Hufford, R. J. Achatz, and R. Hoffman, "Study of the local multipoint distribution service radio channel," *Broadcasting, IEEE Transactions on*, vol. 43, pp. 175-184, 1997.
- [51] K. Siwiak, "Ultra-wide band radio: introducing a new technology," in *Vehicular Technology Conference, 2001. VTC Spring. IEEE VTS 53rd*, pp. 1088-1093, 2001.
- [52] M.-G. Di Benedetto and G. Giancola, *Understanding ultra wide band radio fundamentals*: Prentice Hall, 2004.
- [53] J. J. Lee, C. S. Hong, J. M. Kang, and J. W. K. Hong, "Power line communication network trial and management in Korea," *International journal of network Management*, vol. 16, pp. 443-457, 2006.
- [54] Y. Miyamoto, A. Sano, H. Masuda, E. Yoshida, and S. Aisawa, "Enhancing the capacity beyond terabit per second for transparent optical transport network," in *Optical Communication (ECOC), 33rd European Conference and Exhibition of*, pp. 1-2, 2007.
- [55] H. Shinohara, "NTT's deployment of FTTH services," in *Optical Fiber Communication Conference, 2004. OFC, 2004*.
- [56] M. Anastasopoulos, D. Petraki, and H.-H. Chen, "Secure communications in local multipoint distribution service (LMDS) networks," *Wireless Communications, IEEE Transactions on*, vol. 8, pp. 5400-5403, 2009.
- [57] E. Boch and T. A. Duxbury, "Transceiver for fixed wireless access network applications," ed: Google Patents, 2002.
- [58] A. Ishimaru, S. Jaruwatanadilok, J. A. Ritcey, and Y. Kuga, "A MIMO propagation channel model in a random medium," *Antennas and Propagation, IEEE Transactions on*, vol. 58, pp. 178-186, 2010.
- [59] K. P. Liolis, A. D. Panagopoulos, and P. G. Cottis, "Bit-error outage over simo spatially correlated rain-fading channels [Wireless Corner]," *Antennas and Propagation Magazine, IEEE*, vol. 53, pp. 204-209, 2011.
- [60] K. P. Liolis, A. D. Panagopoulos, P. G. Cottis, and B. D. Rao, "On the applicability of MIMO principle to 10-66GHz BFWA networks: capacity enhancement through spatial multiplexing and interference reduction through selection diversity," *Communications, IEEE Transactions on*, vol. 57, pp. 530-541, 2009.
- [61] K.-H. Chen, J.-H. Lu, B.-J. Chen, and S.-I. Liu, "An ultra-wide-band 0.4–10-GHz LNA in 0.18- m CMOS," *Circuits and Systems II: Express Briefs, IEEE Transactions on*, vol. 54, pp. 217-221, 2007.

- [62] H. Willebrand and B. Ghuman, "Fiber optics without the fiber," *IEEE Spectrum*, vol. 38:, pp. 40-45, 2001.
- [63] E. Leitgeb, M. Gebhart, and U. Birnbacher, "Optical networks, last mile access and applications," *Journal of Optical and Fiber Communications Research*, vol. 2, pp. 56-85, 2005.
- [64] F. Deicke, W. Fisher, and M. Faulwasser, "Optical wireless communication to eco-system," in *Future Network & Mobile Summit (FutureNetw)*, pp. 1-8, 2012.
- [65] W. O. Popoola, Z. Ghassemlooy, J. I. H. Allen, E. Leitgeb, and S. Gao, "Free-space optical communication employing subcarrier modulation and spatial diversity in atmospheric turbulence channel," *Journal of Optoelectronics, IET*, vol. 2, pp. 16-23, 2008.
- [66] M. Uysal, S. M. Navidpour, and J. Li, "Error rate performance of coded free-space optical links over strong turbulence channels," *Communications Letters, IEEE*, vol. 8, pp. 635-637, 2004.
- [67] H. Nistazakis, T. Tsiftsis, and G. Tombras, "Performance analysis of free-space optical communication systems over atmospheric turbulence channels," *Communications, IET*, vol. 3, pp. 1402-1409, 2009.
- [68] S. M. Navidpour, M. Uysal, and M. Kavehrad, "BER performance of free-space optical transmission with spatial diversity," *Wireless Communications, IEEE Transactions on*, vol. 6, pp. 2813-2819, 2007.
- [69] M. Gebhart, E. Leitgeb, S. S. Muhammad, B. Flecker, C. Chlestil, M. Al Naboulsi, F. de Fornel, and H. Sizun, "Measurement of light attenuation in dense fog conditions for FSO applications," in *Optics & Photonics 2005*, pp. 58910-12, 2005.
- [70] G. Xu, X. Zhang, J. Wei, and X. Fu, "Influence of atmospheric turbulence on FSO link performance," in *Proceedings of SPIE*, pp. 816-823, 2003.
- [71] N. Cvijetic, S. G. Wilson, and M. Brandt-Pearce, "Performance bounds for free-space optical MIMO systems with APD receivers in atmospheric turbulence," *Selected Areas in Communications, IEEE Journal on*, vol. 26, pp. 3-12, 2008.
- [72] E. Bayaki, R. Schober, and R. K. Mallik, "Performance analysis of MIMO free-space optical systems in gamma-gamma fading," *Communications, IEEE Transactions on*, vol. 57, pp. 3415-3424, 2009.
- [73] H. Yuksel, S. Milner, and C. Davis, "Aperture averaging for optimizing receiver design and system performance on free-space optical communication links," *Journal of Optical Networking*, vol. 4, pp. 462-475, 2005.
- [74] W. O. Popoola, Z. Ghassemlooy, J. Allen, E. Leitgeb, and S. Gao, "Free-space optical communication employing subcarrier modulation and spatial diversity in atmospheric turbulence channel," *Optoelectronics, IET*, vol. 2, pp. 16-23, 2008.
- [75] Z. Wang, W.-D. Zhong, S. Fu, and C. Lin, "Performance comparison of different modulation formats over free-space optical (FSO) turbulence links with space diversity reception technique," *Photonics Journal, IEEE*, vol. 1, pp. 277-285, 2009.
- [76] X. Tang, Z. Ghassemlooy, W. O. Popoola, and C. Lee, "Coherent polarization shift keying modulated free space optical links over a Gamma-Gamma turbulence channel," *American Journal of Engineering and Applied Sciences*, vol. 4, pp. 520-530, 2011.

- [77] F. Nadeem, B. Flecker, E. Leitgeb, M. Khan, M. Awan, and T. Javornik, "Comparing the fog effects on hybrid network using optical wireless and GHz links," in *Communication Systems, Networks and Digital Signal Processing, 2008. CNSDSP 2008. 6th International Symposium on*, pp. 278-282, 2008.
- [78] V. Kvicera, M. Grabner, and O. Fiser, "Visibility and attenuation due to hydrometeors at 850 nm measured on an 850 m path," in *Communication Systems, Networks and Digital Signal Processing, CNSDSP, 6th International Symposium on*, 2008, pp. 270-272, 2008.
- [79] I. I. Kim, B. McArthur, and E. Korevaar, "Comparison of laser beam propagation at 785 nm and 1550 nm in fog and haze for optical wireless communications," in *Proc. SPIE 4214*, Boston, MA, USA, 2001.
- [80] M. A. Naboulsi, H. Sizun, and D. F. Frédérique, "Wavelength selection for the free space optical telecommunication technology," *SPIE* vol. 5465 pp. 168-179, 2004.
- [81] M. A. Naboulsi, H. Sizun, and F. d. Fornel "Fog attenuation prediction for optical and infrared waves,," *Journal of Optical Engineering*, vol. 43, pp. 319-329, 2004.
- [82] P. W. Kruse, L. D. McGlauchlin, E. B. McQuistan, and . "Elements of infrared technology: Generation, transmission and detection," *J. Wiley and sons*, 1962.
- [83] P. Corrigan, R. Martini, E. A. Whittaker, and C. Bethea, "Mid-infrared lasers and the Kruse-Mie theorem in fog for free-space optical communication applications," in *Conference on Lasers, Electro-Optics, Quantum Electronics and Laser Science. CLEO/QELS*, pp. 1-2, 2008.
- [84] F. Nadeem, T. Javornik, E. Leitgeb, V. Kvicera, and G. kandus, "Continental fog attenuation empirical relationship from measured visibility data," *Radio Engineering*, vol. 19 (4), 2010.
- [85] K. Su, L. Moeller, R. B. Barat, and J. F. Federici, "Experimental comparison of performance degradation from terahertz and infrared wireless links in fog," *Journal of Opt. Soc. Am. A*, vol. 29, pp. 179-184, 2012.
- [86] M. Ijaz, Z. Ghassemlooy, H. Le Minh, S. Rajbhandari, J. Perez, and A. Gholami, "Bit error rate measurement of free space optical communication links under laboratory-controlled fog conditions," in *16th European Conference on Networks and Optical Communications (NOC)*, pp. 52-550, 2011.
- [87] C. P. Colvero, M. C. R. Cordeiro, and J. P. von der Weid, "Real-time measurements of visibility and transmission in far mid and near-IR free space optical links," *IEEE Electronics Letters*, vol. 41, pp. 610-611, 2005.
- [88] M. Grabner and V. Kvicera, "On the relation between atmospheric visibility and optical wave attenuation," in *Mobile and Wireless Communications Summit, 16th IST*, pp. 1-5, 2007.
- [89] J. Perez, Z. Ghassemlooy, S. Rajbhandari, M. Ijaz, and H. Lee-Minh, "Ethernet FSO Communications Link Performance Study Under a Controlled Fog Environment," *Communications Letters, IEEE*, pp. 1- 3, 2012.
- [90] H. Le-Minh, Z. Ghassemlooy, M. Ijaz, S. Rajbhandari, S. Adebajo, Ansari, and E. Leitgeb, "Experimental study of bit error rate of free space optics communications in laboratory controlled turbulence," *IEEE Globecom 2010*

Workshop on Optical Wireless Communications in Miami, Florida, USA, 2010.

- [91] J. de Carvalho, N. Marques, H. Veiga, C. Pacheco, and A. Reis, "Experimental performance evaluation of a Gbps FSO link: A case study," *Wireless Information Networks and Systems (WINSYS), Proceedings of the 2010 International Conference on*, pp. 1-6, 2010.
- [92] U. Birnbacher, E. Leitgeb, S. S. Muhammad, M. Gebhart, and C. Chlestil, "Applications of Free Space Optics for Broadband Access," *International Federation for Information Processing Digital Library*, vol. 164, 2010.
- [93] R. Peach, G. Burdge, F. Reitberger, C. Visone, M. Oyler, C. Jensen, and J. Sonnenberg, "Performance of a 10 Gbps QoS-based buffer in a FSO/RF IP network," in *SPIE Optical Engineering Applications*, pp. 781402-781402-12, 2010.
- [94] N. Perlot, E. Duca, J. Horwath, D. Giggenbach, and E. Leitgeb, "System requirements for optical HAP-satellite links," in *Communication Systems, Networks and Digital Signal Processing, 2008. CNSDSP, 6th International Symposium on*, pp. 72-76, 2008.
- [95] J. C. Juarez, J. E. Sluz, and D. W. Young, "Optical automatic gain controller for high-bandwidth free-space optical communication links," in *applications of lasers for sensing and free space communications*, 2011.
- [96] M. Toyoshima, "Trends in satellite communications and the role of optical free-space communications [Invited]," *Journal of Optical Networking*, vol. 4, pp. 300-311, 2005.
- [97] H. Takenaka, M. Toyoshima, and Y. Takayama, "Experimental verification of fiber-coupling efficiency for satellite-to-ground atmospheric laser downlinks," *Optics Express*, vol. 20, pp. 15301-15308, 2012.
- [98] A. Dolma and K. Karayahşi, "Free Space Optic/Radio Frequency (FSO/RF) hybrid communication systems and various applications," in *Signal Processing and Communications Applications Conference (SIU), IEEE 18th*, 2010, pp. 236-239, 2010.
- [99] J. A. Anguita and J. E. Cisternas, "Experimental evaluation of transmitter and receiver diversity in a terrestrial FSO link," in *GLOBECOM Workshops (GC Wkshps), 2010 IEEE*, pp. 1005-1009, 2010.
- [100] M. Ijaz, Z. Ghassemlooy, J. Pesek, O. Fiser, H. Le Minh, and E. Bentley, "Modeling of Fog and Smoke Attenuation in Free Space Optical Communications Link under Controlled Laboratory Conditions," *Lightwave Technology, Journal of*, vol. PP, pp. 1-1, 2013.
- [101] O. Bouchet, *Wireless Optical Telecommunications*: Wiley, 2013.
- [102] H. Sizun, *Radio Wave Propagation for Telecommunication Applications*: Springer, 2005.
- [103] S. V. Kartalopoulos, "Free space optical networks for ultra-broad band services " *John Wiley & Sons, New Jersey*, 2011, pp. 35-36, 2011
- [104] H. Hemmati, *Near-Earth Laser Communications*: Taylor & Francis, 2009.
- [105] X.-d. YU, T.-f. ZHAO, X.-r. WANG, and G. WANG, "Design and implementation of wireless UV communication system based on LED," *Electronic Design Engineering*, vol. 11, p. 008, 2011.
- [106] R. Martini and E. Whittaker, "Quantum cascade laser-based free space optical communications," *Journal of Optical and Fiber Communications Research*, vol. 2, pp. 279-292, 2005.

- [107] F. Demers, H. Yanikomeroglu, and M. St-Hilaire, "A survey of opportunities for free space optics in next generation cellular networks," in *Communication Networks and Services Research Conference (CNSR), 2011 Ninth Annual*, pp. 210-216, 2011.
- [108] E. Leitgeb, M. S. Awan, P. Brandl, T. Plank, C. Capsoni, R. Nebuloni, T. Javornik, G. Kandus, S. S. Muhammad, F. Ghassemlooy, M. Loschnigg, and F. Nadeem, "Current optical technologies for wireless access," in *Telecommunications, ConTEL 2009. 10th International Conference on*, pp. 7-17, 2009.
- [109] A. Sikora and V. F. Groza, "Coexistence of IEEE802. 15.4 with other Systems in the 2.4 GHz-ISM-Band," in *Instrumentation and Measurement Technology Conference, 2005. IMTC 2005. Proceedings of the IEEE* , pp. 1786-1791, 2005.
- [110] L. Rakotondrainibe, Y. Kokar, G. Zaharia, and G. El-Zein, "60 ghz high data rate wireless communication system," in *Vehicular Technology Conference, 2009. VTC Spring 2009. IEEE 69th*, pp. 1-5, 2009.
- [111] D. Sinefeld, D. Shayovitz, O. Golani, and D. M. Marom, "Adaptive Rate and Bandwidth WDM Optical Sampling Pulse Streams with LCoS-based Photonic Spectral Processor," *Optical Fiber Communication Conference*, 2013.
- [112] J. I. Saari, M. M. Krause, B. R. Walsh, and P. Kambhampati, "Terahertz bandwidth all-optical modulation and logic using multiexcitons in semiconductor nanocrystals," *Nano letters*, 2013.
- [113] Z. Ghaseemlooy, W. Poopola, and S. Rajbhandri, "Optical wireless communications, system and channel modelling with matlab," *CRC Press, London, UK*, 2012.
- [114] K. Biesecker, "The promise of broadband wireless," *IT Professional*, vol. 2, pp. 31-39, 2000.
- [115] P. Sadorsky, "Information communication technology and electricity consumption in emerging economies," *Energy Policy*, 2012.
- [116] G. e.-S. Initiative, "SMART 2020: Enabling the low carbon economy in the information age," *press release, Brussels, Belgium, June*, vol. 20, 2008.
- [117] E. Bonetto, S. Buzzi, D. Cuda, G. A. G. Castillo, and F. Neri, "Optical technologies can improve the energy efficiency of networks," in *Optical Communication, ECOC, 35th European Conference on*, pp. 1-4, 2009.
- [118] E. Gulsen, E. Olivetti, L. C. Kimerling, and R. Kirchain, "Energy concerns in information and communication technology and the potential for photonics integration," *Sustainable Systems and Technology (ISSST), IEEE International Symposium on*, pp. 1-1, 2010.
- [119] M. Matsumoto, K. Kazaura, P. Dat, A. Shah, K. Omae, T. Suzuki, K. Wakamori, T. Higashino, K. Tsukamoto, and S. Komaki, "An alternative access technology for next generation networks based on full-optical wireless communication links," in *Innovations in NGN: Future Network and Services, 2008. K-INGN, First ITU-T Kaleidoscope Academic Conference*, pp. 221-228, 2008.
- [120] H. Willebrand and B.S. Ghuman, "Free space optics: enabling optical connectivity in today's networks. ," *Sams Publishing, London*, 2002.
- [121] H. A. Fadhil, A. Amphawan, H. A. Shamsuddin, T. Hussein Abd, H. M. Al-Khafaji, S. Aljunid, and N. Ahmed, "Optimization of free space optics

- parameters: An optimum solution for bad weather conditions," *Optik-International Journal for Light and Electron Optics*, 2013.
- [122] X. Liu, "Secrecy capacity of wireless channels subject to log-normal fading," *Security and Communication Networks*, pp. n/a-n/a, 2013.
 - [123] L. F. Abdulameer, U. Sripati, and M. Kulkarni, "Enhancement of security for free space optics based on reconfigurable chaotic technique," in *International Conference on Communication and Electronics System Design*, pp. 876000-876000-7, 2013.
 - [124] R. McClintock, A. Haddadi, and M. Razeghi, "Free-space optical communication using mid-infrared or solar-blind ultraviolet sources and detectors," *Proc. of SPIE Vol.*, pp. 826810-1, 2012.
 - [125] S. M. Cherry, "The wireless last mile," *Spectrum, IEEE*, vol. 40, pp. 18-22, 2003.
 - [126] S. Ahmad Anas, F. Hamat, S. Hitam, and R. K. Sahbudin, "Hybrid fiber-to-the-x and free space optics for high bandwidth access networks," *Photonic Network Communications*, pp. 1-7, 2012.
 - [127] G. Kramer and G. Pesavento, "Ethernet passive optical network (EPON): building a next-generation optical access network," *Communications magazine, IEEE*, vol. 40, pp. 66-73, 2002.
 - [128] E. Leitgeb, J. Bregenzer, P. Fasser, and M. Gebhart, "Free space optics-extension to fiber-networks for the," in *Lasers and Electro-Optics Society, 2002. LEOS, The 15th Annual Meeting of the IEEE*, pp. 459-460, 2002.
 - [129] A. Acampora, "Last mile by laser," *Scientific American*, vol. 287, pp. 32-7, 2002.
 - [130] N. Blaunstein, S. Arnon, A. Zilberman, and N. Kopeika, "Applied aspects of optical communication and LIDAR," *Boca Raton : CRC Press, London*, pp. 53-55, 2010.
 - [131] O. Awwad, A. Al-Fuqaha, B. Khan, and G. B. Brahim, "Topology control schema for better qos in hybrid rf/fso mesh networks," *Communications, IEEE Transactions on*, vol. 60, pp. 1398-1406, 2012.
 - [132] V. Vishnevskii, O. Semenova, and S. Y. Sharov, "Modeling and analysis of a hybrid communication channel based on free-space optical and radio-frequency technologies," *Automation and Remote Control*, vol. 74, pp. 521-528, 2013.
 - [133] J. Libich, M. Mudroch, P. Dvorak, and S. Zvanovec, "Performance analysis of hybrid FSO/RF link," in *Antennas and Propagation (EUCAP), 6th European Conference on*, pp. 1235-1238, 2012.
 - [134] F. Nadeem, V. Kvicera, M. S. Awan, E. Leitgeb, S. Muhammad, and G. Kandus, "Weather effects on hybrid FSO/RF communication link," *Selected Areas in Communications, IEEE Journal on*, vol. 27, pp. 1687-1697, 2009.
 - [135] Z. Kolka, Z. Kincl, V. Biolkova, and D. Biolek, "Hybrid FSO/RF test link," in *Ultra Modern Telecommunications and Control Systems and Workshops (ICUMT), 4th International Congress on*, pp. 502-505, 2012.
 - [136] Y. Tang, M. Brandt-Pearce, and S. Wilson, "Link Adaptation for Throughput Optimization of Parallel Channels with Application to Hybrid FSO/RF Systems," 2012.
 - [137] L. Hanzo, H. Haas, S. Imre, D. O'Brien, M. Rupp, and L. Gyongyosi, "Wireless myths, realities, and futures: from 3G/4G to optical and quantum wireless," *Proceedings of the IEEE*, vol. 100, pp. 1853-1888, 2012.

- [138] I. E. Lee, Z. Ghassemlooy, W. P. Ng, and A. Khalighi, "Green-inspired hybrid fso/rf wireless backhauling and basic access signalling for next generation metrozones," in *International Symposium on Environment-Friendly Energies and Applications (EFEA)*, pp. 230-236, 2012.
- [139] S. V. Kartalopoulos, "Seamless integration of wireless access, free space optical, and fiber-based backbone networks," in *Network Operations and Management Symposium (NOMS), 2012 IEEE*, pp. 1399-1402, 2012.
- [140] Y. Ai, Z. Xiong, J. Chen, F. Zhang, Y. Liu, S. Zhang, R. Dong, and Y. Xiao, "The analysis of 7.5 Gbps 40 Km FSO experiments," in *Photonics Society Summer Topical Meeting Series, IEEE*, pp. 128-129, 2012.
- [141] M. Väänänen, "Broadband base station comprising means for free space optical communications," ed: EP Patent 2,523,369, 2012.
- [142] W. Hameed, S. S. Muhammad, and N. M. Sheikh, "Integration scenarios for free space optics in next generation (4G) wireless networks," *Communication Systems Networks and Digital Signal Processing (CSNDSP), 7th International Symposium on*, pp. 571-575, 2010.
- [143] J. Derenick, C. Thorne, and J. Spletzer, "On the deployment of a hybrid free-space optic/radio frequency (FSO/RF) mobile ad-hoc network," in *Intelligent Robots and Systems, 2005.(IROS 2005). 2005 IEEE/RSJ International Conference on*, 2005, pp. 3990-3996.
- [144] Z. Dayong, H. H. Refai, P. G. LoPresti, and M. Atiquzzaman, "Control algorithm development for mobile FSO node alignment," in *Digital Avionics Systems Conference. DASC, IEEE/AIAA 28th*, 2009, pp. 6.A.3-1-6.A.3-12, 2009.
- [145] X. Jin, X. Wang, and C. Y. Hsu, "Design and implementation of mobile free space optical communication system," *Avionics, Fiber-Optics and Photonics Technology Conference, IEEE*, pp. 37-38, 2008.
- [146] G. Wu, Y. A. Zhang, X. G. Yuan, J. N. Zhang, M. L. Zhang, and Y. P. Li, "Design and Realization of 10Gbps DPSK System for Free Space Optical Communication," *Applied Mechanics and Materials*, vol. 263, pp. 1150-1155, 2013.
- [147] Y. Arimoto, "Robust fiber-to-fiber free-space optical communications under strong atmospheric turbulences," in *Applications of Lasers for Sensing and Free Space Communications*, 2011.
- [148] A. Sharma and R. Kaler, "Designing of high-speed inter-building connectivity by free space optical link with radio frequency backup," *IET Communications*, vol. 6, pp. 2568-2574, 2012.
- [149] H. A. Willebrand and B. S. Ghuman, "Fiber optics without fiber," *Spectrum, IEEE*, vol. 38, pp. 40-45, 2001.
- [150] T. L. Tidwell, J. T. Gregory, C. H. Chalfant III, F. J. Orlando, and M. Leftwich, "Rapid acquisition, pointing and tracking optical system for free space optical communications," ed: Google Patents, 2012.
- [151] J. Libich and S. Zvanovec, "Utilization of route diversity in free-space optical networks," in *Avionics, Fiber- Optics and Photonics Technology Conference (AVFOP), IEEE*, pp. 65-66, 2011.
- [152] H. Manor and S. Arnon, "Performance of an optical wireless communication system as a function of wavelength," *Applied optics*, vol. 42, pp. 4285-4294, 2003.

- [153] S. Bloom, E. Korevaar, J. Schuster, and H. Willebrand, "Understanding the performance of free-space optics," *Journal of Optical Networking*, vol. 2, pp. 178-200, 2003.
- [154] J. C. Palais. *Fiber optic communication*, Prentice Hall, UK, 2005.
- [155] J. Liao, A. Mirvakili, A. Boryssenko, V. Joyner, and Z. R. Huang, "Integration of LED chip within patch antenna geometry for hybrid FSO/RF communication," *Electronics Letters*, vol. 46, pp. 1332-1333, 2010.
- [156] A. Jabeena, B. Praneeth, and P. Arulmozhivarman, "Laser Based Optical Transceiver for Data Transfer of Free Space Optical Communication," *European Journal of Scientific Research*, vol. 67, pp. 294-300, 2012.
- [157] Y. H. Kho, L. Yong, K. L. Lau, and K. P. Kiu, "Design of an indoor wireless optical transceiver system with source and channel coding," in *Industrial Electronics and Applications (ISIEA), 2012 IEEE Symposium on*, pp. 45-49, 2012.
- [158] O. Ziemann, *POF Handbook: Optical Short Range Transmission Systems*: Springer-Verlag Berlin Heidelberg, 2008.
- [159] M. Yahya, M. K. Salleh, N. A. M. Akib, S. A. Jamalullail, and Z. Awang, "Link performance analysis of experimental LED based Free Space Optics," in *TENCON 2011 - 2011 IEEE Region 10 Conference*, pp. 1298-1302, 2011.
- [160] D. A. Rockwell and G. S. Mecherle, " Wavelength selection for optical wireless communication systems," *Optical Wireless Communications IV, Proc. of SPIE*., 2001.
- [161] E. Leitgeb, T. Plank, M. S. Awan, P. Brandl, W. Popoola, Z. Ghassemlooy, F. Ozek, and M. Wittig, "Analysis and evaluation of optimum wavelengths for free-space optical transceivers," *Transparent Optical Networks (ICTON), 12th International Conference on*, pp. 1-7, 2010.
- [162] M. Ijaz, Z. Ghassemlooy, H. Le Minh, S. Rajbhandari, and J. Perez, "Analysis of fog and smoke attenuation in a free space optical communication link under controlled laboratory conditions," in *Optical Wireless Communications (IWOW), International Workshop on*, pp. 1-3, 2012.
- [163] M. Khalighi, N. Aitamer, N. Schwartz, and S. Bourennane, "Turbulence mitigation by aperture averaging in wireless optical systems," *Telecommunications, ConTEL, 10th International Conference on*, pp. 59-66, 2009.
- [164] F. Xu, M. Khalighi, and S. Bourennane, "Impact of different noise sources on the performance of PIN-and APD-based FSO receivers," in *Telecommunications (ConTEL), Proceedings of the 11th International Conference on*, pp. 211-218, 2011.
- [165] K. Kiasaleh, "Performance of APD-based, PPM free-space optical communication systems in atmospheric turbulence," *Communications, IEEE Transactions on*, vol. 53, pp. 1455-1461, 2005.
- [166] S. Hranilovic, *Wireless Optical Communication Systems*: Springer New York, 2005.
- [167] J. R. Barry, J. M. Kahn, W. J. Krause, E. A. Lee, and D. G. Messerschmitt, "Simulation of multipath impulse response for indoor wireless optical channels," *Selected Areas in Communications, IEEE Journal on*, vol. 11, pp. 367-379, 1993.

- [168] J. M. Kahn, W. J. Krause, and J. B. Carruthers, "Experimental characterization of non-directed indoor infrared channels," *Communications, IEEE Transactions on*, vol. 43, pp. 1613-1623, 1995.
- [169] F. Fidler, M. Knappek, J. Horwath, and W. R. Leeb, "Optical communications for high-altitude platforms," *IEEE Journal of Selected Topics in Quantum Electronics*, vol. 16, pp. 1058-1070, 2010.
- [170] D. J. T. Heatley, D. R. Wisely, I. Neild, and P. Cochrane, "Optical wireless: the story so far," *Communications Magazine, IEEE*, vol. 36, pp. 72-74, 79-82, 1998.
- [171] S. Karp, R. M. Gagliardi, S. E. Moran, and L. B. Stotts. *Optical Channels: fibers, clouds, water and the atmosphere*, Plenum Press New York, 1988.
- [172] J. C. Ricklin, S. M. Hammel, F. D. Eaton, and S. L. Lachinova, "Atmospheric channel effects on free-space laser communication," *Journal of Optical and Fiber Communications Research*, vol. 3, pp. 111-158, 2006.
- [173] J. Libich and S. Zvanovec, "Measurement statistics of three joint wireless optical links," in *Optical Wireless Communications (IWOW), International Workshop on*, pp. 1-3, 2012.
- [174] Y. Cai, O. Korotkova, H. T. Eyyuboglu, and Y. Baykal, "Active laser radar systems with stochastic electromagnetic beams in turbulent atmosphere," *Optics Express*, vol. 16, pp. 15834-15846, 2008.
- [175] Z. Jia, Q. Zhu, and F. Ao, "Atmospheric attenuation analysis in the FSO link," in *Communication Technology, ICCT'06. International Conference on*, pp. 1-4, 2006.
- [176] D. A. Rockwell and G. S. Mecherle, "Wavelength selection for optical wireless communications systems," in *Proc. SPIE*, pp. 27-35, 2001.
- [177] M. S. Awan, "Statistical-dynamical channel modeling of outdoor optical wireless links," *PhD thesis, TU Graz*, 2010.
- [178] H. Weichel, *Laser beam propagation in the atmosphere*. Bellingham: SPIE Optical Engineering, 1990.
- [179] V. Gudimetla, R. B. Holmes, C. Smith, and G. Needham, "Analytical expressions for the log-amplitude correlation function of a plane wave through anisotropic atmospheric refractive turbulence," *JOSA A*, vol. 29, pp. 832-841, 2012.
- [180] S. Takashi, T. Morio, and T. Hideki, "Fading simulator for satellite-to-ground optical communication," *Journal of the National Institute of Information and Communications Technology*, vol. 59, pp. 95-102, 2012.
- [181] V. Sofieva, F. Dalaudier, and J. Vernin, "Using stellar scintillation for studies of turbulence in the Earth's atmosphere," *Philosophical Transactions of the Royal Society A: Mathematical, Physical and Engineering Sciences*, vol. 371, 2013.
- [182] S. Arnon, "Optical wireless communication through random media," in *Proceedings of SPIE*, p. 79240D, 2011.
- [183] F. Fidler, M. Knappek, J. Horwath, and W. R. Leeb, "Optical communications for high-altitude platforms," *Selected Topics in Quantum Electronics, IEEE Journal of*, vol. 16, pp. 1058-1070, 2010.
- [184] X. Tang, Z. Ghassemlooy, S. Rajbhandari, W. Popoola, M. Uysal, and D. Wu, "Experimental demonstration of polarisation shift keying in the free space optical turbulence channel," in *Communications in China Workshops (ICCC), 2012 1st IEEE International Conference on*, pp. 31-36, 2012.

- [185] S. Randel, F. Breyer, S. C. J. Lee, and J. W. Walewski, "Advanced modulation schemes for short-range optical communications," *Selected Topics in Quantum Electronics, IEEE Journal of*, vol. 16, pp. 1280-1289, 2010.
- [186] Z. Jinlong, "Modulation analysis for outdoors applications of optical wireless communications," in *Communication Technology Proceedings, 2000. WCC - ICCT 2000. International Conference on*, pp. 1483-1487, 2000.
- [187] S. Rajbhandari, Z. Ghassemlooy, J. Perez, H. Le Minh, M. Ijaz, E. Leitgeb, G. Kandus, and V. Kvicera, "On the study of the FSO link performance under controlled turbulence and fog atmospheric conditions," *Telecommunications (ConTEL), Proceedings of the 11th International Conference on*, pp. 223-226, 2011.
- [188] R. N. Mahalati and J. M. Kahn, "Effect of fog on free-space optical links employing imaging receivers," *Optics Express*, vol. 20, pp. 1649-1661, 2012.
- [189] B. Wilson and Z. Ghassemlooy, "Pulse time modulation techniques for optical communications: a review," *Optoelectronics, IEE Proceedings*, pp. 347-357, 1993.
- [190] M. Ijaz, Z. Ghassemlooy, H. Le Minh, S. Rajbhandari, J. Perez, and A. Gholami, "Bit error rate measurement of free space optical communication links under laboratory-controlled fog conditions," *16th European Conference on Networks and Optical Communications (NOC)*, pp. 52-550, 2011.
- [191] N. A. Mohammed, A. S. El-Wakeel, and M. H. Aly, "Performance evaluation of fso link under nrz-rz line codes, different weather conditions and receiver types in the presence of pointing errors," *Open Electrical & Electronic Engineering Journal*, vol. 6, pp. 28-35, 2012.
- [192] J. Perez, Z. Ghassemlooy, S. Rajbhandari, M. Ijaz, and H. Lee-Minh, "Ethernet FSO communications link performance study under a controlled fog environment," *IEEE Communications Letters*, pp. 1- 3, 2012.
- [193] M. Ijaz, Z. Ghassemlooy, S. Ansari, O. Adebajo, H. Le Minh, S. Rajbhandari, and A. Gholami, "Experimental investigation of the performance of different modulation techniques under controlled FSO turbulence channel," *Telecommunications (IST), 5th International Symposium on*, pp. 59-64, 2010.
- [194] M. Selvi and K. Murugesan, "The performance of orthogonal frequency division multiplexing in the weak turbulence regime of free space optics communication systems," *Journal of Optics*, vol. 14, p. 125401, 2012.
- [195] D. J. Barros, S. K. Wilson, and J. M. Kahn, "Comparison of Orthogonal Frequency-Division Multiplexing and Pulse-Amplitude Modulation in Indoor Optical Wireless Links," *Communications, IEEE Transactions on*, vol. 60, pp. 153-163, 2012.
- [196] W. Shieh and I. Djordjevic, *OFDM for Optical Communications*: Elsevier Science, 2009.
- [197] R. Mesleh, H. Elgala, and H. Haas, "An overview of indoor OFDM/DMT optical wireless communication systems," *7th Int. Symp. on Communication Systems Networks and Digital Signal Processing (CSNDSP)*, pp. 566-570, 2010.
- [198] R. Mesleh, H. Elgala, and H. Haas, "LED Nonlinearity Mitigation Techniques in Optical Wireless OFDM Communication Systems," *Journal of Optical Communications and Networking*, vol. 4, pp. 865-875, 2012.

- [199] S. S. Muhammad, T. Javornik, I. Jelovčan, Z. Ghassemlooy, and E. Leitgeb, "Comparison of hard-decision and soft-decision channel coded M-ary PPM performance over free space optical links," *Transactions on Emerging Telecommunications Technologies*, vol. 20, pp. 746-757, 2009.
- [200] W. Hongxing, X. Sun, X. Sun, T. Zhang, and Y. Zhu, "Performance of current digital pulse modulation schemes for optical wireless communications," in *Wireless, Mobile and Multimedia Networks, IET International Conference on*, pp. 1-4. , 2006
- [201] G. A. Mahdiraji and E. Zahedi, "Comparison of selected digital modulation schemes (OOK, PPM and DPIM) for wireless optical communications," in *Research and Development, SCOREd. 4th Student Conference on*, pp. 5-10, 2006.
- [202] M. Faridzadeh, A. Gholami, Z. Ghassemlooy, and S. Rajbhandari, "Hybrid pulse position modulation and binary phase shift keying subcarrier intensity modulation for free space optics in a weak and saturated turbulence channel," *JOSA A*, vol. 29, pp. 1680-1685, 2012.
- [203] I. B. Djordjevic, J. A. Anguita, and B. Vasic, "Error-correction coded orbital-angular-momentum modulation for fso channels affected by turbulence," *Lightwave Technology, Journal of*, vol. 30, pp. 2846-2852, 2012.
- [204] S. Rajbhandari, "Application of wavelets and artificial neural network for indoor optical wireless communication systems, Doctor of Philosophy, Northumbria University, UK, 2009.
- [205] S. Trisno, " Design and analysis of advanced free space optical communication system," Doctor of Philosophy, University of Maryland, 2006.
- [206] L. W. Couch, H. Shao, X. Li, and L. Liu, *Digital and analog communication systems*: Macmillan, 1993.
- [207] G. W. Marsh and J. M. Kahn, "Channel reuse strategies for indoor infrared wireless communications," *Communications, IEEE Transactions on*, vol. 45, pp. 1280-1290, 1997.
- [208] M. D. Audeh and J. M. Kahn, "Performance evaluation of L-pulse-position modulation on non-directed indoor infrared channels," in *Communications, 1994. ICC'94, SUPERCOMM/ICC'94, Conference Record, 'Serving Humanity Through Communications. IEEE International Conference on*, pp. 660-664, 1994.
- [209] T. O'Farrell and M. Kiatweerasakul, "Performance of a spread spectrum infrared transmission system under ambient light interference," in *The Ninth IEEE International Symposium on Personal, Indoor and Mobile Radio Communications*, pp. 703-707, 1998.
- [210] W. O. Popoola, "Subcarrier intensity modulated free space optical communication systems," Doctor of Philosophy, Northumbria University, UK, 2009.
- [211] M. D. Audeh and J. M. Kahn, "Performance evaluation of L-pulse-position modulation on non-directed indoor infrared channels," in *IEEE International Conference on Communications (ICC)*, pp. 660-664, 1994.
- [212] C. Morgan, "Modulation Used in Legacy & Premium Backplane Channels," *White paper*, 2012.

- [213] M. Rouissat, R. A. Borsali, and M. Chick-Bled, "Dual amplitude-width ppm for free space optical systems," *International Journal of Information Technology and Computer Science (IJITCS)*, vol. 4, p. 45, 2012.
- [214] Y. Zeng, R. Green, and M. Leeson, "Multiple pulse amplitude and position modulation for the optical wireless channel," in *Transparent Optical Networks, ICTON 2008. 10th Anniversary International Conference on*, pp. 193-196, 2008.
- [215] Y. Zeng, R. J. Green, S. Sun, and M. S. Leeson, "Tunable pulse amplitude and position modulation technique for reliable optical wireless communication channels," *Journal of Communications*, vol. 2, pp. 22-28, 2007.
- [216] T. Ohtsuki, "Multiple-subcarrier modulation in optical wireless communications," *Communications Magazine, IEEE*, vol. 41, pp. 74-79, 2003.
- [217] R. You and J. M. Kahn, "Average power reduction techniques for multiple-subcarrier intensity-modulated optical signals," in *Communications, ICC 2000. 2000 IEEE International Conference on*, pp. 1620-1627, 2000.
- [218] S. Hwang, K. Hoon, K. Byungjik, S. K. Kim, L. Hanlim, K. Yonggyoo, L. Gyuwoong, K. Sangho, and O. Yunje, "RoF technologies for in-building wireless systems," *IEICE transactions on electronics*, vol. 90, pp. 345-350, 2007.
- [219] W. O. Popoola and Z. Ghassemlooy, "BPSK subcarrier intensity modulated free-space optical communications in atmospheric turbulence," *Journal of Lightwave Technology*, vol. 27, pp. 967-973, 2009.
- [220] X. Song and J. Cheng, "Subcarrier intensity modulated optical communications in strong atmospheric turbulence," in *Communications in China Workshops (ICCC), 2012 1st IEEE International Conference on*, pp. 26-30, 2012.
- [221] X. Tang, S. Rajbhandari, W. Popoola, Z. Ghassemlooy, E. Leitgeb, S. Muhammad, and G. Kandung, "Performance of bpsk subcarrier intensity modulation free-space optical communications using a log-normal atmospheric turbulence model," in *Photonics and Optoelectronic (SOPO) Symposium on*, pp. 1-4, 2010.
- [222] H. Willebrand and B. S. Ghuman, *Free-space optics: enabling optical connectivity in today's networks*. Indianapolis: SAMS publishing, 2002.
- [223] M. O. Zaatari, "Wireless optical communication systems in enterprise networks," *The Telecommunications Review*, pp. 49-57, 2003.
- [224] S. Hranilovic, *Wireless optical communication systems*: Springer, 2004.
- [225] J. Alwan, "Eye safety and wireless optical networks (WONs)," *white paper available at <http://www.airfiber.com/index.shtml>*, 2001.
- [226] V. J. Schaefer and J. A. Day, *A Field Guide to the Atmosphere*: Houghton Mifflin, 1998.
- [227] R. Nebuloni and C. Capsoni, "Effect of hydrometeor scattering on optical wave propagation through the atmosphere," in *Antennas and Propagation (EUCAP), Proceedings of the 5th European Conference on*, pp. 2513-2517, 2011.
- [228] M. S. Awan, Marzuki, E. Leitgeb, B. Hillbrand, F. Nadeem, and M. S. Khan, "Cloud attenuations for free-space optical links," in *International Workshop on Satellite and Space Communications*, pp. 274-278, 2009.

- [229] A. Z. Suriza, A. K. Wajdi, M. Rafiqul, and A. W. Naji, "Preliminary analysis on the effect of rain attenuation on Free Space Optics (FSO) propagation measured in tropical weather condition," in *Space Science and Communication (IconSpace), 2011 IEEE International Conference on*, pp. 96-101, 2011.
- [230] M. S. Awan, Marzuki, E. Leitgeb, F. Nadeem, M. S. Khan, and C. Capsoni, "Weather Effects Impact on the Optical Pulse Propagation in Free Space," in *Vehicular Technology Conference, VTC Spring, IEEE 69th*, pp. 1-5, 2009.
- [231] M. S. Awan, P. Brandl, E. Leitgeb, F. Nadeem, T. Plank, and C. Capsoni, "Results of an optical wireless ground link experiment in continental fog and dry snow conditions," *10th International Conference on Telecommunications (ConTEL)*, pp. 45-49, 2009.
- [232] R. M. Pierce, J. Ramaprasad, and E. C. Eisenberg, "Optical attenuation in fog and clouds," *Proc. SPIE 4530*, vol. 58, 2001.
- [233] M. S. Awan, E. Leitgeb, C. Capsoni, R. Nebuloni, Marzuki, F. Nadeem, and M. S. Khan, "Attenuation analysis for optical wireless link measurements under moderate continental fog conditions at milan and graz," in *Vehicular Technology Conference, 2008. VTC 2008-Fall. IEEE 68th*, pp. 1-5, 2008.
- [234] B. Flecker, M. Gebhart, E. Leitgeb, S. Sheikh Muhammad, and C. Chlestil, "Results of attenuation measurements for optical wireless channels under dense fog conditions regarding different wavelengths," pp. 63030P-63030P, 2006.
- [235] M. Gebhart, E. Leitgeb, S. Sheikh Muhammad, B. Flecker, C. Chlestil, M. Al Naboulsi, F. de Fornel, and H. Sizun, "Measurement of light attenuation in dense fog conditions for fso applications," pp. 58910K-1-58910K-12, 2005.
- [236] M. Grabner and V. Kvicera, "Fog attenuation dependence on atmospheric visibility at two wavelengths for FSO link planning," in *Antennas and Propagation Conference (LAPC), Loughborough*, pp. 193-196, 2010.
- [237] M. S. Awan, R. Nebuloni, C. Capsoni, L. Csurgai-Horváth, S. Sheikh Muhammad, E. Leitgeb, F. Nadeem, and M. S. Khan, "Prediction of drop size distribution parameters for optical wireless communications through moderate continental fog," *International Journal on Satellite Communications and Networks*, vol. 28, 2 010.
- [238] U. Ketprom, S. Jaruwatanadilok, Y. Kuga, A. Ishimaru, and J. Ritcey, "Channel modeling for optical wireless communication through dense fog," *J. Opt. Netw.*, vol. 4, pp. 291-299, 2005.
- [239] K. W. Fischer, M. R. Witiw, and E. Eisenberg, "Optical attenuation in fog at a wavelength of 1.55 micrometers," *Atmospheric Research*, vol. 87, pp. 252-258, 2008.
- [240] E. Ferdinandov, K. dimitrov, A. Dandarov, and I. Bakalski, "A general model of the atmospheric scattering in the wavelength interval 300 - 1100nm," *Journal of Radio Engineering*, vol. 18, pp. 517-521, 2009.
- [241] J. Pesek, O. Fiser, J. Svoboda, and V. Schejbal, "Modeling of 830 nm FSO link attenuation in fog or wind turbulence," *Radio Engineering*, vol. 19, 2010.
- [242] J. Yang, Z. Niu, C. Shi, D. Liu, and Z. A. Li, "Microphysics of atmospheric aerosols during winter haze/fog events in nanjing," *Journal of Environmental Science*, vol. 31, pp. 1425-1431, 2010.

- [243] WMO, "Guide to meteorological instruments and methods of observation," *world meteorological organisation, ITU, Geneva, Switzerland*, 2006.
- [244] W. Eugster, "Fog Research," *Special Issue, Erde*, pp. 1-10, 2008.
- [245] J. Bendix, "A satellite-based climatology of fog and low-level stratus in Germany and adjacent areas " *Atmospheric Research* vol. 64, pp. 3-18, 2002.
- [246] P. Cereceda, P. Osses, H. Larrain, M. Farías, M. Lagos, R. Pinto, R. S. Schemenauer, and "Advective, orographic and radiation fog in the Tarapacá region, Chile," *Atmospheric Research*, vol. 64, pp. 261-271, 2002.
- [247] N. Blaunstein, S. Arnon, A. Zilberman, and N. Kopeika, "Applied aspects of optical communication and LIDAR," *Boca Raton : CRC Press, London*, pp. 53-55, 2010.
- [248] M. Z. Jacobson, *Atmospheric Pollution: History, Science, and Regulation*: Cambridge University Press, 2002.
- [249] A. K. Majumdar and J. C. Ricklin. *free-space laser communications, principles and advantages*, Springer, New York, 2008.
- [250] J. Rheims, J. Koser, and T. Wriedt, "Refractive-index measurements in the near-IR using an Abbe refractometer," *Journal of Meas. Sci. Technol*, vol. 8, pp. 601–605, 1997.
- [251] C. F. Bohren and D. R. Huffman, "Absorption and scattering of light by small particles " John Wiley and sons, New York, 1983.
- [252] H. C. Hulst and H. C. Van De Hulst, *Light scattering: by small particles*: Dover, 1957.
- [253] H. Weichel, "Laser beam propagation in the atmosphere.," *Bellingham: SPIE Optical Engineering*, vol. TT3, pp. 25-39, 1990.
- [254] G. M. Hale and M. R. Querry, "Optical Constants of Water in the 200-nm to 200- μ m Wavelength Region," *Journal of Applied Optics*, vol. 12, pp. 555-563, 1973.
- [255] C. E. Junge, "Atmospheric Chemistry," *Advances in Geophysics*. vol. Volume 4, ed: Elsevier, pp. 1-108, 1958.
- [256] R. A. McClatchey and A. F. C. R. Laboratories, *optical properties of the atmosphere*: United States Air Force, 1970.
- [257] M. S. khan, "FSO channel characterization for continental fog environments," *PhD thesis, Institute of Microwave and Photonic Engineering, TU Graz*, 2012.
- [258] A. Prokes, "Atmospheric effects on availability of free space optics systems," *Journal of Optical Engineering*, vol. 48, pp. 066001-10, 2009.
- [259] V. Kvicera, M. Grabner, and J. Vasicek, "Assessing availability performances of free space optical links from airport visibility data," in *Communication Systems Networks and Digital Signal Processing (CSNDSP), 7th International Symposium on*, pp. 562-565, 2010.
- [260] A. Prokes, "Atmospheric effects on availability of free space optics systems," *Journal of Optical Engineering*, vol. 48, pp. 066001-10, 2001.
- [261] I. I. Kim, B. McArthur, and E. Korevaar, "Comparison of laser beam propagation at 785 nm and 1550 nm in fog and haze for optical wireless communications," in *Proc. SPIE 4214*, Boston, MA, USA , 2001.
- [262] M. Grabner and V. Kvicera, "The wavelength dependent model of extinction in fog and haze for free space optical communication," *Journal of Optics Express*, vol. 19, pp. 3379-3386, 2012.

- [263] E. Ferdinandov, Kalin dimitrov, A. Dandarov, and I. Bakalski, "A general model of the atmospheric scattering in the wavelength interval 300 - 1100nm," *Radio Engineering*, vol. 18, 2009.
- [264] K. W. Fischer, M. R. Witiw, and E. Eisenberg, "Optical attenuation in fog at a wavelength of 1.55 micrometers," *Atmospheric Research*, vol. 87, pp. 252-258, 2008.
- [265] R. M. Pierce, J. Ramapras, and E. C. Eisenberg, "Optical attenuation in fog and clouds", " *Proc. SPIE 4530*, vol. 58 2001.
- [266] F. Nadeem, T. Javornik, E. Leitgeb, V. Kvicera, and G. Kandus, "Continental fog attenuation empirical relationship from measured visibility data," *Radio Engineering*, vol. 19, 2010.
- [267] M. Grabner and V. Kvicera, "Case study of fog attenuation on 830 nm and 1550 nm free-space optical links," in *Proceedings of the Fourth European Conference on Antennas and Propagation (EuCAP)*, pp. 1-4, 2010.
- [268] W. O. Popoola, Z. Ghassemlooy, C. G. Lee, and A. C. Boucouvalas, "Scintillation effect on intensity modulated laser communication systems - a laboratory demonstration," *Optics & Laser Technology*, vol. 42, pp. 682-692, 2009.
- [269] X. Zhu and J. M. Kahn, "Free-space optical communication through atmospheric turbulence channels," *IEEE Transactions on Communications*, vol. 50, pp. 1293-1300, 2002.
- [270] J. Zeller and T. Manzur, "Free-space optical communication at 1.55 μm and turbulence measurements in the evaporation layer," pp. 85400C-85400C, 2012.
- [271] A. Labeyrie, S. G. Lipson, and P. Nisenson, *An introduction to optical stellar interferometry*: Cambridge University Press, 2006.
- [272] H. Hemmati, "Near earth laser communications," *CRC Press, London, UK*, 2009.
- [273] H. E. Nistazakis, T. A. Tsiftsis, and G. S. Tombras, "Performance analysis of free-space optical communication systems over atmospheric turbulence channels," *Journal of IET Communications*, vol. 3, pp. 1402-1409, 2009.
- [274] K. Wakamori, K. Kazaura, and I. Oka, "Experiment on regional broadband network using free-space-optical communication systems," *Journal of Lightwave Technology*, vol. 25, pp. 3265-3273, 2007.
- [275] M. Cole and K. Kiasaleh, "Signal intensity estimators for free-space optical communications through turbulent atmosphere," *IEEE Photonics Technology Letters*, vol. 16, pp. 2395-2397, 2004.
- [276] M. Uysal, J. T. Li, and M. Yu, "Error rate performance analysis of coded freespace optical links over gamma-gamma atmospheric turbulence channels," *IEEE Transactions on Wireless Communications*, vol. 5, pp. 1229-1233, 2006.
- [277] L. Zhang, Z. Wu, Y. Zhang, and H. Detian, "Improved maximum likelihood detection for mitigating fading estimation error in free space optical communication," *Optical Engineering*, vol. 52, pp. 015004-015004, 2013.
- [278] X. Tang, S. Rajbhandari, W. O. Popoola, Z. Ghassemlooy, E. Leitgeb, S. S. Muhammad, and G. Kandus, "Performance of bpsk subcarrier intensity modulation free-space optical communications using a log-normal atmospheric turbulence model," in *Symposium on Photonics and Optoelectronic (SOPPO)*, pp. 1-4, 2010.

- [279] T. A. Tsiftsis, H. G. Sandalidis, G. K. Karagiannidis, and M. Uysal, "Optical wireless links with spatial diversity over strong atmospheric turbulence channels," *IEEE Transactions on Wireless Communications*, vol. 8, pp. 951-957, 2009.
- [280] L. C. Andrews, R. L. Phillips, and C. Y. Hopen, *laser beam scintillation with applications*: SPIE Press, 2001.
- [281] S. F. Clifford, "The classical theory of wave propagation in a turbulent medium," in *Laser Beam Propagation in the Atmosphere*. vol. 25, J. Strohbehn, Ed., ed: Springer Berlin Heidelberg, pp. 9-43, 1978.
- [282] P. A. Davidson, *Turbulence : An Introduction for Scientists and Engineers: An Introduction for Scientists and Engineers*: OUP Oxford, 2004.
- [283] L. C. Andrews and R. L. Phillips, *Laser beam propagation through random media*, second ed. Washington: SPIE Press, 2005.
- [284] L. C. Andrews, *Field Guide to Atmospheric Optics*: SPIE Press, 2004.
- [285] C. Rino, *The Theory of Scintillation with Applications in Remote Sensing*: Wiley, 2011.
- [286] L. B. Pedireddi and B. Srinivasan, "Characterization of atmospheric turbulence effects and their mitigation using wavelet-based signal processing," *IEEE Transactions on Communications*, vol. 58, pp. 1795-1802, 2010.
- [287] G. R. Osche, *Optical detection theory for laser applications*: Wiley-Interscience, 2002.
- [288] X. Tang, "Polarisation shift keying modulated free-space optical communication systems," *School of Computing, Engineering and Information Sciences, Doctor of Philosophy, University of Northumbria, Newcastle*, 2012.
- [289] J. Vitasek, J. Latal, S. Hejduk, J. Bocheza, P. Koudelka, J. Skapa, P. Siska, and V. Vasinek, "Atmospheric turbulences in Free Space Optics channel," in *Telecommunications and Signal Processing (TSP), 34th International Conference on*, pp. 104-107, 2011.
- [290] J. Libich and S. Zvanovec, "Influences of turbulences in near vicinity of buildings on free-space optical links," *Microwaves, Antennas & Propagation, IET*, vol. 5, pp. 1039-1044, 2011.
- [291] J. W. Strohbehn and S. F. Clifford, *Laser beam propagation in the atmosphere*: Springer-Verlag, 1978.
- [292] V. I. Tatarskiĭ, *Wave propagation in a turbulent medium*: Dover Publications, 1967.
- [293] J. W. Goodman, *Statistical Optics*. New York: John Wiley, 1985.
- [294] N. D. Chatzidiamantis, H. G. Sandalidis, G. K. Karagiannidis, and M. Matthaiou, "Inverse gaussian modeling of turbulence-induced fading in free-space optical systems," *IEEE/ OSA Journal of Lightwave Technology*, vol. 29, pp. 1590-1596,, 2011.
- [295] R. J. Sasiela, *Electromagnetic Wave Propagation in Turbulence: Evaluation and Application of Mellin Transforms*: SPIE Press, 2007.
- [296] H. Hodara, "Laser wave propagation through the atmosphere," *Proceedings of the IEEE*, vol. 54, pp. 368-375, 1966.
- [297] N. Perlot, "Characterization of signal fluctuations in optical communications with intensity modulation and direct detection through the turbulent

- atmospheric channel," *PhD thesis, School of Electronique, Université de Valenciennes*, 2005.
- [298] X. Tang, S. Rajbhandari, W. O. Popoola, Z. Ghassemlooy, E. Leitgeb, S. S. Muhammad, and G. Kandus, "Performance of BPSK Subcarrier Intensity Modulation Free-Space Optical Communications using a Log-normal Atmospheric Turbulence Model," in *Symposium on Photonics and Optoelectronic (SOPO)*, pp. 1-4, 2010.
 - [299] H. Le-Minh, Z. Ghassemlooy, M. Ijaz, S. Rajbhandari, O. Adebajo, S. Ansari, and E. Leitgeb, "Experimental study of bit error rate of free space optics communications in laboratory controlled turbulence," in *GLOBECOM Workshops (GC Wkshps), IEEE*, pp. 1072-1076, 2010.
 - [300] W. Xueying, L. Peng, and M. Matsumoto, "a study on atmospheric turbulence effects in full-optical free-space communication systems," in *Wireless Communications Networking and Mobile Computing (WiCOM), 2010 6th International Conference on*, pp. 1-5, 2010.
 - [301] F. S. Vetelino, C. Young, L. Andrews, and J. Reclons, "Aperture averaging effects on the probability density of irradiance fluctuations in moderate-to-strong turbulence," *Applied Optics*, vol. 46, pp. 2099-2108, 2007.
 - [302] A. K. Majumdar and J. C. Ricklin, "Free-Space Laser Communications: Principles and Advances," *Springer Science*, vol. LLC, 233, New York, USA, 2008.
 - [303] Z. Ghassemlooy, W. Popoola, and E. Leitgeb, "free-space optical communication using subcarrier modulation in gamma-gamma atmospheric turbulence," in *Transparent Optical Networks, ICTON. 9th International Conference on*, pp. 156-160, 2007.
 - [304] H. E. Nistazakis, E. A. Karagianni, A. D. Tsigopoulos, M. E. Fafalios, and G. S. Tombras, "Average capacity of optical wireless communication systems over atmospheric turbulence channels," *Journal of Lightwave Technology*, vol. 27, pp. 974-979, 2009.
 - [305] M. Al-Habash, L. C. Andrews, and R. Phillips, "Mathematical model for the irradiance probability density function of a laser beam propagating through turbulent media," *Optical Engineering*, vol. 40, pp. 1554-1562, 2001.
 - [306] J. W. Strohbehn, "Line-of-sight wave propagation through the turbulent atmosphere," *Proceedings of the IEEE*, vol. 56, pp. 1301-1318, 1968.
 - [307] W. Popoola, Z. Ghassemlooy, and V. Ahmadi, "Performance of sub-carrier modulated free-space optical communication link in negative exponential atmospheric turbulence environment," *International Journal of Autonomous and Adaptive Communications Systems*, vol. 1, pp. 342-355, 2008.
 - [308] J. H. Churnside and S. F. Clifford, "Log-normal Rician probability-density function of optical scintillations in the turbulent atmosphere," *J. Opt. Soc. Am. A*, vol. 4, pp. 1923-1930, 10/01 1987.
 - [309] Y. Fan and J. Cheng, "coherent free-space optical communications in lognormal-rician turbulence," *Communications Letters, IEEE*, vol. 16, pp. 1872-1875, 2012.
 - [310] L. C. Andrews and R. L. Phillips, "I-K distribution as a universal propagation model of laser beams in atmospheric turbulence," *J. Opt. Soc. Am. A*, vol. 2, pp. 160-163, 1985.
 - [311] G. Parry and P. Pusey, "K distributions in atmospheric propagation of laser light," *JOSA*, vol. 69, pp. 796-798, 1979.

- [312] S. F. Clifford and R. J. Hill, "Relation between irradiance and log-amplitude variance for optical scintillation described by the K distribution," *JOSA*, vol. 71, pp. 112-114, 1981.
- [313] M. S. Khan, S. S. Muhammad, M. S. Awan, V. Kvicera, M. Grabner, and E. Leitgeb, "Further results on fog modeling for terrestrial free-space optical links," *Optical Engineering*, vol. 51, pp. 031207-1, 2012.
- [314] F. S. Marzano, P. Nocito, S. Mori, F. Frezza, P. Lucantoni, M. Ferrara, E. Restuccia, and G. M. T. Beleffi, "Characterization of hydrometeor scattering effects and experimental measurements using near-infrared free-space urban links," in *Antennas and Propagation (EUCAP) 6th European Conference on*, pp. 330-334, 2012.
- [315] S. A. Zabidi, W. A. Khateeb, M. R. Islam, and A. W. Naji, "The effect of weather on free space optics communication (FSO) under tropical weather conditions and a proposed setup for measurement," in *International Conference on Computer and Communication Engineering (ICCCE)*, pp. 1-5, 2010.
- [316] M. S. Khan, E. Leitgeb, R. Nebuloni, C. Capsoni, M. Grabner, and V. Kvicera, "Effects of PSA on free-space optical links," in *Antennas and Propagation (EUCAP), 6th European Conference on*, pp. 1244-1247, 2012.
- [317] O. Wilfert, V. Kvicera, Z. Kolka, M. Grabner, and O. Fiser, "Propagation study of 850nm/58 GHz hybrid municipal system," pp. 781414-781414, 2010.
- [318] A. R. Raja, Q. J. Kagalwala, T. Landolsi, and M. El-Tarhuni, "Free-space optics channel characterization under uae weather conditions," in *Signal Processing and Communications, 2007. ICSPC 2007. IEEE International Conference on*, pp. 856-859, 2007.
- [319] W. O. Popoola, Z. Ghassemlooy, H. Haas, E. Leitgeb, and V. Ahmadi, "Error performance of terrestrial free space optical links with subcarrier time diversity," *Communications, IET*, vol. 6, pp. 499-506, 2012.
- [320] E. Leitgeb, S. S. Muhammad, B. Flecker, C. Chlestil, M. Gebhart, and T. Javornik, "The influence of dense fog on optical wireless systems, analysed by measurements in graz for improving the link-reliability," in *Transparent Optical Networks, 2006 International Conference on*, pp. 154-159, 2006.
- [321] D. K. Borah and D. G. Voelz, "Pointing error effects on free-space optical communication links in the presence of atmospheric turbulence," *Lightwave Technology, Journal of*, vol. 27, pp. 3965-3973, 2009.
- [322] V. Brazda, O. Fiser, and J. Svoboda, "FSO and radio link attenuation: meteorological models verified by experiment," pp. 81620N-81620N, 2011.
- [323] A. Jurado-Navas and A. Garcia-Zambrana, "Efficient lognormal channel model for turbulent FSO communications," *Electronics Letters*, vol. 43, pp. 178-179, 2007.
- [324] M. A. Khalighi, N. Schwartz, N. Aitamer, and S. Bourennane, "Fading reduction by aperture averaging and spatial diversity in optical wireless systems," *IEEE/OSA Journal of Optical Communications and Networking*, vol. 1, pp. 580-593, 2009.
- [325] B. Braua and D. Barua, "Channel capacity of MIMO FSO under strong turbulence conditions," *International Journal of Electrical & Computer Sciences*, vol. 11, pp. 1-5, 2011.

- [326] F. S. Vetelino, C. Young, L. Andrews, and J. Rekolons, "Aperture averaging effects on the probability density of irradiance fluctuations in moderate-to-strong turbulence," *Appl. Opt.*, vol. 46, pp. 2099-2108, 2007.
- [327] T. A. Tsiftsis, H. G. Sandalidis, G. K. Karagiannidis, and M. Uysal, "Optical wireless links with spatial diversity over strong atmospheric turbulence channels," *IEEE Transactions on Wireless Communications*, vol. 8, pp. 951-957, 2009.
- [328] M. S. Awan, L. C. Horwath, S. S. Muhammad, E. Leitgeb, F. Nadeem, and M. S. Khan, "Characterization of fog and snow attenuations for free-space optical propagation," *Journal of Communications*, vol. 4, pp. 533-545, 2009.
- [329] M. S. Awan, E. Leitgeb, M. Loeschig, F. Nadeem, and C. Capsoni, "Spatial and time variability of fog attenuations for optical wireless links in the troposphere," in *IEEE 70th Vehicular Technology Conference Fall (VTC)*, pp. 1-5, 2009.
- [330] R. N. Clark, "Spectroscopy of rocks and minerals, and principles of spectroscopy," in *Manual of remote sensing*. vol. 3, ed New York: John Wiley & Sons, Inc., pp. 3-58, 1999.
- [331] E. Leitgeb, M. Löschnigg, and T. Plank, "Relevant wavelengths for free space optics in future broadband networks," in *Access Networks and In-house Communications*, 2012.
- [332] S. A. Al-Gailani, A. B. Mohammad, and R. Q. Shaddad, "Evaluation of a 1 Gb/s Free Space Optic system in typical Malaysian weather," in *Photonics (ICP), IEEE 3rd International Conference on*, pp. 121-124, 2012.
- [333] A. Vavoulas, H. G. Sandalidis, and D. Varoutas, "Weather effects on FSO network connectivity," *Optical Communications and Networking, IEEE/OSA Journal of*, vol. 4, pp. 734-740, 2012.
- [334] T. Plank, M. Czaputa, E. Leitgeb, S. S. Muhammad, N. Djaja, B. Hillbrand, P. Mandl, and M. Schonhuber, "Wavelength selection on FSO-links," in *Antennas and Propagation (EUCAP), Proceedings of the 5th European Conference on*, pp. 2508-2512, 2011.
- [335] R. Babari, N. Hautière, É. Dumont, N. Paparoditis, and J. Misener, "Visibility monitoring using conventional roadside cameras—Emerging applications," *Transportation research part C: emerging technologies*, vol. 22, pp. 17-28, 2012.
- [336] R. Sabatini and M. Richardson, "Novel atmospheric extinction measurement techniques for aerospace laser system applications," *Infrared Physics & Technology*, 2012.
- [337] M. Grabner and V. Kvicera, "Fog attenuation dependence on atmospheric visibility at two wavelengths for FSO link planning," in *Antennas and Propagation Conference (LAPC), Loughborough*, pp. 193-196, 2010.
- [338] M. A. Naboulsi, F. D. Fornel, H. Sizun, M. Gebhart, E. Leitgeb, S. S. Muhammad, B. Klecker, and C. Chlestit, "Measured and predicted light attenuation in dense coastal upslope Fog at 650, 850 and 950 nm for free space optics applications. ," *Journal of Optical Engineering*, vol. 47, pp. 036001-14, 2008.
- [339] P. S. Chandran, C. Krishnakumar, W. Yuen, M. J. Rood, and R. Varma, "An open-path laser transmissometer for atmospheric extinction measurements," in *AIP Conference Proceedings*, p. 288, 2011.

- [340] D. Bäumer, S. Versick, and B. Vogel, "Determination of the visibility using a digital panorama camera," *Atmospheric Environment*, vol. 42, pp. 2593-2602, 2008.
- [341] C. P. Colvero, M. C. R. Cordeiro, G. V. de Faria, and J. P. von der Weid, "Experimental comparison between far- and near-infrared wavelengths in free-space optical systems," *Microwave and Optical Technology Letters*, vol. 46, pp. 319-323, 2005.
- [342] H. Koschmieder, "Theorie der horizontalen Sichtweite," *Beitrage zur physik der freien Atmosphere*, vol. 12, pp. 33-53, 1924.
- [343] M. Gregory and S. Badri-Hoeher, "Characterization of maritime RF/FSO channel," in *Space Optical Systems and Applications (ICSOS), International Conference on* pp. 21-27, 2011,.
- [344] S. S. Muhammad, P. Kohldorfer, and E. Leitgeb, "Channel modeling for terrestrial free space optical links," in *Transparent Optical Networks, Proceedings of 2005 7th International Conference*, pp. 407-410, 2005.
- [345] F. Nadeem, T. Javornik, E. Leitgeb, V. Kvicera, and G. kandus, "Continental fog attenuation empirical relationship from measured visibility data," *Journal of Radio Engineering*, vol. 19 (4), 2010.
- [346] S. Mori, F. Marzano, F. Frezza, G. Beleffi, V. Carrozzo, A. Busacca, and A. Ando, "Model analysis of hydrometeor scattering effects on free space near-infrared links," in *Optical Wireless Communications (IWOW), International Workshop on*, pp. 1-3, 2012.
- [347] R. Peach, J. Vickers, and T. Tidwell, "Scattering effect on link range for a 10 Gbps free space optical communication system," in *Avionics, Fiber-Optics and Photonics Technology Conference (AVFOP), 2012 IEEE*, 2012, pp. 78-79.
- [348] J. Vitasek, J. Látal, V. Vašínek, S. Hejduk, A. Liner, M. Papes, P. Koudelka, and A. Ganiyev, "The fog influence on bit error ratio," pp. 86970L-86970L, 2012.
- [349] M. T. Rahman, S. Iqbal, and M. M. Islam, "Modeling and performance analysis of free space optical communication system," in *Informatics, Electronics & Vision (ICIEV), 2012 International Conference on*, pp. 211-218, 2012.
- [350] M. Ijaz, Z. Ghassemloooy, H. Le Minh, S. Rajbhandari, J. Perez, and A. Gholami, "Bit error rate measurement of free space optical communication links under laboratory-controlled fog conditions," in *16th European Conference on Networks and Optical Communications (NOC)*, pp. 52-550, 2011.
- [351] N. A. M. Nor, I. M. Rafiqul, W. Al-Khateeb, and S. A. Zabidi, "Environmental effects on free space earth-to-satellite optical link based on measurement data in Malaysia," in *Computer and Communication Engineering (ICCCE), International Conference on*, pp. 694-699, 2012.
- [352] A. A. G. Abushagur, F. M. Abbou, M. Abdullah, and N. Misran, "Performance analysis of a free-space terrestrial optical system in the presence of absorption, scattering, and pointing error," *Optical Engineering*, vol. 50, pp. 075007-075007, 2011.
- [353] F. Nadeem, M. Khan, and E. Leitgeb, "Optical wireless link availability estimation through Monte Carlo simulation," in *Telecommunications*

- (ConTEL), *Proceedings of the 11th International Conference on*, pp. 345-350, 2011.
- [354] S. S. Muhammad, B. Flecker, E. Leitgeb, and M. Gebhart, "Characterization of fog attenuation in terrestrial free space links," *Journal of Optical Engineering*, vol. 46, pp. 066001-066006, 2007.
 - [355] M. Aharonovich and S. Arnon., "Performance improvement of optical wireless communication through fog with a decision feedback equalizer," *J. Opt. Soc. Am. A*, vol. 22, pp. 1646-1654, 2005.
 - [356] O. Barsimantov and V. V. Nikulin, "Adaptive Optimization of a Free Space Laser Communication System Under Dynamic Link Attenuation," *Optical Communications and Networking, IEEE/OSA Journal of*, vol. 3, pp. 215-222, 2011.
 - [357] Z. Kolka, V. Biolkova, and D. Biolek, "Statistical analysis of fade events on FSO systems," in *Proceedings of the 11th WSEAS international conference on Applied Computer and Applied Computational Science*, pp. 184-187, 2012.
 - [358] M. Awan, E. Leitgeb, F. Nadeem, M. Khan, and C. Capsoni, "A new method of predicting continental fog attenuations for terrestrial optical wireless link," in *Next Generation Mobile Applications, Services and Technologies, NGMAST. Third International Conference on*, pp. 245-250, 2009.
 - [359] B. R. Strickland, M. J. Lavan, E. Woodbridge, and V. Chan, "Effects of fog on the bit-error rate of a free space laser communication system," *Journal of applied optics*, vol. 38, pp. 424-431, 1999.
 - [360] J. M. Senior, *Optical Fiber Communication Principles And Practice 2ed*: Pearson Education, 2006.
 - [361] M. Azadeh, *Fiber Optics Engineering*: Springer London, Limited, 2009.
 - [362] H. Le-Minh, Z. Ghassemlooy, M. Ijaz, S. Rajbhandari, O. Adebajo, S. Ansari, and E. Leitgeb, "Experimental study of bit error rate of free space optics communications in laboratory controlled turbulence," *IEEE Globecom Workshop on Optical Wireless Communications in Miami, Florida, USA*, 2010.
 - [363] R. Paudel, Z. Ghassemlooy, H. Le-Minh, and S. Rajbhandari, "Modelling of free space optical link for ground-to-train communications using a Gaussian source," *Optoelectronics, IET*, vol. 7, pp. 1-8, 2013.
 - [364] S. Zvanovec, J. Perez, Z. Ghassemlooy, S. Rajbhandari, and J. Libich, "Route diversity analyses for free-space optical wireless links within turbulent scenarios," *Optics Express*, vol. 21, pp. 7641-7650, 2013.
 - [365] M.-A. Khalighi, N. Schwartz, N. Aitamer, and S. Bourennane, "Fading reduction by aperture averaging and spatial diversity in optical wireless systems," *Optical Communications and Networking, IEEE/OSA Journal of*, vol. 1, pp. 580-593, 2009.
 - [366] M. Ijaz, O. Adebajo, S. Ansari, Z. Ghassemlooy, S. Rajbhandari, H. Le Minh, A. Gholami, and E. Leitgeb, "Experimental Investigation of the Performance of OOK-NRZ and RZ Modulation Techniques under Controlled Turbulence Channel in FSO Systems," *IEEE Trans*, 2010.
 - [367] N. Liu, W. D. Zhong, Y. He, K. H. Heng, and T. H. Cheng, "Comparison of nrz and rz modulations in laser intersatellite communication systems,"

Proceedings of the 2008 International Conference on Advanced Infocomm Technology, p. 677, 2008.

- [368] W. R. Leeb, P. J. Winter, and M. Pauer, "The potential of return-to-zero coding in optically amplified lasercom systems " *LEOS '99*, vol. 1, pp. 224-225, 1999.
- [369] N. Chand, J. J. Loriz, A. J. Hunton, and B. M. Eteson, "Performance comparison of NRZ and RZ modulations with and without forward error corrections for free-space optical communication " presented at the Proceedings of SPIE 58920U, 2005.
- [370] N. Chand, A. J. Hunton, and B. M. Eteson, "A comparative study of 2.667 Gb/s OOK, DPSK, and PPM modulation formats for FSO applications," pp. 70910G-70910G, 2008.
- [371] H. Burris, A. Reed, N. Namazi, W. Scharpf, M. Vicheck, and M. Stell, "Adaptive thresholding for free-space optical communication receivers with multiplicative noise," in *Aerospace Conference Proceedings, IEEE*, pp. 3-1473-3-1480 vol. 3, 2002.
- [372] H. Burris Jr, C. Moore, L. Swingen, L. Wasiczko, R. Mahon, M. Stell, W. Rabinovich, J. Murphy, G. Gilbreath, and W. Scharpf, "Laboratory implementation of an adaptive thresholding system for free-space optical communication receivers with signal dependent noise," in *Optics & Photonics 2005*, 2005, pp. 58920W-58920W-20.
- [373] X. Tang, "Polarisation shift keying modulated free-space optical communication systems," *School of Computing, Engineering and Information Sciences, Doctor of Philosophy, University of Northumbria, Newcastle*, 2009.
- [374] Z. G. X.Tang, S. Rajbhandari, W. O.Popoola, and C. G, Lee, "Coherent optical binary polarization shift keying heterodyne system in the free space optical turbulence channel," *IET Microwaves, Antennas and Propagation*, vol. 5, pp. 1031-1038, 2011.
- [375] H. Kaushal, V.K.Jain, and S. Ka, "International Journal of Electrical and Computer Engineering," *Effect of atmospheric turbulence on acquisition time of ground to deep space optical communication system*, vol. 4, pp. 730-734, 2009.
- [376] S. Ohteru and N. Takachio, "Optical signal quality monitor using direct Q -factor measurement," *IEEE Photonics Technology Letters*, vol. 11, pp. 1307-1309, 1999.
- [377] F. Matera and M. Settembre, "Role of Q -factor and of time jitter in the performance evaluation of optically amplified transmission systems," *Selected Topics in Quantum Electronics, IEEE Journal of*, vol. 6, pp. 308-316, 2000.
- [378] I. Shake, H. Takara, K. Uchiyama, and Y. Yamabayashi, "Quality monitoring of optical signals influenced by chromatic dispersion in a transmission fiber using averaged Q -factor evaluation," *Photonics Technology Letters, IEEE*, vol. 13, pp. 385-387, 2001.
- [379] C. Abou-Rjeily and A. Slim, "Cooperative diversity for free-space optical communications: transceiver design and performance analysis," *Communications, IEEE Transactions on*, vol. 59, pp. 658-663, 2011.

- [380] W. O. Popoola, Z. Ghassemlooy, C. Lee, and A. Boucouvalas, "Scintillation effect on intensity modulated laser communication systems—a laboratory demonstration," *Optics & Laser Technology*, vol. 42, pp. 682-692, 2010.
- [381] H. Kaushal, V. Kumar, A. Dutta, H. Aennam, V. Jain, S. Kar, and J. Joseph, "Experimental study on beam wander under varying atmospheric turbulence conditions," *Photonics Technology Letters, IEEE*, vol. 23, pp. 1691-1693, 2011.
- [382] A. Garcia-Zambrana, C. Castillo-Vazquez, B. Castillo-Vazquez, and A. Hiniesta-Gomez, "Selection transmit diversity for FSO links over strong atmospheric turbulence channels," *Photonics Technology Letters, IEEE*, vol. 21, pp. 1017-1019, 2009.
- [383] N. Letzepis and A. Fabregas, "Outage probability of the MIMO Gaussian free-space optical channel with PPM," in *Information Theory, 2008. ISIT, IEEE International Symposium on*, pp. 2649-2653, 2008.
- [384] T. Fath and H. Haas, "Performance Comparison of MIMO Techniques for Optical Wireless Communications in Indoor Environments," 2013.
- [385] J. Libich, S. Zvanovec, and M. Mudroch, "Mitigation of time-spatial influence in free-space optical networks utilizing route diversity," in *SPIE LASE*, pp. 82460-6, 2012.
- [386] I. B. Djordjevic, "Adaptive modulation and coding for free-space optical channels," *J. Opt. Commun. Netw.*, vol. 2, pp. 221-229, 2010.
- [387] H. G. Sandalidis, "Coded free-space optical links over strong turbulence and misalignment fading channels," *Communications, IEEE Transactions on*, vol. 59, pp. 669-674, 2011.
- [388] D. Pham Tien, A. M. Shah, K. Kazaura, K. Wakamori, T. Suzuki, K. Omae, M. Matsumoto, Y. Aburakawa, K. Takahashi, T. Nakamura, T. Higashino, K. Tsukamoto, and S. Komaki, "Investigation of suitability of RF signal transmission over FSO links," in *High Capacity Optical Networks and Enabling Technologies, HONET, International Symposium on*, pp. 1-6, 2007.
- [389] K. Kazaura, P. Dat, A. Shah, T. Suzuki, K. Wakamori, M. Matsumoto, T. Higashino, K. Tsukamoto, and S. Komaki, "Studies on a next generation access technology using radio over free-space optic links," in *Next Generation Mobile Applications, Services and Technologies, NGMAST, The Second International Conference on*, pp. 317-324, 2008.